VOLUME 81 APRIL 21, 1977 NUMBER 8

JPCHAx

THE JOURNAL OF PHYSICAL CHEMISTRY

PUBLISHED BIWEEKLY BY THE AMERICAN CHEMICAL SOCIETY

THE JOURNAL OF

PHYSICAL CHEMISTRY

Published by the
AMERICAN CHEMICAL SOCIETY
BOOKS AND JOURNALS DIVISION

D. H. Michael Bowen, Director

Marjorie Laflin, Assistant to the Director

Editorial Department: Charles R. Bertsch, Head; Marianne C. Brogan, Associate Head; Celia B. McFarland, Joseph E. Yurvati, Assistant Editors

Magazine and Production Department: Bacil Guiley, Head

Research and Development Department: Seldon W. Terrant, Head

Advertising Office: Centcom, Ltd., 50 W. State St., Westport, Conn. 06880.

Published biweekly by the American Chemical Society at 20th and Northampton Sts., Easton, Pennsylvania 18042. Second class postage paid at Washington, D.C. and at additional mailing offices.

Editorial Information

Instructions for authors are printed in the first issue of each volume. Please conform to these instructions when submitting manuscripts.

Manuscripts for publication should be submitted to *The Journal of Physical Chemistry*, Department of Chemistry, University of Minnesota, Minneapolis, Minn. 55455. Correspondence regarding **accepted papers and proofs** should be directed to the Editorial Department at the ACS Easton address.

Page charges of $60.00 per page may be paid for papers published in this journal. Ability to pay does not affect acceptance or scheduling of papers.

Bulk reprints or photocopies of individual articles are available. For information write to Business Operations, Books and *Journals Division at the ACS Washington* address.

Requests for **permission to reprint** should be directed to Permissions, Books and Journals Division at the ACS Washington address. The American Chemical Society and its Editors assume no responsibility for the statements and opinions advanced by contributors.

Subscription and Business Information

1977 Subscription rates—including surface postage

	U.S.	PUAS	Canada, Foreign
Member	$24.00	$33.00	$34.00
Nonmember	96.00	105.00	106.00
Supplementary material	15.00	19.00	20.00

Air mail and air freight rates are available from Membership & Subscription Services, at the ACS Columbus address.

New and renewal subscriptions should be sent with payment to the Office of the Controller at the ACS Washington address. **Changes of address** must include both old and new addresses with ZIP code and a recent mailing label. Send all address changes to the ACS Columbus address. Please allow six weeks for change to become effective. **Claims for missing numbers** will not be allowed if loss was due to failure of notice of change of address to be received in the time specified: if claim is dated (a) North America—more than 90 days beyond issue date, (b) all other foreign—more than 1 year beyond issue date; or if the reason given is "missing from files". Hard copy claims are handled at the ACS Columbus address.

Microfiche subscriptions are available at the same rates but are mailed first class to U.S. subscribers, air mail to the rest of the world. *Direct all inquiries to Special Issues* Sales, at the ACS Washington address or call (202) 872-4554. **Single issues** in hard copy and/or microfiche are available from Special Issues Sales at the ACS Washington address. Current year $4.75. Back issue rates available from Special Issues Sales. **Back volumes** are available in hard copy and/or microform. Write to Special Issues Sales at the ACS Washington address for further information. **Microfilm** editions of ACS periodical publications are available from volume 1 to the present. For further information, contact Special Issues Sales at the ACS Washington address. **Supplementary material** mentioned *in the journal appears in the microfilm* edition. Single copies may be ordered directly from Business Operations, Books and Journals Division, at the ACS Washington address.

	U.S.	PUAS, Canada	Other Foreign
Microfiche	$2.50	$3.00	$3.50
Photocopy			
1–7 pages	4.00	5.50	7.00
8–20 pages	5.00	6.50	8.00

Orders over 20 pages are available only on microfiche, 4 × 6 in., 24X, negative, silver halide. Orders must state photocopy or microfiche if both are available. Full bibliographic citation including names of all authors and prepayment are required. Prices are subject to change.

American Chemical Society
1155 16th Street, N.W.
Washington, D.C. 20036
(202) 872-4600

Member & Subscription Services
American Chemical Society
P.O. Box 3337
Columbus, Ohio 43210
(614) 421-7230

Editorial Department
American Chemical Society
20th and Northampton Sts.
Easton, Pennsylvania 18042
(215) 258-9111

Notice to Authors last printed in the issue of January 13, 1977

THE JOURNAL OF

PHYSICAL CHEMISTRY

Volume 81, Number 8 April 21, 1977

JPCHAx 81(8) 687–810 (1977)

ISSN 0022-3654

COMMUNICATIONS TO THE EDITOR

■ Supplementary and/or miniprint material for this paper is available separately (consult the masthead page for ordering information); it will also appear following the paper in the microfilm edition of this journal.

* In papers with more than one author, the asterisk indicates the name of the author to whom inquiries about the paper should be addressed.

AUTHOR INDEX

ANNOUNCEMENT

On the last two pages of this issue you will find reproduced the table of contents of the April 1977 issue of the *Journal of Chemical and Engineering Data.*

THE JOURNAL OF
PHYSICAL CHEMISTRY

VOLUME 81, NUMBER 8 APRIL 21, 1977

The Triplet Mercury Photosensitized Decomposition of Ethane at High Intensity

Jung-Tsang Cheng, Ying-Sheng Lee, and Chuin-Tih Yeh*

Institute of Chemistry, National Tsing Hua University, Hsinchu, Taiwan 300, Republic of China *(Received October 3, 1975; Revised Manuscript Received February 4, 1977)*

The triplet mercury photosensitized decomposition of ethane at high intensity and low conversion leads to H_2, CH_4, C_3H_8, and n-C_4H_{10} as major products. The generation rates of these products vary with light intensity, pressure, and photolysis time. A mechanism is proposed for ethane decomposition and products formation. Steady state concentrations of radicals were calculated from the experimental data. A rate constant value has been obtained for the following reaction at 300 Torr ethane pressure and 35 °C: $H + CH_3 \rightarrow CH_4$, $k = 1.5 \times 10^{14}$ cm^3 mol^{-1} s^{-1}.

Introduction

Radical reaction has been of interest to gas kineticists for many years. The discharge method (microwave or high frequency) is generally used to measure the combination rate of hydrogen atoms and methyl radicals.[1-4] Because the excited methane molecule generated in the combination reaction tends to decompose, only a small portion of methane will remain as the stable product through collision at pressures of less than 10 Torr, which will permit the microwave discharge. An alternative system to measure the rate constant of the combination reaction at higher pressure is the mercury photosensitization of alkanes.

The interaction between the $^3P_1$ mercury atom and alkane molecule has been known for several decades.[6-9] Although molecular phosphorescence,[10] $Hg(6^3P_0)$,[11] and HgH[12] have been detected as metastable intermediates, the final chemical effect of this interaction may be regarded as the dissociation of a hydrogen atom from an alkane molecule:

$$Hg(6^3P_1) + RH \rightarrow R + H + Hg(6^1S_0)$$

It has been found that n-butane and hydrogen molecules are the major products of the reaction of the mercury-photosensitized decomposition of ethane[13-15] at low light intensities. In this investigation, high resonance radiation intensity is used at room temperature to dissociate the ethane molecule. Under these conditions, the detailed mechanism of the primary process and the combination of hydrogen atom and methyl radical may be elucidated.

Experimental Section

Ethane gas was obtained from the China Petroleum Co. It was purified through vacuum fractional distillation in a vacuum system. After purification, only 40 ppm of propane and 2 ppm of ethylene were detected as impurity.

Cylindrical quartz reaction cells were used for all photolysis work. A drop of mercury was added to supply the mercury vapor pressure at 35 °C. The 2537-Å light was delivered from a low-pressure mercury lamp. The projected light intensity in the cell was adjusted by varying the distance between the light source and the cell.

The product mixture was analyzed with a gas chromatograph. Hydrocarbons were separated by a 0.25 in. × 40 ft DMS column and a 0.25 in. × 6 ft Ucon column. A flame ionization detector was used for this analysis. The relative yield of hydrogen to ethane was measured by injecting another portion of mixture into a $^1/_8$ in. × 10 ft column of silica gel. A thermal conductivity detector was used here.

Results and Discussion

The products detected in low conversion experiments were hydrogen, methane, propane, n-butane, and minor amounts of ethylene. In the high conversion experiments, isobutane and other hydrocarbons (higher than C_4) were also found. Table I shows the variation of the yield of

TABLE I: Effect of Light Intensity on $2\Delta[n\text{-}C_4H_{10}]/-\Delta[C_2H_6]$[a]

Distance between lamp and cell, cm	Photolysis time, min	Relative yield of products					% conversion	$2\Delta[n\text{-}C_4H_{10}]/-\Delta[C_2H_6]$[b]
		H_2	CH_4	C_2H_6	C_3H_8	$n\text{-}C_4H_{10}$		
5	3	5.98	2.13	1000	0.84	5.31	1.32	0.804
10	10	9.79	2.36	1000	0.97	6.21	1.50	0.830
125	150	5.33	1.21	1000	0.51	4.43	1.02	0.870
250	210	5.78	0.30	1000	0.15	3.43	0.72	0.952
500	480	4.90	c	1000	c	4.44	0.89	1.0

[a] Ethane pressure, 300 Torr; temperature, 25 °C. [b] $-\Delta[C_2H_6] = {}^1/_2\Delta[CH_4] + {}^3/_2\Delta[C_3H_8] + 2\Delta[C_4H_{10}]$. [c] Negligible.

major products on the light intensity. At the lowest intensity (the distance between the light source and the photolysis cell is 500 cm), the yield of methane and propane was small and considered negligible. All the decomposed ethane molecules were converted into hydrogen molecule, *n*-butane, and some ethylene at low conversion. These products can be attributed to the following simple mechanism:

$$Hg(6^1S_0) + h\nu(2537\ A) \rightarrow Hg(6^3P_1) \quad I_a$$

$$Hg(6^3P_1) + C_2H_6 \rightarrow H + C_2H_5 + Hg(6^1S_0)$$

$$H + C_2H_6 \rightarrow H_2 + C_2H_5 \quad (1)$$

$$2C_2H_5 \rightarrow n\text{-}C_4H_{10} \quad (2)$$

$$2C_2H_5 \rightarrow C_2H_6 + C_2H_4 \quad (3)$$

As the light intensity increases, propane and methane will be additionally produced. The following reactions will therefore become necessary:

$$H + C_2H_5 \rightarrow 2CH_3 \quad (4)$$

$$H + C_2H_5 \rightarrow C_2H_6 \quad (5)$$

$$H + CH_3 \rightarrow CH_4 \quad (6)$$

$$2CH_3 \rightarrow C_2H_6 \quad (7)$$

$$CH_3 + C_2H_5 \rightarrow C_3H_8 \quad (8)$$

$$CH_3 + C_2H_5 \rightarrow CH_4 + C_2H_4 \quad (9)$$

The kinetic relationship between reaction 4 and reaction 1 derived from the preceding mechanism can be expressed by

$$\text{rate } 4/\text{rate } 1 = k_4[C_2H_5]/k_1[C_2H_6] \quad (I)$$

The steady state ethyl radical concentration is, more or less, proportional to $I_a^{1/2}$. Therefore process 4 will be favored at high intensity and, as a result, the yield of methane and propane will be significant.

At constant light intensity, the effect of ethane pressure on the nature of photolyzed products has also been investigated. In Figure 1, the yield of methane and propane per decomposed ethane molecule, at constant irradiation time, decreases as the pressure increases. Two factors are involved.

(a) *Unimolecular Decomposition of Excited Ethane.* The excited ethane molecule which is temporarily produced on the combination of a hydrogen atom and an ethyl radical may decompose (D) into methyl radicals or become stabilized (S) through collision, i.e., processes 4 and 5, respectively. The relative rate of these two processes is pressure dependent as has been shown by the extensive work of Rabinovitch and Setser on a variety of alkanes.[5] At high pressure, S/D has a large value, the production of CH_3 radical is less. Consequently, the yield of methane and propane is minimal.

(b) *Ethane Molecule Concentration.* The decrease in the production of methane and propane at the high ethane pressure can also be partially explained by eq I. Since ethane pressure has minor effect on the $(k_4/k_1)[C_2H_5]$ value under the present experimental condition of which the $Hg(6^3P_1)$ is almost completely quenched, rate 4/rate 1 will be more or less inversely proportional to the ethane pressure. As a result, hydrogen molecule and *n*-butane (rather than methane and propane) will become the favorable products at high ethane pressure as was predicted by the preceding reaction mechanism.

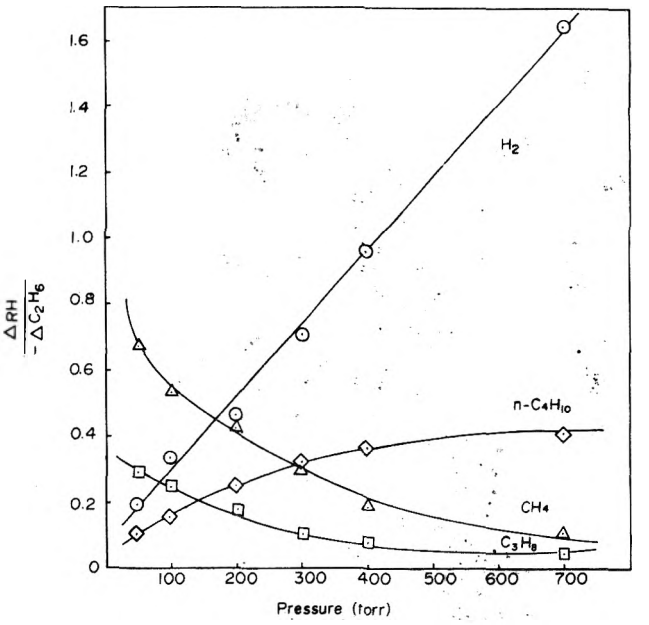

Figure 1. Effect of ethane pressure on the nature of the products; irradiation time, 10 min, temperature, 20 °C, distance between lamp and cell, 5 cm; $-\Delta[C_2H_6] = {}^1/_2\Delta[CH_4] + {}^3/_2\Delta[C_3H_8] + 2\Delta[n\text{-}C_4H_{10}]$.

TABLE II: Effect of Photolysis Time on the Nature of the Products at 300 Torr of Ethane

Time, s	Relative yields of products (Y_{RHt})					
	H_2	CH_4	C_2H_6	C_3H_8	$n\text{-}C_4H_{10}$	C_2H_4
0	0.000	0.030	1000	0.055	0.000	0.002
120	1.301	0.444	1000	0.535	0.960	0.022
180			1000	0.888	1.876	
240	2.636	0.895	1000	1.064	1.960	0.022
300	3.636	1.233	1000	1.301	2.383	
420	4.732	2.197	1000	1.671	3.109	0.018
600	6.473	2.771	1000	2.383	4.005	0.018

Investigations also have been made on the effect of reaction conversion upon the composition of the photolytic products at constant light intensity and 300 Torr ethane pressure (Table II). The average generation rate (R_{RHt}) of each product at time t can be calculated from its relative yield (Y_{RHt} of Table II), and illustrated by the following equation:

$$R_{RHt} = \frac{[RH]_t}{t} = \frac{Y_{RHt}P/RT}{1000t}$$

$$= 5.38 \times 10^{-11}\frac{Y_{RHt}P(\text{Torr})}{t}\ \text{mol cm}^{-3}\ \text{s}^{-1} \quad (II)$$

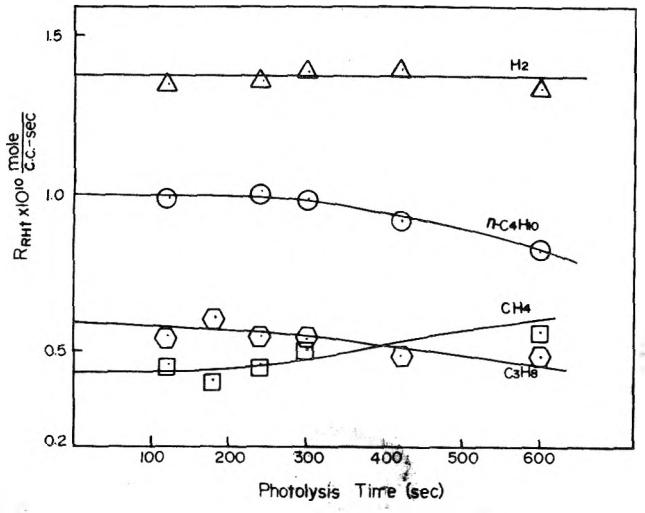

Figure 2. The variations of the averaged generation rates of the photolytical products (see text) as a function of irradiation time at 300 Torr ethane pressure and 35 °C.

In Figure 2, R_{RHt} values are seen varying with the photolysis time. It is quite clear that the participation of accumulated products in the reaction causes this variation. In order to minimize the complication of secondary reactions, only the initial product rates (R_{RH}) are under consideration. These R_{RH} values may be correlated with radical concentrations according to the following equations:

$$R_{H_2} = k_1[H][C_2H_6] \quad \text{(III)}$$

$$R_{CH_4} = k_6[H][CH_3] + k_9[CH_3][C_2H_5] \quad \text{(IV)}$$

$$R_{C_3H_8} = k_8[CH_3][C_2H_5] \quad \text{(V)}$$

$$R_{C_4H_{10}} = k_2[C_2H_5]^2 \quad \text{(VI)}$$

where [H], [CH_3], and [C_2H_5] represent the steady state radical concentrations at the initial photolytic stage. Process 8 is the cross combination reaction between methyl and ethyl radicals. Theoretically, its rate constant, k_8, can be calculated from the rate constants of autocombination reactions, k_2 and k_7, through the following equation:[16]

$$k_8^2 = 4k_2k_7 \quad \text{(VII)}$$

From (III)

$$[H] = R_{H_2}/k_1[C_2H_6] \quad \text{(VIII)}$$

Substitute eq VI and VII into eq V, we obtain

$$[CH_3] = R_{C_3H_8}/2k_7^{1/2}R_{n\text{-}C_4H_{10}}^{1/2} \quad \text{(IX)}$$

Equations VIII and IX have been used to calculate the steady state concentrations of hydrogen atom and methyl radical. The reliability of these calculated concentrations depends heavily on the accuracy of k_1 and k_7. Fortunately both these constants have been measured through many experimental techniques. Their values are in excellent agreement. Recently log k_1 = (1.40 ± 0.2) − (9400 ± 300)/2.3RT[17] and log k_7 = 13.4 ± 0.1[18] were generally accepted. The corresponding k_1 and k_7 at 35 °C are (2.0 ± 1.2) × 10^7 and (2.4 ± 0.4) × 10^{13} cm^3 mol^{-1} s^{-1}, respectively.

The disproportionation-combination ratios of alkyl radicals have also been reviewed recently.[19] The observed k_d/k_c of the reaction between methyl and ethyl radicals is 0.039, i.e.

$$k_9[CH_3][C_2H_5] = 0.039R_{C_3H_8} \quad \text{(X)}$$

TABLE III: Summary of the Determined Rate Constant Values of the Combination Reactions between Hydrogen Atom and Methyl Radical

Reaction	Rate constant	Pressure	Ref
H + CH_3 → CH_4	1 × 10^{12}	1.2 Torr of H_2	1
	3 × 10^{12}	1.3 Torr of Ar	2
	1 × 10^{13}	6.7 Torr of Ar	3
	2.3 × 10^{12}	8 Torr of Ar	4
	1.5 × 10^{14}	300 Torr of ethane	This work
	2.3 × 10^{14}	theoretical high pressure limit prediction	20

Then eq IV may be revised as

$$k_6 = \frac{R_{CH_4} - 0.039R_{C_3H_8}}{[H][CH_3]} \quad \text{(XI)}$$

k_6 is the reaction rate constant for the combination of a hydrogen atom and a methyl radical. This constant has been determined many times in the literature and is seen in the Table III increasing with pressure. Its experimental value is on the order of 10^{12} in the pressure range of few Torr, but has already increased to 1.5 × 10^{14} cm^3 mol^{-1} s^{-1} at a pressure of 300 Torr according to the calculations of eq XI. This variation is, again, expected from the following mechanism:

$$H + CH_3 \underset{k_{6b}}{\overset{k_{6a}}{\rightleftharpoons}} CH_4^* \xrightarrow{k_{6c}[M]} CH_4 \qquad (k_6)$$

Under high pressure, $k_{6c}[M] \gg k_{6b}$. Under this condition k_6 reaches a limiting high value, k_{6a}. This limiting value has already been theoretically calculated[20] to be 2.3 × 10^{14} cm^3 mol^{-1} s^{-1}. It is of interest to know that this theoretical value is only slightly larger than 1.5 × 10^{14} cm^3 mol^{-1} s^{-1} of the present study. Doubtlessly, the rate of the reaction 6c must be comparable to, if not larger than, that of the reaction 6b at 300 Torr pressure.

Conclusion

The mechanism of Hg photosensitization of ethane at high intensity and low conversion has been proposed. With this mechanism, the measured generation rates of major products may be used to investigate the rate of the H + CH_3 → CH_4 reaction. A competitive technique is used in this investigation. Since both of the rate constants that have been referred to are very reliable, the error on the absolute value of this measured rate is assessed to be less than 100%. Practically, the Hg photosensitization reaction may be performed at any pressure. Consequently the pressure effect on the rate constant of this important radical reaction may be studied with this classical technique.

Acknowledgment. We gratefully acknowledge the support of the National Science Council of Republic of China under Contract No. NSC-64M-0204-03(02).

References and Notes

(1) T. Teng and W. E. Jones, *J. Chem. Soc., Faraday Trans. 1*, **68**, 1267 (1972).
(2) J. M. Brown, P. B. Coates, and B. A. Thrush, *Chem. Commun.*, 843 (1966).
(3) A. F. Dodonov, G. K. Lavroskaya, and V. L. Talroze, *Kinet. Katal.*, **10**, 477 (1969).
(4) M. P. Halstead, D. A. Leathard, R. M. Marshall, and J. H. Purnell, *Proc. R. Soc. London, Ser. A*, **316**, 575 (1970).
(5) B. S. Rabinovitch and D. W. Setser, *Adv. Photochem.*, **3**, 1 (1964).
(6) G. Cario and J. Frank, *Z. Phys.*, **11**, 161 (1922); S. D. Gleditsch and J. V. Michael, *J. Phys. Chem.*, **79**, 409 (1975).
(7) J. G. Calvert and J. N. Pitts, Jr., "Photochemistry", Wiley, New York, N.Y., 1966.

(8) R. J. Cvetanovic, *Prog. React. Kinet.*, **2**, 39 (1964).
(9) C. H. Bamford and C. F. H. Tipper, "Comprehensive Chemical Kinetics", Vol. 5, Elsevier, New York, N.Y., 1972.
(10) O. P. Strausz, J. M. Campbell, S. De Paoli, H. S. Sandhu, and H. E. Gunning, *J. Am. Chem. Soc.*, **95**, 732 (1973).
(11) A. C. Vikis, G. Torrie, and D. J. LeRoy, *Can. J. Chem.*, **48**, 3771 (1970).
(12) A. C. Vikis and D. J. LeRoy, *Can. J. Chem.*, **50**, 595 (1972).
(13) E. W. R. Steacie, "Atomic and Free Radical Reactions", Reinhold, New York, N.Y., 1954.
(14) R. A. Back, *Can. J. Chem.*, **37**, 1834 (1959).
(15) B. deB. Darwent and E. W. R. Steacie, *J. Chem Phys.*, **16**, 381 (1948).
(16) J. A. Kerr and A. F. Trotman-Dickenson, *Prog. React. Kinet.*, **1**, 107 (1961).
(17) W. E. Jones, S. D. MacKnight, and L. Teng, *Chem. Rev.*, **73**, 407 (1973).
(18) E. Whittle, *MTP Int. Rev. Sci.*, 9, 75 (1972).
(19) M. J. Gibian and R. C. Corley, *Chem. Rev.*, **73** 441 (1973).
(20) S. W. Benson and H. E. O'Neil, *Natl. Stand. Ref. Data Ser., Natl. Bur. Stand.*, **No. 21** (1970).

Porphyrin Films. 3. Photovoltaic Properties of Octaethylporphine and Tetraphenylporphine

Frank J. Kampas and Martin Gouterman*

Department of Chemistry, University of Washington, Seattle, Washington 98195 *(Received October 7, 1976)*

Publication costs assisted by the National Institutes of Health

Electrical and photovoltaic properties of Al|octaethylporphine|Ag and also Al|tetraphenylporphine|Ag sandwich cells are reported. These properties indicate the presence of a Schottky barrier formed by transfer of electrons from the aluminum to the porphyrin. Most or all of the porphyrin is depleted of holes for films several hundred nanometers thick. Charge carriers are produced by three processes: (i) direct production of electron–hole pairs by photons with energies of 3 eV or more; (ii) dissociation of excitons at the aluminum–porphyrin interface; and (iii) dissociation of excitons in the bulk material. At low light levels the quantum yield for current production is 3.4% for octaethylporphine illuminated by 400-nm light and 0.9% for tetraphenylporphine illuminated by 440-nm light. At higher light levels the quantum yield for current production decreases due to recombination of electrons and holes.

1. Introduction

In two previous papers[1,2] we discussed the optical absorption and emission properties of crystalline and amorphous films of octaethylporphine. Fluorescence from trace impurities in those films revealed extensive exciton migration. However the small quantum yield for fluorescence of octaethylporphine in the solid state as compared to its solution quantum yield implied the existence of radiationless decay mechanisms intrinsic to the solid state. A further decrease in quantum yield was observed for excitation of crystalline films with light of wavelength less than 400 nm. Several possible explanations for this further decrease in quantum yield were proposed, including the production of separated electron–hole pairs which then recombine radiationlessly.[1] However the difficulty of ascertaining reflection effects made the decrease in yield uncertain.[2]

Production of charge carriers by light can be studied by measuring the photoconductivity or the photovoltaic properties of the solid. In a photoconductivity experiment, two similar metal electrodes are attached to the solid and the current flow in response to an applied voltage is measured as a function of the illumination. In a photovoltaic measurement two dissimilar metal electrodes are attached. Current flows upon illumination due to an electric field caused by the difference of the work functions of the two metals.

We decided to study the photovoltaic properties of porphyrins, rather than the photoconductivity, for two reasons. The first is that the photoconductivity of a number of porphyrins has been reported in the literature[3-5] but the photovoltaic properties have not. Secondly, there have been recent reports of the photovoltaic properties of magnesium phthalocyanine[6] and chlorophyll a,[7-9] two compounds closely related to porphyrins. Those studies indicated peak energy efficiencies of 10^{-4} for magnesium phthalocyanine and 5×10^{-4} for chlorophyll a. These values are quite high for organic compounds and implied that porphyrins might also have high photovoltaic efficiencies.

Here we report the photovoltaic properties of octaethylporphine and tetraphenylporphine. Octaethylporphine was chosen because of our previous experience with it. Tetraphenylporphine was chosen because it is easily synthesized and purified. Both porphyrins are commercially available and have been extensively studied. Also they represent the two common types of porphyrins: the methine substituted porphyrin and the pyrrole substituted porphyrin.

2. Theory of Schottky Barrier Photovoltaic Devices

The photovoltaic devices described here are sandwich cell, Schottky barrier devices similar to those described for magnesium phthalocyanine[6] and chlorophyll a.[7-9] In such a device the organic compound is sandwiched between semitransparent films of a metal with a low work function and a metal with a high work function. In the ideal situation the work function of the organic compound is intermediate between the work functions of the two metals.

We have used aluminum for the low work function metal and silver for the high work function metal. In order to reach equilibrium, electrons are transferred from the aluminum to the porphyrin and from the porphyrin to the silver. Porphyrins,[4] like phthalocyanines[6] and chlorophyll,[8] are p-type semiconductors. Therefore the electrons transferred from the aluminum to the porphyrin "fill in" the holes in the porphyrin valence band near the aluminum

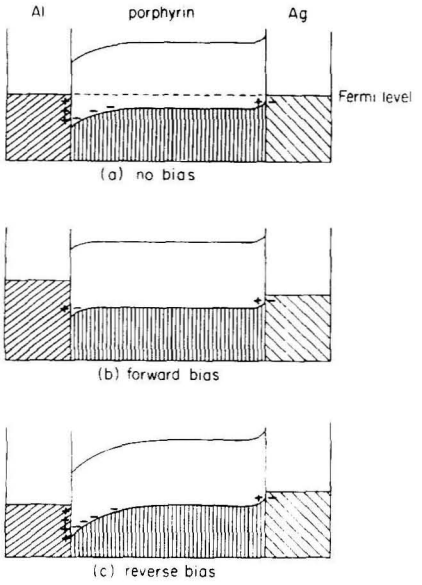

Figure 1. Electron energy diagram for an Al|porphyrin|Ag cell showing filled porphyrin valence and empty conduction band with (a) no bias, (b) forward bias, and (c) reverse bias.

and produce a region depleted of carriers. The transfer of electrons from the porphyrin to the silver results in an increase in the density of holes near the silver.

An electron energy diagram for an unbiased sandwich cell is shown in Figure 1a. The transfer of charge between the metals and the porphyrin results in a spatial variation of the electric potential in the porphyrin and causes the valence and conduction bands to bend. If the aluminum is made negative with respect to the silver (forward bias) the bands are shifted upward at the aluminum and the depletion region becomes thinner, as shown in Figure 1b. If the aluminum is made positive with respect to the silver (reverse bias) the opposite occurs. See Figure 1c. Current flow is large for forward bias and small for reverse bias. The equation describing the current flow is the same equation which describes a p–n junction, the Schockley equation:[10]

$$I = I_0\left[\exp(qV/nkT) - 1\right] \quad (1)$$

I is the current and V is the voltage with positive V meaning forward bias. T is the absolute temperature; q is the electronic charge; k is the Boltzmann constant; and n is a parameter near 1.

The capacitance of a Schottky barrier device is determined by the thickness of the depleted region since it has a higher resistance than the rest of the material. Therefore it increases with forward bias and decreases with reverse bias.

Light acting on an organic Schottky barrier device can produce charge carriers directly by raising an electron from the valence band to the conduction band if the photon has enough energy. Charge carriers can also be produced indirectly by the dissociation of excitons. Electrons will migrate to the aluminum and holes will migrate to the silver. The net result is the transfer of an electron from the silver to the aluminum. The maximum voltage available is therefore approximately equal to the difference in the work functions of the two metals, about 0.65 V for aluminum and silver.

3. Experimental Section

Octaethylporphine was purchased from Strem Chemicals and used as purchased. Tetraphenylporphine was synthesized by the method of Adler and co-workers[11,12] and

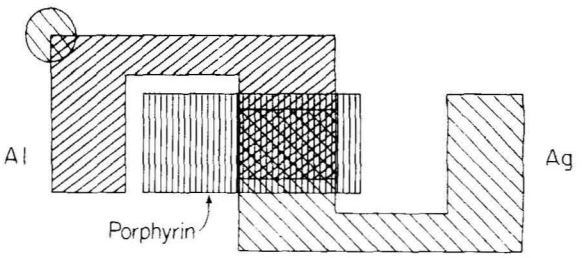

Figure 2. Top view of an Al|porphyrin|Ag photovoltaic cell.

purified by dry column chromatography on alumina using chloroform as the solvent.[13] This was done under low illumination to reduce the amount of photooxidation. Octaethylporphine is more light sensitive and attempts to further purify it increased the amount of photooxidized products.

Sandwich cells are fabricated in a diffusion pump system capable of 10^{-6} Torr. The substrate used is Corning 7059 glass. Aluminum is evaporated from a tungsten boat; silver is evaporated from an alumina coated molybdenum boat. The porphyrin is evaporated from a glass cone with a spiral of nichrome wire around it. A gooch crucible around the cone reflects heat back into the cone. A plug of glass wool is placed over the porphyrin.

Once the system is pumped down, the first step is to heat the porphyrin source until the porphyrin has completely sublimed onto the glass wool and is starting to sublime off of the glass wool. This releases the solvent and gas trapped in the porphyrin crystals. During this operation the pressure can rise as high as 10^{-4} Torr. The porphyrin source is then turned off and the system pumped back down to the low 10^{-6} Torr range. Next a semitransparent aluminum film is evaporated onto the substrate. The aluminum film has a transmission of from 10 to 20%. A porphyrin film several hundred nanometers thick is deposited next. The pressure does not rise above 5×10^{-6} Torr during this step. Finally a semitransparent silver film is evaporated.

A top view of the resulting device is shown in Figure 2. The sandwich cell itself has an area of 1 cm^2. This geometry has the advantage that the transmission spectrum of each layer can be determined separately. A silver spot is evaporated on the aluminum film to facilitate electrical connection. Copper wires are attached to the silver film and to the silver spot on the aluminum film with silver epoxy. The epoxy is cured by heating to 120 °C for 1 h.

Voltages produced by the sandwich cells were measured with a Keithley 610A electrometer. Currents were measured with the same electrometer in the "fast" position or with a Keithley 416 high-speed picoammeter. The light source consists of a 1000-W tungsten halogen source and a Bausch and Lomb 250-mm monochromator. Light intensities were measured by a Hewlett-Packard 8330A radiant flux meter.

The action spectra of the sandwich cells were measured with the photon flux held constant as the wavelength was varied. The light coming from the monochromator was split into two beams: one going to the sandwich cell and the other to the Hewlett-Packard flux meter. The sandwich cell was connected to an electrometer, the recorder output of which was connected to an A/D converter of a PDP 8/e computer. The recorder output of the flux meter was connected to a second A/D converter. The current through the tungsten lamp was controlled by a solid-state controller which was connected to a D/A converter on the computer. The wavelength of the light from the monochromator was determined by a stepping motor also operated by the computer. In the course of the

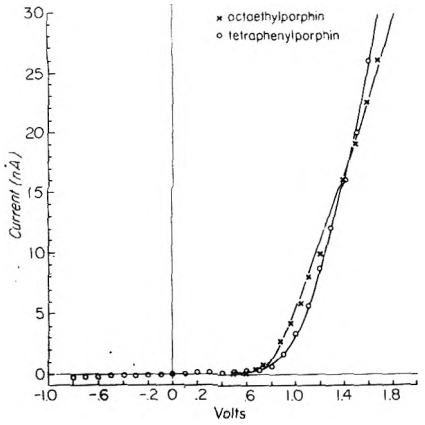

Figure 3. *I–V* curve for Al|octaethylporphine|Ag and Al|tetraphenylporphine|Ag cells in the dark.

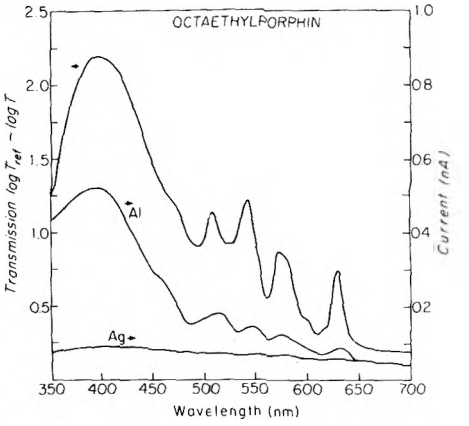

Figure 4. Log transmission spectrum of octaethylporphine film and photovoltaic action spectra of Al|octaethylporphine|Ag cell for illumination through the aluminum and through the silver films.

experiment the computer sets the wavelength, adjusts the current through the tungsten lamp until the proper photon flux is achieved, records the current from the sandwich cell, and then steps the wavelength.

The thickness of the porphyrin film is measured by dissolving the film in a known amount of a solvent in which the extinction coefficients are known and taking an absorption spectrum. The density of the film is assumed to be the same as the density of macroscopic crystals of the same porphyrin.

4. Results

Results are presented for one octaethylporphine sandwich cell and one tetraphenylporphine sandwich cell. There is not a great deal of variation among cells made from the same porphyrin. The octaethylporphine film is approximately 230 nm thick and the tetraphenylporphine film is approximately 260 nm thick.

The *I–V* curves for the two sandwich cells are shown in Figure 3. Both cells are strongly rectifying, indicating that a Schottky barrier has formed. The current through the octaethylporphine cell is indistinguishable from zero for voltages less than 0.5 V on the scale of Figure 3. These points are not shown to reduce clutter. As the forward bias is increased the dynamic resistance (dV/dI) tends to decrease toward a constant value. Therefore the data was fitted to a modified Schockley equation:[7]

$$I = I_0\left[\exp\left[(q/nkT)(V - IR_s)\right] - 1\right] \qquad (2)$$

R_s is a series resistance. The other symbols are the same as before. The fitted values of R_s are 29.5 megohms for the octaethylporphine sandwich cell and 13.4 megohms for the tetraphenylporphine sandwich cell.

The capacitance of the octaethylporphine sandwich cell is 7.2 nF; the tetraphenylporphine sandwich cell has a capacitance of 9.8 nF. These were measured at a frequency of 1000 Hz. The capacitance of the octaethylporphine film was observed to be independent of bias voltage. The voltage dependence of the capacitance of the tetraphenylporphine sandwich cell was not measured. Its capacitance was observed to be independent of frequency from 200 to 10000 Hz.

In order to calculate the thickness of the depleted region in the two films from the capacitance, it is necessary to know the dielectric constant of the porphyrin. Schechtman measured the optical absorption of evaporated films of protoporphyrin over a wide range of energies and calculated the index of refraction and dielectric constant as a function of frequency.[14] From that data one can extrapolate to zero frequency to estimate a dielectric constant of 2.0. It is possible to calculate thicknesses of 250 and 180 nm for the depleted regions of the octaethylporphine film and the tetraphenylporphine film, respectively, using that value and the standard parallel plate capacitor formula:

$$C = \kappa \epsilon_0 A/d \qquad (3)$$

C is the capacitance; κ is the dielectric constant; ϵ_0 is the permittivity of free space; A is the area of the film; and d is the thickness of the depleted region. The close agreement between the measured thickness of the octaethylporphine film (230 nm) and the calculated thickness of the depleted region (250 nm) and the fact that the capacitance did not depend on voltage both imply that the entire octaethylporphine film was depleted of holes. About 70% of the tetraphenylporphine film seems to have been depleted.

Upon illumination the aluminum electrode of the sandwich cells becomes negative with respect to the silver. Under room lights both types of sandwich cells produce an open circuit voltage of about 0.6 V. The short circuit current produced by the octaethylporphine cell is about 20 nA under room lights. The tetraphenylporphine cell produced about 5 nA under room lights. In direct sunlight the short circuit currents are 0.25 and 0.1 μA for the octaethylporphine and tetraphenylporphine cells, respectively.

In the dark the sandwich cells produce a small current of the same sign as the current produced under illumination. The current is about 0.03 nA when the cells are first placed in darkness and slowly decreases as a function of time. This current is presumably due to the thermal activation of trapped carriers.

By varying the load resistance, *I–V* plots for the illuminated cells can be obtained. These plots are very close to straight lines.

Photovoltaic action spectra for the two kinds of porphyrin sandwich cells are shown in Figures 4 and 5 along with plots of the log transmission of the porphyrin film itself. The transmission plots are given as log T_{ref} − log T where T_{ref} is the transmission of the glass substrate. The photovoltaic action spectra are plots of the short circuit current produced by the cell vs. wavelength for illumination through the aluminum film and for illumination through the silver film. As described earlier the photon flux was kept constant as the wavelength was varied. In order to get data out to 350 nm it was necessary to operate at a very low photon flux. That is why the dark current is a substantial part of the total current measured, especially for the tetraphenylporphine cell. The log transmission curves do not come down to zero because of

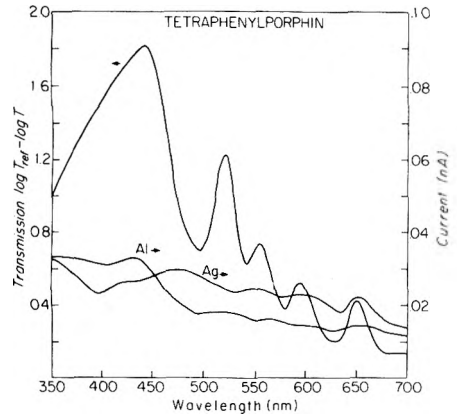

Figure 5. Log transmission spectrum of tetraphenylporphine film and photovoltaic action spectra of Al|tetraphenylporphine|Ag cell for illumination through the aluminum and through the silver films.

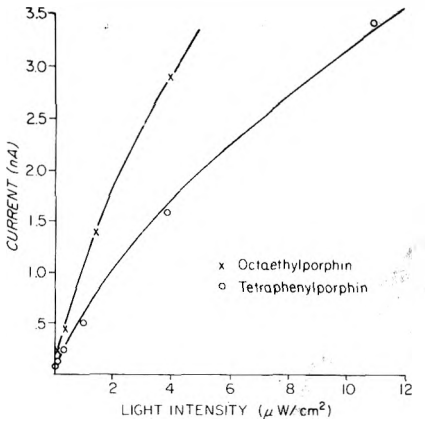

Figure 6. Current output vs. light intensity for illumination through the aluminum film: octaethylporphine cell illuminated by 400-nm light; tetraphenylporphine cell illuminated by 440-nm light.

reflection effects. In both cases the value of current and log transmission at 700 nm may be regarded as the "zero" for the plots.

The log transmission spectra and the photovoltaic action spectra for illumination through the aluminum film agree fairly well for light with wavelength greater than 400 nm. For wavelengths less than 400 nm the current becomes progressively larger compared to the log transmission as the wavelength decreases. This is especially noticeable for the tetraphenylporphine sandwich cell.

For octaethylporphine the photovoltaic action spectrum for illumination from the silver is similar to the one generated by illumination from the aluminum film but is much flatter. For the tetraphenylporphine cell the photovoltaic action spectrum has a dip in the Soret region for illumination through the silver film. For thicker films the octaethylporphine action spectra also have a dip in the action spectrum in the Soret region.

The dependence of the short circuit current on light intensity for illumination through the aluminum film was studied by using neutral density filters. Wavelengths of 400 nm for the octaethylporphine cell and 440 nm for the tetraphenylporphine cell were chosen from the action spectra as having the highest quantum yield. The results of these studies are shown in Figure 6. The current is not a linear function of light intensity. A log–log plot of current minus the dark current vs. light intensity has a slope of 1.0 for low light levels and a slope of 0.8 for high light levels for the octaethylporphine cell. The slope is 0.8 over the whole range for the tetraphenylporphine cell. The curves fitted to the points of Figure 6 have the form:

$$L = A + BI + CI^2 \tag{4}$$

For L given in microwatts per square centimeter and I given in nanoamperes the fitted parameters have the following values: for octaethylporphine: $A = -3.6 \times 10^{-2}$, $B = 7.45 \times 10^{-1}$, $C = 2.25 \times 10^{-1}$; for tetraphenylporphine: $A = -3.12 \times 10^{-2}$, $B = 1.40$, $C = 5.65 \times 10^{-1}$. The form of eq 4 was suggested by the idea that electron–hole recombination is responsible for the nonlinearity of the current vs. intensity relation. Equation 4 provides a good fit to the data over three orders of magnitude.

5. Discussion

The electrical properties of the two sandwich cells imply that most of the porphyrin films are depleted of holes. As stated earlier, electrons flow from the aluminum into the porphyrin until the Fermi levels of the two materials are equal. The thickness of the region depleted of holes (d) is determined by the difference in the work function of the aluminum and the porphyrin (ΔW), the dielectric constant of the porphyrin (κ), and the density of the acceptors that produce the holes (N).[15]

$$d = \left[2(\Delta W)\kappa\epsilon_0/q^2N\right]^{1/2} \tag{5}$$

The constant ϵ_0 is the permittivity of free space in MKS units. If we estimate the difference in work functions to be less than or equal to 0.5 eV, we find an upper limit on N of about 3×10^{15} cm^{-3} for a value of d of 200 nm. This is fairly small. Ghosh et al.[6] found that the depleted region in Al|magnesium phthalocyanine|Ag sandwich cells was 25 nm and estimated a "trap" density of 10^{18} cm^{-3}. However Ghosh and Feng[16] found that Al|tetracene|Au cells were entirely depleted. Acceptor states in porphyrins[4] and phthalocyanines[6] are often ascribed to the presence of oxygen. Ghosh et al. do not state whether the magnesium phthalocyanine was sublimed prior to the fabrication of the sandwich cell to eliminate trapped gas.

The photovoltaic action spectra (Figures 4 and 5) provide a considerable amount of information about the processes responsible for the formation of charge carriers. A comparison of the spectrum for photovoltaic current and that for log transmission at wavelengths λ <400 nm shows an increasing yield of charge carrier production for photons absorbed with energies above 3 eV. We believe that this increased quantum yield arises from direct production of separated electron–hole pairs, a process we shall refer to as mechanism (i). For reasons to be given below, 3 eV is a reasonable estimate for the energy required to produce a separated electron–hole pair in a porphyrin crystal. Thus direct conversion of photons with λ <400 nm into separated electron–hole pairs is not unexpected. It is, after all, the dominant process for current production in silicon photovoltaic devices.

[It might be objected that overlap considerations suggest that the optical cross section for production of separated electron–hole pairs in a molecular crystal should be very small. There are, however, localized porphyrin excited states in this energy region with moderately strong optical cross sections, which can couple to the isoenergetic separated electron–hole states. Conversion from the localized excited state to the separated electron–hole state is thus a radiationless transition, which the data tell us occurs quickly relative to relaxation to the lower energy localized excited singlet states. This latter process occurs within ~1 ps. Thus, on the time scale of ~1 ps there is "direct conversion" of the absorbed photon to a separated electron–hole pair.]

Schechtman[14] measured the optical and photoemission properties of evaporated films of protoporphyrin. He

estimated that the energy gap was less than or equal to 3.1 eV from the photoemission results and between 3 and 4 eV from the optical data. This is in agreement with our result.

It is possible to estimate the energy gap from simple arguments. The energy required to transfer an electron from one porphyrin molecule to another should be equal to a constant plus an electrostatic term which would be inversely proportional to the dielectric constant of the environment.

$$E = C + D/\kappa \tag{6}$$

The energy required to transfer the electron in vacuo is equal to the difference of the ionization energy[17] and the electron affinity[18] and is about 5 eV. The dielectric constant of the vacuum is, of course, equal to one.

By cyclic voltammetry one can measure the reduction potential and oxidation potential of porphyrins. Their difference is usually close to 2 V.[19] Cyclic voltammetry is usually performed in a solvent such as acetonitrile, which has a dielectric constant of 36. The electrostatic term is negligible under those circumstances. In this way we estimate that the constant term, C, is equal to 2 eV and the electrostatic term is 3 eV divided by the dielectric constant. For a film with a dielectric constant of 2, the energy required to transfer an electron is 3.5 eV, by this argument. That is in fair agreement with our estimate from the action spectra.

The action spectra for illumination through the aluminum film do follow the log transmission spectra for wavelengths larger than 400 nm. This implies that the light is first absorbed to produce an exciton which then produces charge carriers by some secondary mechanism. Since these action spectra do not saturate, even though the log transmission reaches values above 2, the photoactive region must be located adjacent to the aluminum and must be only a fraction of the total thickness of the film. We shall refer to the process of carrier generation that occurs near the aluminum surface as mechanism (ii), which can be explained as exciton diffusion to the aluminum followed by dissociation into an electron in the aluminum and a hole in the porphyrin. The fraction of excitons which diffuse to the aluminum is given by $\ell_s/(\ell_a + \ell_s)$ where ℓ_s is the exciton diffusion length and ℓ_a is the penetration depth of the light.[20]

The exciton diffusion length in crystalline films of octaethylporphine is 50 nm or less.[2] We know that the film in the octaethylporphine sandwich is crystalline because of the characteristic shoulder at 460 nm.[2] An exciton diffusion length of 50 nm or less is consistent with our interpretation of the action spectra for illumination through the aluminum film.

If exciton migration to the aluminum were the only mechanism for charge carrier production for light with wavelength greater than 400 nm, the action spectra for illumination through the silver film should have peaks where the log transmission spectra have valleys, and vice versa. That is because of light absorption by the intervening porphyrin. Actually the action spectrum for illumination of the octaethylporphine film through the silver film is very flat, like a linear transmission spectrum. The action spectrum of the tetraphenylporphine film illuminated through the silver film has a dip in the Soret region, but no dips for the visible peaks. These spectra thus imply a mechanism (iii) for production of charge carriers, which has a much larger photoactive region than the 50 nm or less deduced for mechanism (ii).

We shall assume that for mechanism (iii) the film can be divided into two regions: a photoactive region extending from the aluminum a distance p into the film, and a nonphotoactive region with a thickness $s - p$, where s is the total thickness of the film. For illumination through the silver film, the light absorbed by the photoactive region will be given by the following expression:

$$I_{abs} = \int_{s-p}^{s} I_0 K e^{-Kx}\, dx = I_0\left[e^{(p-s)K} - e^{-sK}\right] \tag{7}$$

I_0 is the intensity of light incident on the porphyrin film at the porphyrin–silver interface. K is the absorption coefficient per unit length of the porphyrin and is a function of wavelength. Differentiating eq 7 with respect to K and setting the result equal to zero informs us that the light absorbed in the photoactive region will be a maximum when K has the following value:

$$K = (1/p) \ln (s/(s - p)) \tag{8}$$

The tetraphenylporphine action spectra show a maximum at 470 nm for illumination through the silver film, but not through the aluminum film. The log transmission at that wavelength is about 0.9. The log transmission at 700 nm is about 0.15. Subtracting that value to give a crude correction for reflection effects, we obtain a log transmission of 0.75. Hence K(470 nm) is about 6.6×10^{-3} nm^{-1}. With s equal to 260 nm, the value of p that gives that value of K when substituted into eq 8 is 180 nm. Using that value of p and determining K as a function of wavelength from the log transmission, eq 7 can be used to generate a simulated action spectrum that reproduces all of the features of the actual photovoltaic action spectrum for illumination of the tetraphenylporphine through the silver film, except for the dip at 400 nm.

For the octaethylporphine sandwich cell there is no maximum in the action spectrum for illumination through the silver film that does not correspond to a maximum in the other action spectrum. We can set a lower limit on p by using the largest value of K that occurs, which is 2.0×10^{-2} nm^{-1}. The result is that p equals 227 nm, or all of the film to the accuracy of the calculation. These values for the thickness of the photoactive region for mechanism (iii) agree very closely with the calculated thicknesses of the depleted regions in the two kinds of porphyrin sandwich cells. Since there is an electric field in the depleted region which can separate electron–hole pairs, we conclude that mechanism (iii), like mechanism (i), involves production of charge carriers in the bulk material. The only difference between mechanism (i) and mechanism (iii) is the lower quantum yield for the latter, which occurs for photons with wavelength greater than 400 nm.

Thus there are three mechanisms for production of charge carriers: (i) Photons with energy above 3 eV can directly produce electron–hole pairs in the bulk of the film, since most or all of the film has an electric field which causes some of the electron–hole pairs to separate to the Al and Ag surfaces. (iii) Photon energies below 3 eV are insufficient for direct production of an electron–hole pair; however, an initially produced exciton may dissociate into charge carriers at some impurity trap or grain boundary. (ii) More efficient carrier production occurs for a low energy exciton that can diffuse to the aluminum–porphyrin interface.

These results may partly account for the low quantum yield for fluorescence of porphyrin films relative to that of porphyrins in solution. Inside a film there are mechanisms for radiationless decay of excitons into charge carriers, which presumably recombine radiationlessly. Whether or not these mechanisms completely account for the low quantum yield for film fluorescence is not yet known.

The quantum yield for current production in the limit of low light level can be calculated from the parameters of eq 4 which is used to fit the data shown in Figure 6. Correcting for the optical density of the aluminum film, which is 0.92 for the octaethylporphine cell and 0.68 for the tetraphenylporphine cell, the quantum yield is 3.4% for the octaethylporphine cell and 0.9% for the tetraphenylporphine cell. These values are for the wavelength with the highest yield (Figures 4 and 5) for each porphyrin, which is 400 nm for the octaethylporphine and 440 nm for the tetraphenylporphine. Values obtained for other materials are 0.7% for Cr|chlorophyll a|Hg sandwich cells[7] and 0.15% for Al|magnesium phthalocyanine|Ag cells.[6]

Since the I–V curve of an illuminated porphyrin sandwich cell is nearly a straight line, the energy efficiency can be calculated from the short circuit current (I_{sc}) and the open circuit voltage (V_{oc}). The maximum energy efficiency is given by

$$\eta_{max} = V_{oc} I_{sc}/4LA \quad (9)$$

L is the light intensity (W/cm^2) and A is the area of the sandwich cell which is 1 cm^2.

The quantum yield for current production is given by

$$\phi_{pc} = E_{photon} I_{sc}/LA \quad (10)$$

E_{photon} is the energy of a photon of the illuminating light, and must be given in electron volts for the formula to have the proper dimensions. From these two expressions the energy efficiency can be written as a function of the quantum yield:

$$\eta_{max} = (\phi_{pc}/4)(V_{oc}/E_{photon}) \quad (11)$$

V_{oc} is about 0.4 V at the maximum light level at which the quantum yield has not dropped significantly below 3.4% for the octaethylporphine sandwich cell for illumination by 400-nm light. Therefore the maximum efficiency is about 0.1% or 10^{-3}. This is based on photons actually incident on the porphyrin film. The best efficiency of the Al|magnesium phthalocyanine|Ag sandwich cell is given as 0.01%.[6] The best efficiency for the Cr|chlorophyll a|Hg sandwich cells is given as 0.05%.[7] However it should be noted that the chlorophyll a cells maintain their efficiency to a higher light level than the octaethylporphine cells.

6. Conclusion

Electrical properties of Al|octaethylporphine|Ag sandwich cells and Al|tetraphenylporphine|Ag sandwich cells indicate the presence of a Schottky barrier with all of the octaethylporphine depleted of holes and most of the tetraphenylporphine depleted. Action spectra indicate charge carrier production by three mechanisms: (i) Light with energy above 3 eV, the gap between valence and conduction bands, can produce electron–hole pairs directly. Light of any energy can produce excitons which can produce charge carriers by (ii) diffusion to the aluminum–porphyrin interface or (iii) by a bulk process probably involving collision with traps, defects, or grain boundaries. The maximum quantum yield for current production at low light levels is 3.4% for octaethylporphine and 0.9% for tetraphenylporphine for light incident on the aluminum–porphyrin interface. For octaethylporphine, most of the carrier production results from mechanism (ii), and the maximum photovoltaic efficiency is 0.1% based on light incident on the porphyrin. Quantum yields and efficiencies fall off as the light level increases due to electron–hole recombination.

Acknowledgment. Dr. J. S. Bonham designed the geometry used for the sandwich cells. The tetraphenylporphine was synthesized by Mr. S. Kim. This research was supported in part by Public Health Services Research Grant AM 16508.

References and Notes

(1) J. S. Bonham, M. Gouterman, and D. B. Howell, *J. Lumin.*, **10**, 295 (1975).
(2) F. J. Kampas and M. Gouterman, *J. Lumin.*, **14**, 121 (1976).
(3) J. W. Weigl, *J. Mol. Spectrosc.*, **1**, 216 (1957).
(4) A. T. Vartanyan, *Fiz. Tekh. Poluprovodn.*, **1**, 1515 (1967) [*Sov. Phys. Semicond.*, **1**, 1261 (1968)].
(5) V. A. Livshits, *Zh. Struk. Khim.*, **8**, 440 (1967) [*J. Struct. Chem.*, **8**, 389 (1967)].
(6) A. K. Ghosh, D. L. Morel, T. Feng, R. F. Shaw, and C. A. Rowe, *J. Appl. Phys.*, **45**, 230 (1974).
(7) C. W. Tang and A. C. Albrecht, *Nature (London)*, **254**, 507 (1975).
(8) C. W. Tang and A. C. Albrecht, *J. Chem. Phys.*, **62**, 2139 (1975).
(9) C. W. Tang and A. C. Albrecht, *J. Chem. Phys.*, **63**, 953 (1975).
(10) S. M. Sze, "Physics of Semiconductor Devices", Wiley, New York, N.Y., 1969, p 393.
(11) A. D. Adler, F. R. Longo, J. D. Finarelli, J. Goldmacher, J. Assour, and L. Korsakoff, *J. Org. Chem.*, **32**, 476 (1967).
(12) A. D. Adler, L. Sklar, F. R. Longo, J. D. Finarelli, and M. G. Finarelli, *J. Heterocycl. Chem.*, **5**, 669 (1968).
(13) A. D. Adler, F. R. Longo, F. Kampas, and J. Kim, *J. Inorg. Nucl. Chem.*, **32**, 2443 (1970).
(14) B. H. Schechtman, Thesis, Solid State Laboratory, Stanford Electronics Laboratory, Stanford University, 1968.
(15) J. G. Simmons in "Handbook of Thin Film Technology", L. I. Maissel and R. Glang, Ed., McGraw-Hill, New York, N.Y., 1970, p 14-9
(16) A. K. Ghosh and T. Feng, *J. Appl. Phys.*, **44**, 2781 (1973).
(17) J. N. A. Ridyard, *Mol. Spectrosc.*, 96 (1971).
(18) A. Fulton, L. E. Lyons, and G. C. Morris, *Aust. J. Chem.*, **21**, 2853 (1968).
(19) J. H. Fuhrhop in "Structure and Bonding", Vol. 18, Springer-Verlag, New York, N.Y., 1974, p 44.
(20) H. Killesreiter and H. Baessler, *Chem. Phys. Lett.*, **11**, 411 (1971).

New Differential Bottcher–Onsager Method Used to Determine Polarizability and Apparent Radius of $SiO_4(WO_3)_{12}^{4-}$

H. R. Petty,[†]

Department of Physics and Chemistry, Manchester College, North Manchester, Indiana 46962

J. A. Crumb,[‡]

Department of Physics, Western Kentucky University, Bowling Green, Kentucky 42101

V. E. Anderson, E. T. Arakawa, and J. K. Baird*

Health Physics Division, Oak Ridge National Laboratory, Oak Ridge, Tennessee 37830 *(Received October 12, 1976)*

Publication costs assisted by the Oak Ridge National Laboratory

A differential form for the Bottcher–Onsager law is derived. Based on this form, a new method is presented for determining the polarizability and apparent radius of the molecules of a solute from measurements of the *temperature variation* of the density and specific refractive increment of its solutions. The method is particularly applicable to solutes which are only slightly soluble in a given solvent. The density and specific refractive increment of aqueous solutions of tungstosilicic acid have been measured at four temperatures: nominally, 20, 25, 35, and 45 °C. The densities are found to be linear functions of concentration in the range 0–0.03 M. From the density measurements, the apparent molar volume of $H_4SiO_4(WO_3)_{12}$ at each temperature is determined. The specific refractive increment is determined for radiation at 589 mμ. Using our differential method, we find $\alpha_2 = 50 \pm 5$ Å^3 and $a_2 = 3.2 \pm 0.2$ Å, where α_2 and a_2 are the polarizability and effective radius, respectively, of $SiO_4(WO_3)_{12}^{4-}$.

Introduction

According to the theory of Onsager, the index of refraction of a fluid depends upon the polarizabilities and radii of the molecules it contains.[1] In Onsager's model, a molecule in the fluid is considered to be a spherical cavity of molecular size surrounded by an otherwise continuous dielectric. At the center of the cavity, there is a point electric dipole whose magnitude is proportional to the local electric field. The electric field is assumed to be established by a light wave passing through the fluid. Since the period of oscillation of the light wave is short compared with the relaxation times of the permanent multipole moments of a molecule, these moments do not contribute to the polarization in the fluid. The induced dipole thus represents the leading term of a multipole expansion of the interaction of the electric field with the molecule.[2] Moreover, if $(\lambda/a) >> 1$, where λ is the wavelength, and a is the molecular radius, then the time dependence of the wave is unimportant, and the interaction of the wave with the molecule may be considered as a problem in electrostatics. Employing this model, Bottcher derived from Onsager's work the formula

$$\frac{(n^2-1)(2n^2+1)}{12\pi n^2} = \sum_{j=1}^{r} \frac{N_j\alpha_j}{1-\frac{2\alpha_j}{a_j^3}\left(\frac{n^2-1}{2n^2+1}\right)} \qquad (1)$$

where n is the refractive index of a solution containing r components, and N_j, α_j, and a_j are the molecular number density, electric dipole polarizability, and molecular radius of the jth component.[3-5] Bottcher used the equation to determine the radii and polarizabilities of a number of simple inorganic molecules and ions.[5-9] In two recent papers, the equation has been applied to the biologically interesting molecules, glycine[10] and urea.[11]

As a test of the application of eq 1 to an inorganic macromolecule, we have measured the densities and refractive increments of aqueous solutions of tungstosilicic acid, $H_4SiO_4(WO_3)_{12}$. This substance was chosen because (1) it forms solutions which are monodisperse;[12,13] (2) as a strong electrolyte, it involves no complex equilibria;[13] and (3) x-ray diffraction measurements on the variously hydrated crystals and on the aqueous solution have shown that the molecule is essentially a cube–octahedron[14]—a shape which can be closely approximated as a sphere for the purposes of the Bottcher–Onsager theory.

In preparing our solutions, we found that tungstosilicic acid had a solubility in water at room temperature of less than 0.03 M. The measured density and refractive index of this solution differed little from that of pure water. This observation led us to develop a differential form of eq 1 and apply it to our data in a fashion which has heretofore not been reported.

Theory

Consider for the moment a system consisting of the solvent alone. We rearrange eq 1 to the familiar Bottcher form

$$\frac{12\pi n_0^2 N_1^0}{(n_0^2-1)(2n_0^2+1)} = \frac{1}{\alpha_1} - \frac{1}{a_1^3}\frac{2n_0^2-2}{2n_0^2+1} \qquad (2)$$

where n_0 and N_1^0 are the index of refraction and number density, respectively, of the pure solvent. In order to determine α_1 and a_1 for the solvent, the index of refraction and the number density are measured as functions of temperature[15,16] or pressure.[2,3] A plot of the left-hand side

[†] Consultant (1976), Health Physics Division, Oak Ridge National Laboratory. Undergraduate summer trainee (1975) under appointment by the Oak Ridge Associated Universities. Presently, graduate student in Biophysics, Biophysical Laboratory, Harvard Medical School, Boston Mass. 02115.

[‡] Consultant (1975), Health Physics Division, Oak Ridge National Laboratory. Presently, graduate student, Department of Physics, Kansas University, Lawrence, Kan. 66044.

TABLE I: Summary of Data and Derived Quantities[a]

t, °C	k, g M^{-1} mL^{-1}	V_2, cm^3/mol	β	$\theta(\times 10^{-22})$ mL^{-3}	α_2 (LL), $Å^3$	ρ_0,[b] g/mL	n_0[c]
20.00	2.531	347.4	−19.25	4.741	88.79	0.998 234	1.333 345 9
24.76	2.532	347.4	−19.23	4.731	88.65	0.997 137	1.332 880 0
34.85	2.534	347.8	−19.19	4.723	88.53	0.994 115	1.331 667 9
45.01	2.536	339.1	−19.01	4.719	88.31	0.990 240	1.330 182 6
$\alpha_1 = 1.32$ $Å^3$		$a_1 = 1.39$ Å					
$\alpha_2 = 50 \pm 5$ $Å^3$		$a_2 = 3.2 \pm 0.2$ Å					

[a] Estimated random errors in k, V_2, β, θ, α_1, and a_1 and the Lorentz-Lorenz values of α_2 lie beyond the last digit quoted. [b] Water density data from ref 26. [c] Water refractive index data from ref 27.

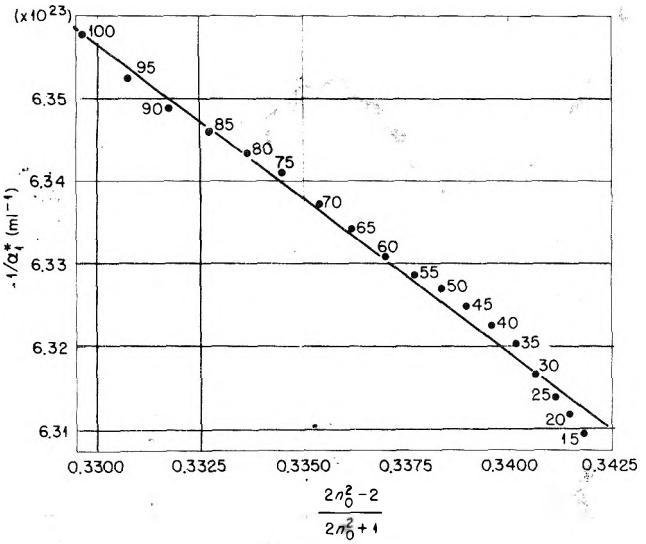

Figure 1. Bottcher plot for water. Numbers by each point specify the temperature in °C.

of this equation (usually referred to as $1/\alpha_1^*$) as a function of $(2n_0^2 - 2)/(2n_0^2 + 1)$ should give a straight line with intercept $1/\alpha_1$ and slope $-1/a_1^3$. A sample plot for water is shown in Figure 1. The values of α_1 and a_1 listed in Table I were derived in this manner from the data in Figure 1.

To determine the radius and polarizability of the second component in a two-component system, eq 1 is put in the form[7]

$$\frac{1}{\alpha_2^*} = \frac{1}{\alpha_2} - \frac{1}{a_2^3}\frac{2n^2 - 2}{2n^2 + 1} \tag{3a}$$

where

$$\frac{1}{\alpha_2^*} = N_2\left[\frac{(n^2 - 1)(2n^2 + 1)}{12\pi n^2} - \frac{N_1\alpha_1}{1 - \frac{\alpha_1}{a_1^3}\frac{2n^2 - 2}{2n^2 + 1}}\right]^{-1} \tag{3b}$$

In this case, n, N_1, and N_2 are varied by changing the composition of the solution. If the values of α_1 and a_1 have been determined as above, then $1/\alpha_2^*$ as a function of $(2n^2 - 2)/(2n^2 + 1)$ yields a straight line with intercept $1/\alpha_2$ and slope $-1/a_2^3$. In the situation in which the solute is only slightly soluble, however, the difference between the two terms inside the brackets in eq 3b is very small. Hence, high precision measurements of n and N_2 are required if α_2 and a_2 are to be determined.

This difficulty can be ameliorated somewhat by replacing n by the refractive increment $\Delta n = n - n_0$. The refractive increment can generally be measured more accurately than n.[17] In order to analyze measurements of

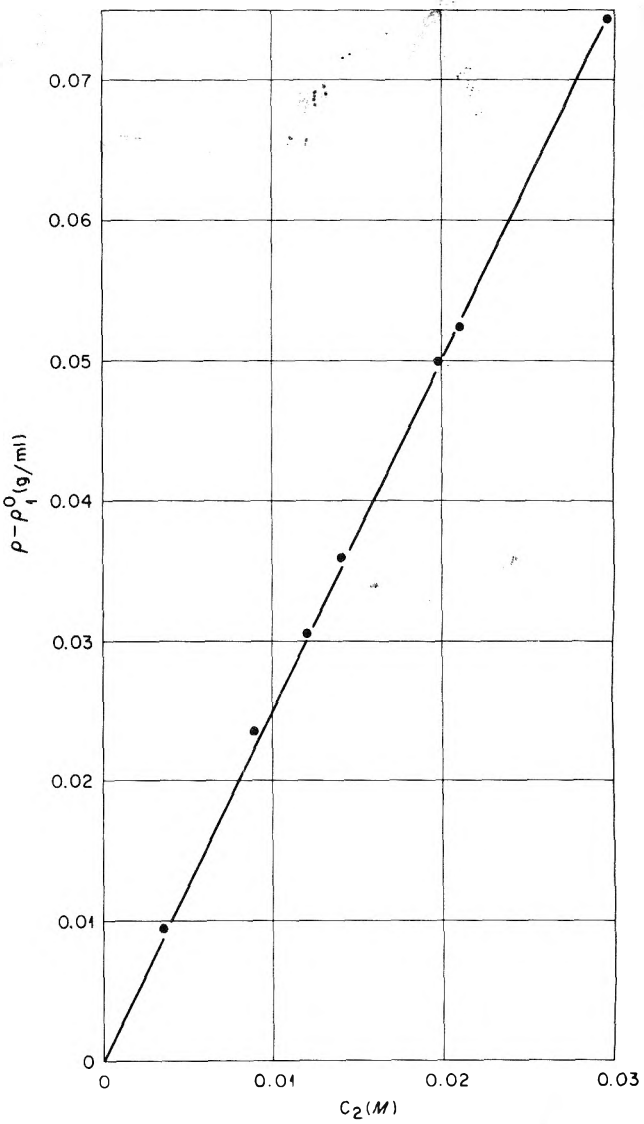

Figure 2. Density at 20 °C of an aqueous solution of tungstosilicic acid as a function of concentration.

Δn, however, it is helpful to have eq 1 in differential form. We wish to form a Taylor series expansion of the right- and left-hand sides of this equation about the values they would have if only the solvent were present. In so doing, we shall rely on some experimental facts.

Taylor Series for the Density. The density of an aqueous solution of tungstosilicic acid is a linear function of the solute concentration[18] (see also Figure 2). Thus

$$\rho = \rho_1^0 + kc_2 \tag{4}$$

where ρ is the solution density, ρ_1^0 is the density of water, k is a constant, and c_2 is the concentration in moles/liter of tungstosilicic acid. Equation 4 can be made the basis for establishing a linear relation between N_1^0, N_1, and N_2.

With the relations $c_2 = 1000N_2/A$ and $\rho_1^0 = N_1^0M_1/A$, eq 4 may be put in the form

$$\rho = \frac{N_1^0M_1}{A} + \frac{1000kN_2}{A} \tag{5}$$

The density of a solution can also be expressed as

$$\rho = \frac{N_1M_1}{A} + \frac{N_2M_2}{A} \tag{6}$$

where A is Avagadro's number, and M_1 and M_2 are molecular weights of the solvent and solute, respectively. Combining eq 5 and 6, we arrive at the desired relation

$$N_1 = N_1^0 + \beta N_2 \tag{7a}$$

where

$$\beta = (1000k - M_2)/M_1 \tag{7b}$$

On the basis of eq 4, it is easy to show also that

$$\beta = -V_2/V_1 \tag{8}$$

where V_1 and V_2 are the respective apparent molar volumes.[18] Equation 7a constitutes a Taylor series expansion in two terms of N_1 about N_1^0.

Taylor Series for the Refractive Increment. To proceed further, we must take note of the fact that tungstosilicic acid is a binary electrolyte. Hence, we turn our attention to a three-component system. We shall label the anion as species 2 and the cation as species 3. For a general strong, binary electrolyte with formula $(2)_p(3)_q$, we have

$$qN_2 = pN_3 \tag{9}$$

In eq 1, we treat $(n^2 - 1)(2n^2 + 1)/12\pi n^2$ and $(1 - 2(\alpha_j/a_j^3)(2n^2 - 2)/(2n^2 + 1))$ as functions of n and expand them in a Taylor's series about n_0. If we retain only first-order terms in the difference $\Delta n = n - n_0$, the expansions are

$$\frac{(n^2 - 1)(2n^2 + 1)}{12\pi n^2} = \frac{(n_0^2 - 1)(2n_0^2 + 1)}{12\pi n_0^2} + \left(\frac{2n_0^4 + 1}{6\pi n_0^3}\right)\Delta n \tag{10}$$

and

$$\left[1 - \frac{\alpha_j}{a_j^3}\frac{2n^2 - 2}{2n^2 + 1}\right]^{-1} = \left[1 - \frac{\alpha_j}{a_j^3}\frac{2n_0^2 - 2}{2n_0^2 + 1}\right]^{-1} + \frac{12n_0}{(2n_0^2 + 1)^2}\frac{\alpha_j}{a_j^3}\left[1 - \frac{\alpha_j}{a_j^3}\frac{2n_0^2 - 2}{2n_0^2 + 1}\right]^{-2}\Delta n \tag{11}$$

Final Result. We now substitute eq 7a, 9, 10, and 11 into eq 1 and retain only first-order terms in Δn and N_2/N_1^0. The result is

$$\frac{(n_0^2 - 1)(2n_0^2 + 1)}{12\pi n_0^2} + \frac{2n_0^4 + 1}{6\pi n_0^3}\Delta n = N_1^0\alpha_1D_1 + \frac{12n_0(\alpha_1/a_1^3)}{(2n_0^2 + 1)^2}N_1^0\alpha_1D_1^2\Delta n + (\beta\alpha_1D_1 + \alpha_2D_2 + (q/p)\alpha_3D_3)N_2 \tag{12a}$$

where

$$D_j = \left[1 - \frac{\alpha_j}{a_j^3}\frac{2n_0^2 - 2}{2n_0^2 + 1}\right]^{-1} \tag{12b}$$

The first term on the left of eq 12a and the first term on the right constitute the leading terms in the Taylor series. Each of these terms depends upon the properties of the solvent alone. By rearranging eq 2, one may show that these terms cancel exactly. The remaining terms which involve D_1 may also be simplified by use of eq 2. The result of these simplifications is

$$\alpha_2' + (q/p)\alpha_3' = \left(\frac{2n_0^2 + 1}{6\pi n_0^3}\right) \times \left[\frac{(4\pi N_1^0\alpha_1 - 1)n_0^2 + (4\pi N_1^0\alpha_1 + 1)}{4\pi N_1^0\alpha_1}\right]\left(\frac{\Delta n}{N_2}\right) - \frac{(n_0^2 - 1)(2n_0^2 + 1)}{12\pi n_0^2N_1^0}\beta \tag{13a}$$

where

$$\alpha_j' = \alpha_j\left[1 - 2\frac{\alpha_j}{\alpha_j^3}\frac{n_0^2 - 1}{2n_0^2 + 1}\right]^{-1} \tag{13b}$$

For tungstosilicic acid, $\Delta n/N_2$ is independent of concentration[18] (see also Figure 3). To simplify eq 13, we may thus use the relation

$$\Delta n = \theta N_2 \tag{14}$$

where θ is the specific refractive increment.

Because of the charge neutrality required of ionic solutions, the quantities α_2' and α_3' occur together in eq 13. Hence, one must be known if the other is to be determined from measurements of β and θ. Bottcher solved this difficulty by taking the polarizability of one of the least polarizable ions, Li^+, to be zero.[7] Then from measurements of the refractive index of solutions of $LiClO_4$ he determined the radius and polarizability of ClO_4^-. With this information known, it was then possible to determine the radii and polarizabilities of a number of other simple ions.[7]

In our case, it was impossible to follow this procedure since the completely neutralized salts of tungstosilicic acid are thought to be unstable.[18] The acid, on the other hand, ionizes to produce protons, the stable form of which in aqueous solution is the hydronium ion. Whatever the structure of the hydronium ion, it must certainly contain fewer optically active electrons than the complex ion $SiO_4(WO_3)_{12}^{4-}$. Consequently, the hydronium ion should have much the smaller polarizability. We thus set $\alpha_3 = 0$ in comparison with α_2. Combining this simplification with eq 14, we find for eq 13a

$$\alpha_2' = \left(\frac{2n_0^2 + 1}{6\pi n_0^3}\right) \times \left[\frac{(4\pi N_1^0\alpha_1 - 1)n_0^2 + (4\pi N_1^0\alpha_1 + 1)}{4\pi N_1^0\alpha_1}\right]\theta - \frac{(n_0^2 - 1)(2n_0^2 + 1)}{12\pi n_0^2N_1^0}\beta \tag{15}$$

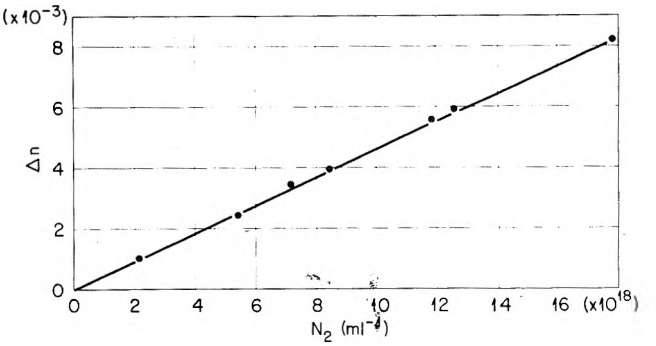

Figure 3. Na D line refractive increment at 20 °C of aqueous solution of tungstosilicic acid as a function of concentration.

Description of the Differential Method. Equations similar in form to eq 13 and 15 have previously been obtained by Bottcher.[9] Our results differ from his, however, in two ways.

First, in passing from eq 12a to eq 13a, Bottcher did not use eq 2 to remove the dependence upon a_1 from the terms involving D_1. Consequently, when density and refractive index data on the solvent were too poor to determine a_1 accurately, he was required to assume a_1 to be identical with the molecular radius measured by x-ray diffraction studies of the solid.

Secondly, by combining measurements of the density and refractive increment of a solution at a given temperature, Bottcher determined α_2' from his form of eq 15. The quantity α_2', however, is a function of both α_2 and a_2. Hence, a value for either α_2 or a_2 must be known before the other can be determined. Bottcher chose to identify a_2 with the crystallographic radius of the ion and calculated α_2. We wish to show, however, that *both α_2 and a_2 can be calculated from measurements of the temperature dependence of the density and refractive increment of the solutions.* The quantities n_0, N_1^0, β, and θ, which appear on the right-hand side of eq 15, are implicit functions of the temperature. Hence, by varying the temperature, we may obtain a range of values of α_2'. A plot of $1/\alpha_2'$

$$\frac{1}{\alpha_2'} = \frac{1}{\alpha_2} - \frac{1}{a_2^3}\frac{2n_0^2 - 2}{2n_0^2 + 1} \tag{16}$$

as a function of $(2n_0^2 - 2)/(2n_0^2 + 1)$ is a straight line with intercept $1/\alpha_2$ and slope $-1/a_2^3$. This is the method which we have used to determine α_2 and a_2 for $SiO_4(WO_3)_{12}^{4-}$.

Experimental Section

Apparatus. A Brice-Phoenix differential refractometer was used for the determination of the refractive increment. The limiting precision of this instrument is $\pm 3 \times 10^{-6}$ within a range of 0.01 unit of Δn.[17] A Na D line (589 mμ) light source was used for all measurements. Nominal 25-mL pyncnometers were employed for the density determinations. Experiments were carried out at 20.00 ± 0.02, 24.76 ± 0.01, 34.85 ± 0.02, and 45.01 ± 0.05 °C. An open-air water bath with sensitive heating and cooling elements was used at the two lower temperatures. A closed Neslab bath was used at the two higher temperatures.

Materials. Analytical grade KCl obtained from the Fisher Scientific Co. was used in the refractometer calibrations. This material was dried at 150 °C in a vacuum oven for 24 h prior to use. The tungstosilicic acid was Fisher Scientific lot no. 734937, nominally the 24 hydrate, $H_4SiO_4(WO_3)_{12}{\cdot}24H_2O$. All solutions were prepared from water which was doubly distilled from a glass apparatus.

Procedures. All weighings were corrected for air buoyancy and had a precision of ±0.1 mg. The temperature of the refractometer cell was maintained by pumping water from the bath through the cell jacket. During the experiments at 35 and 45 °C, both the tubing leading to the cell jacket and the jacket itself were heavily insulated. At 45 °C, a holdup container fitted with a thermometer was placed in the flow line to measure the temperature of the water just before it entered the cell. Our standard thermometer was calibrated by the ORNL Metrology Research and Development Laboratory. The Brice-Phoenix refractometer contains a divided sample cell. On one side of the cell is placed the solvent and on the other side the solution. A light beam passing from the solvent into the solution (or vice versa) is refracted at the interface. The deflection of the light beam is read on a calibrated micrometer eyepiece. The refractive increment is a function of the difference Δd given by

$$\Delta d = (d_1 - d_2)_{soln} - (d_1 - d_2)_{solv} \tag{17}$$

where d_1 and d_2 are measured deflections. The subscripts 1 and 2 correspond to the 180 and 0° positions of the cell, respectively. The difference $(d_1 - d_2)_{solv}$ was read with the solvent on both sides of the cell and the difference $(d_1 - d_2)_{soln}$ was read with the solution on one side and the solvent on the other. The reading of the individual deflections was commonly repeated 12 times with a typical standard deviation of 0.32 in d. The values of d lay in the range 50–970.

Calibration. It was found that the 589-mμ refractive increment data of Kruis[19] for aqueous solutions of KCl at 20 °C was closely followed by the equation

$$\Delta n = AC + BC^{1.7375} \tag{18}$$

where $A = 1.369 \times 10^{-5}$ and $B = -2.64 \times 10^{-5}$. The KCl concentration in units of g of KCl per 100 g of water is C. The value of the exponent was determined by treating it as a free parameter in a routine in which A and B were least-squares parameters. The sum of the squares of the residuals was minimized with respect to the exponent. Errors in the value of the exponent are confined to the fifth decimal place. The calibration of our refractometer consisted of determining Δd for a number of aqueous KCl solutions. Fitting our results to the equation

$$C = K\Delta d \tag{19}$$

we found $K = 7.009 \times 10^{-3}$. By combining eq 18 and 19

$$\Delta n = AK\Delta d + B(K\Delta d)^{1.7375} \tag{20}$$

which allowed us to calculate Δn from a measurement of Δd.

Results

Number Density Determination. Besides the 24 hydrate, there are several other crystalline forms of tungstosilicic acid including the 29, 21, 14, and 6 hydrates.[20] Since the Fisher material, nominally the 24 hydrate, might contain one or more of these as an impurity, we decided to make a determination of the water content by thermogravimetry (TG). Simultaneously with the TG, we recorded a differential thermal analysis (DTA).[21] As the temperature increased during the DTA, we observed four endotherms followed by a single exotherm. We presume the endotherms to be caused by transitions between crystalline structures containing different numbers of water of hydration. Noe-Spirlet et al. have described some of these structures as observed in tungstophosphoric acid, which is isomorphous with tungstosilicic acid.[22] The position of our highest temperature endotherm and the exotherm which followed it agree with those observed for the 6 hydrate by West and Audrieth.[23] We observed the center of the exothermic peak to occur at approximately 515 °C. X-ray diffraction patterns of the Fisher material which had been heated through the exotherm were consistent with a mixture of SiO_2 and WO_3.[24] Hence, we concluded that this exotherm was associated with the complete dehydration of the crystal. From the weight registered after the exotherm, we calculated the weight fraction of H_2O in the original Fisher material. Three TG runs gave a mean value of 0.1454 for this quantity. From this we calculated the weight fraction of $H_4SiO_4(WO_3)_{12}$ in the Fisher material to be 0.8527. This information combined with weighings of the Fisher material allowed us to determine the number densities N_1 and N_2 of solvent

and $H_4SiO_4(WO_3)_{12}$, respectively, from the formulae

$$N_1 = [(1 - w_2)\rho A]/M_1 \quad (21)$$

$$N_2 = w_2\rho A/M_2 \quad (22)$$

where w_2 is the weight fraction of $H_4SiO_4(WO_3)_{12}$ in the solution. We took, for the molecular weight of water, M_1 = 18.0154, and for $H_4SiO_4(WO_3)_{12}$, M_2 = 2878.294. For Avagadro's number we took the value 6.022169×10^{23}.

Least-Squares Methods. We used the method of least squares to fit the data set (N_2, $N_1 - N_1^0$) to eq 7a and the data set (N_2, Δn) to eq 14. Both abscissa and ordinate in each of these data sets are subject to experimental error. The usual method of least squares, however, assumes that the error is confined to the ordinate alone. Since we regarded the effect of error in both abscissa and ordinate to be important, we followed York's method which allows both to be taken into account.[25] York's method assumes that the data may be represented by a linear equation containing a slope and an intercept. Each of eq 7a and 14 contains only a slope (β and θ, respectively). This fact required some specialization of York's results. The derivation of these formulae is presented in the Appendix. In these formulae, a statistical weight is associated with each measurement. The statistical weights are related to the random errors in the measurements through eq A.3 and A.4 of the Appendix.

For the case of the data to be fitted to eq 7a, the errors were estimated by a propagation of error analysis of eq 21 and 22. We found the errors to be dominated by the error incurred in determining the water weight fraction in the TG analysis. The statistical weights were found to satisfy eq A.10, so that β could be calculated from eq A.11.

For the case of the data to be fitted to eq 14, the errors were estimated by propagation of error analysis of eq 20 and 22. The statistical weights were found to be different for each measurement, so that θ was calculated by solving eq A.9 as a "cubic".

The results of the calculation of β and θ are shown in Table I. Also shown are values of the density of water at each temperature interpolated from a table given by Kell.[26] The values of the refractive index of water were calculated from data given by Tilton and Taylor.[27] Tilton and Taylor reported the ratio of the refractive index of water to that of air. To produce the values in Table I, we corrected Tilton and Taylor's data at each temperature to absolute values according to the procedure they recommended.[28]

In Figure 1, we show a Bottcher plot for water which spans the temperature range 15–100 °C. The plot is based upon the density data of Kell and the refractive index data listed in the "Handbook of Chemistry and Physics",[29] which cover a wider range of temperature than that of Tilton and Taylor. In agreement with Bottcher[15] and Orttung,[16] we find that the data for temperatures below about 50 °C differ noticeably from a straight line. Unlike the plot presented by Bottcher,[15] who did not have access to data at the boiling point, we can observe no definite curvature above 75 °C. We show the least-squares line running through the data. The least-squares parameters, α_1 and a_1, are given in Table I.

Figure 4 shows a plot of $1/\alpha_2'$ as a function of $(2n_0^2 - 2)/(2n_0^2 + 2)$. The values of α_2' were computed using eq 15. We show the least-squares line (eq 16) with parameters calculated according to the procedure of York for the case of a line with a nonzero intercept.[25] The statistical weights required by York's method were calculated from a propagation of error analysis of eq 15. We report the least-squares values for α_2 and a_2 in Table I. The least-squares errors in α_2 and a_2 are dominated by the points

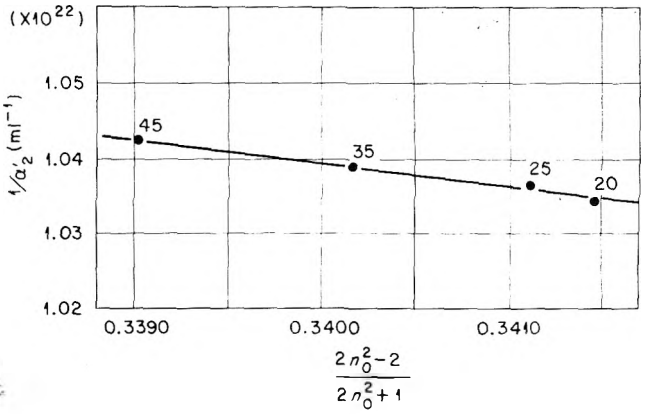

Figure 4. Bottcher plot for tungstosilicic acid dissolved in water. Numbers above each point specify the temperature in °C.

in Figure 4 at 20 and 25 °C, respectively, which lie the farthest off the least-squares line. Hence, the values of α_2 and a_2 have a lower precision than the precision estimated for the values of β and θ. The difference is probably due to some random error which was not taken into account in the propagation of error analysis of eq 15.

Lorentz–Lorenz Results. It is useful to compare the above results with those obtained using the Lorentz–Lorenz formula

$$\frac{n^2 - 1}{n^2 + 2} = \frac{4\pi}{3}\sum_{j=1}^{r} N_j\alpha_j \quad (23)$$

This equation may also be put in differential form by following the procedures described above. For a two-component system, the result is

$$\Delta n = \frac{2\pi}{9}\frac{(n_0^2 + 2)^2}{n_0}(\beta\alpha_1 + \alpha_2)N_2 \quad (24)$$

which when we use eq 8 to remove β, we obtain

$$\Delta n = -\frac{2\pi}{9}\frac{(n_0^2 + 2)^2}{n_0}V_2\left(\frac{\alpha_1}{V_1} - \frac{\alpha_2}{V_2}\right)N_2 \quad (25)$$

For a strong, binary electrolyte

$$\Delta n = \frac{2\pi}{9}\frac{(n_0^2 + 2)^2}{n_0}(\beta\alpha_1 + \alpha_2 + (q/p)\alpha_3)N_2 \quad (26)$$

As before, if we set $\alpha_3 = 0$ and use eq 14 to remove the dependence of N_2, we obtain

$$\alpha_2 = \frac{9}{2\pi}\frac{n_0\theta}{(n_0^2 + 2)^2} - \beta\alpha_1 \quad (27)$$

Using the values of β and θ listed in Table I, we calculated α_2 from eq 27. The results, which are slightly temperature dependent, are listed in Table I.

Discussion

The data which we have presented above constitute a test of our concept of determining α_2 and a_2 from measurements of the temperature dependence of β and θ. It should be possible to apply the method to nonaqueous systems as well. The method would be the one of choice in a case where the solute was only slightly soluble in the solvent. For best results, the solvent should have a long liquid range and its density and refractive index should be strong functions of temperature. These requirements are desirable so that the coefficients of β and θ in eq 15 and the quantity $(2n_0^2 - 2)/(2n_0^2 + 1)$ in eq 16 may be varied through ranges which are large compared with any

uncertainties associated with the values of N_1^0 and n_0.

Our measurements indicate that the Lorentz–Lorenz value for α_2 is about 44% higher than the Bottcher value. This is similar to Bottcher's results for the halide ions F^-, Cl^-, Br^-, and I^- for which he found the Lorentz–Lorenz values for the polarizabilities to be respectively, 3, 14, 17, and 18% larger than his own.[9] The results suggest that the difference may increase with increasing number of electrons in the ion.

X-ray diffraction studies of $SiO_4(WO_3)_{12}^{4-}$ in solution have indicated that the 12 tungsten atoms are situated on the edges of a cube 4.99 Å on a side.[14] The SiO_4 group is located inside the cube. For the purpose of assessing the validity of the Onsager model, it is useful to compare our value for α_2 with the radii of the two spheres which can be associated with a cube of side 4.99 Å. An inscribed sphere (tangent to the faces of the cube) has a radius of 2.495 Å and a circumscribed sphere (passes through the corners of the cube) has a radius of 4.321 Å. These two radii bracket our value of a_2. Both the x-ray measurements and our optical measurements indicate that $SiO_4(WO_3)_{12}^{4-}$ has a very compact structure.

Johnson, Kraus, and Scatchard[18] measured the density of aqueous solutions of tungstosilicic acid at 25 °C and found that eq 4 was satisfied with $k = 2.463$. From Table I, it can be seen that our value of k at this temperature is in good agreement. The small difference is probably due to the fact that Johnson et al. calculated their value of k by a simple numerical average, while we used the least-squares method of York. Such varying statistical methods applied to similar sets of data often lead to differences of this order of magnitude.[30] By combination of eq 7b and 8, we find

$$V_2 = \frac{V_1}{M_1}(M_2 - 10^3 k) \tag{28}$$

Since 10^3k is very nearly equal to $M_2 = 2878.294$, any differences in values for k show up as a magnified difference in values for V_2. Our value for V_2 at 25 °C is listed in Table I. From their value of k, Johnson et al. found $V_2 = 414$ cm^3/mol at 25 °C. Because of the general agreement between the values of k, the molar volumes should also be considered to be in satisfactory agreement. In Table I, we also list V_2 at three other temperatures. Although k varies uniformly with temperature, V_2 does not because the molar volume of water V_1 is also changing with temperature.

In recent work, Scholte has used the Lorentz–Lorenz formula to derive an equation linking the refractive increment of a solution to the molar volume of the solute.[31] Within the validity of the Lorentz–Lorenz formula, his equation is general in the sense that it holds at any concentration. For dilute solutions, his result reduces to eq 24. Scholte also mentions the possibility of using the Bottcher–Onsager equation as the starting point for deriving a relation between the refractive increment and the molar volume. For the case of dilute solutions (i.e., eq 4 applies), our eq 15 and 16 form that relation.

Effect of Dissolved Air. Tilton and Taylor used water which was saturated with air in their refractive index experiments.[27] Although they made no careful study of the effect of dissolved air, they noticed, however, that water saturated with air had a refractive index which was lower by roughly 5×10^{-6} than water that had been freshly degassed by heating. They proceeded to estimate on the basis of an assumed linear relationship between the refractive index and the density of water that the effect of the dissolved air was to decrease the measured refractive indices by about 1×10^{-6}. Equation 25 allowed us to check Tilton and Taylor's observations and estimates. Of the major constituents in the atmosphere, we considered only nitrogen and oxygen. Although the solubility of CO_2 in water is much greater than either nitrogen or oxygen, the effect of dissolved CO_2 on the refractive index of water can be neglected in comparison with the former two gases because of its small abundance (0.033%) in the atmosphere. Since eq 25 was derived from the Lorentz–Lorenz formula, we calculated the polarizability of water α_1 from $\alpha_1 = (3/4\pi N_1^0)(n_0^2 - 1)/(n_0^2 + 2)$ in order to be consistent. At 20 °C, we found $\alpha_1 = 1.47$ Å^3 using the refractive index and density data listed in Table I. For nitrogen we took a partial pressure of 0.78 atm, a Henry's law constant[32] of 8.24×10^4, estimated the molar volume from the liquified gas density[33] as 0.8081 g/cm^3, and used a polarizability of 1.76 Å^3 calculated from the Lorentz–Lorenz formula and the refractive index and density of nitrogen gas.[34] Substituting the data into eq 25, we found $\Delta n = -3 \times 10^{-7}$. For oxygen, the equivalent data were partial pressure of 0.20 atm, a Henry's law constant[32] of 4.58×10^4, liquified gas density[35] of 1.149 g/cm^3, and a polarizability[34] of 1.61 Å^3. The result was $\Delta n = -7 \times 10^{-7}$. The refractive increments are negative because in both cases α_1/V_1 is greater than α_2/V_2. The effects of nitrogen and oxygen combine to produce a total refractive increment of -1×10^{-6}. This result is in excellent agreement in regard to both sign and magnitude with the observations and estimates of Tilton and Taylor.

In the derivation of eq 1, it is assumed that the relation $n^2 = \epsilon$ holds where ϵ is the dielectric constant of the solution. If the highest accuracy is desired, Orttung[16] has pointed out that the exact relationship $\epsilon = n^2/\mu$ should be used, where μ is the magnetic permeability of the solution. The frequency dispersion of the magnetic permeability μ_0 of water does not seem to be known, but for a static magnetic field $\mu_0 - 1 = -9 \times 10^{-6}$.[36] The combined effect on the water dielectric constant of (1) ignoring the presence of dissolved air ($\Delta n = -1 \times 10^{-6}$) and (2) assuming the permeability to be unity is given by $\epsilon_0 = n_0^2(1 + \Delta n/n_0)^2/\mu_0 \approx n_0^2(1 + (9 - 1.5) \times 10^{-6})$. Hence, we see that the two systematic errors contribute in opposite directions and tend to cancel. If Δn is as large as -5×10^{-6} as suggested by Tilton and Taylor, then the two errors cancel nearly identically.

Effect of Curvature in the Water B–O Plot. Chen and Orttung[38] have argued that the curvature seen in Figure 1 is due to a small temperature dependence of α_1 which amounts to −0.0018 A^3 between 0 and 62 °C. They point out that the molecules in water are partially oriented due to hydrogen bonding. Hence, the directions of the molecular dipole moments are not completely random. Furthermore, each dipole moment is the source of an electric field. There is, consequently, a contribution to the local electric field at the site of any given molecule which is due to correlations between the orientations of its neighbors. The local field is enhanced by as much as 2×10^5 esu by this effect. Since the degree of ordering by the hydrogen bonds is a function of temperature, the local field changes with temperature. Now, due to the existence of hyperpolarizabilities, the observed molecular polarizability is a weak function of the local field. Hence, they argue, the observed polarizability may be temperature dependent.

Although of considerable interest, this argument has little influence on our data. This is because in eq 15 only the product $N_1^0\alpha_1$ appears. From Table I, it may be seen that N_1^0 undergoes a fractional change of -8×10^{-3}, while according to the results of Chen and Orttung, α_1 suffers a fractional change of at most -5×10^{-4} over this tem-

perature range (see Table I of ref 38). Consequently, the change in $N_1^0\alpha_1$ with temperature is dominated by the change in N_1^0. The use of a least-squares average polarizability thus seemed to us to be the best approach.

Acknowledgment. This research was sponsored by the Energy Research and Development Administration under contract with Union Carbide Corporation.

Appendix

Consider N pairs of observations (X_i, Y_i). We wish to find adjusted values (x_i, y_i) and slope b, such

$$y_i = bx_i \tag{A.1}$$

Following York, we answer this question by minimizing S, the sum of the squares of the deviations

$$S = \sum_i^N \{w(X_i)(x_i - X_i)^2 + w(Y_i)(y_i - Y_i)^2\} \tag{A.2}$$

subject to the constraint expressed by eq A.1. In eq A.2, $w(X_i)$ and $w(Y_i)$ are statistical weights which can be calculated from the relations

$$w(X_i) = 1/(\epsilon(X_i))^2 \tag{A.3}$$

$$w(Y_i) = 1/(\epsilon(Y_i))^2 \tag{A.4}$$

where $\epsilon(X_i)$ and $\epsilon(Y_i)$ are estimates of the errors in X_i and Y_i, respectively.

The results of this approach are

$$x_i = -\frac{\lambda_i b}{w(X_i)} + X_i \tag{A.5}$$

$$y_i = \frac{\lambda_i}{w(Y_i)} + Y_i \tag{A.6}$$

$$\lambda_i = W_i(bX_i - Y_i) \tag{A.7}$$

where $\{\lambda_i\}$ are Lagrange multipliers and

$$W_i = \frac{w(X_i)w(Y_i)}{w(X_i) + b^2 w(Y_i)} \tag{A.8}$$

The slope b satisfies the equation

$$b^3 \sum_i \frac{W_i^2 X_i^2}{w(X_i)} - 2b^2 \sum_i \frac{W_i^2 X_i Y_i}{w(X_i)} + b\left[\sum_i \frac{W_i^2 Y_i^2}{w(X_i)} - \sum_i W_i X_i^2\right] + \sum_i W_i X_i Y_i = 0 \tag{A.9}$$

As York points out, eq A.9 would be a cubic in b, except for the fact that W_i depends upon b.

If the statistical weights happen to be related according to

$$w(X_i) = cw(Y_i) \tag{A.10}$$

where c is a constant, then substantial simplification arises. Equation A.9 becomes a quadratic in b and has the solution

$$b = \Big([\Sigma w(Y_i)(Y_i^2 - cX_i^2)] \pm \{[\Sigma w(Y_i)(Y_i^2 - cX_i^2)]^2 + 4c[\Sigma w(Y_i)X_i Y_i]^2\}^{1/2} \Big) \Big/ (2[\Sigma w(Y_i)X_i Y_i]) \tag{A.11}$$

The upper sign corresponds to $b > 0$, the lower sign to $b < 0$. Only one of these cases will have physical significance. An estimate of the error in b is often desired. To calculate this, we follow Rose[37] and start with the propagation of error formula

$$\epsilon_b^2 = \sum_i \left\{\left(\frac{\partial b}{\partial X_i}\right)^2 (\epsilon(X_i))^2 + \left(\frac{\partial b}{\partial Y_i}\right)^2 (\epsilon(Y_i))^2\right\} \tag{A.12}$$

where $\epsilon(X_i)$ and $\epsilon(Y_i)$ are the errors in X_i and Y_i, respectively. Performing the indicated partial derivatives implicitly using eq A.9, we find

$$\epsilon_b = (b^2 + c)\left[\sum_i (Y_i^2 + cX_i^2)w(X_i)\right]^{1/2} \Big/ \left[\sum_i w(X_i)(cX_i^2 + 2bX_i Y_i - Y_i^2)\right] \tag{A.13}$$

where we have assumed that $w(X_i) = 1/(\epsilon(X_i))^2$ and $w(Y_i) = 1/(\epsilon(Y_i))^2$.

In the general case where there is no relation between the statistical weights, we must use some method of successive approximations to obtain b from eq A.9. We have found it useful to begin by estimating b from a linear plot of the data. We then calculate the W_i from eq A.8. We next treat eq A.9 as a cubic and solve it for b. With this value for b, we recompute the W_i and repeat the cycle until convergence is achieved.

Treated as a cubic, eq A.9 has the form

$$b^3 - 3\alpha b^2 + 3\beta b - \gamma = 0 \tag{A.14}$$

where

$$\alpha = (2/3)\left[\sum_i W_i^2 X_i Y_i / w(X_i)\right]\left[\sum_i W_i^2 X_i^2 / w_i(X_i)\right]^{-1} \tag{A.15a}$$

$$\beta = (1/3)\left[\sum_i W_i^2 Y_i^2 / w(X_i) - \Sigma W_i X_i^2\right]\left[\sum_i W_i^2 X_i^2 / w(X_i)\right]^{-1} \tag{A.15b}$$

$$\gamma = -\left[\sum_i W_i X_i Y_i\right]\left[\sum_i W_i^2 X_i^2 / w(X_i)\right]^{-1} \tag{A.15c}$$

Equation A.13 has three roots given by

$$b_{j+i} = \alpha + 2(\alpha^2 - \beta)^{1/2} \cos\left[(1/3)(\phi + 2\pi j)\right] \quad j = 0, 1, 2 \tag{A.16a}$$

where

$$\cos\phi = [\alpha^3 - (3/2)\alpha\beta + (1/2)\gamma][\alpha^2 - \beta]^{-3/2} \tag{A.16b}$$

In our work, we have always found that the physically meaningful root corresponded to $j = 0$. Equation A.12 may be used in conjunction with eq A.14 and A.15 to estimate the error in b.

References and Notes

(1) L. Onsager, *J. Am. Chem. Soc.*, **58**, 1486 (1936).
(2) J. K. Baird, *J. Phys. Chem.*, **79**, 2862 (1975).
(3) C. J. F. Bottcher, *Physica*, **9**, 945 (1942).
(4) C. J. F. Bottcher, *Recl. Trav. Chim. Pays-Bas*, **62**, 325 (1943).
(5) C. J. F. Bottcher, "Theory of Electric Polarization", Elsevier, New York, N.Y., 1952.
(6) C. J. F. Bottcher, *Recl. Trav. Chim. Pays-Bas*, **62**, 503 (1943).
(7) C. J. F. Bottcher, *Recl. Trav. Chem. Pays-Bas*, **65**, 19 (1946).
(8) C. J. F. Bottcher, *Recl. Trav. Chim. Pays-Eas*, **65**, 39 (1946).
(9) C. J. F. Bottcher, *Recl. Trav. Chim. Pays-Eas*, **65**, 91 (1946).
(10) W. H. Orttung, *J. Phys. Chem.*, **67**, 1102 (1963).
(11) M. Katz, P. W. Lobo, and A. S. Minano, *J. Chim. Phys. Phys. Biol.*, **66**, 1045 (1969).
(12) M. C. Baker, P. A. Lyons, and S. J. Singer, *J. Am. Chem. Soc.*, **77**, 2011 (1955).
(13) M. J. Kronman and S. N. Timasheff, *J. Phys. Chem.*, **63**, 629 (1959).
(14) H. A. Levy, P. A. Argon, and M. D. Danford, *J. Chem. Phys.*, **30**, 1486 (1959).
(15) C. J. F. Bottcher, *Recl. Trav. Chim. Pays-Bas*, **65**, 14 (1946).
(16) W. H. Orttung, *J. Phys. Chem.*, **67**, 503 (1963).
(17) B. A. Brice and M. Halwer, *J. Opt. Soc. Am.*, **41**, 1033 (1951).
(18) J. S. Johnson, K. A. Kraus, and G. Scatchard, *J. Phys. Chem.*, **64**, 1967 (1960).

(19) A. Kruis, *Z. Phys. Chem.*, **34B**, 13 (1936).
(20) H. A. Levy, private communication.
(21) TG and DTA performed by L. M. Steckel of Y-12 Plant Laboratory, Union Carbide Nuclear Division, Oak Ridge, Tenn. 37830.
(22) (a) M.-R. Noe-Spirlet, G. M. Brown, W. R. Busing, and H. A. Levy, Chemistry Division Annual Progress Report for the Period Ending May 20, 1974. Oak Ridge National Laboratory, Oak Ridge, Tenn. 37830. ORNL Report No. 4976. (b) G. M. Brown, M.-R. Noe-Spirlet, W. R. Busing, and H. A. Levy, *Acta Crystallogr.*, submitted for publication.
(23) S. F. West and L. F. Audrieth, *J. Phys. Chem.*, **59**, 1070 (1955).
(24) X-ray diffraction measurements performed by H. L. Perdue of the Y-12 Plant Laboratory, Union Carbide Nuclear Division, Oak Ridge, Tenn. 37830.
(25) D. York, *Can. J. Phys.*, **44**, 1079 (1966).
(26) G. S. Kell, *J. Chem. Eng. Data*, **12**, 66 (1967).
(27) L. W. Tilton and J. K. Taylor, *J. Res. Natl. Bur. Stand.*, **20**, 419 (1938).
(28) L. W. Tilton, *J. Res. Natl. Bur. Stand.*, **14**, 393 (1935).
(29) "Handbook of Chemistry and Physics", 54th ed, Chemical Rubber Company Press, Cleveland, Ohio, 1973–1974, p E-221.
(30) D. R. Barker and L. M. Diana, *Am. J. Phys.*, **42**, 224 (1974).
(31) Th. G. Scholte, *J. Polymer Sci., Part A2*, **10**, 519 (1972).
(32) W. J. Moore, "Physical Chemistry", 3rd ed, Prentice-Hall, Englewood Cliffs, N.J., 1962, p 126.
(33) Reference 29, p B-115.
(34) Reference 29, p E-222.
(35) Reference 29, p B-116.
(36) D. Eisenberg and W. Kauzmann, "The Structure and Properties of Water", Oxford University Press, Oxford, England, 1969.
(37) M. E. Rose, *Phys. Rev.*, **91**, 610 (1953).
(38) Y. Chen and W. H. Orttung, *J. Phys. Chem.*, **76**, 216 (1972).

Comparison between the Experimental and Calculated Excess Free Energy of Solution of Helium, Hydrogen, and Argon in Some Water + Alcohol Systems

M. Lucas*

Service de Chimie-Physique, C.E.N. Saclay, B.P. No. 2-91190 Gif-Sur-Yvette, France

and R. W. Cargill*

Molecular and Life Sciences Department, Dundee College of Technology, Dundee DD 1 1HG, Great Britain *(Received November 30, 1976)*

Publication costs assisted by Commissariat a l'Energie atomique

The excess free energy of solution of helium, hydrogen, and argon in water–ethanol and water–2-methyl-2-propanol mixtures is compared to the calculated values by means of equations derived from the scaled particle theory. An important part of the observed effect is reproduced in the calculations.

I. Introduction

A previous paper has considered the prediction of free energies of transfer of nonpolar solutes from water to aqueous solutions[1] by means of calculations based on the scaled particle theory (SPT).[2,3] New and accurate data are just appearing on the solubility of He, H_2, Ar, and O_2 in water–ethanol and water–2-methyl-2-propanol mixtures.[4,5] Thus it is now possible to compare experimental data with those computed from the SPT, for the solution of these nonpolar gases into water–alkanol mixtures, in which structural effects related to hydrophobic hydration are considered important. In this paper we present a comparison between experimental and calculated free energies of solution of the sparingly soluble gases He, H_2, and Ar into these water–alkanol mixtures at various alkanol mole fractions and temperatures.

II. Calculations

The standard partial molal free energy of solution of a nonpolar solute (with a hard sphere diameter D) is $\Delta G = RT \ln K$ where K is the Henry constant K ($= p/x_s$ where p is the pressure and x_s the solute mole fraction in the water alkanol mixture). In the SPT frame

$$\Delta G = \Delta G_{HS} + RT \ln (RT/V) + G_i \qquad (1)$$

where V is the mean apparent molar volume of the mixture defined as

$$V = \frac{xM_{ROH} + (1 - x)M_{H_2O}}{d}$$

(M_{ROH} and M_{H_2O} being respectively the alkanol and water molecular weight, d is the mixture density, and x is the alkanol mole fraction in the mixture[2,3]). Now ΔG_{HS} is given by the equation[6]

$$(1/RT)\Delta G_{HS} = -\ln (1 - y) + \{3X/(1 - y)\}D + \{3Y/(1 - y) + 4.5X^2/(1 - y)^2\}D^2 \qquad (2)$$

where y, X, and Y are each given by the relation

$$y,\ X,\ Y = \frac{\Pi N}{6} \frac{x_1 a^p + x_2 b^p}{x_1 V^0_{H_2O} + x_2 \phi_{V_{ROH}}}$$

(a, b, $V^0_{H_2O}$, and $\phi_{V_{ROH}}$ being respectively the water hard sphere diameter, the alkanol hard sphere diameter, the pure water molar volume, and the alkanol apparent molal volume, and values of p are 3 for y, 2 for X, and 1 for Y.

It must be noticed at this point that in using eq 2 we assume that the water–alkanol mixture is a collection of hard spheres, but that in using the experimental (real) mixture density (or $\phi_{V_{ROH}}$), we partly take into account structural effects. They are only partly taken into account mainly because in eq 2 it is assumed that the mixture has the radial distribution functions of a hard sphere fluids mixture, which are certainly different from the radial distribution functions of the real water alkanol mixture.

G_i is the free energy of interaction resulting from the existence of dispersion forces between the nonpolar gases and the solvent molecules and it is given by very approximate equations only. However it has been found previously that when a gas is transferred from water to another solvent S, G_i nearly cancels, i.e., $\Delta G_i = G_{iS} - G_{iH_2O} = 0$. Therefore G_i will be neglected in the calculations.

TABLE I: Experimental and Calculated Free Energies of Transfer $\Delta G_{ROH} - \Delta G_{H_2O}$ (kJ mol^{-1})

	Water–ethanol, 5 °C			Water–*t*-BuOH, 12 °C		
	He	H_2	Ar	He	H_2	Ar
Experimental	4.9	5.6	6.6	6.2	7.1	8.2
Computed	4.7	5.2	6.2	6.5	7.1	9.1

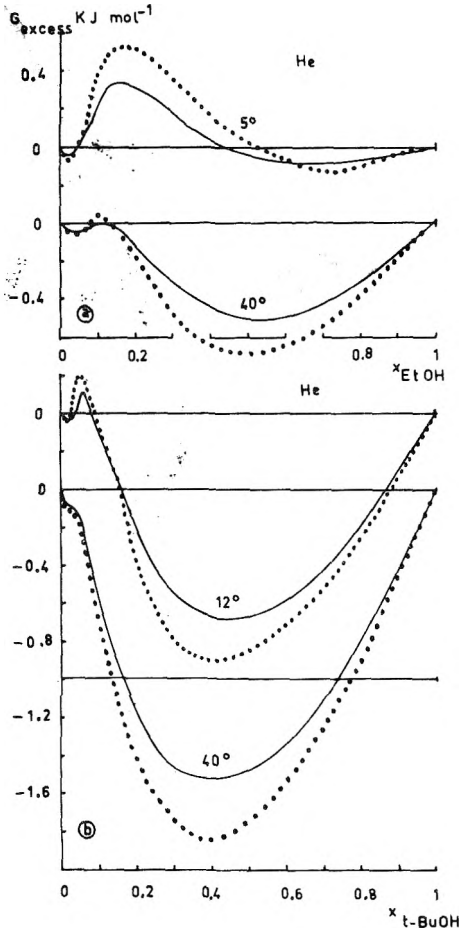

Figure 1. Plots of the excess free energy of solution for He in water–ethanol (a) and water–2-methyl-2-propanol mixtures (b) against alkanol mole fraction x. (dotted line) experimental data; (solid line) calculated data.

The values of a and b are taken respectively as 2.76 Å for water, 4.36 Å for ethanol, and 5.29 Å for 2-methyl-2-propanol.[8,9]

The densities of water–ethanol mixtures, and of water–2-methyl-2-propanol mixtures have been taken respectively from ref 10 and 11, 12.

The hard sphere diameter for the solutes are respectively[2] 2.60 Å for He, 2.87 Å for H_2, and 3.40 Å for Ar.

The accuracy in the experimental values of ΔG is approximately 1% for He and somewhat better for H_2 and for Ar.

III. Discussion

First of all, the computed and experimental free energy of transfer (in kJ mol^{-1}) from H_2O to pure alkanol for the considered solutes is given in Table I. It is apparent from this table that the experimental and computed data are similar, even though, in the calculations, no account has been taken of the interaction free energy arising from dispersion forces.

Now the free energy of transfer to the mixtures at various alkanol mole fractions should be considered in more detail. In order to have a more stringent test we have considered a comparison between computed and experimental G_{excess} where G_{excess} is given by the relation

$$G_{excess} = G_x - \{xG_{ROH} + (1 - x)G_{H_2O}\}$$

where G_x, G_{ROH}, and G_{H_2O} are respectively the experimental (or calculated) value of the free energy of solution in the mixture of alkanol mole fraction x, in pure alkanol, and in pure water, and standard states become irrelevant.

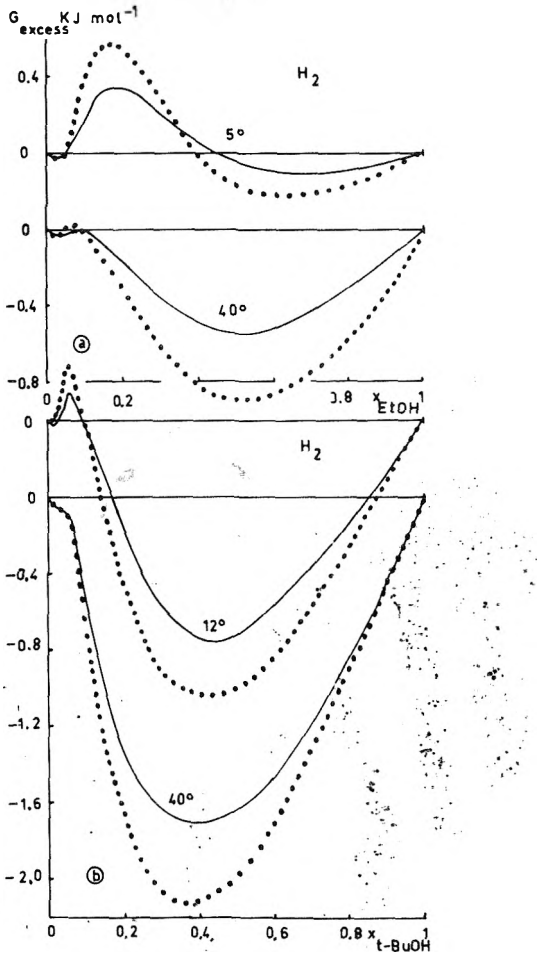

Figure 2. Plots of the excess free energy of solution for H_2 in water–ethanol (a) and water–2-methyl-2-propanol mixtures (b) against alkanol mole fraction x. (dotted line) experimental data; (solid line) calculated data.

Experimental and calculated G_{excess} are plotted in Figure 1 for He, against alkanol mole fraction as abscissa. Figures 2 and 3 show similar plots for H_2 and Ar. A consideration of Figure 1 shows that the qualitative features of experimental curves are reproduced and that the computed G_{excess} accounts for between 60 and 80% of the experimental one. Figures 2 and 3 show that the fit becomes poorer as the size of the solute molecule increases. This is not unexpected. In the original SPT, the solvent structure is not accounted for except implicitly since the experimental density is used in the calculations. Stillinger has shown, when water is taken as the solvent, how to take account of structure more explicitly in the calculations, making use of the experimental radial distribution function for water.[13]

We have used this model previously[7] and found that when the solute molecule is sufficiently small, then the calculated free energy of solution into pure water, using Stillinger's modification, is very similar to that computed using SPT without this modification, but that a discrepancy exists which increases with the size of the solute

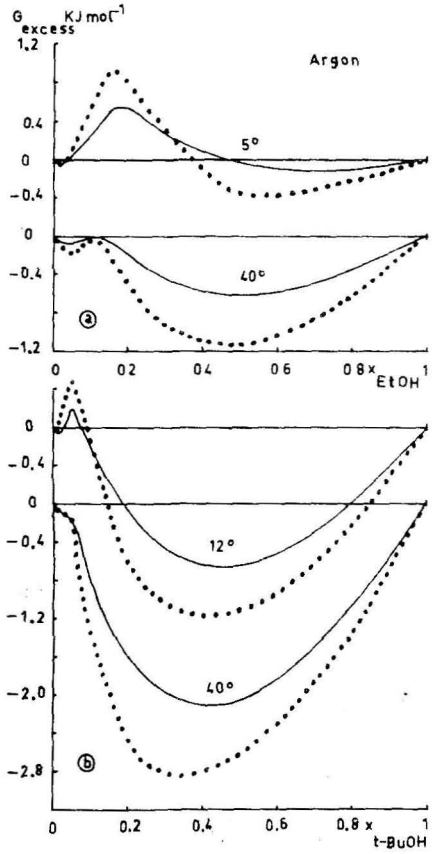

Figure 3. Plots of the excess free energy of solution for argon in water–ethanol (a) and water–2-methyl-2-propanol mixtures (b) against alkanol mole fraction x: (dotted line) experimental data; (solid line) calculated data.

molecule. This is possibly due to the fact that, when a solute molecule is sufficiently small, its free energy of cavity formation (ΔG_{HS}) should depend largely on the mixture compactness, which is fully taken into account in eq 2, but should depend to a lesser extent on the details of the radial distribution function. Probably this is also the case when water–alkanol mixtures are used instead of pure water. The experimental RDF are not known for such mixtures so that Stillinger's modification cannot be used in present calculations.

Another interesting point, resulting from Stillinger's modification is that, the more "structured" is the solvent (compared to a hard sphere fluid), the more positive is the difference between the free energy computed when the solvent structure is taken into account and when it is not.

In this treatment, structure is not accounted for, so the calculated G_{excess} will be in error in the negative direction. If the Stillinger modification could be applied, this calculated G_{excess} would become more positive, and be nearer the experimental values, if the solvent is "structured".

This is what Figure 1 shows. For He in aqueous ethanol at $x < 0.15$ and in aqueous 2-methyl-2-propanol at $x < 0.06$, and at the temperatures 5 and 12 °C, the calculated G_{excess} values are more negative than the experimental ones. This may be taken as evidence for the enhanced structure in these mixtures compared to pure water, as has been suggested before.[4,11] The change from negative to the positive deviations as x increases could also be evidence for a decrease in the structure of the solvent as alcohol is added.

The fact that this correlation is observed for He only and not for H_2 and Ar (the discrepancy for Ar being greater) is in accord with the effect of the size of solute molecule to above. However, this type of explanation is highly tentative.

Finally it should be concluded that in view of all approximations involved in the calculations, the results are, in our opinion, surprisingly good for He. Although they are not so good for H_2 and Ar, in every case, an important part of the observed G_{excess} can be accounted for, using a theory which deals with volume effects. Structural interpretations, however, are not completely ruled out, since the density of water–alkanol mixtures is obviously dependent on structural features of these mixtures.

References and Notes

(1) M. Lucas, *Bull. Soc. Chim. Fr.*, 2994 (1969).
(2) R. A. Pierotti, *J. Phys. Chem.*, **67**, 1840 (1963).
(3) R. A. Pierotti, *J. Phys. Chem.*, **69**, 281 (1965).
(4) R. W. Cargill and T. J. Morrison, *J. Chem. Soc., Faraday Trans. 1*, **71**, 618 (1975).
(5) (a) R. W. Cargill, *J. Chem. Soc., Faraday Trans. 1*, **72**, 2296 (1976), (b) to be published.
(6) J. L. Lebowitz, E. Helfand, and E. Praestgaard, *J. Chem. Phys.*, **43**, 774 (1965).
(7) M Lucas, *J. Phys. Chem.*, **80**, 359 (1976).
(8) C. L. de Ligny and N. G. Van der Veen, *Chem. Eng. Sci.*, **27**, 391 (1972).
(9) E. Wilhelm and R. Battino, *J. Chem. Phys.*, **55**, 4012 (1971).
(10) J. Timmermans, "Physico Chemical Constants of Binary Systems", Vol. 4, Interscience, New York, N.Y., 1960.
(11) L. Avedikian, G. Perron, and J. E. Desnoyers, *J. Solution Chem.*, **4**, 331 (1975).
(12) J. Kenttamaa, E. Tommila, and M. Martti, *Ann. Acad. Sci. Fenn., Ser A2*, 93 (1959).
(13) F. H. Stillinger, *J. Solution Chem.*, **2**, 141 (1973).

A Mass Spectrometric Study of K_2CO_3 and K_2O

L. L. Simmons, L. F. Lowden, and T. C. Ehlert*

Chemistry Department, Marquette University, Milwaukee, Wisconsin 53233 *(Received September 1, 1976)*

Publication costs assisted by the International Minerals and Chemical Corporation

Mass spectrometric analyses of the vapors over K_2CO_3 between 1037 and 1184 K show that the sublimation pressure is described by $\ln P_{atm} = [(-3.67 \pm 0.09 \times 10^4)/T] + 15.65 \pm 0.9$. Decomposition to $K_2O(c)$ and $CO_2(g)$ is more important than sublimation and obeys the equation $\ln P_{atm}(CO_2) = [(-3.045 \pm 0.1 \times 10^4)/T] + 14.69 \pm 0.9$. Sublimation of $K_2O(c)$ obeys the equation $\ln P_{atm}(K_2O) = [(-3.817 \pm 0.08 \times 10^4)/T] + 17.28 \pm 0.7$. The equilibrium constant for $K_2O(g) \rightleftharpoons 2K(g) + {}^1/_2O_2(g)$ obeys the equation $\ln K = [(-3.86 \pm 0.11 \times 10^4)/T] + 17.9 \pm 1.0$. Derived ΔH_{1100K} values are $\Delta H_f(K_2CO_3,g) = -234$, $\Delta H_{subl}(K_2CO_3) = 73.0 \pm 2$, $\Delta H_f(K_2O,g) = -76.8 \pm 2$, $\Delta H_{atom}(K_2O,g) = 137 \pm 2$, $\Delta H_{subl}(K_2O) = 75.8 \pm 1.4$, $\Delta H_f(K_2O,c) = -153 \pm 4$ kcal mol^{-1}. It appears K_2CO_3 is not detectably soluble in K_2O.

Introduction

Although potassium compounds generally constitute less than 1% of the ore, coke, limestone, and sinter materials used in blast furnaces, it has been recognized[1,2] that potassium in several forms reaches a much higher steady state concentration in certain regions of an operating blast furnace. Predictions of the extremely complex processes present and the mechanisms by which potassium is transported in these furnaces are hampered by lack of reliable thermodynamic data for many of these simple compounds. The high temperature behavior of K_2CO_3, for example, which can exist in blast furnaces under certain conditions and is an important raw material in glass making, is still inadequately understood.[3,4] It is generally recognized that K_2CO_3 decomposes at elevated temperatures, and although certainly CO_2 is one of the products, previous investigators[5-7] were unable to tell if $K_2O(g)$ or $K(g)$ and $O_2(g)$ or all three species are also formed. It appeared, then, that knowledge of the behavior of K_2O was essential to interpreting the available data on K_2CO_3. Since K_2O is difficult to prepare and, because of its hygroscopicity, even more difficult to load into an effusion cell without exposure to H_2O or CO_2, we attempted to prepare it in situ in our apparatus by thermally decomposing K_2CO_3.

Method

The apparatus used was a near duplicate of that described previously[8] and consisted of a quadrupole mass spectrometer used to identify and monitor the constituents of a molecular beam from a Knudsen effusion cell. The only important differences between the present apparatus and that described previously were the use of Pt–Pt, 13% Rh thermocouples for cell temperature measurements and a modification to the analyzer power supply to reduce the mass dependence of the ion transmission efficiency.

Certified, ACS grade, anhydrous K_2CO_3 was used without further purification. Since our sensitivity calibration is based on sample weight loss, impurities are tolerable if they do not contribute to the weight loss or alter the activity of the K_2CO_3. Neither problem appeared in these experiments. The effusion cell, made of 0.005-cm thick platinum foil, was essentially an oblate sphere with a 1 cm long diameter and 0.8 cm short diameter. A circular effusion orifice, 3.7×10^{-3} cm^2 in area and 0.96 Clausing factor,[9] was located on the short axis. The sample area was over a hundred times greater than the orifice area to enhance achievement of equilibrium. The cell was secured in the center of a massive, cylindrical tantalum jacket which opened to a diameter of 1 cm to permit unimpeded escape of the effusing vapors. The jacket and cell were placed in the beam source furnace so the beam was sampled normal to the orifice plane, a geometry which minimizes discrimination in sampling.[10] The power applied to two separate filaments was adjusted until the cell top and base temperatures differed by less than 3 K. All four thermocouples were calibrated at the melting point of 99.999% Al in the Pt effusion cell. A thermocouple welded to the bottom of the Pt cell indicated 943 K vs. the accepted value 934 K (IPTS-68) with <1 K temperature difference between the cell and its jacket top and bottom. Thermocouple voltages were converted to IPTS-68 temperatures using standard tables[11] and decreased by 1% as indicated by the calibration results. We believe that temperatures reported here are within 0.5% of true, thermodynamic temperatures. Our procedure was to make all temperature changes as abrupt as possible and to remain at each temperature for a time which was long compared to the nonisothermal period. In this way, the effusion and the mass spectrometer equations can be combined to provide an internal calibration.[12] Appearance potentials were obtained by a semilogarithmic plot method described previously.[8]

Spectral searching was begun at 700 K to avoid inadvertant decomposition of the sample. After the experiment the empty cell's weight and orifice area were checked and found to be unchanged.

Results

The spectrum of vapors over K_2CO_3 at 1122 K consisted of O^+, O_2^+, K^+, CO_2^+, K_2O^+, and $K_2CO_3^+$, according to ionic masses and isotopic abundances. Using the known ionization potentials (IP) of O_2 and CO_2, 12.1 and 13.8 eV, respectively, the appearance potentials of K^+, K_2O^+, and $K_2CO_3^+$ were found to be 4.1, 10.7, and 7.4 eV, respectively, all ±0.3 eV. Comparisons with the known IP(K), 4.3 eV, showed K^+ was formed by ionization of K(g). The IPs of R_2O oxides range from about 7 eV (Li_2O) to 12.6 eV (H_2O)[13] so we assumed $K_2O(g)$ to be the precursor of K_2O^+ and likewise K_2CO_3 to be the precursor of $K_2CO_3^+$. For subsequent studies we used 20 eV electrons because the ionization efficiency curves showed no evidence of fragment contributions up to this energy. Table I summarizes, in the order obtained, these ion current–temperature data. All data reported are net signals, the differences between shutter-open and shutter-closed ion currents. The present

TABLE I: Data for K_2CO_3 Decomposition[a]

Point, n	T, K	t, s	$I^+/A \times 10^9$ $K_2CO_3^+$	K_2O^+	CO_2^+	K^+	O_2^+
1	1114	6 300	0.004 6	0.0320	1.2	10.5	0.24
2	1122	13 560	0.005 8	0.0429	1.4	13	0.25
3	1131	4 380	0.007 9	0.0538	2.0	17	0.40
4	1140	1 800	0.010 3	0.0642	2.5	21.3	0.54
5	1157	1 860	0.015	0.100	3.2	31	0.75
6[b]	1184	4 620	0.035 7	0.25	6.9	59	1.2
7[c]	1134	4 920	0.009 6	0.069	4.0	22	0.60
8	1122	1 620	0.006 3	0.0485	2.0	16.8	0.33
9	1104	1 200	0.003 9	0.026	1.3	9.6	0.22
10	1094	2 160	0.003 1	0.0174	0.90	6.9	0.18
11	1082	26 460	0.002 0	0.015	0.60	6.1	0.143
12	1060	1 680	0.000 95	0.0066	0.35	3.4	0.060
13	1042	2 280	0.000 49	0.0028	0.20	1.7	0.039
14	1037	2 760	0.000 36	0.0026	0.18	1.52	0.033
15	1170	1 380	0.017 4	0.143	4.5	41	0.84

[a] In order taken. [b] Above the melting point of K_2CO_3. Not used in least-squares analyses for eq 1 and 3. [c] Not used for least-square analysis. Insufficient equilibration time.

TABLE II: Relative Sensitivity Factors

Factor	Ions (i) $K_2CO_3^+$	K_2O^+	CO_2^+	K^+	O_2^+
τ_K/τ_i	20	5.2	1.2	1.00	0.79
G_K/G_i	1.7	1.4	1.05	1.00	0.92
τ_K/τ_i	1.4	0.88	14	1.00	24
k_i/k_K	48	8.3	18	1.00	17

apparatus allows no pressure differential between the molecular beam source and the mass spectrometer so even noncondensible species exhibit a "shutter effect" if they originate in the effusion cell.

Least-squares analyses of the Table I data in second law form gave

$K_2CO_3^+$

$$\ln (IT) = \frac{-36730 \pm 950}{T} + 13.90 \pm 8.86 \quad (1)$$

K_2O^+

$$\ln (IT) = \frac{-38165 \pm 765}{T} + 17.14 \pm 0.69 \quad (2)$$

CO_2^+

$$\ln (IT) = \frac{-30454 \pm 990}{T} + 13.92 \pm 0.90 \quad (3)$$

K^+

$$\ln (IT) = \frac{-30805 \pm 663}{T} + 16.41 \pm 0.60 \quad (4)$$

O_2^+

$$\ln (IT) = \frac{-31005 \pm 875}{T} + 12.76 \pm 0.79 \quad (5)$$

To convert these data to partial pressures we applied the internal calibration procedure based on the combined effusion and mass spectrometer equations[12]

$$\Delta w = 44.33aC \sum_i k_i M_i^{1/2} \left(\sum_n \Delta t_n T_n^{1/2} I_{i,n}\right) \quad (6)$$

where Δw is the total weight lost in the experiment, 13.67 mg, 44.33 is a units-conversion factor, a is the cell orifice area in cm^2, C is the Clausing factor, Δt is the time in seconds, and k_i, m_i, and I_i are the sensitivity constant, molecular weight, and ion current for the ith vapor species. Since there were six vapor species it was necessary to express all the sensitivity constants k_i in terms of one species to reduce eq 6 to an equation in just one unknown. This was done with the relation

$$k_i = k_j \frac{\sigma_j G_j \tau_j}{\sigma_i G_i \tau_i} \quad (7)$$

where σ is the ionization cross section, G is the detector gain, and τ is the ion transmission efficiency of the analyzer.[14] The τ_j/τ_i ratios were measured using potassium isotope ratio measurements as described previously.[14] These showed an essentially constant 3% decrease in transmission per mass unit over the mass range used. Gains were taken to vary inversely as the 0.4 power of the ionic mass[15] since the ion intensities of K_2O^+ and $K_2CO_3^+$ were too low to detect without using the secondary electron multiplier detector.

The 20-eV ionization cross sections were taken from the literature for K,[16] O_2, and CO_2.[17] We assumed $G_K\sigma_K/G_{K_2O}\sigma_{K_2O} = G_{Li}\sigma_{Li}/G_{Li_2O}\sigma_{Li_2O} = 1.6$,[18] to find σ_{K_2O} and that $\sigma_{K_2CO_3} = \sigma_{K_2O} + \sigma_{CO_2}$, in analogy with data for NaF, ZrF_4, and $NaZrF_5$.[19]

The relative sensitivity factors except for isotopic terms are summarized in Table II. Table I data were used to find the summations needed for eq 6. Then, with the above values of k_i/k_K plus corrections for isotopic abundances, eq 6 was solved for k_K. This value, 0.12 atm A^{-1} K^{-1}, and the ratios in Table II then gave the constants for each vapor species. We, thus, arrived at the absolute pressures of the various species shown in Table III, using the $P = kIT$ equation,[20] applied at the melting point of K_2CO_3. These data show that sublimation is much less important than decomposition for K_2CO_3 and that $K_2O(g)$ is extensively decomposed under these conditions.

From eq 1 and the calibration constant the sublimation pressure of K_2CO_3 in the range 1037–1174 K is given by

TABLE III: Absolute Pressures over K_2CO_3 at 1174 K

Factors	Species K_2CO_3	K_2O	CO_2	K	O_2
I^+ from eq 1-5, A	2.4×10^{-11}	1.8×10^{-10}	5.1×10^{-9}	4.6×10^{-8}	1.03×10^{-9}
Isotopic corr	1.15	1.15	1.00	1.08	1.00
k_i, atm A^{-1} K^{-1}	48×0.12	8.3×0.12	18×0.12	0.12	17×0.12
P, atm	1.9×10^{-7}	2.4×10^{-7}	1.3×10^{-5}	7.0×10^{-6}	2.4×10^{-6}

$$\ln P_{atm} = \frac{-3.67 \pm 0.09 \times 10^4}{T} + 15.65 \pm 0.86 \quad (8)$$

so that $\Delta H_{subl}(K_2CO_3) = 73.0 \pm 2.0$ kcal mol^{-1} in this range.[21] A third law value cannot be calculated since the properties of $K_2CO_3(g)$ are unknown.

If K_2CO_3 decomposed directly to $K_2O(g)$ and $CO_2(g)$ the temperature dependences of K_2O and CO_2 would be the same when, in fact they differ by more than eight standard deviations. The presence of condensed K_2O is indicated by Kosugi's observation[6] of K and K_2O evolution from K_2CO_3 long after CO_2 evolution ceased. However, the matter is complicated by a report[22] stating that K_2O_2 forms by disproportionation of K_2O at elevated temperatures while another study[23] found K_2O_2 to be unstable with respect to K_2O and O_2 at least to 750 K. Comparison of the melting temperature of KCl (1044 K), NaCl (1074 K), and Na_2O (1405 K) suggests K_2O melts near 1370 K. Consequently, we have assumed that decomposition occurred according to

$$K_2CO_3(c) \rightleftharpoons K_2O(c) + CO_2(g) \quad (9)$$

The constant for this equilibrium, P_{CO_2}, was obtained by combining eq 3 and the sensitivity factor, Table III, to give

$$\ln P_{atm}(CO_2) = \frac{-3.045 \pm 0.1 \times 10^4}{T} + 14.69 \pm 0.9 \quad (10)$$

From eq 10 the second law ΔH_{1100} for this reaction is 61.0 ± 2 kcal mol^{-1} or 62.2 kcal mol^{-1} at 298 K, compared to 68.3 kcal mol^{-1} by the third law method. Considering that the thermal functions for K_2O are estimates,[3] the second law value is believed more reliable. With heat of formation data for CO_2 and K_2CO_3[3] the second law ΔH (eq 9) result gives a $\Delta H_f(K_2O,c) = -152.8$ kcal mol^{-1} at 1100 K. As there was no detectable time dependence for either $K_2CO_3^+$ or K_2O^+ at a constant temperature one may infer that $K_2CO_3(c)$ and $K_2O(c)$ are mutually insoluble. Thus, from eq 2 and our sensitivity constants, the sublimation pressure of K_2O is

$$\ln P_{atm} = \frac{-3.82 \pm 0.07 \times 10^4}{T} + 17.28 \pm 0.07 \quad (11)$$

From eq 11 $\Delta H_{subl}(K_2O) = 75.8 \pm 1.4$ kcal mol^{-1} at 1100 K by the second law. The molecular constants for gaseous K_2O are unknown so a third law treatment is not possible.

The final equilibrium in the cell resulted from the decomposition of $K_2O(g)$ according to

$$K_2O(g) \rightleftharpoons 2K(g) + {}^1/_2O_2(g) \quad (12)$$

It is gratifying to note in this regard that the temperature dependences of P_K and P_{O_2} are almost identical and that $P_K = 2.9P_{O_2}$ at 1174 K which is within experimental error of the stoichiometric requirement $P_K = 4P_{O_2}$ for eq 12. The least-squares value for K_{eq} (eq 12) is given by

$$\ln K_{eq} = \frac{-3.86 \pm 0.11 \times 10^4}{T} + 17.9 \pm 1.0 \quad (13)$$

from which ΔH (eq 12) = 76.8 ± 2.2 kcal mol^{-1} at 1100 K, the mean temperature. Since 1100 K is above the boiling point of potassium $\Delta H_f(K_2O,g) = -\Delta H$ (eq 12) at this temperature. Thus D(KO–K) + D(O–K) = 137 ± 2 kcal mol^{-1} at 1100 K. D(O–K) has been reported[24] as 71 ± 3 kcal mol^{-1} so D(KO–K) = 66 ± 5 kcal mol^{-1}. From ΔH (eq 12) and ΔH (eq 11) we find $\Delta H_f(K_2O,c) = -153 \pm 4$ kcal mol^{-1} at 1100 K in agreement with the value derived from ΔH (eq 9). This consistency lends support to the reported value for $\Delta H_f(K_2CO_3,c)$,[3] albeit indirectly.

Discussion

Although our effusion rate near 1174 agrees with that found in the mass spectrometric-effusion work by Kosugi, ours exhibits a greater temperature dependence. He reported a sharp decrease in the rate above 990 K, where no transition was found in previous, extensive calorimetric studies[25,26] and a sharp increase above the melting point which is contrary to thermodynamic principles. His results differ from ours in that (1) he observed neither O_2^+ nor $K_2CO_3^+$, (2) he apparently did not distinguish background CO_2^+ from that escaping from the effusion cell, (3) his K_2CO_3 dissociation pressure equation is based on the temperature dependence of CO_2^+ and on his lowest temperature effusive flux measurement, and (4) his data extend far beyond the effusion range. Nevertheless, his dissociation pressures agree with those of previous workers[5,7] and are roughly 20 time higher than ours. Further comparisons were hampered by lack of information in these papers. We therefore performed a silver sublimation experiment to calibrate our system and to check our method. The apparatus used, including the effusion cell and the instrument settings, were identical with those used to take our Table I data. A total of 5.85 × 10^{-3} g of NBS-SRM 748 silver was evaporated in three stages: 138 min at 1210 K, 154 min at 1246 K, and 221 min at 1285 K. The corresponding $^{107}Ag^+$ currents were 3.0 × 10^{-10}, 5.5 × 10^{-10}, and 7.1 × 10^{-10} A. Equation 6 gave $k^{107}_{Ag} = 3.32$ atm A^{-1} K^{-1} while the $P = kIT$ equation (eq 10) gave $k^{107}_{Ag} = 3.00$ atm A^{-1} K^{-1} using the silver pressures from its certificate analysis. After normalizing for the lower gain during the silver experiment, a factor of 0.54, correcting for isotope abundances and ion transmission efficiencies, estimating the K^+ and Ag^+ gains as before, and using $k_{Ag} = 6.9 \times 10^{-16}$ cm^2,[27] we found $k_K = 0.12 \pm 0.04$ atm A^{-1} K^{-1}, in exact agreement with our previous result. This value of k_K was subsequently verified six more times in studies of the K–graphite system and the K_2O–SiO_2 system. The accuracy of the sensitivity constants of the other species depends mostly on the ionization cross sections which, fortunately, required estimation only for K_2CO_3. Consequently, it is believed that the pressures obtained from our equations are accurate to ±30% and are not reconcilable with those reported previously.[28]

At 1100 K $\Delta H_f(K_2CO_3,g) = -234$ kcal mol^{-1}, $\Delta H_f(K_2O,c) = -153$ kcal mol^{-1}, $\Delta H_f(K_2O,g) = -76.8 \pm 2$ kcal mol^{-1}, and $\Delta H_{atom}(K_2O,g) = 137 \pm 2$ kcal mol^{-1} can be obtained from our data using the appropriate thermodynamic cycles and supplementary data.[3] Our atomization heat for K_2O is 20 kcal mol^{-1} greater than that estimated via the third law using an unspecified model for $K_2O(g)$ and pressures estimated from ion currents in a mass spectrometric study of the K–K_2O_2 system.[29] These authors concluded KO(g) is the most stable oxide under conditions at least comparable to ours. However, they saw no KO^+. We regard their rationale for this, dissociative ionization to an extent comparable to that in KF and KCl, as being incorrect. One would not expect the K–O bond to depend on the most easily removed electron in an odd-electron molecule. These authors did not attempt a second law study because the ion currents were time dependent.

From eq 8 and $\Delta H_{fus}(K_2CO_3)$, 6.6 kcal mol^{-1},[3] the boiling point of K_2CO_3 is estimated to be 2500 K. Similarly, the boiling point of K_2O is about 2500 K from eq 11 and estimated ΔH_{fus} as 10 kcal mol^{-1}. Up to its boiling point the vapors over K_2O are 5–10% $K_2O(g)$ so as a first approximation the vapors over K_2CO_3 are K, O_2, and CO_2.

Using eq 11 and 13 we find $\Delta G_f°(K_2O,c) = -(1.52 \pm 0.02)10^5 - (71.4 \pm 3)T$ above the boiling point of potassium. Essentially the same result is obtained using eq 10 with JANAF free energy data for CO_2 and $K_2CO_3(c)$. Because $K_2O(c)$ is substantially more stable than previously thought the oxygen potential of the $K-K_2O$ system is a good deal lower on the Ellingham diagram.[1,2] Roughly, the effect is to raise the temperature required for carbon to reduce K_2O in a blast furnace to over 1300 K. It is more likely, however, that sublimation or reaction with SiO_2, for example, would prevent K_2O per se from reaching this temperature region. We are presently investigating the K_2O-SiO_2 and K–graphite systems to ascertain the stabilities of the several compounds occurring there. Studies here have shown that blast furnace slags evolve K(g) but not O_2 on heating, e.g., to 1300 K. It remains to be learned if the source is trapped elemental potassium or the reduction of a potassium compound.

Acknowledgment. The financial support of The International Minerals and Chemical Corp. is gratefully acknowledged as are the helpful comments of Dr. J. W. Currier of IMC.

References and Notes

(1) F. D. Richardson and J. H. E. Jeffes, *J. Iron Steel Inst.*, **163**, 397 (1949).
(2) K. P. Abraham and L. I. Staffansson, *Scand. J. Metall.*, **4**, 193 (1975).
(3) "JANAF Thermochemical Tables", 2nd ed, U.S. Department of Commerce, National Bureau of Standards, Washington, D.C., 20402, 1971.
(4) "High Temperature Properties and Decomposition of Inorganic Salts, Part 2. Carbonates", *Natl. Stand. Ref. Data Ser., Natl. Bur. Stand.*, **No. 30** (1969).
(5) J. T. Howarth and W. E. S. Turner, *J. Soc. Glass. Tech.*, **15**, 360 (1931).
(6) T. Kosugi, *Bull. Chem. Soc. Jpn.*, **45**, 15 (1972).
(7) C. Kröger and J. Stratmann, *Glasstechn. Ber.*, **34**, 311 (1961).
(8) T. C. Ehlert and M. Hsia, *J. Fluorine Chem.*, **2**, 33 (1972–1973).
(9) R. P. Iczkowski, J. L. Margrave, and S. M. Robinson, *J. Phys. Chem.*, **67**, 229 (1963).
(10) R. T. Grimley, L. C. Wagner, and P. M. Castle, *J. Phys. Chem.*, **79**, 302 (1975).
(11) "Thermocouple Reference Tables", *Natl. Bur. Stand. Monogr.*, **No. 125** (1974).
(12) T. C. Ehlert and M. Hsia, J. Chem. Eng. Data, **17**, 18 (1972).
(13) "Ionization Potentials, Appearance Potentials, and Heats of Formation of Gaseous Ions", *Natl. Stand. Ref. Data Ser., Natl. Bur. Stand.*, **No. 26** (1969).
(14) T. C. Ehlert, *J. Phys. E*, **3**, 237 (1970).
(15) R. F. Pottie, D. L. Cocke, and K. A. Gingerich, *Int. J. Mass Spectrom. Ion Phys.*, **11**, 41 (1973).
(16) Yu. P. Korchevoi and A. M. Przonski, *J. Exptl. Theort. Phys. (USSR)*, **51**, 1617 (1966).
(17) D. Rapp and P. Englander-Golden, *J. Chem. Phys.*, **43**, 1464 (1965).
(18) D. White, K. S. Sesardi, D. F. Dever, D. E. Mann, and M. I. Linevsky, *J. Chem. Phys.*, **39**, 2463 (1963).
(19) L. N. Siderov and P. A. Akiskin, *J. Phys. Chem. (USSR)*, **151**, 581 (1963).
(20) W. A. Chupka and M. G. Inghram, *J. Phys. Chem.*, **59**, 100 (1955).
(21) Throughout this paper 1 cal = 4.184 J.
(22) F. Natola and P. Touzain, *Can. J. Chem.*, **48**, 1955 (1970).
(23) J. Riley, Diss. Abstr. Int. B., **30**, 598 (1969).
(24) R. R. Herm and D. R. Herschbach, *J. Chem. Phys.*, **52**, 5783 (1970).
(25) G. I. Janz, E. Neuenschwander, and E. Kelly, *Trans. Faraday Soc.*, **59**, 841 (1963).
(26) M. Rolin and J. M. Recapet, *Bull. Soc. Chim. Fr.*, 2504 (1964).
(27) This is σ_{Ag} at 50 eV reported by Piacente et al., *High Temp. Sci.*, **5**, 395 (1973), multiplied by our observed value of I_{20eV}/I_{50eV} for Ag^+.
(28) There is reason to suspect a systematic error in the data from ref 7 since it has been shown by Piacente et al. (*J. Electrochem. Soc.*, **119**, 75 (1972)) that the Na_2O decomposition pressures reported in this paper are 20 times too great.
(29) A. V. Gusarov and L. N. Gorokhov, *Teplofiz. Vys. Temp.*, **9**, 505 (1971).

A Mass Spectrometric Study of Potassium Cyanide

L. L. Simmons, L. F. Lowden, and T. C. Ehlert*

Chemistry Department, Marquette University, Milwaukee, Wisconsin 53233 *(Received September 1, 1976)*

Publication costs assisted by the International Minerals and Chemical Corporation

KCN sublimes without decomposition. From 700 K up to the estimated boiling point, 1405 K, the vapor consists predominantly of dimer (D) although the monomer (M) abundance is substantial and a small amount of trimer (T) is also present. Sublimation pressures are given by $\ln P_{M,atm} = [(-25930 \pm 600)/T] + 17.37 \pm 0.17$; $\ln P_{D,atm} = [(-29762 \pm 500)/T] + 22.32 \pm 0.16$; and $\ln P_{T,atm} = [(-36796 \pm 600)/T] + 24.39 \pm 0.20$. KCN(c) has no first-order transitions between room temperature and the melting point, 908 ± 1 K. At 850 K second law values of ΔH_{subl} to M, D, and T are 51.5 ± 1.2, 59.1 ± 1.0, and 73.1 ± 1.2 kcal mol^{-1}, respectively. For M the third law ΔH_{subl} is in approximate agreement but for D the difference is very large. $\Delta H_f°_{298}$ for M, D, and T are 24.2 ± 1.5, 7.0 ± 3, and -8.3 ± 4 kcal mol^{-1}, respectively. Dimerization and trimerization enthalpies at 850 K are −41 and −81 kcal mol^{-1}, respectively. $D°_{298}(K-CN) = 101.1 \pm 3$ kcal mol^{-1}.

Introduction

In our previous paper[1] we described the results of studies on the high temperature properties of K_2CO_3 and K_2O, compounds likely to exist under certain conditions in blast furnaces. KCN is clearly another such compound yet its vapor pressure, vapor composition, heat of fusion, and other important thermodynamic properties have not been determined. We, therefore, undertook a study of the vaporization of KCN under effusion conditions in order to improve predictions[2,3] regarding the complex processes occurring in blast furnaces.

Method

The apparatus and general procedure have been described previously.[1] Reagent grade KCN (98.4% minimum) was used without purification. Since our vapor

TABLE I: Mass Spectra of KCN, KF, and KCl

Ion	Rel abundances X = CN[a]	X = F[b]	X = Cl[b]
K^+	1500	1050	1110
KX^+	100	1.9	186
K_2X^+	130	184	238
$K_3X_2^+$	0.2	1.3	0.64

[a] Including all isotopic species and corrected for analyzer discrimination against heavy ions. 70 eV data. [b] From ref 7. 75 eV data.

TABLE II: Data for KCN Sublimination, Run 1[a]

Point n	T, K	t, min	I^+, A × 10^9 KCN$^+$	K_2CN^+	$K_3C_2N_2^+$
1	824	222	0.95	1.3	0.002 5
2	854	52	3.0	6.6	0.019
3	803	23	0.673	1.09	0.002 2
4	792	26	0.418	0.725	0.000 90
5	780	45	0.263	0.425	0.000 71
6	766	37	0.156	0.217	0.000 30
7	853	38	3.14	6.9	0.021 2
8	869	38	5.9	16	0.057
9	872	40	6.8	18.2	0.069
10	874	24	7.4	20.5	0.073 5
11	877	22	8.6	25.2	0.078
12	881	24	9.4	27.8	0.097
13	890	62	13.	39	0.144

[a] 14.97 mg weight loss.

pressure calibration is based on sample weight loss, impurities are tolerable if they do not contribute to the weight loss or alter the KCN activity. This material exhibited less than 0.1% weight loss, and only during the sublimation endotherm, upon scanning to 900 K as part of our thermal analyses. Activity changes would cause ion currents to vary with time under isothermal conditions. Such behavior was not observed. The orifice area for the Pt effusion cell used was 3.7×10^{-3} cm^2 and the orifice Clausing factor[4] was 0.96. As previously, the axial temperature gradient in the effusion cell jacket was kept under 3 K, thermocouple readings were converted to IPTS-68 and these cell temperatures decreased by 1% as indicated by our temperature calibration at the melting point of Al.[1] Appearance potentials were obtained by a semilogarithmic method.[5] A Mettler thermal analyzer was used for DTA and TGA analyses. These were performed under Ar using a Pt container and with Al_2O_3 as the reference material.

Results

Thermal analysis verified the previously reported melting point, 908 K,[6] and showed the KCN has no first-order transitions between room temperature and the melting point.

Mass spectrometric analysis of the vapors at 900 K showed K^+, KCN^+, K_2CN^+, and $K_3C_2N_2^+$ to be the only important species using 70-V electrons. See Table I. The identity of these species was based on the ionic masses and on the isotopic satellites. By the semilog plot method, the corrected electron energy thresholds for forming KCN^+, K_2CN^+, and $K_3C_2N_2^+$ were found to be 9.3 ± 0.3, 10.3 ± 0.3, and 10 ± 1 eV, respectively, using the ionization potentials of H_2O (12.6 eV) and H_2 (15.4 eV) as energy scale calibrants. Based on the low threshold energies and the striking similarity to the KCl and KF spectra[7] we have assumed that KCN^+, K_2CN^+, and $K_3C_2N_2^+$ at low electron energies are derived entirely from KCN (M), $(KCN)_2$ (D), and $(KCN)_3$ (T), respectively. For subsequent studies we used 20-eV electrons to minimize fragment contributions. Two independent experiments were performed. These

TABLE III: Data for KCN Sublimation, Run 2[a,b]

Point n	T, K	t, min	I^+, A × 10^9 KCN$^+$	K_2CN^+	$K_3C_2N_2^+$
1	828	309	1.09	2.37	0.004 5
2	800	25	0.405	0.735	0.001 02
3	770	22	0.135	0.199	0.000 2
4	828	27	1.06	2.43	0.004 5
5	854	35	2.53	6.9	0.017
6	861	30	3.7	9.0	0.022
7	871	48	5.5	15.0	0.044
8	875	77	6.5	18.3	0.056
9	878	35	7.1	20.0	0.063 8
10	865	42	5.04	13.8	0.037
11	862	137	4.4	12.0	0.031
12	870	45	5.5	15.6	0.044 5
13	873	46	6.2	18.0	0.049

[a] 14.35 mg loss. [b] Gains 1.19 times smaller than run 1.

data are shown in Tables II and III in which all data are net signals, the differences between shutter-open and shutter-closed ion currents.

Least-squares analyses of the Tables II and III data in second law form gave

KCN^+ run 1

$$\ln (IT) = \frac{-24998 \pm 640}{T} + 16.58 \pm 0.76 \quad (1a)$$

run 2

$$\ln (IT) = \frac{-26200 \pm 590}{T} + 17.83 \pm 0.70 \quad (1b)$$

K_2CN^+ run 1

$$\ln (IT) = \frac{-29358 \pm 1200}{T} + 22.56 \pm 1.45 \quad (2a)$$

run 2

$$\ln (IT) = \frac{-30400 \pm 584}{T} + 23.68 \pm 0.69 \quad (2b)$$

$K_3C_2N_2^+$ run 1

$$\ln (IT) = \frac{-35438 \pm 1450}{T} + 23.84 \pm 1.73 \quad (3a)$$

run 2

$$\ln (IT) = \frac{-37380 \pm 628}{T} + 25.84 \pm 0.74 \quad (3b)$$

To convert these data to partial pressures we applied the internal calibration procedure on the combined effusion and mass spectrometer equations[8]

$$\Delta w = 44.33 a C \Sigma_i k_i m_i^{1/2} (\Sigma_n \Delta t_n T_n^{1/2} I_{i,n}) \quad (4)$$

where 44.33 is a units conversion factor, a is the cell orifice area in cm^2, C is the Clausing factor, Δt is the time in seconds, and k_i, M_i, and I_i are the sensitivity constant, molecular weight, and ion current for the ith vapor species. Equation 4 was solved using Table II data and the total weight lost by the sample in the experiment, 14.97 mg for run 1 and 14.35 mg in run 2. Since there were three vapor species it was necessary to express all the sensitivity constants k_i in terms of one species to reduce eq 4 to an equation in just one unknown. This was done with the relation

$$k_i = k_j \frac{\sigma_j G_j \tau_j}{\sigma_j G_j \tau_j} \quad (5)$$

where σ is the ionization cross section, G is the detector gain, and τ is the ion transmission efficiency of the analyzer.[9] The absence of impurities and the simplicity of the

TABLE IV: Partial Pressures (atm) over KCN at 890 K

		Ion/molecule	KCN/KCN^+	$K_2CN^+/K_2C_2N_2$	$K_3C_2N_2^+/K_3C_3N_3$
I^+, A	run 1		1.13×10^{-8}	3.3×10^{-8}	1.29×10^{-10}
	run 2		1.02×10^{-8}	3.2×10^{-8}	1.08×10^{-10}
k atm A^{-1} K^{-1}	run 1		0.80	0.51	0.41
	run 2		0.83	0.53	0.42
P, atm	run 1		8.0×10^{-6}	1.50×10^{-5}	4.7×10^{-8}
	run 2		7.5×10^{-6}	1.45×10^{-5}	4.0×10^{-8}

spectrum permitted reduction of the resolution to the point where total transmission of a given ion occurred. Consequently, the τ_j/τ_i factors in eq 5 become unity. The peaks are about 10 amu wide under these conditions so all isotopic varieties of a given ion are included in the currents measured. Detector gains for KCN^+, K_2CN^+, and $K_3C_2N_2^+$ were found experimentally to be 26 000, 29 000, and 27 000, respectively. For the alkali halides the average value of σ_D/σ_M is 1.4 [10] so we assumed $\sigma_M:\sigma_D:\sigma_T$ = 1:1.4:1.8. Thus, eq 5 gives $k_D = 0.64k_M$ and $k_T = 0.51k_M$. Solving eq 4 for k_M gives k_M = 0.80 atm A^{-1} K^{-1} so k_D = 0.51 atm A^{-1} K^{-1} and k_T = 0.41 atm A^{-1} K^{-1} using run 1 data and k_M, k_D, and k_T = 0.83, 0.53, and 0.42 atm A^{-1} K^{-1}, respectively, using run 2 data corrected for the smaller detector gain in run 2. The monomer, dimer, and trimer partial pressures at 890 K obtained from the $P = kIT$ equation[11] using these factors are shown in Table IV. Agreement between runs 1 and 2 is excellent.

Since $P_T < P_M$ and P_D it should be possible to neglect the trimer contribution to the weight lost and to obtain k_M and k_D by simultaneous solution of the two equations in the form of eq 4, one based on run 1 and the other based on run 2. When this is done, however, k_D is found to be slightly negative. This physically impossible result indicates our data are not sufficiently accurate, although the resulting equations do suggest the constants are of the order of unity.

To obtain accurate vapor pressure equations one must avoid the slope–intercept interaction resulting from least-squares analysis of vapor pressure data in second law form. One way to do this is to combine the best value for the slope with the best absolute pressure at some temperature. To accomplish this we made additional measurements of the slopes of eq 1a–3b. Based on 22 data points over the temperature range 709–901 K we obtained −26 574 ± 645 and −29 383 ± 500 K as the slopes of the monomer (eq 1) and dimer (eq 2) equations, respectively. These values and runs 1 and 2 values were combined by weighting each value in proportion to the inverse of its standard deviation. The resulting best slopes in kcal mol^{-1}, −25 930 ± 600, −29 762 ± 500, and −36 796 ± 600 K for M, D, and T, respectively, were combined with the run 1–run 2 average pressure for each species from Table IV to give

$$\ln P_{M,atm} = \frac{-25930 \pm 600}{T} + 17.37 \pm 0.17 \quad (6)$$

$$\ln P_{D,atm} = \frac{-29762 \pm 500}{T} + 22.32 \pm 0.16 \quad (7)$$

$$\ln P_{T,atm} = \frac{-36796 \pm 600}{T} + 24.39 \pm 0.54 \quad (8)$$

In eq 6, 7, and 8 the uncertainties assigned to the intercepts are those arising from differences between run 1 and run 2 pressures, the effect of a ±4 K temperature uncertainty,[1] and a ±40% uncertainty in σ_T/σ_M.

Since the melting temperature of KCN is 908 K, eq 6, 7, and 8 give sublimation pressures. At the melting point the vapor composition is 32.4% M, 67.4% D, and 0.2% T. Using the estimated[12] heat of fusion, 3.5 kcal mol^{-1}, the vaporization equations are

$$\ln P_{M,atm} = \frac{-24180}{T} + 15.43 \quad (9)$$

$$\ln P_{D,atm} = \frac{-26262}{T} + 18.44 \quad (10)$$

$$\ln P_{T,atm} = \frac{-31546}{T} + 18.57 \quad (11)$$

From eq 9, 10, and 11 the boiling point of KCN is predicted to be about 1405 K vs. 1896 K estimated[12] apparently on the basis of a completely monomeric vapor. However, at the boiling point the vapor composition is about 17% M, 81% D, and 2% T.

From eq 6, 7, and 8 the second law ΔH_{subl} near 850 K are 51.5 ± 1.2, 59.1 ± 1.0, and 73.1 ± 1.2 kcal mol^{-1} for M, D, and T, respectively.[13] Corrected to 298 K, using the JANAF values altered to include recent experimental vibrational frequencies for M,[14] ΔH_{subl} = 52.9 ± 1.2 and 61.2 ± 1.0 kcal mol^{-1} for M and D, respectively. The corresponding third law values are 48.2 ± 1.5 and 43.7 ± 1.5 kcal mol^{-1}. The agreement between the second and third law values is not good for M and very poor for D, suggesting large errors in the tabulated functions[12] or in our pressures. We subsequently verified our absolute pressures, Table IV, in each of two additional experiments on KCN. It was not possible to check our calibration by means of a silver vaporization experiment.[15] Recent theoretical studies of alkali halide polymer structures[16] suggest that the model used for D is incorrect while the free energy functions for the solid are based on a long extrapolation of heat capacity data. Under the circumstances, second law results must be given greater credence.

From $\Delta H_{f,298}$(KCN,c), −27.12 ± 0.2 kcal mol^{-1},[12] one can obtain $\Delta H_{f,298}$ for gaseous M, D, and T: 24.2 ± 1.5, 7.0 ± 3, and −8.3 ± 4 kcal mol^{-1} using our second $\Delta H_{subl,298}$ for M and D and $\Delta H_{subl,850}$ for T. Similarly, dimerization of KCN(g) is exothermic by 41 kcal mol^{-1} and trimerization is exothermic by 81 kcal mol^{-1}. The dimerization result seems reasonable when compared to the values for KF and KCl, −50 and −45 kcal mol^{-1}, respectively, and to the value for NaCN, −47 kcal mol^{-1}.[12,17]

Also, $D°_{298}$(K–CN) = 101.1 ± 3 kcal mol^{-1} compared to 119 ± 5 kcal mol^{-1} obtained from flame studies[16] in which concentrations were estimated from optical intensities and from mass spectrometric samples of the flame. The flame study result seems too high when compared to $D°_{298}$(K–Cl), 101 kcal mol^{-1}, and to $D°_{298}$(K–F), 118 kcal mol^{-1}.

Conclusion

KCN sublimes without decomposition, the vapor being predominately $(KCN)_2$ up to the boiling point. Consequently, the sublimation pressure rises more rapidly with temperature and the vapor is thermodynamically more stable. Applying a crude but useful approximation that in a blast furnace KCN will accumulate in the temperature zone where it moves upward by sublimation or vaporization at the same rate the burden moves downward leads

to the prediction that KCN would be abundant in the 900 K region of the furnace. Of course, oxidation destroys the compound if, under operating conditions, the oxygen potential is sufficiently great.

Acknowledgment. This work was supported by the International Minerals and Chemical Corp. Discussions with Dr. J. W. Currier have been most helpful to us. We also wish to thank Mr. E. Bilinski for providing the thermal analysis.

References and Notes

(1) L. L. Simmons, L. F. Lowden, and T. C. Ehlert, *J. Phys. Chem.*, preceding paper in this issue.
(2) F. D. Richardson and J. H. E. Jeffes, *J. Iron Steel Inst.*, **163**, 397 (1949).
(3) K. P. Abrahamn and L. I. Staffansson, *Scand. J. Metall*, **4**, 193 (1975).
(4) R. P. Iczkowski, J. L. Margrave, and S. M. Robinson, *J. Phys. Chem.*, **67**, 229 (1963).
(5) T. C. Ehlert and M. Hsia, *J. Fluorine Chem.*, **2**, 33 (1972–1973).
(6) R. Granadam, *Compt. Rend.*, **180**, 1598 (1925).
(7) J. Berkowitz and W. A. Chupka, *J. Chem. Phys.*, **29**, 653 (1958).
(8) T. C. Ehlert and M. Hsia, *J. Chem. Eng. Data*, **17**, 18 (1972).
(9) T. C. Ehlert, *J. Phys. E*, **3**, 237 (1970).
(10) R. F. Pottie, *J. Chem. Phys.*, **44**, 916 (1966).
(11) W. A. Chupka and M. G. Inghram, *J. Phys. Chem.*, **59**, 100 (1955).
(12) "JANAF Thermochemical Tables", 2nd ed. U.S. Department of Commerce, National Bureau of Standards, Washington, D.C. 20402.
(13) Throughout this paper 1 cal = 4.184 J.
(14) Z. K. Ismail, R. H. Hauge, and J. L. Margrave, *J. Mol. Spectrosc.*, **45**, 304 (1973). The thermodynamic functions given for KCN and NaCN in this paper are incorrect.
(15) An attempt to use silver vaporized under identical conditions, including using the same effusion cell, to check our values of k_M, k_D, and k_T failed because there is no reliable means to estimate the relative cross sections, e.g., $\sigma_{Ag}:\sigma_M$. In fact, comparison of our KCN and Ag data suggests that $\sigma_{Ag}:(\sigma_M \approx \sigma_D \approx \sigma_T) = 5.0 \pm 0.2$ at 20 eV. This large ratio is understandable on the basis that fragmentation to K^+ is much more probable than forming the ions we monitored. Table I data clearly support this idea.
(16) D. O. Welch, O. W. Lazareth, G. L. Dienes, and R. D. Hatcher, *J. Chem. Phys.*, **64**, 835 (1976).
(17) R. F. Porter, *J. Chem. Phys.*, **35**, 318 (1961).
(18) J. N. Mulvihill and L. F. Phillips, *Chem. Phys. Lett.*, **33**, 608 (1975).

On the Application of Radioisotope Techniques for the Study of Phthalocyanine Catalyzed Electrochemical Processes in Fuel Cells

H. Meier,* U. Tschirwitz, E. Zimmerhackl, W. Albrecht, and G. Zeitler

Staatliches Forschungsinstitut für Geochemie, Bamberg, Federal Republic of Germany *(Received June 3, 1976)*

The behavior of polymeric iron phthalocyanine catalysts during the cathodic reduction of oxygen in sulfuric acid was studied by labeling central iron atoms with ^{59}Fe. Moreover, in order to get an insight into the interaction between iron polyphthalocyanines and carbon supports, Mössbauer spectroscopic investigations have been undertaken. The experiments showed that iron polyphthalocyanine electrocatalysts, which are built in carbon–teflon electrodes, could be classified in (a) phthalocyanine molecules with low stability and large quadrupole splitting which have only a low influence on the electrochemical operation of the electrode and (b) phthalocyanine molecules with high stability and low quadrupole splitting which are decisive in electrocatalysis. In agreement with the mechanism of long-life electrocatalytic operation and deactivation, derived from these experiments, carbon–teflon cathodes with polymeric iron polyphthalocyanine catalysts could be constructed which are characterized by a high stability during continuous operation in 6 N H_2SO_4 up to 3000 h.

I. Introduction

Radionuclides are a useful tool for the study of electrochemical processes. They permit a rapid and selective study of reactions which occur at electrodes. By the labeling of electrodes or electrolyte ions radioisotopes may be used, e.g., in passivation studies,[1,2] electroplating,[3] corrosion investigations,[4] or electrosorption experiments.[5] Moreover, in radioelectrochemistry radioisotopes may be used as sources of radiation, e.g., ^{60}Co for direct conversion of radiation energy into electrical energy through electrochemical processes;[6] see reviews in ref 7 and 8.

In spite of the breadth of application there are only relatively few studies in which isotopic techniques are used in the field of batteries or fuel cells.[9,10] In this paper shall be given a further example which demonstrates that also in this complex field problems which are beyond the scope of a conventional physicochemical treatment can be solved. Above all, it is shown that the results of radioisotope experiments may be helpful for a further improvement of oxygen cathodes for fuel cells.

The development of oxygen cathodes has been stimulated by the discovery of the ability of metal phthalocyanines and other chelates for catalyzing the cathodic reduction of oxygen[11–19]

$$O_2 + 4H^+ + 4e^- = 2H_2O \quad (1)$$

In a series of experiments it could be found that the electrocatalytic activity depends not only on structural parameters (nature of the central atom, degree of polymerization, etc.) and physical properties (conductivity, catalase activity), but also on the nature of the substrate.[13,17,20–22] Moreover, the stability could be improved by optimizing these factors. However, because of a slow decrease of the electrocatalytic activity of cathodes in acid electrolytes which seems to be the result of a decomposition of the organic catalyst,[13,14,19] the applicability of chelate-catalyzed electrodes has been doubted in spite of an operating life on the order of several hundred hours. Therefore, experiments are necessary for a clear understanding of the mechanism which is responsible for the decrease of the electrocatalytic activity with time.[13,23,24] This knowledge may be taken as a guide for a further improvement of chelate-catalyzed cathodes.

II. Experimental Section

1. *Electrochemical Measurements.* The electrocatalytic properties of polymeric iron phthalocyanines that are being discussed in this paper have been tested in teflon-bonded porous electrodes. For details of synthesis see, e.g., ref 22

and 25–27. For obtaining good conductive electrodes phthalocyanines have been contacted with carbon powder. This was done after dissolving purified phthalocyanines in concentrated sulfuric acid by precipitating them on suspended carbon by adding water. The electrodes were prepared by pressing thin cylindrical tablets of 7 cm^2 area onto a sheet of porous teflon with a pressure of 1000 kp/cm^2.

Several experiments have shown that different phthalocyanines can be compared in relation to their electrocatalytic activity in compact electrodes of the last mentioned type.[20] Therefore, these electrodes have been used for radioelectrochemical tests which were carried out in half-cells in 6 N H_2SO_4 at room temperature against autogenous hydrogen reference electrodes.[28] For characterizing the electrocatalytic activity the following electrochemical measurements have been performed: (a) cyclic potentiostatic current–voltage curves by a triangular voltage sweep between 900 and 400 mV (vs. a hydrogen electrode) with a scan rate of 60 mV/min; (b) galvanostatic current–voltage curves with a scan rate of 5 mA/min; (c) galvanostatic long-time tests, in which the potential as a function of the operating time is registered during a constant cathodic current density (e.g., 20 mA/cm^2).

2. *Radioisotopic Studies.* A. *Measurement of the Demetallation of Polymeric Iron Phthalocyanines.* The behavior of polymeric iron phthalocyanines during the cathodic reduction of oxygen in sulfuric acid was studied radiochemically with ^{59}Fe labeled polyphthalocyanines. This technique was necessary because during the electrochemical operation changes of the electrolyte volume had to be avoided as much as possible. For instance, by taking a large volume of electrolyte for analysis, the concentration of hydrogen peroxide would be disturbed. It is formed according to

$$O_2 + 2H^+ + 2e^- = H_2O_2 \qquad (2)$$

as an intermediate in the cathodic reduction of oxygen, whereby current potential curves may be shifted. However, the use of ^{59}Fe as a tracer permitted measurements on samples of small volume. Therefore the behavior of phthalocyanines could immediately be observed during their catalytic operation.

Iron-59 labeled polyphthalocyanines were prepared by adding iron in the form of chloride, etc. which contained ^{59}Fe and inactive iron in a constant ratio of the starting compounds (derivatives of aromatic or fatty acids, urea, catalysts, etc.[25–27]) before heating. In this way the specific radioactivity of iron central atoms was brought to a value of 3 $\mu Ci/mg$. Furthermore, solutions with iron of the same specific radioactivity were prepared for the measurement of calibration curves. These curves were taken as the basis for the direct determination of the amount of phthalocyanines demetallated during their operation in oxygen cathodes.

From a calibration line a detection limit down to the order of 10^{-8} g of Fe/mL could be derived. In this context it should be remembered that the radionuclide ^{59}Fe decays with a half-life of 45.1 days by β emission to excited states of ^{59}Co, i.e.

$$^{59}_{26}Fe \xrightarrow{\beta^-} {}^{59}_{27}Co$$

They go to the ground state of ^{59}Co by the emission of γ rays with E_γ = 1.10 MeV (57%) and E_γ = 1.29 MeV (43%). For the measurement of γ ray spectra of solutions containing ^{59}Fe a borehole NaI(Tl) scintillation detector in conjunction with a 400 channel pulse-height analyzer FHT 400 B has been used.

Because of the relatively short half-life of ^{59}Fe, the count rates, measured in samples which were taken from fuel cell electrolytes (0.1 mL) over longer periods, have to be normalized by

$$R(t_0) = R(t_0 + \Delta t)\left[\exp\frac{0.693}{T_{1/2}}\Delta t\right] \qquad (3)$$

$R(t_0)$ is the normalized count rate; $R(t_0 + \Delta t)$ is the measured count rate; Δt the difference (in hours) between time of measurement and reference time t_0; i.e., $\Delta t < 0$ (>0) in the case of the measurement before (after) the reference time t_0; $T_{1/2}$ is the half-life (h).

B. *Mössbauer Measurements.* In order to obtain an insight into the interaction between iron phthalocyanines and carbon supports, Mössbauer spectroscopic investigations have been undertaken. In this context it should be mentioned that in several studies iron-57 Mössbauer spectra have been used for an investigation of monomeric iron phthalocyanine because of its structural similarity with biologically important porphyrins.[29–34] However, there are only few Mössbauer data about polymeric iron phthalocyanines.[35]

Mössbauer spectra were measured between 77 K and room temperature in the transmission geometry using 14.4-keV γ rays of a $^{57}Co/Pt$ source (11 mCi). They are registered after passing the absorber by a proportional counter LB 6047 in conjunction with a 400 channel pulse-height analyzer FHT 400 B. As a source drive unit the system FHT 800 A was used.[36] As absorbers powered samples of following samples have been investigated: polymeric iron phthalocyanines without carbon as substrate material; polymeric iron phthalocyanines precipitated in different weight ratios onto carbon supports (Norit BRX); polymeric iron phthalocyanines prepared in porous carbon–teflon electrodes which are used for the cathodic oxygen reduction.

III. Results

1. *Radiation Influence of the ^{59}Fe Tracer.* In several studies, influence of the radiation of tracers on electrode processes has been reported.[7] As an example, the observation of a change in the mechanism of the oxygen reduction on platinum electrodes in alkaline solutions resulting from ^{60}Co γ radiation should be mentioned.[37] Moreover, by the incorporation of radionuclides, such as ^{14}C, ^{63}Ni, or ^{60}Co, in porous carbon electrodes, an improvement of current–voltage curves has been described.[38–40]

Therefore, in order to be sure that any influence from the radiation of the ^{59}Fe marker can be excluded, the electrochemical behavior of carbon–teflon electrodes with and without iron-59-containing polyphthalocyanines have been tested. From the example given in Figure 1, it can be seen that the radiation of the ^{59}Fe tracer does *not* exert any influence on the behavior of the electrode. However, this result should not be considered as a contradiction to the effects discussed in the literature because of differences in the activities used. The activity was in the order of 10 μCi for the electrodes used here and more than 10 mCi for the electrodes used elsewhere.

2. *Tracer Experiments.* As described above, the low rate of demetallation of polymeric iron phthalocyanines can be studied radiochemically in acid electrolytes under the condition of cathodic oxygen reduction. The example given in Figure 2, in which the amount of dissolved iron is plotted as a function of time, shows that only some of the phthalocyanine molecules lose their central atoms during their electrocatalytic action. After several hundred

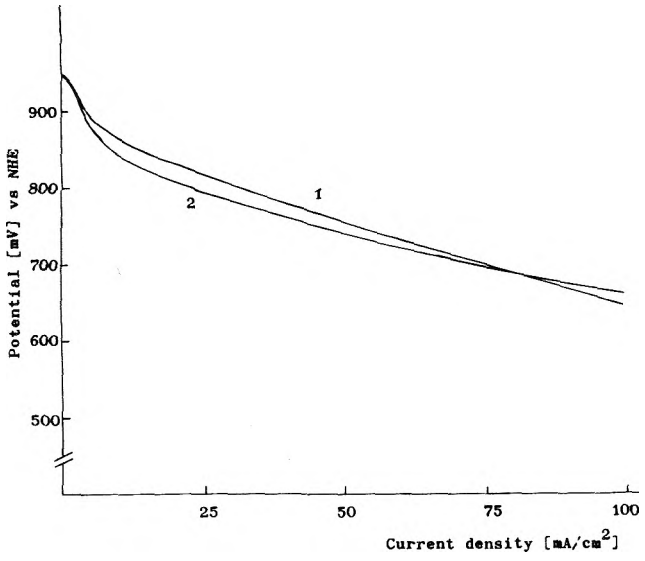

Figure 1. Galvanostatic current/voltage curves for oxygen reduction at polymeric iron phthalocyanine (synthesis no. 21): (1) without ^{59}Fe; (2) labeled with ^{59}Fe (about 10 μCi/cm^2).

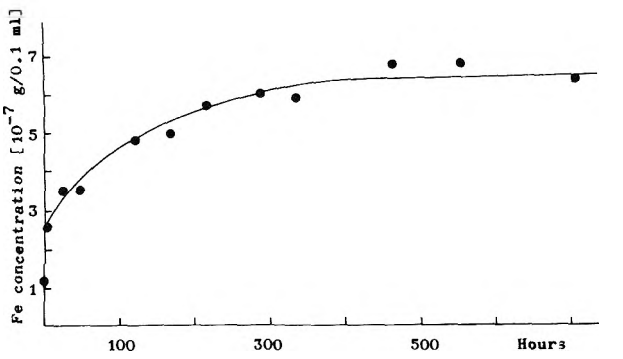

Figure 2. Plot of dissolved iron during electrochemical oxygen reduction as a function of time: polymeric iron phthalocyanine 21, 6 N H_2SO_4, current density 40 mA/cm^2.

hours of continuous cathodic oxygen reduction, the amount of iron demetallated from polymeric phthalocyanines approaches a limiting value. This value does not agree with the amount of metal atoms which are fixed in the phthalocyanine catalyst.

The electrocatalytic behavior is not directly connected with the loss of central iron atoms into solutions. This could be recognized by a comparison of the electrochemical long-time stability of polymeric iron phthalocyanine electrodes with the rate of demetallation. Figure 3 shows a galvanostatic long-time test which is compared with the amount of iron passing into solution during this test. The potential shows only a small decay under a continuous galvanostatic service of 1000 h in spite of the fact that a part of phthalocyanine molecules is demetallated rapidly.

On the other hand, a limited operating life of electrodes cannot be generally attributed to a decomposition of all phthalocyanine molecules which are acting as catalyst in carbon–teflon electrodes. As can be seen from Figure 4, the sudden decrease of the activity, which may be observed under special conditions and methods of operation, must not be connected with the demetallation of the catalyst. It is probable that the limitation of the operating life may often be the result of a disturbance of the three-phase boundary gas, liquid, and solid. The sudden increase of the concentration of hydrogen peroxide, which is shown in Figure 4, may be in connection with this defect.

Former observations[41] showed that some metal phthalocyanines may be demetallated by the attack of concentrated sulfuric acid. In addition it can be derived from Figure 5 that a portion of iron atoms are passing into solution without any electrochemical process. This depends remarkably on the presence of oxygen dissolved in the acid solution. In a nitrogen atmosphere the degree of demetallation is strongly reduced.

It should be mentioned that, after closing the radioelectrochemical and chemical experiments, the *whole* amount of iron which passed into solution during the long-time tests, was also measured by a parallel spectrophotometric test. With this additional test the results obtained radioelectrochemically could be confirmed.

3. *Mössbauer Experiments.* As shown in Figure 6a, the Mössbauer spectra of polymeric iron phthalocyanines precipitated on carbon supports (e.g., Norit BRX) consist of two main quadrupole-split doublets I and II. The quadrupole splitting of doublet I, which depends on the electric field gradient and therefore on the symmetry of the nuclear environment, is on the order of $\Delta = 2.6$ mm/s and the Δ values of doublet II are on the order of 0.58 mm/s. The isomer shift is, in relation to metallic iron, in the range of 0.49 ± 0.03 mm/s for both doublets.

By analyzing the observed doublets, the following coordination seems possible: 1. Doublet I with $\Delta = 2.6$ mm/s can be attributed to polymeric iron phthalocyanine *without* any carbon support. This can be derived from Figure 6b in which the Mössbauer spectrum of a support-free iron polyphthalocyanine sample is given. In this context it should be mentioned that the Mössbauer spectrum of

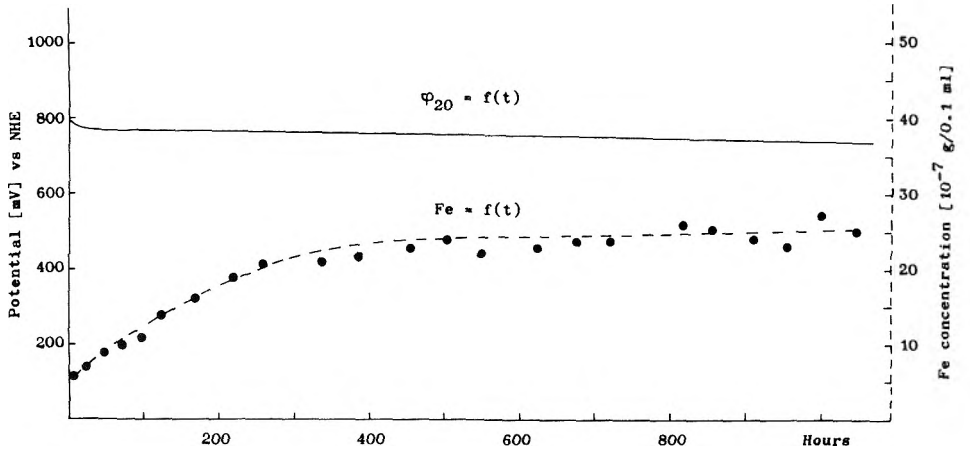

Figure 3. Comparison between demetallation of iron polyphthalocyanine catalyst (synthesis no. 4) and electrocatalytic stability: $\varphi_{20} = f(t)$, galvanostatic potential/time curve, 6 N H_2SO_4, current density 20 mA/cm^2; $^{57}Fe = f(t)$, iron dissolution during electrochemical oxygen reduction as a function of time.

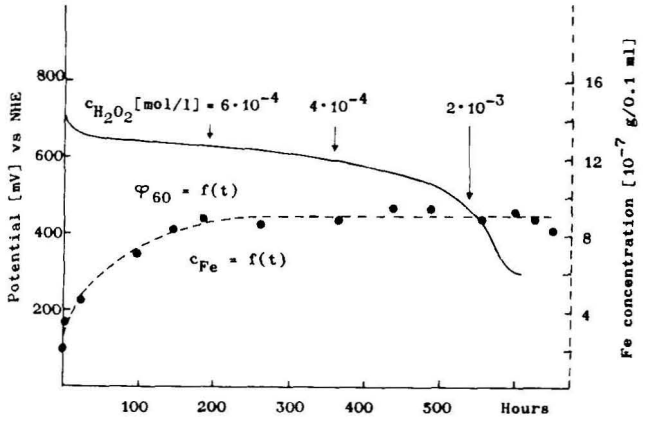

Figure 4. Comparison between demetallation of iron polyphthalocyanine catalyst (synthesis no. 21) and electrocatalytic stability, example of electrode disturbance: φ_{60} = f(t), galvanostatic potential/time curve, 6 N H_2SO_4, current density 60 mA/cm^2; Fe = f(t), iron dissolution during electrochemical oxygen reduction as a function of time.

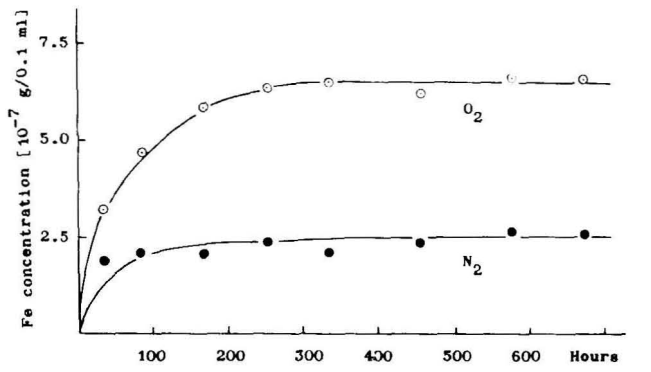

Figure 5. Demetallation of polymeric iron phthalocyanines in 6 N H_2SO_4 as a function of time in nitrogen (N_2) and oxygen (O_2) atmosphere.

phthalocyanineiron(II) monomer is also characterized by a large quadrupole splitting[29,34] and a low isomer shift.[31] Therefore, the electric field gradient at the iron nucleus may be taken similar both in monomeric and polymeric iron phthalocyanines. In order to understand this fact, Mössbauer studies of α and β polymorphs of phthalocyanines[34] and Mössbauer data of iron phthalocyanine derivatives under pressure[30] should be taken into consideration. These studies show that, as a result of σ bonding and π back-bonding (see Figure 7) between iron d orbitals (i.e., $3d_{z^2}$ and $3d_{xz,yz}$, respectively) and ligands which are coordinated perpendicular to the phthalocyanine plane, an asymmetry parameter of the electric field gradient may arise.

Such ligands cannot only be organic bases, e.g., pyridine etc., or oxygen molecules, but also nearly axially situated nitrogens of the aromatic rings of neighboring phthalocyanine molecules.[34] However, it seems important for an asymmetry effect that only *a single* antibonding π^* orbital is π bonded with the d_{xz} *or* d_{yz} orbitals of the central iron atom. For instance, hemoglobin carbon monoxide, in which a pair of antibonding π^* orbitals can simultaneously interact with d_{xz} and d_{yz} orbitals of iron, shows a small quadrupole splitting, whereas oxyhemoglobin in which oxygen is back-bonded with its single antibonding π^* orbital is characterized by a large splitting.[29,42]

Probably, the large quadrupole splitting of polymeric iron phthalocyanines can be explained in an analogous manner, i.e., there may be an interaction between nearly axially situated nitrogens of neighboring phthalocyanine molecules or oxygen molecules with $3d_{xz}$ and $3d_{yz}$ orbitals of iron atoms (see Figure 8).

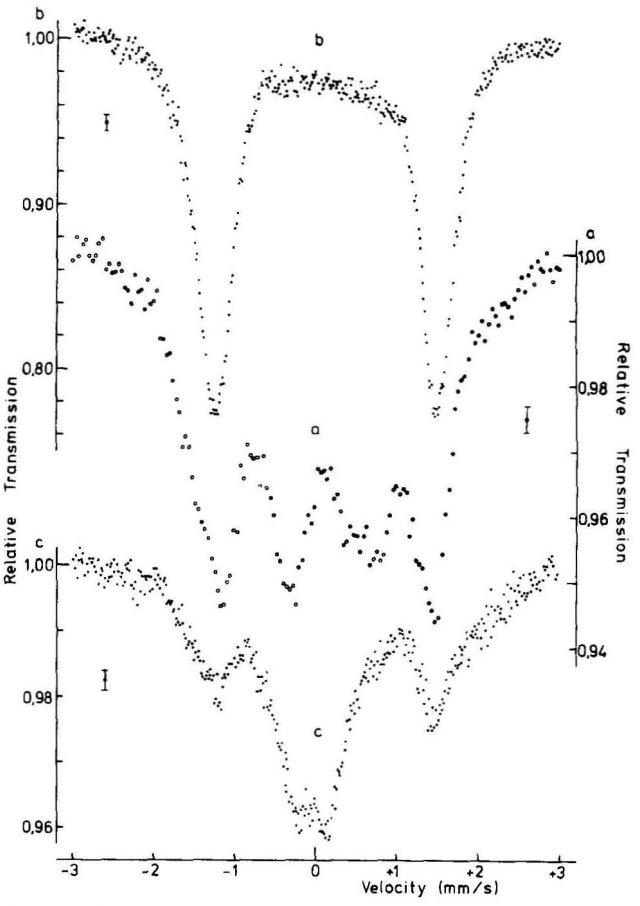

Figure 6. Mössbauer absorption spectra of iron polyphthalocyanine–Norit BRX carbon support; source ^{57}Co/Pt: (a) phthalocyanine–BRX (weight ratio 40:60); (b) phthalocyanine without BRX support; (c) phthalocyanine–BRX (weight ratio 20:80).

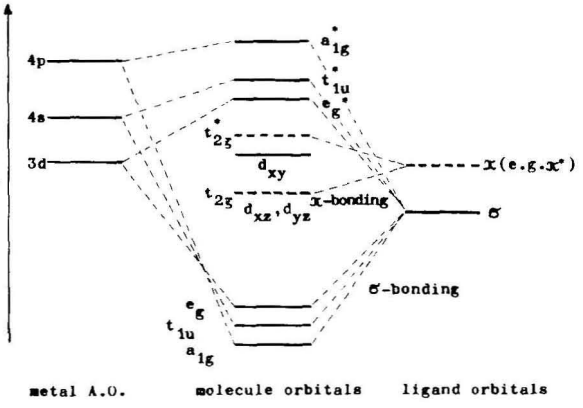

Figure 7. Simple scheme of the t_{2g} (d_{xz}, d_{yz}) splitting by σ–π bonding for hexacoordinated polymeric ferrous phthalocyanine derivatives: configuration $(a_{1g})^2$ $(t_{1u})^6$ $(e_g)^4$ $(t_{2g})^6$.

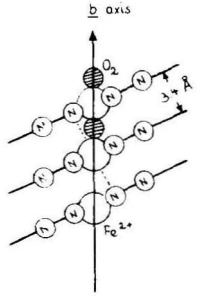

Figure 8. Probable arrangement scheme of ferrous phthalocyanine molecules for illustration of the formation of a distorted octahedron (a) by back-bonding of oxygen molecules or (b) by two axial nitrogens which are asymmetrically situated.

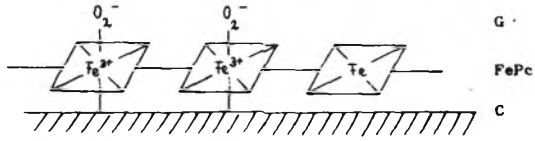

Figure 9. Schematic representation of the arrangement of iron polyphthalocyanine macromolecules at carbon substrates with basic groups: C, carbon support; FePc, polymeric iron phthalocyanine; G, gas/electrolyte phase.

2. Doublet II with $\Delta = 0.58$ mm/s can be attributed to the iron polyphthalocyanine/carbon system because doublet II is formed only in the *presence* of a carbon substrate. As shown in Figure 6c the intensity of the iron polyphthalocyanine doublet I is strongly depressed by the precipitation of the polymer onto the carbon substrate so that the main peaks are given by doublet II.

The formation of doublet II at the costs of doublet I by contacting phthalocyanine with carbon points to a strong interaction between iron polyphthalocyanines and carbon. There seems to be no doubt that alkaline oxygen-containing groups on the carbon surface are responsible for this interaction. Moreover, they are decisive for the electrocatalytic activity of phthalocyanine/dye systems.[12]

The small value of the quadrupole splitting confirms this assumption. Mössbauer studies on phthalocyanine adducts with different axially coordinated ligands, such as pyridine or 3-picoline, have shown that the quadrupole splitting decreases as the basicity of the donor ligands increases.[29,30] This can be explained by a decrease in the degree of π back-bonding from the metal to the donor ligand. Therefore, because of the alkaline character of the surface "carbon ligands", which may be σ bonded to the iron d orbitals (i.e., $3d_{z^2}$) without any π back-bonding, only a small quadrupole splitting is possible as experimentally proven.

The scheme of Figure 9 gives an insight into the structure of the iron polyphthalocyanine–carbon system.

In this context it should be remembered that biologically important metalloporphyrins (e.g., hemoproteins) are bonded to their specific proteins in an analogous manner. The bond between a ligand of the protein and the metal of the porphyrin chelate is perpendicular to the plane of the chelate. Moreover, the sixth coordination position may be occupied in protein–porphyrin systems by another ligand of the same protein or by oxygen etc., and in phthalocyanin–carbon systems by a second polyphthalocyanine, by another carbon layer, or by other ligands such as oxygen, water etc.

3. In contrast to the quadrupole-split doublet I there seems to be only a small change in the intensity of the quadrupole-split doublet II during an electrochemical operation in sulfuric acid. That is, iron polyphthalocyanine macromolecules which are bonded to the carbon substrate may be characterized by a higher stability during their electrocatalytic operation than iron polyphthalocyanine macromolecules which are not directly linked to the carbon support. Further experiments with enriched ^{57}Fe are needed in order to confirm this observation.

IV. Discussion

From the results of tracer experiments and Mössbauer studies some conclusions can be drawn about the electrocatalytic behavior of phthalocyanine catalysts.

(1) As shown in Figures 2–5, a portion of phthalocyanine molecules which are built in carbon–teflon electrodes as catalysts are demetallated in acid solution during their electrochemical operation. Moreover, it is shown that oxygen dissolved in the electrolyte had a considerable influence on this effect.

It is known that metal phthalocyanines and metalloporphrins are relatively stable complexes if the radii of central metal ions fit exactly into the center of the ligands and if the ligands do not contain too sensitive substituents.[41–44] For instance, iron polyphthalocyanine with Fe(II) can be arranged in this group. However, the ferric complex may be considered as a relatively labile complex because of the smaller radius of Fe(III) in comparison to Fe(II). Furthermore, it is known that the azaporphin nucleus is usually destroyed in concentrated sulfuric acid in slow reactions but not before demetallation.[41]

Therefore, for the demetallation of iron(II) polyphthalocyanines ($Fe^{2+}Pc$) in oxygen-containing sulfuric acid, the following processes can be discussed:

$$Fe^{2+}Pc \underset{k_2}{\overset{k_1}{\rightleftharpoons}} Fe^{3+}Pc + e^- \qquad (4a)$$

$$O_2 + e^- = O_2^- \cdot \quad \text{or} \quad O_2 + 4H^+ + 4e^- = 2H_2O \qquad (4b)$$

$$Fe^{3+}Pc \xrightarrow{k_3} Fe^{3+} + Pc \qquad (4c)$$

$$Pc \rightarrow \text{decomposition products} \qquad (4d)$$

That is, the observed passing of iron from phthalocyanine electrodes into solution is the result of a rapid oxidation of ferrous central ions by oxygen (eq 4a, b) followed by a slow demetallation step (eq 4c). According to this mechanism, the decisive steps of demetallation may be considered, for instance, analogous to the dissolution processes of amalgams (e.g., Tl/Hg or Zn/Hg[45,46]) in contact with oxidizing agents dissolved in acid solutions. In the anodic part of the process, $Fe^{2+}Pc$ is oxidized to $Fe^{3+}Pc$, whereas in the cathodic (rate-determining) part of the process oxygen is reduced. The following results are in agreement with this hypothesis.

(a) As a consequence of the electrochemical part of the processes, an equilibrium in which the oxidation rate of the chelated ferrous ions equals that of the reduction of oxygen

$$(d[Fe^{2+}]/dt)_{\mathcal{E}_M} = (d[O_2]/dt)_{\mathcal{E}_M} \qquad (5)$$

should be reached; $[Fe^{2+}]$ is the amount of Fe(II) central ions oxidized and in further steps dissolved; $[O_2]$ is the amount of oxygen reduced at the same time t.

Therefore, neither the equilibrium potential of reaction 4a ($\mathcal{E}_{Fe^{2+}/Fe^{3+}} = 0.77$ V) nor the equilibrium potential of reactions 4b ($\mathcal{E}_{H_2O/O_2} = 1.23$ V) can develop on the interface between iron phthalocyanine and dissolved oxygen. At equilibrium a uniform potential, the mixed potential $\mathcal{E}_M$, may develop. It cannot be excluded that the rest potentials of various types of polymeric iron phthalocyanines, which have been observed on the order of $^0U_H = 900$–1000 mV vs. NHE, are not only given by the formation of hydrogen peroxide (see eq 2) but also by the mixed potential $\mathcal{E}_M$.

(b) From Figures 2–5, in which the amount of dissolved iron is plotted as a function of time, it can be derived that an equilibrium seems to be attained between the dissolved iron and iron left in the electrode. According to the assumption that, first, the redox equilibrium of process 4a is decisive for demetallation and, second, that the amount of iron measured in solution [Fe] is connected with labile ferric phthalocyanine, the rate of demetallation may be formally described by the differential equation for reversible chemical reactions

$$d[Fe]/dt = k_1([FePc]_{t=0} - [Fe]) - k_2[Fe] \qquad (6)$$

where k_1 and k_2 are the rate constants of eq 4a. In accordance with this assumption, linear ranges between log $(1 - ([Fe]/[Fe_\infty]))$ and time could be taken from dissolution

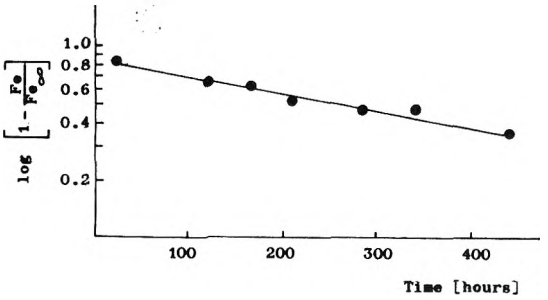

Figure 10. Plot of log (1 – (Fe/Fe$_\infty$)) vs. time during electrochemical reduction of oxygen: current density, 40 mA/cm^2; electrolyte, 6 N H_2SO_4/O_2; iron polyphthalocyanine 21.

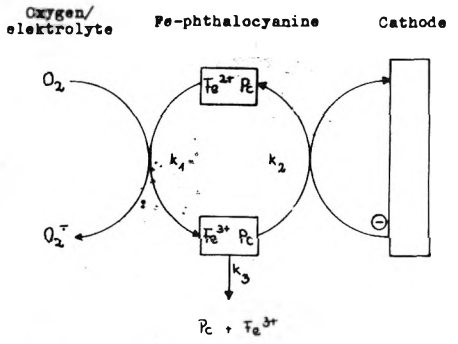

Figure 11. Redox mechanism of stabilization and electrocatalysis with iron polyphthalocyanine/carbon catalysts: $k_2 >> k_3$, stabilization of the iron polyphthalocyanine catalyst by a rapid electron exchange [class I molecules]; $k_3 > k_2$, passing of Fe^{3+} into solution as a consequence of a slow electron exchange [class II molecules].

curves in agreement with the solution of eq 6, i.e.

$$\ln\left(1 - \frac{[Fe]}{[Fe_\infty]}\right) = (k_1 + k_2)t \qquad (7)$$

where [Fe$_\infty$] is the amount of iron measured in the equilibrium state (see Figure 10).

2. The electrochemical activity is not changed significantly during the demetallation of some of the phthalocyanine molecules. Therefore, two kinds of iron polyphthalocyanine molecules seem to be distinguishable in carbon–teflon cathodes: molecules of class I with low stability and low influence on the electrochemical operation of the electrode, and molecules of class II with high stability and high electrocatalytic activity for cathodic reduction of oxygen. By identifying molecules of class I with the Mössbauer doublet group I and molecules of class II with the doublet group II, the different behavior of phthalocyanine molecules of carbon–teflon electrodes can be understood.

On one hand, the different values of the quadrupole splitting show that molecules of class I are situated in the outer parts of phthalocyanine layers, whereas molecules of class II are in intimate contact with the carbon substrate. On the other hand, there is an intimate contact between iron polyphthalocyanine molecules of class II and the carbon support. So electrons may be transferred to molecules of class II more rapidly than to those of class I far from the substrate.

Since a demetallation and deactivation, respectively, of iron polyphthalocyanines occurs after the oxidation of central iron atoms, the different behavior of phthalocyanine molecules can be understood (see the scheme in Figure 11). Central ferric ions of phthalocyanine molecules far from the carbon support (class I) may pass into solution more rapidly than they accept electrons from the support. However when, conversely, central ferric ions of

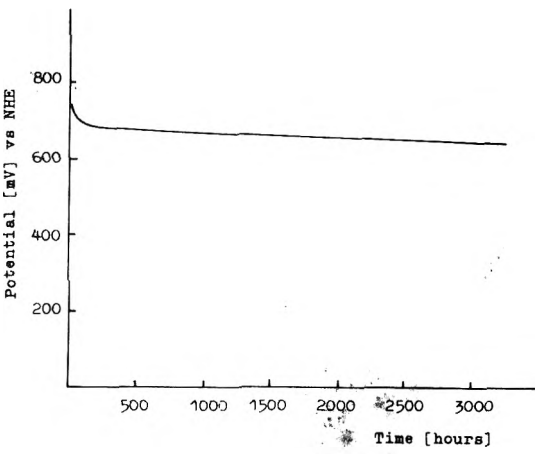

Figure 12. Galvanostatic potential/time curve: 6 N H_2SO_4; current density 20 mA/cm^2; iron polyphthalocyanine catalyst (synthesis no. 195).

phthalocyanine macromolecules are in intimate interaction with the carbon substrate (class II), an acceptance of electrons from the support is possible before demetallation. This effect can be intensified by using polymeric phthalocyanines with high conductivity.[20,47] A high stability, as a further consequence of the strong interaction, is connected with a rapid electron exchange in the system carbon–phthalocyanine–oxygen, which is necessary in the redox mechanism of electrocatalysis.[19] Besides, the activity for electrochemical reduction of oxygen in sulfuric acid can be very high even after operation for many hundred hours.

It should be stressed that, as a *consequence* of these results, carbon–teflon cathodes with polymeric iron phthalocyanines could be constructed which could be loaded, e.g., at a potential of 840 mV (690 mV) to 20 mA/cm^2 (100 mA/cm^2) at 25 °C in 6 N H_2SO_4 with an utilization of the catalyst in the order of about 7–14 A/g.[48] Under galvanostatic conditions at 20 mA/cm^2 over continuous operation the potential falls only by about 4% between 100 and 3000 h as shown in Figure 12. However, further experiments are necessary for extending the electrocatalytic action up to current densities on the order of 60 to 100 mA/cm^2.

Acknowledgment. The authors wish to express their thanks to the Bundesministerium der Verteidigung for support of this work and the Fonds der Chemischen Industrie for a financial grant. They also wish to thank the Fraunhofer Gesellschaft für Angewandte Forschung, München, for administrative services.

References and Notes

(1) J. J. Randall, Jr., and W. J. Bernard, *Electrochim. Acta*, **20**, 653 (1975).
(2) G. Reinhard and J. Pirrwitz, *Isotopenpraxis*, **11**, 134 (1975).
(3) B. Stverak, M. Srb, and L. Vrobel, *Radioisotopy*, **15**, 465 (1974).
(4) Yu. M. Kolotyrkin, *Electrochim. Acta*, **18**, 593 (1973).
(5) A. Wieckowski, *J. Electrochem. Soc.*, **122**, 252 (1975).
(6) Z. P. Zagorski and P. P. Panta, *Electrochim. Acta*, **16**, 1261 (1971).
(7) H. P. Raaen, *Anal. Chem.*, **46**, 1265 (1974).
(8) P. L. Airey, *Radiat. Res Rev.*, **5**, 341 (1973).
(9) J. Euler, *Chem. Ing. Techn.*, **38**, 631 (1966).
(10) T. Z. Palágyi, *J. Electrochem. Soc.*, **106**, 846 (1959).
(11) R. Jasinski, *Nature (London)*, **201**, 1212 (1964); *J. Electrochem. Soc.*, **112**, 526 (1965).
(12) H. Jahnke and M. Schönborn, "Comptes Rendus, Troisièmes Journées Internationales d'Etude des Piles à Combustible", Presses Académiques Européennes, Bruxelles, 1969, p 60.
(13) H. Jahnke, M. Schönborn, and G. Zimmermann, *Bosch Tech. Ber.*, **4**, 98 (1973).
(14) H. Alt, H. Binder, and G. Sandstede, *J. Catal.*, **28**, 8 (1973).
(15) R. Larsson and J. Mrha, *Electrochim. Acta*, **18**, 391 (1973).
(16) F. Beck, W. Dammert, J. Heiss, H. Hiller, and R. Polster, *Z. Naturforsch. A.*, **28**, 1009 (1973).
(17) H. Jahnke, M. Schönborn, and G. Zimmermann, *Top. Current Chem.*, **61**, 133 (1976).
(18) M. Savy, P. Andro, and C. Bernard, *Electrochim. Acta*, **19**, 403 (1974).
(19) F. Beck, *Ber. Bunsenges. Phys. Chem.*, **77**, 353 (1973).

(20) H. Meier, W. Albrecht, U. Tschirwitz, and E. Zimmerhackl, *Ber. Bunsenges. Phys. Chem.*, **77**, 843 (1973).
(21) H. Meier, E. Zimmerhackl, W. Albrecht, and U. Tschirwitz in "Katalyse an Phthalocyaninen", H. Kropf and F. Steinbach, Ed., G. Thieme Verlag, Stuttgart, 1973.
(22) H. Meier, U. Tschirwitz, E. Zimmerhackl, and W. Albrecht, BMVg-FBWT 75-6, 1975.
(23) L. Y. Johansson, J. Mrha, and R. Larsson, *Electrochim. Acta*, **18**, 255 (1973).
(24) G. Luft, K. Mund, G. Richter, R. Schulte, and F. v. Sturm, *Siemens Forsch. Entwicklungsber.*, **3**, 177 (1974).
(25) G. Booth in "Chemistry of Synthetic Dyes", Vol. 5, K. Venkataraman, Ed., Academic Press, New York, N.Y., 1971, p 271.
(26) D. Wöhrle, *Adv. Polym. Sci.*, **10**, 35 (1972).
(27) A. A. Berlin and A. I. Sherle, *Inorg. Macromol. Rev.*, **1**, 235 (1971).
(28) H. Binder, A. Köhling, and G. Sandstede, *Chem. Ing. Techn.*, **40**, 543 (1968).
(29) A. Hudson and H. J. Whitfield, *Inorg. Chem.*, **6**, 1120 (1967).
(30) D. C. Grenoble and H. G. Drickamer, *J. Chem. Phys.*, **55**, 1626 (1971).
(31) E. Fluck in ref 21, p 37.
(32) J. Blomquist and L. C. Moberg, *Phys. Scr.*, **9**, 350 (1974).
(33) J. R. Sams and T. B. Tsin, *Chem. Phys. Lett.*, **25**, 599 (1974).
(34) T. S. Srivastava, J. L. Przyblinski, and A. Nath, *Inorg. Chem.*, **13**, 1562 (1974).
(35) R. Larsson, J. Mrha, and J. Blomquist, *Acta Chem. Scand.*, **26**, 3386 (1972).
(36) J. W. Klein and H. Faatz, G-I-T Z. Lab. H. 6/7, 645, 741 (1969).
(37) T. I. Zalkind, V. A. Shepelin, and V. I. Veselovskii, *Sov. Elektrochem.*, **2**, 1066 (1966).
(38) K. Schwabe, R. Köpsel, K. Wiesener, and E. Winkler, *Electrochim. Acta*, **9**, 413 (1964); **12**, 873 (1969).
(39) K. Schwabe, *Z. Phys. Chem.*, **226**, 391 (1964).
(40) J. F. Henry and E. Gevenois, cited in ref 9.
(41) A. B. P. Lever in "Advances in Inorganic Chemistry and Radiochemistry", Vol. 7, H. J. Emeléus and A. G. Sharpe, Ed., Academic Press, New York, N.Y., 1965, p 89.
(42) G. Lang and W. Marshall, *Proc. Phys. Soc. (London)*, **87**, 3 (1966).
(43) J. E. Falk and J. N. Phillips in "Chelating Agents and Chelate Compounds", Mellor and Dwyer, Ed., Academic Press, New York, N.Y., 1964.
(44) U. Eisner and M. J. C. Harding, *J. Chem. Soc.*, 4089 (1964).
(45) I. Madi, *Ber. Bunsenges. Phys. Chem.*, **68**, 601 (1964); *Inorg. Nucl. Chem. Lett.*, **9**, 767 (1973).
(46) I. Madi and A. Bolyós, *Radiochem. Radioanal. Lett.*, **20**, 215 (1975).
(47) H. Meier, "Organic semiconductor: Dark- and photoconductivity in organic solids", Verlag Chemie, Weinheim, Bergstrasse, 1974, p 455.
(48) H. Meier, U. Tschirwitz, E. Zimmerhackl, and W. Albrecht, *Ger. Offenlegungsschrift*, submitted for publication.

Two-Constant Model to Describe Amine and Alcohol Association from Vapor Pressure Measurements

Heiner Landeck, Hans Wolff,* and Rainer Götz

Physikalisch-chemisches Institut, Universität Heidelberg, 69 Heidelberg, Federal Republic of Germany *(Received July 1, 1976; Revised Manuscript Received January 18, 1977)*

Publication costs assisted by Fonds der Chemie, Frankfurt

Equations are developed to describe the association of the most simple aliphatic amines and alcohols in saturated hydrocarbons from vapor pressure measurements by means of a two-constant model. The equations permit the calculation of the dimerization constant K_2 and of the constant K_3 for formation of higher polymers direct from the constants of the equations for the representation of the activity coefficients. The expression for K_2 agrees with that for the dimerization constant of the model allowing for differences between the constants for the higher equilibria, while the expression for K_3 differs from the trimerization constant of this model. The numerical values of constants K_2 and K_3 and of the corresponding association energies prove the alcohols to be more strongly associated than the amines. The dimerization energy and the energy for the formation of higher polymers are nearly the same, 2–3 kcal/mol for the amines and 5 kcal/mol for the alcohols. This result and the observation of only one NH stretching vibration for the hydrogen-bonded species suggest the presence of only one kind of hydrogen bonds, probably of linear bonds, in the amines. The observation of two OH stretching vibrations, on the other hand, suggests the presence of two kinds of hydrogen bonds in the alcohols. The determination of the same energy value for dimer and polymer formation does not exclude the description of these bonds as the bonds of cyclic dimers and linear higher polymers, as suggested by previous authors. However, due to the complications of the alcohol association as well as to the inherent simplifications of the model the calculated energies may not be related to the bonds in a simple manner. From K_2 and K_3 the activity coefficients and the excess free energy can be recalculated. The comparison of the obtained values with the conventionally calculated values proves that the amines and the short chain alcohols fit the two-constant model within a wide range of concentrations, while this is not the case with long chain alcohols.

A. Introduction

The association of simple aliphatic amines and alcohols in *n*-hexane and other saturated hydrocarbons has been described in vapor pressure investigations[1,2] by the chemical theory of solution nonideality, i.e., by the theory of ideal associated solutions.[3-5] The assumption that the successive equilibria $A_{i-1} + A_1 \rightleftarrows A_i$ ($i = 2$, 3, etc.) exist in the solutions and that all constants of these equilibria are different,[1,2] is the most general form of this approach. However, considering the solutions in a wider range of concentrations, it is difficult to determine the constants of the equilibria with $i > 3$ with sufficient accuracy. Therefore, it is of interest to examine whether a description may be possible where only the dimerization constant is assumed to be different, the other constants being equal. Such a model has already been used by Van Ness et al.[4] to describe the association of ethanol in *n*-heptane. They determined K_2 and K_3 by varying the initial values until accordance was reached with experimental values of the excess free energy and the heat of mixing.

B. Determination of the Association Constants

1. *Dimerization Constant.* In the following derivation the calculation of the association constants starts from the

assumption that the analytical mole fraction x_A of the amine or alcohol, the activity coefficient γ_B of the hydrocarbon, and the true mole fractions x_1 of the amine or alcohol monomers, x_2 of the dimers, etc., are related by

$$x_1 + 2x_2 + 3x_3 + 4x_4 + \ldots = x_A\gamma_B \quad (1)$$

(cf. eq 8 in ref 2a; cf. also ref 1a and 3). If x_2, x_3, etc., are replaced by means of the relations for the equilibrium constants, i.e., by $K_{1,2} = x_2/x_1^2$, $K_{2,3} = x_3/x_2x_1$, etc., eq 1 can be formulated as

$$x_1 + 2K_{1,2}x_1^2 + 3K_{1,2}K_{2,3}x_1^3 + 4K_{1,2}K_{2,3}K_{3,4}x_1^4 + \ldots = x_A\gamma_B \quad (2)$$

Assuming the two-constant model, where K_2 is the dimerization constant and K_3 the constant for the formation of higher polymers, the following equation results

$$x_1 + 2K_2x_1^2 + 3K_2K_3x_1^3 + 4K_2K_3^2x_1^4 + \ldots = x_A\gamma_B \quad (3)$$

Using the model which allows differences between the higher constants, the dimerization constant $K_{1,2}$ is obtained, if for a sufficiently high dilution the terms containing x_1^3, x_1^4, . . ., are neglected. The trimerization constant follows by omission of the terms containing x_1^4, x_1^5, . . ., etc.[1a] This procedure may also be applied for the determination of K_2 from eq 3. The terms in which eq 2 and 3 differ are omitted. Therefore, after considering[1a]

$$x_1 = x_A\gamma_B\beta_1 \quad (4)$$

(β_1 denotes the fraction of the associating component present as monomers), K_2 results in accordance with the expression for $K_{1,2}$[1a,2a]

$$K_2 = \frac{1 - \beta_1}{2x_A\gamma_B\beta_1^2} \quad (5)$$

Furthermore, the same expressions result if γ_A and γ_B are replaced by the equations used for their representation, simultaneously applying the relation[1a,2a,3]

$$\beta_1 = \frac{\gamma_A}{\gamma_B \lim_{x_A \to 0} \gamma_A} \quad (6)$$

Replacement of γ_A and γ_B by the Redlich–Kister equations[6]

$$\gamma_A = \exp\{Ax_B^2 - Bx_B^2(1 - 4x_A) + Cx_B^2(1 - 8x_A + 12x_A^2)\} \quad (7a)$$

$$\gamma_B = \exp\{Ax_A^2 + Bx_A^2(1 - 4x_B) + Cx_A^2(1 - 8x_B + 12x_B^2)\} \quad (7b)$$

(A, B, and C = constants) yields[1a]

$$K_2 = A - 3B + 5C \quad (8)$$

while replacement of γ_A and γ_B by Wilson's equations[5,7]

$$\gamma_A = \frac{1}{x_A + \Lambda_{AB}x_B} \exp\left\{x_B\left(\frac{\Lambda_{AB}}{x_A + \Lambda_{AB}x_B} - \frac{\Lambda_{BA}}{\Lambda_{BA}x_A + x_B}\right)\right\} \quad (9a)$$

$$\gamma_B = \frac{1}{x_B + \Lambda_{BA}x_A} \exp\left\{-x_A\left(\frac{\Lambda_{AB}}{x_A + \Lambda_{AB}x_B} - \frac{\Lambda_{BA}}{\Lambda_{BA}x_A + x_B}\right)\right\} \quad (9b)$$

(Λ_{AB} and Λ_{BA} = constants) results in[2a]

$$K_2 = \frac{2 - \Lambda_{AB} - \Lambda_{AB}\Lambda_{BA}^2}{2\Lambda_{AB}} \quad (10)$$

2. *Constant for the Formation of Higher Polymers.* The association constant K_3 cannot be determined in the same way as constant $K_{2,3}$. It is derived from the concept that in addition to eq 1 and 2 the relation

$$x_1 + x_2 + x_3 + x_4 + \ldots = \Sigma x_i \quad (11)$$

is valid. After replacement of x_2, x_3, etc., by the equilibrium constants and by equating all higher constants, the following relation results:

$$x_1 + K_2x_1^2 + K_2K_3x_1^3 + K_2K_3^2x_1^4 + \ldots = \Sigma x_i \quad (12)$$

Considering $K_3x_1 < 1$, summation of the terms $K_2x_1^2$, $K_2K_3x_1^3$, etc., yields

$$x_1 + \frac{K_2x_1^2}{1 - K_3x_1} = \Sigma x_i \quad (13)$$

$\Sigma x_i = 1$ for the undiluted amine or alcohol. Denoting the true mole fractions of the monomers in the undiluted state as $x_{1,0}$ and regarding the association constants as independent from the concentration, the expression

$$x_{1,0} + \frac{K_2x_{1,0}^2}{1 - K_3x_{1,0}} = 1 \quad (14)$$

follows. Solving for K_3 yields

$$K_3 = \frac{1}{x_{1,0}} - \frac{K_2}{1/x_{1,0} - 1} \quad (15)$$

To calculate K_3 from this expression, $x_{1,0}$ has to be determined. The solution can be considered as a nonideal binary system of the macroscopic components as well as an ideal multicomponent system of the solvent and of the various forms of the associating component.[3] Viewing the mixture as a nonideal binary system, the chemical potentials of the components can be expressed by

$$\mu_A = \mu_A^\circ + RT \ln (\gamma_A x_A) \quad (16a)$$

$$\mu_B = \mu_B^\circ + RT \ln (\gamma_B x_B) \quad (16b)$$

where

$$x_A = \frac{n_A}{n_A + n_B} \quad (17a)$$

and

$$x_B = \frac{n_B}{n_A + n_B} \quad (17b)$$

indicate the moles of the amine or alcohol and of the solvent. Regarding the mixture as an ideal multicomponent system, the expressions are

$$\mu_i = \mu_i^\circ + RT \ln x_i \qquad (i = 1, 2, \ldots) \quad (18a)$$

$$\mu_{B(1)} = \mu_{B(1)}^\circ + RT \ln x_{B(1)} \quad (18b)$$

where

$$x_i = \frac{n_i}{\Sigma n_i + n_{B(1)}} \quad (19a)$$

and

$$x_{B(1)} = \frac{n_B}{\Sigma n_i + n_{B(1)}} \quad (19b)$$

denote the true mole fractions of the various forms of the associating component and of the solvent, respectively.[1a,3]

From the eq 16a and 16b the free energy of 1 mol of the mixture and the free energy of the components before mixing can be expressed as

$$G_1 = x_A(\mu_A^\circ + RT \ln [\gamma_A x_A]) + x_B(\mu_B^\circ + RT \ln [\gamma_B x_B]) \quad (20)$$

and

$$G_2 = x_A\mu_A^\circ + x_B\mu_B^\circ \quad (21)$$

Hence, the free energy of mixing, given by the difference of G_1 and G_2, is

$$G^M = RT(x_A \ln [\gamma_A x_A] + x_B \ln [\gamma_B x_B]) \quad (22)$$

Considering the equilibrium condition $\mu_i = i\mu_1$, in addition the following equations can be derived from (18a) and (18b):

$$G_1 = x_A(\mu_1^\circ + RT \ln x_1) + x_B(\mu_{B(1)}^\circ + RT \ln x_{B(1)}) \quad (23)$$

and

$$G_2 = x_A(\mu_1^\circ + RT \ln x_{1,0}) + x_B\mu_{B(1)}^\circ \quad (24)$$

and, therefore, the difference

$$G^M = RT(x_A \ln x_1/x_{1,0} + x_B \ln x_{B(1)}) \quad (25)$$

The comparison of (22) and (25) yields

$$\gamma_A = x_1/x_{1,0}x_A \quad (26)$$

At the limiting value of the dilution $x_A = x_1$

$$x_{1,0} = 1/\lim_{x_A \to 0} \gamma_A \quad (27)$$

results.

Inserting relation 27 in eq 15 yields

$$K_3 = \lim_{x_A \to 0} \gamma_A - \frac{K_2}{\lim_{x_A \to 0} \gamma_A - 1} \quad (28)$$

If the calculation of $\lim_{x_A \to 0}\gamma_A$ is based on the three-constant Redlich–Kister equations, we obtain

$$K_3 = \exp(A - B + C) - \frac{K_2}{\exp(A - B + C) - 1} \quad (29)$$

while by using Wilson's equations, there results

$$K_3 = \frac{\exp(1 - \Lambda_{BA})}{\Lambda_{AB}} - \frac{K_2}{\exp[(1 - \Lambda_{BA})/\Lambda_{AB}] - 1} \quad (30)$$

Therefore, constant K_3 can be calculated the same way as constant K_2, direct from the constants of the equations for the activity coefficients.

C. Activity Coefficients and Excess Free Energy Calculated from K_2 and K_3

To test the model, it is of interest to calculate the values of the activity coefficients and the excess free energy from K_2 and K_3.

Considering $\sum x_i = x_1 (d\sum x_i/dx_1)$, where $\sum x_i$ is given by (12) and (13), eq 3 yields

$$x_1 + K_2x_1^2\frac{2 - K_3x_1}{(1 - K_3x_1)^2} = x_A\gamma_B \quad (31)$$

γ_B follows by comparison of (16b) and (18b) as

$$\gamma_B = x_{B(1)}/x_B \quad (32)$$

and, after considering the definitions (17b) and (19b), as

$$\gamma_B = (1 - \Sigma x_i)/(1 - x_A) \quad (33)$$

Inserting this expression in (31) and considering additionally eq 14, there results[8]

$$x_1^3(K_3^2 - K_2K_3) - x_1^2(2[K_3 - K_2] + x_A[K_3^2 + K_2]) + x_1(1 + 2K_3x_A) - x_A = 0 \quad (34)$$

This equation permits us to calculate x_1 for each x_A under the restrictions

$$K_3x_1 < 1,\ x_1 \leq x_A, \text{ and } x_1 \in R \quad (35)$$

Using the values of x_1 thus obtained and the values of $x_{1,0}$ from eq 27, the activity coefficients γ_A can be calculated from eq 26 for the two-constant model. The corresponding values of γ_B result from eq 31. If these values of γ_A and γ_B are inserted in

$$G^E = RT(x_A \ln \gamma_A + x_B \ln \gamma_B) \quad (36)$$

the excess free energy values of the two-constant model are obtained.

D. Results and Discussion

The association constants K_2 and K_3 calculated for the amine and alcohol solutions by eq 8 and 29 or eq 10 and 30, as well as the association energies ΔU_2 and ΔU_3 derived from these constants after van't Hoff, are compiled in Table I. Being identical with the dimerization constant and energy of the multiconstant model, K_2 and ΔU_2 have already been discussed.[1,2] In accordance, K_3 and ΔU_3 demonstrate that alcohols are far more associated than amines and that their association energy, being about 5 kcal/mol, is approximately twice that of the amines.[1,2] An increase of the ratio $K_3/K_{2,3}$ with the transition from the weakly associated dimethylamines to the strongly associated alcohols corresponds to the assumption of K_3 as weighted mean of various differing constants. The stronger the association, the higher is K_3.

If the calculations for the amines are based on Wilson type representations, differences are missing which are observed in the values of ΔU_2 and ΔU_3 when Redlich–Kister equations are used. Therefore the differences may be attributed to the inadequacies of the representations. The approximate accordance of the values obtained by using Wilson's equations for the calculations conforms with the observation of only one IR band for the NH stretching vibration of associated amines,[19] i.e., with the presence of only one kind of hydrogen bonds. If, in addition to dimers, higher polymers are formed and if the energy of a bond of cyclic dimers is assumed to be significantly smaller than that of higher polymers, these bonds may be accepted as linear.

With alcohol systems, ΔU_2 and ΔU_3 likewise approximately coincide. This holds true, although the IR spectra of associated alcohols show two OH stretching vibrations which are shifted against the monomeric vibration by about 150 and 300 cm^{-1}.[20] Van Ness et al.[20] determined the dimerization energy and the energy for the formation of higher polymers to be 8.6 and 5.6 kcal/mol, respectively. Considering the shift of the stretching vibrations in the ratio of 1:2 and the proportionality between the magnitude of the shifts and the strength of the hydrogen bonds,[21] they inferred the presence of two, somewhat weaker hydrogen bonds in the dimers, compared to the higher polymers. This conclusion is equivalent to the assumption of a cyclic structure for the dimers and of a linear structure for the

TABLE I: Association Constants and Energies of Aliphatic Amines and Alcohols in Solution with Saturated Hydrocarbons, Assuming the Two-Constant Model (K_2, K_3, ΔU_2, and ΔU_3) and the Multiconstant Model ($K_{1,2}$, $K_{2,3}$, $\Delta U_{1,2}$, and $\Delta U_{2,3}$)[a]

System	T, °C	Association constants			Association energies, kcal/mol		
		K_2 ($K_{1,2}$)	K_3	$K_{2,3}$	$-\Delta U_2$ ($-\Delta U_{1,2}$)	$-\Delta U_3$	$-\Delta U_{2,3}$
CH_3NH_2-*n*-butane (1b)	+15	1.62 (1.93)	3.81 (4.01)	2.90 (3.33)	2.77 (1.96)	2.76 (2.67)	2.44 (2.10)
	−20	3.17 (3.07)	7.45 (7.62)	5.24 (5.48)			
CH_3NH_2-*n*-hexane (1b, 2a)	+20	1.24 (1.52)	3.39 (3.50)	2.37 (2.56)	2.92 (2.09)	2.76 (2.66)	2.46 (2.27)
	−20	2.74 (2.67)	7.18 (7.18)	4.62 (4.72)			
CH_3ND_2-*n*-hexane (9a, 2a)	+20	1.38 (1.60)	3.68 (3.78)	2.57 (2.75)	2.89 (2.13)	2.82 (2.70)	2.48 (2.25)
	−20	3.03 (2.86)	7.92 (7.87)	5.04 (5.07)			
CD_3NH_2-*n*-hexane (9b, 2a)	+20	1.28 (1.65)	3.44 (3.63)	2.42 (2.77)	2.81 (1.83)	2.72 (2.57)	2.38 (2.03)
	−20	2.74 (2.72)	7.21 (7.30)	4.61 (4.81)			
CD_3ND_2-*n*-hexane (9b, 2a)	+20	1.38 (1.58)	3.69 (3.77)	2.57 (2.72)	2.89 (2.18)	2.84 (2.74)	2.48 (2.29)
	−20	3.02 (2.85)	7.97 (7.92)	5.03 (5.06)			
$C_2H_5NH_2$-*n*-hexane (1b, 2a)	+20	1.04 (1.17)	2.33 (2.35)	1.99 (2.06)	2.54 (2.01)	2.31 (2.29)	2.14 (2.08)
	−20	2.08 (2.02)	4.37 (4.37)	3.55 (3.62)			
n-$C_3H_7NH_2$-*n*-hexane (1b)	+20	1.03 (1.02)	2.03 (2.03)	1.90 (1.91)	2.27 (2.32)	1.96 (2.01)	1.93 (2.09)
	−20	1.91 (1.92)	3.47 (3.51)	3.23 (3.38)			
$(CH_3)_2NH$-*n*-hexane (1c, 2a)	+20	0.74 (0.88)	1.51 (1.49)	1.46 (1.48)	2.24 (2.05)	2.25 (2.41)	1.90 (2.16)
	−20	1.35 (1.53)	2.78 (2.86)	2.43 (2.66)			
$(CH_3)_2ND$-*n*-hexane (1c, 2a)	+20	0.72 (0.96)	1.58 (1.56)	1.46 (1.53)	2.63 (1.94)	2.34 (2.50)	2.13 (2.27)
	−20	1.46 (1.63)	2.98 (3.06)	2.60 (2.84)			
$(CD_3)_2NH$-*n*-hexane (1c, 2a)	+20	0.66 (0.85)	1.49 (1.46)	1.37 (1.38)	2.56 (2.04)	2.28 (2.45)	2.04 (2.31)
	−20	1.31 (1.48)	2.76 (2.83)	2.38 (2.58)			
$(CD_3)_2ND$-*n*-hexane (1c, 2a)	+20	0.74 (1.00)	1.58 (1.56)	1.48 (1.59)	2.46 (1.84)	2.32 (2.51)	2.03 (2.16)
	−20	1.44 (1.65)	2.96 (3.07)	2.56 (2.86)			
CH_3OH-*n*-hexane (2a)	+60	15.0	37.5	23.0	4.93	5.02	4.85
	+40	24.2	60.8	36.9			
CH_3OD-*n*-hexane (2a)	+60	15.9	39.5	24.4	5.13	5.23	5.05
	+40	26.2	65.4	39.7			
CD_3OH-*n*-hexane (2a)	+60	15.2	38.1	23.3	5.25	5.31	5.16
	+40	25.2	63.6	38.3			
CD_3OD-*n*-hexane (2a)	+60	16.0	39.9	24.5	5.15	5.20	5.03
	+40	26.3	65.9	39.9			
C_2H_5OH-*n*-hexane (2b)	+60	10.4	22.1	16.0	4.36	4.45	4.26
	+40	15.8	34.0	24.2			
C_2H_5OD-*n*-hexane (2b)	+60	11.0	23.3	17.0	4.49	4.61	4.39
	+40	17.0	36.4	25.9			
C_2D_5OH-*n*-hexane (2b)	+60	11.0	23.6	17.0	4.53	4.64	4.44
	+40	17.1	36.9	26.1			
C_2D_5OD-*n*-hexane (2b)	+60	11.3	24.0	17.3	4.79	4.88	4.69
	+40	17.9	38.4	27.3			
C_2H_5OH-*n*-heptane (10, 12)	+60	7.9	17.9	12.3	4.65	4.78	4.52
	+40	12.4	28.4	19.1			
1-Propanol-*n*-heptane (10)	+60	7.5	14.6	11.7	5.07	5.05	4.92
	+40	12.2	23.8	18.8			
1-Hexanol-cyclohexane (14, 15)	+81.2	6.6	7.2	10.0	4.66	4.72	4.64
	+50	11.7	12.9	17.6			

[a] The values are calculated by means of Wilson's constants. Values calculated for the amines by means of Redlich-Kister constants are given in parentheses. The Wilson or Redlich-Kister constants used for the calculations were taken from the references indicated or were calculated by the method of Barker[2a,11] from the values for the pressures, molar volumes, and virial coefficients given in these papers. $K_{2,3}$ and $\Delta U_{2,3}$ were likewise taken from these papers or were determined as described therein.

higher polymers. (Cyclic polymers of sufficient size are equivalent to the linear higher polymers.) As is concluded from our results in agreement with other investigations,[20,22] the value of 8.6 kcal/mol for the dimerization energy is presumably too high. The determination of a dimerization energy of about 5 kcal/mol which is in accordance with the value found for the association energy of the higher polymers does not exclude the assumption of cyclic dimers and linear higher polymers. However, due to the complications of the alcohol association[23–25] as well as due to the inherent simplifications of the model a simple correlation between the calculated energy values and the stretching bonds seems rather questionable.[26]

The activity coefficients and the excess free energy calculated from K_2 and K_3 using Wilson's constants and calculated direct from Wilson's equations are reproduced in Figures 1–3. With the amine series the largest deviations of both curves are not greater than 5–10% in the entire range of mole fractions (Figure 1). The same holds true for the solutions of methanol, except when the mole fractions are greater than 0.95; in this range a rapid in-

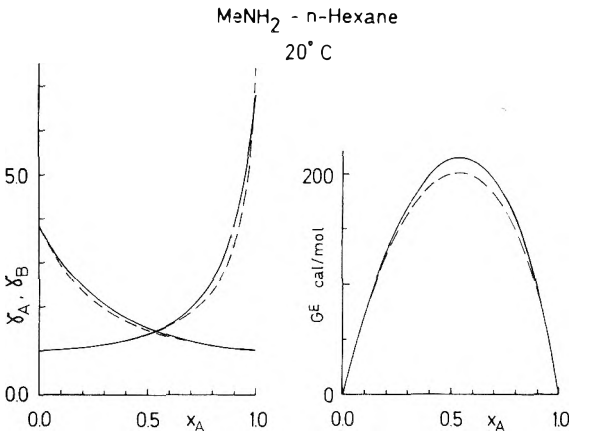

Figure 1. (a) Activity coefficients and (b) excess free energy of the mixtures of methylamine with *n*-hexane at 20 °C, calculated from the equations of the two-constant model using Wilson's constants (- - -) and directly calculated from Wilson's equations (——). γ_A and γ_B are the activity coefficients of methylamine and *n*-hexane, respectively. G^E is the excess free energy, and x_A is the mole fraction of the amine.

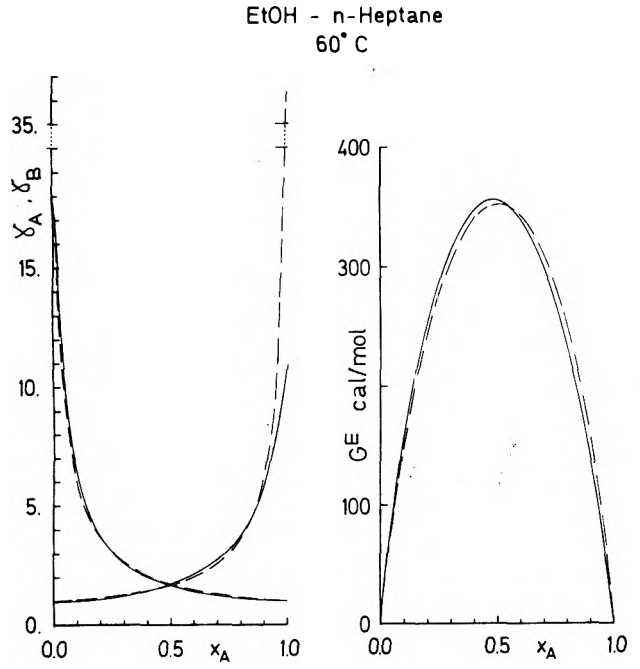

Figure 2. (a) Activity coefficients and (b) excess free energy of the mixtures of ethanol with *n*-heptane at 60 °C, calculated from the equations of the two-constant model using Wilson's constants (- - -) and directly calculated from Wilson's equations (——). γ_A and γ_B are the activity coefficients of ethanol and *n*-heptane, respectively. G^E is the excess free energy, and x_A is the mole fraction of the alcohol.

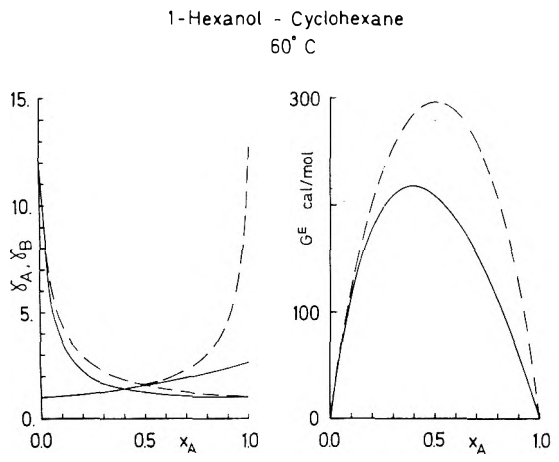

Figure 3. (a) Activity coefficients and (b) excess free energy of the mixtures of hexanol with cyclohexane at 60 °C, calculated from the equations of the two-constant model using Wilson's constants (- - -) and directly calculated from Wilson's equations (——). γ_A and γ_B are the activity coefficients of hexanol and cyclohexane, respectively. G^E is the excess free energy, and x_A is the mole fraction of the alcohol.

crease of the differences occurs. For the solutions of ethanol this range begins at a lower mole fraction (Figure 2). For the solutions of hexanol in cyclohexane, however, the differences of the values are considerably greater than 10% nearly in the entire range of mole fractions (Figure 3). Therefore, the solutions of the alcohols with longer chains cannot be described by the equations of the two-constant model. However, the behavior of the amine solutions is given by these equations with a comparatively small error in the entire mole fraction range. The same holds true for the methanol and ethanol solutions, aside from the range of the highest concentrations.

Acknowledgment. We gratefully acknowledge support of this work by the Deutsche Forschungsgemeinschaft, Bad Godesberg, by the Fonds der Chemie, Frankfurt, and by the BASF, Ludwigshafen.

References and Notes

(1) (a) H. Wolff and A. Höpfner, *Ber. Bunsenges. Phys. Chem.*, **66**, 149 (1962); (b) H. Wolff, A. Höpfner, and H.-M. Höpfner, *ibid.*, **68**, 410 (1964); (c) H. Wolff and R. Würtz, *Z. Phys. Chem.* (*Frankfurt am Main*), **67**, 115 (1969); (d) *J. Phys. Chem.*, **74**, 1600 (1970).
(2) (a) H. Wolff, O. Bauer, R. Götz, H. Landeck, O. Schiller, and L. Schimpf, *J. Phys. Chem.*, **80**, 131 (1976); (b) H. Wolff and R. Götz, *Z. Phys. Chem.* (*Frankfurt am Main*), **100**, 25 (1976).
(3) (a) I. Prigogine, V. Mathot, and A. Desmyter, *Bull. Soc. Chim. Belg.*, **58**, 547 (1949); (b) I. Prigogine and R. Defay, "Chemical Thermodynamics", Longmans Green and Co., London, 1954, p 410.
(4) (a) H. W. Haskell, H. B. Hollinger, and H. C. Van Ness, *J. Phys. Chem.*, **72**, 4534 (1968); (b) H. W. Haskell, Ph.D. Thesis, Reusselaer Polytechnic Institute, Troy, N.Y., 1967, available from University Microfilms, Ann Arbor, Mich.
(5) J. M. Prausnitz, "Molecular Thermodynamics of Fluid-Phase Equilibria", Prentice-Hall, Englewood Cliffs, N.J., 1969.
(6) O. Redlich and A. T. Kister, *Ind. Eng. Chem.*, **40**, 345 (1948).
(7) G. M. Wilson, *J. Am. Chem. Soc.*, **86**, 127 (1964).
(8) Haskell, Hollinger, and Van Ness[4] already used this equation. In their paper the sign of the second term of the sum is plus instead of minus.
(9) (a) H. Wolff and A. Höpfner, *Ber. Bunsenges. Phys. Chem.*, **69**, 710 (1965); (b) *ibid.*, **71**, 461 (1967).
(10) M. Diaz Peña and D. R. Cheda, *Ann. Real. Soc. Espan. Fis. Quim.*, **66**, 737, 747 (1970).
(11) J. A. Barker, *Aust. J. Chem.*, **6**, 207 (1953).
(12) The molar volumes and virial coefficients of ethanol were the same as those which were used for the hexane solutions and which are given in ref 13.
(13) H. Wolff and H.-E. Höppel, *Ber. Bunsenges. Phys. Chem.*, **72**, 710 (1968).
(14) V. Svoboda, R. Holub, and J. Pick, *Collect. Czech. Chem. Commun.*, **36**, 2331 (1971).
(15) The molar volumes of hexanol and cyclohexane were taken from the ref 16 and 17. The virial coefficients of hexanol were estimated from those of propanol and 1-butanol reported in ref 10 and 18. The smoothed values given by Dymond and Smith[18] served as virial coefficients of cyclohexane.
(16) A. J. Vogel, *J. Chem. Soc.*, 1814 (1948).
(17) K. Strubl, V. Svoboda, R. Holub, and J. Pick, *Collect. Czech. Chem. Commun.*, **35**, 3004 (1970).
(18) J. H. Dymond and E. B. Smith, "The Virial Coefficients of Gases", Clarendon Press, Oxford, 1969.
(19) (a) H. Wolff and G. Gamer, *J. Phys. Chem.*, **76**, 871 (1972); (b) H. Wolff, *Z. Elektrochem., Ber. Bunsenges. Phys. Chem.*, **66**, 529 (1962); (c) H. Wolff and U. Schmidt, *Ber. Bunsenges. Phys. Chem.*, **68**, 579 (1964); (d) H. Wolff and D. Horn, *ibid.*, **71**, 469 (1967); **72**, 419 (1968).
(20) H. C. Van Ness, J. Van Winkle, R. R. Richtol, and H. B. Hollinger, *J. Phys. Chem.*, **71**, 1483 (1967).
(21) R. M. Badger and S. H. Bauer, *J. Chem. Phys.*, **5**, 839 (1937).
(22) W. L. Chandler and R. H. Dinius, *J. Phys. Chem.*, **73**, 1596 (1969).
(23) L. J. Bellamy and R. J. Pace, *Spectrochim. Acta*, **22**, 525 (1966).
(24) H. E. Hallam, "Matrix Isolation Technique" in "The Hydrogen Bond", P. Schuster, G. Zundel, and C. Sandorfy, Ed., North-Holland Publishing Co., Amsterdam, 1976, pp 1092–1096.
(25) P. Bordewijk, M. Kunst, and A. Rip, *J. Phys. Chem.*, **77**, 548 (1973).
(26) The entropy changes calculated from $\Delta S = (\Delta U/T) - R \ln K$ for the alcohols are $\Delta S_2 = -8.4$ to -11.2 cal/deg mol for dimer formation and $\Delta S_3 = -7.2$ to -9.8 cal/deg mol for polymer formation. These values do not reveal differences as great as the values calculated on the basis of the higher dimerization energy. However they show the decrease expected for polymer formation.[27] There are neither significant differences between the entropy changes of the alcohols and the amines ($\Delta S_2 = -7.7$ to -9.6 cal/deg mol, $\Delta S_3 = -5.3$ to -7.1 cal/deg mol).
(27) L. Sarolea-Mathot, *Trans. Faraday Soc.*, **49**, 8 (1953).

Thermal and Structural Properties of the Cholestanyl Myristate–Cholesteryl Myristate and Cholestanyl Myristate–Cholesteryl Oleate Binary Systems

Barry E. North[†] **and Donald M. Small***

Biophysics Division, Department of Medicine, Boston University School of Medicine, Boston, Massachusetts 02118 *(Received June 1, 1976; Revised Manuscript Received January 6, 1977)*

Phase maps of two binary systems of sterol esters, cholestanyl myristate–cholesteryl myristate and cholestanyl myristate–cholesteryl oleate, were obtained by examining binary mixtures of the esters by differential scanning calorimetry and polarizing light microscopy. Binary mixtures of cholestanyl myristate and cholesteryl myristate form solid solutions which melt at temperatures from 72 to 92 °C with increasing cholestanyl myristate content. Solid solutions containing up to 15 wt % cholestanyl myristate melt to smectic mesophases and then to cholesteric mesophases before becoming isotropic liquids. Solid solutions with from 15 to 30 wt % cholestanyl myristate melt to cholesteric mesophases before melting to isotropic liquids. Mixtures with greater than 30 wt % cholestanyl myristate melt directly to isotropic liquids but the metastable mesophases can be obtained by undercooling the liquid phase. The cholestanyl myristate–cholesteryl oleate binary system exhibits a eutectic containing 6% cholestanyl myristate and melting at 46 °C. Over a very limited temperature and composition range in the region of the eutectic composition, a stable cholesteric phase exists. Metastable cholesteric and smectic phases are formed when the liquid phase is undercooled. The phase behavior of this system indicates that cholesteryl oleate and cholestanyl myristate are insoluble in each other in the solid state. The different phase behavior for the two binary systems is explained in terms of the crystal structures of the individual esters. X-ray diffraction evidence indicates that cholesteryl myristate and cholestanyl myristate are isostructural and can therefore readily form solid solutions, whereas cholesteryl oleate and cholestanyl myristate have different crystal structures and thus do not allow solid solubility.

Introduction

Long-chain fatty acid esters of cholesterol are normal components of serum lipoproteins[1] and occur pathologically in the arterial lesions of atherosclerosis[2] as well as in the xanthomata of familial hypercholesterolemia.[3] Because of their biological importance and unusual behavior as liquid crystals, the physical properties of cholesteryl esters have been studied extensively.[4-6] Moreover, the phase behavior of multicomponent systems containing cholesteryl esters in combination with other lipids has been investigated as models for biological systems.[4,7,8] For example, the phase equilibrium of cholesterol–cholesteryl ester–phosphatidylcholine–water is useful in analyzing the physical state of lipid deposits in normal and diseased arteries.[9]

In biological systems, more than one cholesteryl ester are usually present, cholesteryl oleate and linoleate being the most abundant in serum lipoproteins and atheromatous lesions.[1] The melting behavior of a number of binary systems of cholesteryl esters has been studied,[4,10-13] but the phase behavior of binary mixtures of a cholesteryl ester and a different sterol ester has not been investigated, except in an early study on sterol mixtures.[14] The presence of small amounts of cholestanyl esters in normal human plasma lipoproteins,[15] in human atherosclerotic deposits,[16,17] and especially the presence of as much as 49% of the total esterified sterols in abnormal brain tissues of patients with cerebrotendinous xanthomatosis, a rare lipid storage disease,[18] prompted us to study the effects of cholestanyl esters on the state and structure of cholesteryl esters. Although the physical states of these lipid containing systems are determined by the complex interactions of all of the components, nevertheless an understanding of the physical properties of sterol ester mixtures is a necessary prerequisite to the study of more complex model systems.

In this paper we examine the phase behavior of two binary systems. In the first, the cholesteryl myristate–cholestanyl myristate binary system, the two esters have almost identical chemical structures but different thermal behavior.[19] Cholesteryl myristate was chosen because it is perhaps the most extensively studied cholesteryl ester. In the second system, the cholesteryl oleate–cholestanyl myristate binary system, the two esters are structurally quite different. Cholesteryl oleate was chosen because of its biological importance.

Experimental Section

Sample Preparation. The esters were obtained from Nu-Chek-Prep, Elysian, Minn., in greater than 99% purity. Purity was checked by thin layer chromatography on silver nitrate impregnated Silica gel G plates.

Mixtures of approximately 30 mg were prepared by weighing the individual esters to 0.01 mg into constricted glass tubes (i.d. 5 mm). The tubes were filled with nitrogen, sealed, and the components equilibrated by centrifuging through the constriction ten times at 90 °C. The mixtures were checked for the absence of breakdown products by thin layer chromatography after the equilibration procedure.

Microscopy. Samples of the ester placed on a microscope slide and covered with a cover slip were examined under a polarizing light microscope equipped with a heating stage and a calibrated thermometer.[4] The samples were heated at approximately 1 °C/min to the isotropic state. Metastable mesomorphic phases were examined by undercooling the isotropic liquid, and mesomorphic transition temperatures were measured if possible by reheating the smectic mesophase at 1 °C/min.

Calorimetry. Differential scanning calorimetry was carried out using a modified Du Pont 900 differential

[†] Present address: Biology Department, Brookhaven National Laboratory, Upton, N.Y. 11973.

thermal analyzer equipped with a differential scanning calorimetry cell and a Perkin-Elmer differential scanning calorimeter Model DSC-2. Samples were prepared by melting the mixtures and transferring 1.5–2.5-mg portions to aluminum pans, which were then sealed. The calorimetry scans were run immediately and duplicate samples were re-run after storing the samples for 3 days at room temperature. Selected samples were re-run after storage for 4 months at room temperature.

After an initial heating scan at 5 or 10 °C/min from 20 to 100 °C, the mesomorphic transitions were obtained by cooling to a temperature below the mesomorphic phase transitions and heating again to 100 °C. The sample was cooled to 0 °C (for the cholesteryl myristate–cholestanyl myristate mixtures) or to −50 °C (for the cholesteryl oleate–cholestanyl myristate mixtures) and then reheated to 100 °C. For the melting transitions of the pure components and for all liquid crystal transitions, the transition temperature was taken as the extrapolated onset temperature (the temperature corresponding to the intersection of the extrapolated baseline and a line through the steepest part of the leading edge of the peak) on the Du Pont instrument or the peak temperature on the Perkin-Elmer. For other transitions, the onset temperature (initial deviation from baseline) and peak temperature (obtained from the Perkin-Elmer DSC-2 thermograms at a scan rate of 5 °C/min) were used to estimate the solidus and liquidus temperatures, respectively.[20] The transition temperatures were calibrated using pure standards with known melting transitions (*p*-nitrotoluene, naphthalene, benzoic acid, and indium).

X-Ray Diffraction. X-ray powder diffraction patterns were obtained using a Searle x-ray camera with toroidal optics (sample to film distance 61.85 mm) mounted on a rotating anode x-ray generator (Ni filtered Cu Kα radiation). The samples were ground with a mortar and pestle and placed between 0.000 25-mm thick Mylar windows, spaced 0.8 mm apart. Microdensitometry of x-ray photographs was performed on a Joyce-Loebl Model 3CS microdensitometer.

Results

Cholesteryl Myristate–Cholestanyl Myristate Binary System. Cholesteryl myristate possesses stable smectic and cholesteric mesophases; that is, the mesophases are formed on heating the crystal as well as cooling the isotropic liquid. The crystal to smectic transition occurs at 72 °C, the smectic to cholesteric transition at 80 °C, and the cholesteric to isotropic transition at 85.5 °C. Cholestanyl myristate, on the other hand, melts directly to an isotropic liquid at 91 °C. The mesophases are metastable; the cholesteric mesophase is only formed when the isotropic liquid is undercooled, and crystallization takes place so rapidly that the smectic phase has an extremely short lifetime.[19]

The differential scanning calorimetry curves of the two esters, shown in Figure 1, illustrate their different thermal behavior. Also shown in Figure 1 is the differential scanning calorimetry curve of a mixture containing 60 wt % cholesteryl myristate and 40 wt % cholestanyl myristate. Its melting behavior is intermediate between that of the two components. It melts directly to an isotropic liquid over a temperature range between the melting temperatures of the pure esters. On cooling the isotropic liquid, the cholesteric and smectic mesophases appear.

The behavior of other mixtures is similar. With increasing cholesteryl myristate content, the crystalline melting transition temperatures decrease while the smectic to cholesteric and cholesteric to isotropic transition

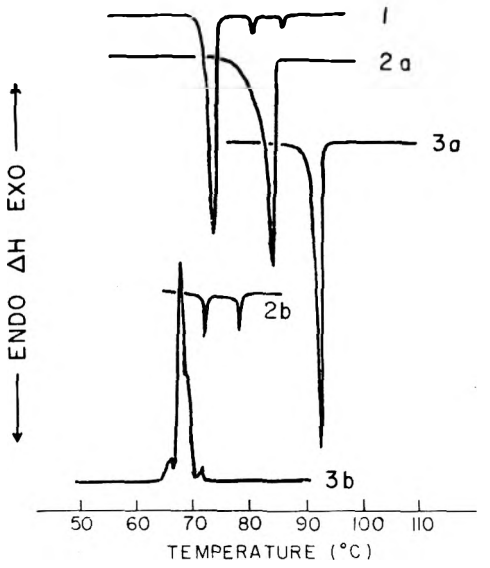

Figure 1. Differential scanning calorimetry curves for the cholesteryl myristate–cholestanyl myristate binary system (recorded on a Perkin-Elmer DSC-2, heating rate 5 °C/min): (1) heating curve of cholesteryl myristate, showing (left to right) crystal to smectic, smectic to cholesteric, and cholesteric to isotropic transitions; (2a) heating curve of a mixture containing 60% cholesteryl myristate, showing crystal to isotropic liquid transition; (2b) heating curve of same mixture showing (left to right) smectic to cholesteric and cholesteric to isotropic transitions obtained by undercooling the isotropic liquid and reheating; (3a) heating curve of cholestanyl myristate showing crystal to isotropic liquid transition; (3b) cooling curve of cholestanyl myristate showing (right to left) isotropic to cholesteric transition and recrystallization transitions. At this heating rate, crystallization occurs before the smectic mesophase appears.

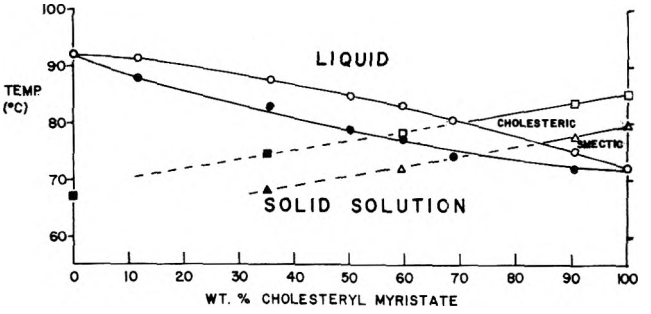

Figure 2. Binary phase map of cholestanyl myristate–cholesteryl myristate system obtained by differential scanning calorimetry and microscopy. *Solidus temperatures* (●) are extrapolated onset temperatures. Liquidus temperatures (O) are peak temperatures (see text for explanation). Smectic to cholesteric transition temperatures (△) and cholesteric to isotropic transition temperatures (□) were obtained from heating scans either directly or by heating the undercooled liquids. Smectic to cholesteric and cholesteric to isotropic transition temperatures from cooling scans for compositions in which crystallization occurs too rapidly to record heating scan are indicated by ▲ and ■, respectively.

temperatures increase. The observed linear variation of mesophase transition temperatures is expected for a binary system in which the two esters are miscible in the mesophases and liquid phases.

A phase map of the cholesteryl myristate–cholestanyl myristate binary system, constructed from the transition temperatures obtained by differential scanning calorimetry and microscopy, is presented in Figure 2. The diagram suggests the formation of solid solutions for all compositions. Melting of the solid solutions occurs over a temperature range indicated by the solidus and liquidus temperatures. Regions containing stable smectic and cholesteric mesophases are also shown. The smectic phase is stable for compositions of 85–100% cholesteryl myristate, where the cholesteric to isotropic liquid transition occurs at temperatures equal to or higher than the liquidus

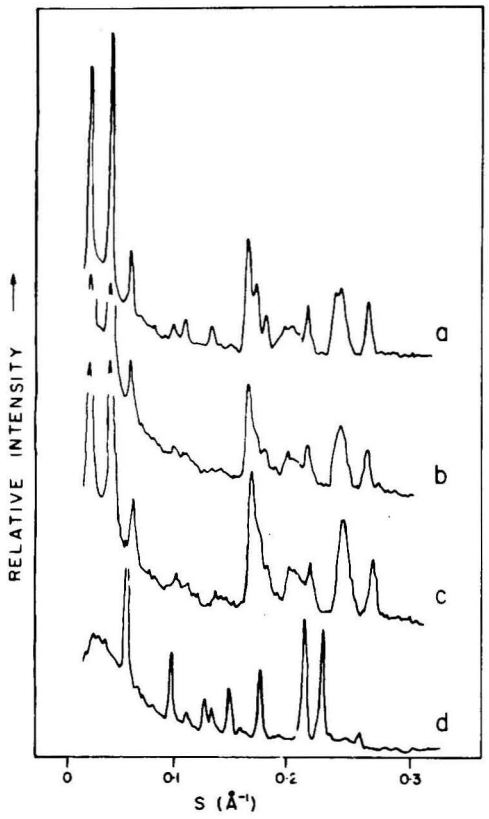

Figure 3. Microdensitometer traces of x-ray diffraction patterns for (a) cholesteryl myristate, (b) cholestanyl myristate, (c) binary mixture of 50% cholestanyl myristate and 50% cholesteryl myristate, and (d) cholesteryl oleate. The positions and relative intensities of the major reflections in a, b, and c are similar, while the diffraction pattern of d is quite different.

temperature. Likewise, the cholesteric phase is stable for compositions of 70–100% cholesteryl myristate, where the smectic to cholesteric transition occurs at the same or higher temperature than the liquidus temperature. At lower cholesteryl myristate content, these phases are metastable.

The x-ray diffraction maxima for cholesteryl myristate and cholestanyl myristate are compared in Figure 3. The d spacings and the relative intensities of the diffraction maxima are strikingly similar, suggesting that the two esters are isostructural. Furthermore, the x-ray diffraction pattern of a 1:1 mixture of the two esters (Figure 3) is nearly identical with the diffraction patterns of the pure esters. These results clearly show that cholesteryl myristate and cholestanyl myristate form solid solutions.

Cholestanyl Myristate–Cholesteryl Oleate Binary System. Like cholestanyl myristate, cholesteryl oleate forms metastable mesophases, i.e., the mesophases are only formed by undercooling the isotropic liquid. The crystal to isotropic transition occurs at 51 °C, and the smectic to cholesteric and cholesteric to isotropic transitions occur at 42 and 47 °C, respectively.[4,5] Unlike the mesophases of cholestanyl myristate, the mesophases of cholesteryl oleate can exist for several minutes below the crystal to isotropic transition temperature before crystallization occurs.

When equilibrated mixtures of cholestanyl myristate and cholesteryl oleate with greater than 75% cholesteryl oleate were cooled to room temperature (25 °C) and examined by polarizing microscopy, two phases, a crystalline phase and a smectic mesophase, were observed in most cases. On heating, the crystals melted at 34 °C, usually crystallizing into a more stable form which melted at approximately

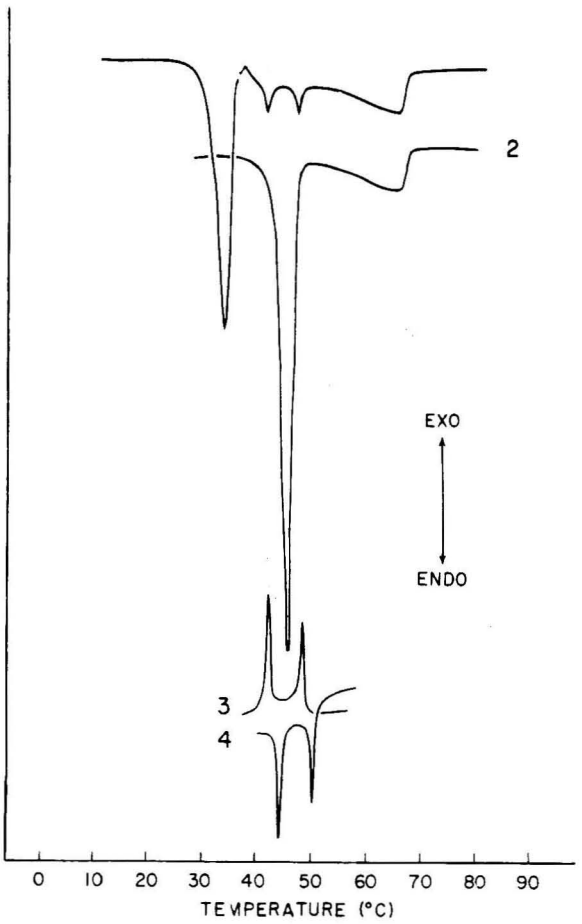

Figure 4. Differential scanning calorimetry curves for a mixture containing 20% cholestanyl myristate and 80% cholesteryl oleate (Perkin-Elmer DSC-2, scan rate 5 °C/min): (1) heating scan recorded immediately after equilibration of mixture; (2) heating scan after 3 days at 25 °C; (3) cooling scan showing (right to left) isotropic to cholesteric and cholesteric to smectic transitions; (4) heating scan obtained immediately after cooling scan 3, showing smectic to cholesteric and cholesteric to isotropic transitions (left to right).

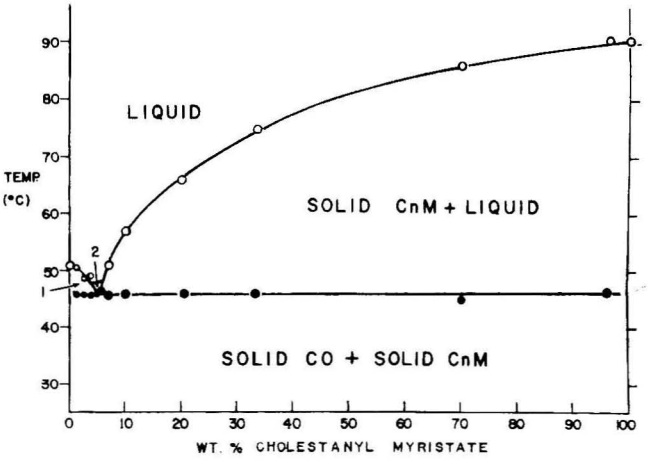

Figure 5. Binary phase map of cholestanyl myristate (CnM) and cholesteryl oleate (CO) obtained by differential scanning calorimetry using a Perkin-Elmer DSC-2 (scanning rate 5 °C/min) and microscopy: (●) eutectic melting temperatures; (O) liquidus temperatures obtained from peak temperatures of heating curves; zone 1, solid cholesteryl oleate plus liquid; zone 2, cholesteric mesophase.

46 °C. When allowed to stand for 72 h or longer at room temperature, the mixtures became totally crystalline and melting occurred at 46 ± 1 °C. No significant changes in the melting behavior were observed when the samples were reexamined after 4 months. The observed thermal be-

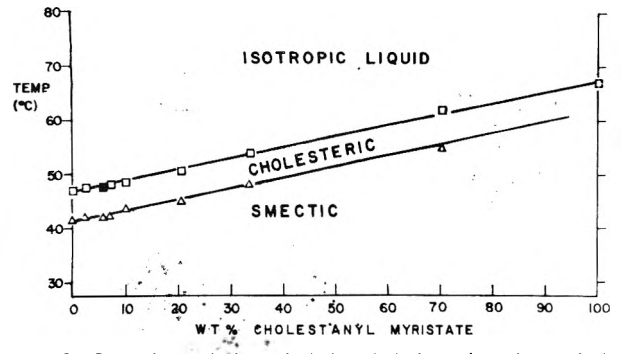

Figure 6. Smectic to cholesteric (△) and cholesteric to isotropic (□) transition temperatures for mixtures of cholestanyl myristate and cholesteryl oleate. ■ indicates a cholesteric to isotropic transition of a stable cholesteric mesophase.

havior of the cholestanyl myristate–cholesteryl oleate mixtures, which suggests formation of metastable crystalline states, was confirmed by differential scanning calorimetry and is illustrated in Figure 4 for a mixture containing 20% cholestanyl myristate. Due to the formation of metastable crystalline states, the phase behavior described below and illustrated in Figure 5 is based on observations made after allowing the samples to stand for 3 days at 25 °C. Mixtures throughout most of the composition range exhibit a sharp melting transition at 46 ± 1 °C, corresponding to the melting of a eutectic. In addition, mixtures containing more than 10% cholestanyl myristate exhibit a broad transition at higher temperature. With increasing cholestanyl myristate content, this transition extends to higher temperatures and its enthalpy increases relative to that of the eutectic transition. By microscopy, this transition corresponds to the melting of crystals into a cholesteric liquid crystalline or isotropic liquid phase. On cooling in the differential scanning calorimeter, two exothermic transitions are observed. The transitions were identified by microscopy as isotropic to cholesteric and cholesteric to smectic transitions. As the isotropic liquid is cooled, the cholesteric phase appears, followed by a transformation to the smectic phase. Mixtures containing 50% or more cholesteryl oleate can be cooled to the smectic phase and reheated through the mesophase transitions before crystallization occurs. (See Figure 6.)

For a mixture containing 10% cholestanyl myristate, the enthalpy of the transition due to the melting of excess cholestanyl myristate is very small. Only a small shoulder on the high temperature side of the eutectic melting transition can be detected. With 7% myristate, a small shoulder is also present, but in a mixture containing 6% myristate, only the single sharp peak at 46 °C is present and suggests that the eutectic composition contains 6% cholestanyl myristate and 94% cholesteryl oleate.

An interesting consequence of the formation of a eutectic is that for mixtures with a composition within a few percent of the eutectic composition, the cholesteric to isotropic transition temperature is higher than the eutectic melting temperature. In this narrow range of composition, the cholesteric phase is truly stable rather than metastable over a narrow temperature range and can be observed by microscopy on melting the eutectic mixture. For example, in a mixture containing 7% cholestanyl myristate, the cholesteric phase is stable 1 °C above the eutectic melting temperature.

For mixtures with less than 6% cholestanyl myristate, one would expect to see, in addition to the eutectic melting transition, a transition corresponding to the melting of excess cholesteryl oleate. However, since the melting temperature of cholesteryl oleate is close to the temperature of the eutectic melting transition, we were not able to discern a separate peak for excess cholesteryl oleate. Under such circumstances it is difficult to determine the exact eutectic composition.

Several mixtures in the composition range from 1 to 6% cholestanyl myristate were examined. On heating, all of these mixtures exhibited an endotherm beginning at 46 ± 1 °C (solidus line). However the peak temperatures occurred at progressively lower temperatures with increasing cholestanyl myristate content. The constant temperature of the solidus line at 46 °C, due to the melting of a eutectic, indicates that cholestanyl myristate is probably insoluble in cholesteryl oleate in the solid phase. Furthermore, at the other end of the composition range, the presence of a eutectic melt at 46.5 °C for a mixture containing only 3% cholesteryl oleate shows that cholesteryl oleate is insoluble in cholestanyl myristate in the solid phase.

The x-ray diffraction pattern of cholesteryl oleate is shown in Figure 2. The overall dissimilarity of the diffraction patterns of cholesteryl oleate and cholestanyl myristate suggests that the two esters have significantly different crystal structures and explains the failure of the two esters to form even limited solid solutions.

Discussion

The thermal behavior of cholesteryl myristate–cholestanyl myristate mixtures, characterized by transition temperatures which change progressively from that of one component to that of the other, suggests the formation of solid solutions for this binary system over the entire composition range. All mixtures examined melt over a narrow temperature range, and no evidence for eutectic or compound formation exists. Since the molecular structures of the two esters are identical except for the presence of the Δ5 double bond in cholesterol, and their crystal structures are nearly identical, as indicated by their virtually identical x-ray diffraction patterns, one would predict that either ester could easily fit into the crystal lattice of the other with little disruption of the order of the crystal.

The formation of a eutectic in the cholesteryl oleate–cholestanyl myristate binary system is in contrast to the simple behavior of the cholesteryl myristate–cholestanyl myristate binary system. Cholesteryl oleate and cholestanyl myristate possess different crystalline structures, as shown by their distinctly different x-ray diffraction patterns (Figure 3). Thus it is not surprising that these two esters, with different acyl chains, fail to form solid solutions. The formation of eutectics in cholesteryl ester binary systems is not uncommon. For example, binary mixtures of cholesteryl myristate with cholesteryl stearate, acetate, and nonanoate form eutectics with 68,[11] 50,[12] and 40%[12] cholesteryl myristate, respectively. The cholesteryl oleate–cholesteryl stearate and cholesteryl linoleate–cholesteryl stearate systems also have eutectics, both containing 6% of the stearate ester.[13]

The thermal behavior of the cholesteryl oleate–cholestanyl myristate binary system is also complicated by the existence of metastable crystalline states. Apparently, a metastable eutectic with a melting temperature of 34 °C is initially formed when mixtures of the two esters are cooled from the isotropic liquid state, and the higher melting stable eutectic forms slowly when the sample is allowed to stand at room temperature. Polymorphism has been observed in other binary systems of cholesteryl oleate and another cholesteryl ester and in cholesteryl oleate itself.[13]

The existence of a eutectic in mixtures of sterol esters may have importance in biological systems. The presence of a few percent of cholestanyl myristate in cholesteryl oleate lowers the melting transition considerably and produces a stable cholesteric mesophase over a narrow range of temperature and composition. Thus minor changes in the composition of the sterols in a pathological lipid deposit may alter the physical state of the lesion. The xanthomata of cerebrotendinous xanthomatosis, which contain large amounts of cholestanyl esters, might be quite different in physical properties from the primarily cholesteryl ester xanathomata associated with familial hypercholesterolemia.

Acknowledgment. The authors wish to acknowledge the help of Dr. Carson Loomis and Dr. G. Graham Shipley. This research was supported by Grant U.S.P.H.S. HL 18623 (D. M. Small, Principal Investigator) and Training Grant GM 00176.

References and Notes

(1) V. P. Skipski in "Blood Lipids and Lipoproteins: Quantitation, Composition, and Metabolism", G. J. Nelson, Ed., Wiley-Interscience, New York, N.Y., 1972, pp 471–583.
(2) E. B. Smith, P. J. Evans, and M. D. Downham, *J. Atheroscler. Res.*, **7**, 171–186 (1967).
(3) J. D. Wilson, *Circ. Res.*, **12**, 472–478 (1963).
(4) D. M. Small in "Surface Chemistry of Biological Systems", M. Blank, Ed., Plenum Press, New York, N.Y., 1970, pp 55–83.
(5) G. J. Davis, R. S. Porter, J. W. Steiner, and D. M. Small, *Mol. Cryst. Liquid Cryst.*, **10**, 331–336 (1970).
(6) G. J. Davis, R. S. Porter, and E. M. Barral, *Mol. Cryst. Liquid Cryst.*, **11**, 319–330 (1970).
(7) C. R. Loomis, M. J. Janiak, D. M. Small, and G. G. Shipley, *J. Mol. Biol.*, **86**, 309–324 (1974).
(8) M. J. Janiak, C. R. Loomis, G. G. Shipley, and D. M. Small, *J. Mol. Biol.*, **86**, 325–339 (1974).
(9) D. M. Small and G. G. Shipley, *Science*, **185**, 222–229 (1974).
(10) S. G. Frank and B. G. Byrd, *J. Pharm. Sci.*, **61**, 1762–1765 (1962).
(11) A. V. Galanti and R. S. Porter, *J. Phys. Chem.*, **76**, 3089–3093 (1972).
(12) C. W. Griffin and R. S. Porter, *Mol. Cryst. Liquid Cryst.*, **21**, 77–98 (1973).
(13) R. J. Krzewki and R. S. Porter, *Mol. Cryst. Liquid Cryst.*, **21**, 99–124 (1973).
(14) H. Lettré, *Justus Leibigs Ann. Chem.*, **495**, 41–60 (1932).
(15) E. H. Mosbach, J. Blum, E. Arroyo, and S. Milch, *Anal. Biochem.*, **5**, 158–169 (1963).
(16) R. Schoenheimer, J. Von Behring, and R. Hummel, *Z. Physiol. Chem.*, **192**, 93 (1930).
(17) R. Fumagalli, G. Galli, and G. Urna, *Life Sci. Part II*, **10**, 25–33 (1971).
(18) J. H. Menkes, J. R. Schimschock, and P. D. Swanson, *Arch. Neurol.*, **19**, 47–53 (1968).
(19) B. E. North, G. G. Shipley, and D. M. Small, *Biochem. Biophys. Acta*, **424**, 376–385 (1976).
(20) In differential scanning calorimetry, the true liquidus temperature in a binary system would correspond to the temperature of the return of the pen to baseline, assuming that the scanning rate is sufficiently slow to allow the system to remain near equilibrium and to elliminate thermal and mechanical lags. At faster scanning rates, the return to baseline would occur at a higher temperature than the true liquidus temperature. To deal with this problem, scans at several rates were performed and the return to baseline temperature extrapolated to zero scan rate was obtained. This temperature should be the liquidus temperature. The liquidus temperature estimated in this way corresponds very closely to the peak temperature at a scan rate of 5 °C/min. Since the difference between the peak temperature and the return to baseline temperature at 5 °C/min is less than 2 °C, the error in these liquidus temperatures is no more than 1 °C.

A Molecular Orbital Theoretical Study on $(SN)_2$ Molecules at the Initial Stage of Polymerization to $(SN)_x$

Tokio Yamabe, Kazuyoshi Tanaka, Kenichi Fukui,*

Department of Hydrocarbon Chemistry, Faculty of Engineering, Kyoto University, Sakyo-ku, Kyoto 606, Japan

and Hiroshi Kato

College of General Education, Nagoya University, Chikusa-ku, Nagoya 464, Japan *(Received May 24, 1976; Revised Manuscript Received December 28, 1976)*

Concerning the initial stage of solid state polymerization of $(SN)_x$, semiempirical INDO-type ASMO-SCF calculations are performed for the precursor S_2N_2, and several "deformed" structures of $(SN)_2$, the dimeric unit $(SN)_4$, and the trimeric unit $(SN)_6$. According to the results of calculations, the triplet biradical nature emerges in appropriately "deformed" structures of $(SN)_2$. This agrees well with the experimental results wherein paramagnetism ($g = 2.005$) is observed at the initial stage of polymerization. $(SN)_4$ and $(SN)_6$, however, show no triplet nature probably corresponding to the fact that the system gradually becomes diamagnetic as the polymerization proceeds. The mechanism of polymerization at the initial stage is discussed based on our calculated results.

Introduction

There has recently been considerable interest in the covalent polymer, polymeric sulfur nitride, $(SN)_x$, since the discovery that it is a low-dimensional metallic conductor.[1,2] The theoretical treatment for $(SN)_x$ has also been carried out to reveal the metallic character of the $(SN)_x$ in its band structure.[3] Recently, MacDiarmid et al. have reported that the crystalline monomeric S_2N_2 polymerizes thermally in the solid state to form the $(SN)_x$ polymer.[4] They have also determined the structure of $(SN)_x$ as well as S_2N_2 shown in Figure 1A and 1B by x-ray diffraction. The initially colorless tabular monoclinic crystal of S_2N_2 turns intense blue-black and becomes paramagnetic giving a weak free radical signal at $g = 2.005$. This substance then changes to golden-colored, diamagnetic crystals of the $(SN)_x$ polymer.

For the mechanism of the solid state polymerization, they have also proposed, particularly at the first step, the thermal opening (widening) of one of the S–N bonds in S_2N_2 to form a biradical species. This radical can then link up with another S_2N_2 molecule in the crystal to give the partly polymerized, paramagnetic $(SN)_2$ of blue-black color, and finally the golden $(SN)_x$ polymer. Moreover, Baughman et al. have studied the polymerization including

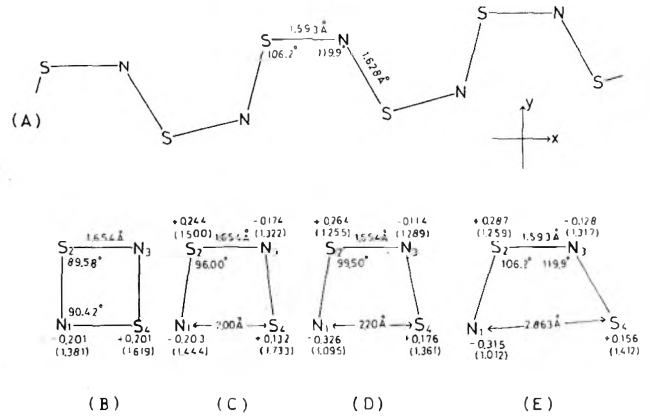

Figure 1. Geometries of the polymer $(SN)_x$ (A), the precursor S_2N_2 (B), and several deformed $(SN)_2$ molecules (C, D, and E) with atomic net charges and π electron densities (bracketed values). For (D) and (E), those of the triplet states are shown.

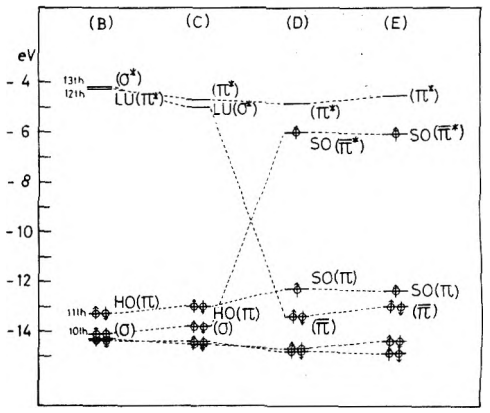

Figure 2. Orbital energy level correlation diagrams for deformed $(SN)_2$ (C, D, and E) together with the precursor, S_2N_2 (B). Changes of the orbital energy levels below the eighth MO are not essential and omitted here.

defect structure crystallographically.[5]

In the present paper, we try to elucidate the polymerization reaction, particularly at the initial stage, and to confirm the mechanism proposed above by MO calculations. At first, we calculate the electronic states of the precursor S_2N_2, and then, of the several "deformed" structures of $(SN)_2$ as shown in Figure 1 in order to investigate the thermal initiation reaction. The calculations are performed with the use of the semiempirical INDO-type ASMO-SCF method for valence electrons including sulfur 3d orbitals,[6a] and the stability of the triplet state (open shell) is examined by the sign of the transition energy from the lowest singlet state (closed shell).[6b] This method has given fairly reasonable results, especially for the transition energies[6c-e] because of good parametrization for Coulomb repulsion integrals.[7] Examined further are the electronic states of the dimeric unit $(SN)_4$ and the trimeric unit $(SN)_6$.

Electronic State of S_2N_2

The molecular structure of S_2N_2 employed here is shown in Figure 1B, which has been determined by MacDiarmid et al.[4a] This is square-planar (D_{2h}) with 90° of the S–N–S angle[8] and almost equal bond lengths, 1.654 Å.[9] The calculation of the electronic state of S_2N_2 has been carried out by using the SCF–Xα scattered wave method, which gives a rather highly polar S–N bond ($S^{0.48+}$–$N^{0.48-}$).[10] This is probably because the method overestimates the contribution from the ionic structure.

The atomic net charges and π electron densities calculated here are also shown in Figure 1. This molecule has six π electrons: two π electrons from each sulfur atom and one π electron from each nitrogen atom. In consequence of the planar D_{2h} structure, the occupied orbitals are separated into σ and π orbitals. In the S–N bond, the charge densities of σ electrons are 4.180 and 3.820 on S and N, respectively, whereas those of π electrons are 1.619 and 1.381, respectively. This means that the charge transfer of π electrons from S to N (0.381) exceeds that of σ electrons from N to S (0.180). Consequently, the net charges on S and N are +0.201 and −0.201, respectively, as is usual for S–N bonds in other molecules[11] reflecting the fact that sulfur is less electronegative than nitrogen. As a matter of course, the highest occupied molecular orbital (HOMO) is of typical π MO, following another π and two σ MOs close together as shown in Figure 2. It should be noticed here that there are two extraordinary low lying unoccupied MOs with negative eigenvalues and large S–N antibonding characters, i.e., π^* and σ^* being very close each other. Such low lying σ^* MO may often induce bond cleavages or drastic rearrangement among MOs.

TABLE I: Transition Energies and CI Improvements for the Stability of the Triplet States of the Deformed $(SN)_2$ (in eV)

Structure	Δ^3E_{π,π^*} (11th MO → 13th MO)	Δ^3E_{π,σ^*} (11th MO → 12th MO)	Δ^3E_{π,σ^*} (after CI)
B	1.922[a]	2.514[b]	2.867
C	1.401	1.223	1.627
D[c]	1.060	−0.693 ($\Delta^3E_{\pi,\bar{\pi}^*}$)	−0.068 ($\Delta^3E_{\pi,\bar{\pi}^*}$)
E[c]	1.876	−0.544 ($\Delta^3E_{\pi,\bar{\pi}^*}$)	−0.153 ($\Delta^3E_{\pi,\bar{\pi}^*}$)

[a] In this case, 11th MO → 12th MO. [b] In this case, 11th MO → 13th MO. [c] In these structures Δ^3E_{π,σ^*} is replaced by $\Delta^3E_{\pi,\bar{\pi}^*}$ because of the orbital crossing occurring in the deformation from C to D (see text).

Electronic States of "Deformed" $(SN)_2$

According to the mechanism of the polymerization reaction proposed by MacDiarmid et al., S_2N_2 is considered to be deformed thermally (near 0 °C) as the first step to open one S–N bond, giving biradical character. In this section, we investigate how the biradical character appears according to the deformation. The geometries of $(SN)_2$ chosen here are shown in Figure 1C–E. In Figure 1C and 1D, the bond lengths of the sides opposite to the opened S–N bond are taken as being equal to the S–N bond length in the precursor, S_2N_2 (Figure 1B), since shortening of them is unfavorable from the viewpoint of nuclear repulsion as found in this calculation. Figure 1E is employed from the fragment of the $(SN)_x$ polymer in Figure 1A. Sulfur 3d orbitals are requisite for the SCF convergence in the calculations for the open forms even though their contribution is not significant. As previously mentioned, we devoted our attention to these calculations in order to investigate the possibility of the triplet biradical by examining the transition energy from the lowest singlet state to the triplet state in each structure.

In the cases of the precursor (Figure 1B) and the slightly deformed structure (Figure 1C), the ground states are, not unexpectedly, singlet, although the triplet π–π^* transition energy (Δ^3E_{π,π^*}) and the triplet π–σ^* transition energy (Δ^3E_{π,σ^*}) of the latter are positively small as shown in Table I. Next, we tried the case of a little more deformed structure (Figure 1D). Δ^3E_{π,π^*} remains positive and almost the same value, while $\Delta^3E_{\pi,\bar{\pi}^*}$ is found to be negative. Hereafter, we define the signs π and $\bar{\pi}$ to represent the

TABLE II: a Spin Densities in $(SN)_2$ of Structures D and E[a]

Atom	s	p_x	p_y	$\bar{\pi}$ spin density	p_z	π spin density
			D			
N_1	0.000	0.272	0.000	0.273	0.187	0.187
N_3	0.008	0.081	0.036	0.125	0.145	0.145
S_2	0.001	0.069	0.005	0.092	0.036	0.082
S_4	0.000	0.469	0.026	0.510	0.572	0.586
			E			
N_1	0.000	0.214	0.000	0 215	0.168	0.168
N_3	0.009	0.067	0.098	0 175	0.171	0.171
S_2	0.000	0.046	0.004	0 052	0.008	0.060
S_4	0.000	0.364	0.172	0.559	0.584	0.601

[a] AO spin densities of 3d orbitals are of small values and hence omitted here. The values of $\bar{\pi}$ and π spin densities, however, contain the 3d contributions.

π-type MO perpendicular to the molecular plane and that in the molecular plane, respectively. The above result means that the ground state of such a structure is a triplet formed from two singly occupied (SO) MOs, i.e., π SOMO and $\bar{\pi}^*$ SOMO, as shown in Figure 2. The same result was obtained for structure E (Figure 1). Furthermore, these results were improved by the configuration interaction (CI) method including one electron excitations for the triplet states and pairing excitations for the singlet states within all ranges from (HO − 3)MO to (LU + 3)MO. The situations are essentially not altered after CI as shown in Table I. Thus, it is probable that the triplet state is energetically favorable for the ground state of such deformed structures rather than the singlet state. The atomic net charges and π electron densities of each structure are also shown in Figure 1, where the values for Figure 1D and 1E are those of the triplet states. We assume here that the open-shell MOs in the triplet state are occupied with two more electrons of α spins. The α spin densities of the π MO and the $\bar{\pi}^*$ MO are shown in Table II. As a whole, one cannot find a large change of the atomic net charges even in the triplet states of Figure 1D and 1E. This implies that the transition from the singlet state to the triplet state is not due to intramolecular charge transfer. On the other hand, such a transition would be expected to cause a drastic change of the number of π electrons from 6 to 5, as one of the π electrons is transferred from the π MO (11th) perpendicular to the molecular plane to the $\bar{\pi}^*$ MO (12th) in the plane in the biradicals of the structures D and E (Figure 2). The large spin densities of both the π electrons and the $\bar{\pi}$ electrons are mainly on S_4 and on N_1. The $\bar{\pi}$ radical electron may be more reactive than π radical electron because the orbital energy of $\bar{\pi}^*$ SOMO is much higher than that of π SOMO. Interestingly, the dominant component of such $\bar{\pi}^*$ SOMO are p_x and as such are consistent with the direction of the polymerization as shown in Figure 1A.

To understand such singlet–triplet transition in detail, we give correlation diagrams of the orbital energy levels for each structure as shown in Figure 2 and pictures of some of these MOs of both Figure 2C and 2D are given in Figure 3. The 10th MO and the 12th MO in Figure 3C are of bonding ($p\sigma$) and antibonding ($p\sigma^*$) character, respectively, to both the N_1–S_4 and the S_2–N_3 bonds, and are of antibonding ($p\bar{\pi}^*$) and bonding ($p\bar{\pi}$) character, respectively, to both the N_1–S_2 and the N_3–S_4 bonds. Thus, if the $p\bar{\pi}$ bond should be stronger than the $p\sigma$ bond by the elongation of the $p\sigma$ bond, there may be a possibility of level crossing between the 10th MO and the 12th MO. In fact, when the structure of $(SN)_2$ changes from Figure 1C to 1D, the occurrence of the level crossing between the

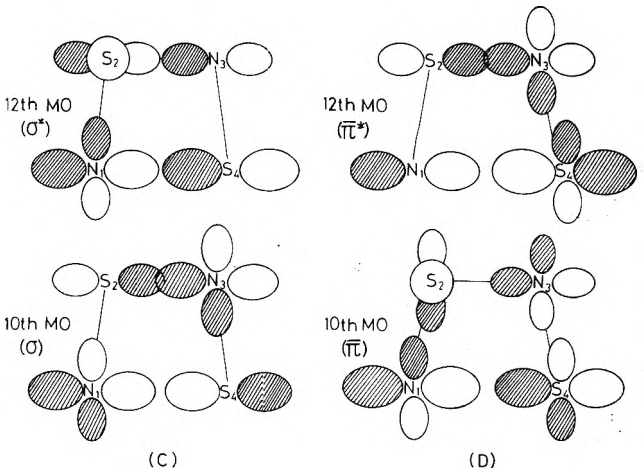

Figure 3. Pictures of 10th and 12th MOs of $(SN)_2$ having structures (C) and (D), respectively. Only the major AO components are depicted.

TABLE III: Values of Fock Matrix Elements Influencing 10th Orbital Energies of C and D (in eV)

r AO	s AO	(C) $C^{10}{}_r C^{10}{}_s \langle r\|F\|s\rangle$[a]	(D) $C^{10}{}_r C^{10}{}_s \langle r\|F\|s\rangle$
N_1 $2p_x$	S_2 $3p_x$	0.373	−0.147
N_1 $2p_x$	S_4 $3p_x$	−1.461	−0.556
N_3 $2p_x$	S_4 $3p_x$	0.372	−0.439
N_3 $2p_y$	S_4 $3p_x$	−0.088	0.133

[a] See the text about the notations $C^{10}{}_r$ and $C^{10}{}_s$.

12th MO (σ^*) and the 10th MO (σ) is seen as shown in Figure 2. Namely, the 10th MO and the 12th MO in Figure 3C are transformed to give bonding ($p\bar{\pi}$) and antibonding ($p\bar{\pi}^*$) character in Figure 3D, respectively, mainly with respect to the N_3–S_4 bond, and somewhat less with respect to the N_1–S_2 bond. These details are clarified by examining the values of the main Fock matrix elements, $C^{10}{}_r C^{10}{}_s \langle r|F|s\rangle$, where r and s are the component atomic orbitals (AOs) of the 10th MO, and C is the AO coefficient. It is seen from Table III that, in Figure 3C, the N_1-$(2p_x)$–$S_4(3p_x)$ matrix element contributes to stabilization for the orbital energy, and that the $N_1(2p_x)$–$S_2(3p_x)$ and $N_3(2p_x)$–$S_4(3p_x)$ matrix elements contribute to destabilization. However, in Figure 3D, the $N_1(2p_x)$–$S_4(3p_x)$ element leads to less stabilization and the $N_3(2p_x)$–$S_4(3p_x)$ to stabilization. Since the orbital level crossing in going from Figure 3C to 3D is caused mainly by the changing of the sign of the $3p_x$ orbital on S_4 and the larger contribution of the 3s orbital on S_2, it would not be so difficult to bring about such a triplet transition, if the widening of the N_1–S_4 bond takes place easily.

In fact, according to the IR spectrum of the solid S_2N_2,[12] the strong bands at 476.2 and 785 cm^{-1} are assigned to the B_{2u} and B_{3u} modes, respectively, which correspond to a widening of one of the S–N bonds (and hence shortening of the opposite S–N bond). These extraordinary low frequencies imply the shallow potential of the S–N bond for such vibrational modes and therefore the widening may easily induced, even thermally, because, e.g., 476.2 cm^{-1} is equal to 1.36 kcal/mol, which is the same order of RT at room temperature (ca. 0.6 kcal/mol). This consideration indicates that the polymerization may be accelerated by applying the appropriate IR radiation.

Thus it is expected that, at the point where the level crossing occurs, the N_1–S_4 $p\sigma$ bond vanishes and the N_3–S_4 $p\bar{\pi}$ bond prevails, and that the triplet state emerges in the course of the deformation probably due to vibrational motion. Furthermore, we have attempted to estimate the

mixing of the triplet configuration with the singlet closed-shell configuration for Figure 2C, and the mixing of the singlet (original closed-shell) configuration with the triplet (biradical) configuration for Figure 2D and 2E through spin–orbit coupling. Considering the perturbation correction,[13] the state function, required at present, $^{1(3)}\Phi_i$, is given by

$$^{1(3)}\Phi_i = {}^{1(3)}\Phi_i{}^0 + \sum_k \frac{\langle {}^{1(3)}\Phi_i{}^0 | H_{SO} | {}^{3(1)}\Phi_k{}^0 \rangle}{\Delta^3 E_{i,k}} {}^{3(1)}\Phi_k{}^0$$

where $^{1(3)}\Phi_i{}^0$ and $^{3(1)}\Phi_k{}^0$ are the unperturbed ith singlet (triplet) ASMO and the unperturbed kth triplet (singlet) ASMO, respectively. H_{SO} is usual spin–orbit coupling operator, and $\Delta^3 E_{i,k}$ is the energy difference. In the case of Figure 2C, $^1\Phi_i{}^0$ refers to the closed-shell configuration and $^3\Phi_k{}^0$ to the $\pi \rightarrow \sigma^*$ (11th MO $\rightarrow$ 12th MO) triplet configuration, whereas in Figure 2D and E, $^3\Phi_i{}^0$ refers to the $\pi \rightarrow \bar{\pi}^*$ (11th MO $\rightarrow$ 12th MO) triplet configuration and $^1\Phi_k{}^0$ to the original closed-shell configuration. These $^{3(1)}\Phi_k{}^0$ states seem to contribute mainly to the second term in the above correction rather than to other configurations, because the energy differences $\Delta^3 E_{\pi,\sigma^*}$ ($\Delta^3 E_{\pi,\bar{\pi}^*}$) are considerably smaller. The matrix element in the numerator is further reduced to $\langle \Psi_\pi{}^{11} | H_{SO} | \Psi_{\sigma^*}{}^{12} \rangle$ ($\langle \Psi_\pi{}^{11} | H_{SO} | \Psi_{\bar{\pi}^*}{}^{12} \rangle$), where $\Psi_\pi{}^{11}$ and $\Psi_{\sigma^*}{}^{12}$ ($\Psi_{\bar{\pi}^*}{}^{12}$) denote the 11th π MO and the 12th σ^* ($\bar{\pi}^*$) MO, respectively. Taking only one-center terms into account as to the matrix element and employing the spin–orbit coupling constants ζ of 74.2 and 363 cm^{-1} for nitrogen and sulfur, respectively,[14] we obtain

$$^1\Phi_i = {}^1\Phi_i{}^0 + 0.009\,{}^3\Phi_k{}^0 \quad \text{for Figure 2C}$$
$$^3\Phi_i = {}^3\Phi_i{}^0 - 0.019\,{}^1\Phi_k{}^0 \quad \text{for Figure 2D}$$

and

$$^3\Phi_i = {}^3\Phi_i{}^0 - 0.006\,{}^1\Phi_k{}^0 \quad \text{for Figure 2E}$$

The orders of the mixing coefficients are considerably larger than those in usual organic hetero compounds[15] on account of the heavy atom (sulfur) effect. Moreover, the 11th π MO and the 12th σ^* ($\bar{\pi}^*$) MO are advantageous, considering the character of the orbital angular momentum operator involved in H_{SO}. Thus, in $(SN)_2$, the degree of mixing of the singlet state is essentially remarkable. In particular, the biradical resulting from the π–$\bar{\pi}^*$ triplet transition would easily be formed from the singlet state. It should be stressed here that the energy difference between the triplet and the singlet state is small (approximately 1 kcal/mol) and hence it would not be unreasonable if the population of the singlet state, even if it were energetically higher, should increase with an increase of temperature according to the Boltzmann distribution. In this respect, it is interesting to note that the ESR spectrum of blue-black, partly polymerized, $(SN)_2$ decreases in intensity with increase in the temperature at which it is measured, e.g., −100 °C vs. 25 °C.[16]

Electronic States of $(SN)_4$ and $(SN)_6$

In order to understand the polymerization steps further, we calculated the electronic states of linear $(SN)_4$ and $(SN)_6$. The geometries employed are those from appropriate fragments of the polymer in Figure 1A. The calculated atomic net charges and π electron densities are shown in Figure 4 and the orbital energy diagrams for these molecules are shown in Figure 5. It is seen that π electron densities are distributed less on N_1 and S_8 in $(SN)_4$, and on N_1 and S_{12} in $(SN)_6$, and that $(SN)_4$ and $(SN)_6$ have a total of 10 and 16 π electrons, respectively. Furthermore the ground states of these molecules are found to be singlet

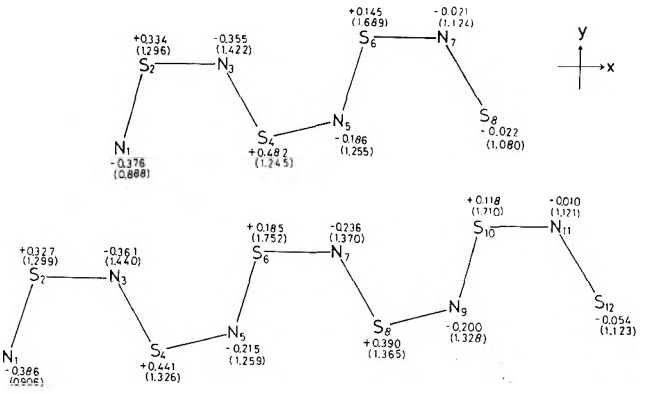

Figure 4. The calculated results for atomic net charges and π electron densities (bracketed values) of $(SN)_4$ and $(SN)_6$ molecules. Note that the total number of π electrons are 10 and 16, respectively, for these fragments.

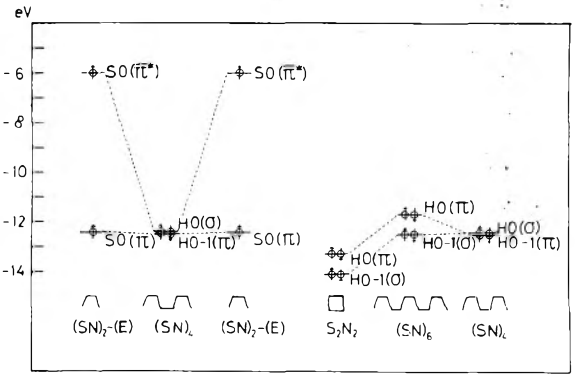

Figure 5. Orbital energy diagrams of S_2N_2, $(SN)_2$, $(SN)_4$, and $(SN)_6$.

rather than triplet states. The HOMO (σ) in $(SN)_4$ is considerably stabilized by the SOMO ($\bar{\pi}^*$)–SOMO ($\bar{\pi}^*$) interaction between two $(SN)_2$ biradicals. The (HO − 1)MO (π) is almost unchanged from the original π MO in structure E (Figure 5) and these two are nearly degenerate. In $(SN)_6$, however, the HOMO (π) is somewhat separated from the (HO − 1)MO (σ). These results and their HOMOs and (HO − 1)MOs suggest that $(SN)_4$ is derived from two $(SN)_2$ molecules in the triplet state ($5\pi + 5\pi$), and that $(SN)_6$ is derived from $(SN)_4$ and square S_2N_2 in the singlet state ($10\pi + 6\pi$).

Thus from the results of these calculations, the paramagnetism is expected to vanish as the polymerization proceeds, which is in agreement with the experimental results.

Conclusion

We have examined the electronic states of the square S_2N_2 molecule and several deformed $(SN)_2$ molecules, and of $(SN)_4$ and $(SN)_6$ molecules.

In the deformed $(SN)_2$, the triplet biradical nature begins to emerge as one of the S–N bonds opens. The appearance of the triplet state seems to correspond to the interaction of the opened S–N pσ bond with the adjacent S–N p$\bar{\pi}$ bond in the molecular plane.

From a simple estimation of the spin–orbit coupling in the deformed $(SN)_2$ molecules, there appears to be considerable mixing of the singlet state with the triplet state or of the triplet state with the singlet state. The opening of the S–N bond might be expected to occur easily, i.e., thermally, in view of the IR spectroscopic data of the appropriate vibrational modes.

$(SN)_4$ and $(SN)_6$, however, do not show triplet ground states. $(SN)_4$ is believed to result through the dimerization of two $(SN)_2$ biradicals, whereas $(SN)_6$ may be regarded

as being formed by the addition of singlet $(SN)_4$ to singlet S_2N_2. Analogous processes would then lead to higher polymers.

Acknowledgment. We are grateful to the Data Processing Center of Kyoto University for its generous permission to use the FACOM 230-75 Computer. We owe thanks to Professor Alan G. MacDiarmid and to his outstanding co-workers for informing us about their valuable experimental result, and to the former for improving our English before the submission. We are also grateful to Dr. Hideyuki Konishi for his kind help in performing the MO calculations. This work was supported by a Grant-in-Aid for Scientific Research from the Ministry of Education of Japan (No. 065101).

References and Notes

(1) (a) V. V. Walatka, Jr., M. M. Labes, and J. H. Perlstein, *Phys. Rev. Lett.*, **31**, 1139 (1973); (b) C. Hsu and M. M. Labes, *J. Chem. Phys.*, **61**, 4640 (1974).
(2) Some recent references are (a) R. L. Greene, P. M. Grant, and G. B. Street, *Phys. Rev. Lett.*, **34**, 89 (1975); (b) A. A. Bright, M. J. Cohen, A. F. Garito, A. J. Heeger, C. M. Mikulski, P. J. Russo, and A. G. MacDiarmid, *ibid.*, **34**, 206 (1975); (c) R. L. Greene, G. B. Street, and L. J. Suter, *ibid.*, **34**, 577 (1975); (d) W. D. Gill, R. L. Greene, G. B. Street, and W. A. Little, *ibid.*, **35**, 1732 (1975); (e) P. M. Grant, R. L. Greene, and G. B. Street, *ibid.*, **35**, 1743 (1975); (f) L. Ley, *ibid.*, **35**, 1796 (1975); (g) P. Mengel, P. M. Grant, W. E. Rudge, B. H. Schlechtman, and D. W. Rice, *ibid.*, **35**, 1803 (1975); (h) L. Pintschovius, H. P. Geserich, and W. Möller, *Solid State Commun.*, **17**, 477 (1975); (i) C. H. Chen, J. Silcox, A. F. Garito, A. J. Heeger, and A. G. MacDiarmid., *Phys. Rev. Lett.*, **36**, 525 (1976).
(3) (a) D. E. Parry and J. M. Thomas, *J. Phys. C*, **8**, L45 (1975); (b) W. E. Rudge and P. M. Grant, *Phys. Rev. Lett.*, **35**, 1799 (1975); (c) W. I. Friesen, A. J. Berlinsky, B. Bergersen, L. Weiler, and T. M. Rice, *J. Phys. C*, **8**, 3549 (1975); (d) V. T. Rajan and L. M. Falicov, *Phys. Rev.*, **B12**, 1240 (1975); (e) A. Zunger, *J. Chem. Phys.*, **63**, 4854 (1975); (f) H. Kamimura, A. M. Glazer, A. J. Grant, Y. Natsume, M. Schreiber, and A. D. Yoffe, *J. Phys. C*, **9**, 291 (1976); (g) A. A. Bright and P. Soven, *Solid State Commun.*, **18**, 317 (1976).
(4) A. G. MacDiarmid, C. M. Mikulski, P. J. Russo, M. S. Saran, A. F. Garito, and A. J. Heeger, *J. Chem. Soc., Chem. Commun.*, 476 (1975); (b) C. M. Mikulski, P. J. Russo, M. S. Saran, A. G. MacDiarmid, A. F. Garito, and A. J. Heeger, *J. Am. Chem. Soc.*, **97**, 6358 (1975).
(5) R. H. Baughman, R. R. Chance, and M. J. Cohen, *J. Chem. Phys.*, **64**, 1869 (1976).
(6) (a) T. Yonezawa, H. Konishi, and H. Kato, *Bull. Chem. Soc. Jpn.*, **42**, 933 (1969); (b) C. C. J. Roothaan, *Rev. Mod. Phys.*, **23**, 69 (1951); (c) H. Konishi, H. Kato, and T. Yonezawa, *Theor. Chim. Acta (Berl.)*, **19**, 71 (1970); (d) H. Yamabe, H. Kato, and T. Yonezawa, *Bull. Chem. Soc. Jpn.*, **44**, 22 (1971); (e) H. Yamabe, H. Kato, and T. Yonezawa, *ibid.*, **44**, 611 (1971).
(7) The two-center Coulomb repulsion integrals are calculated by the Ohno approximation (K. Ohno, *Theor. Chim. Acta (Berl.)*, **2**, 219 (1964)), and the one-center exchange integrals are evaluated by the Slater–Condon parameters estimated by Hinze and Jaffé (J. Hinze and H. H. Jaffé, *J. Chem. Phys.*, **38**, 1834 (1963)).
(8) 90.42 and 89.58° for the S–N–S and the N–S–N angles, respectively.
(9) 1.651 and 1.657 Å alternatively.
(10) D. R. Salahub and R. P. Messmer, *J. Chem. Phys.*, **64**, 2039 (1976).
(11) D. B. Adams, A. J. Banister, D. T. Clark, and D. Kilcast, *Int. J. Sulfur Chem.*, **1**, 143 (1971).
(12) J. Bragin and M. V. Evans, *J. Chem. Phys.*, **51**, 268 (1969).
(13) For example, see D. S. McClure, *J. Chem. Phys.*, **20**, 682 (1952).
(14) M. Blume and R. E. Watson, *Proc. R. Soc. (London), Ser. A*, **271**, 565 (1963).
(15) For example, see T. Yonezawa, H. Katô, and H. Kato, *Theor. Chim. Acta (Berl.)*, **13**, 125 (1969).
(16) Unpublished observations, A. G. MacDiarmid and M. S. Saran.

The Bursting of Soap Films. 8. Rim Velocity in Radial Bursting

Karol J. Mysels*

General Atomic Company, P.O. Box 81608, San Diego, California 92138

and B. R. Vijayendran

Celanese Research Company, P.O. Box 1001, Summit, New Jersey *(Received September 17, 1976)*

Publication costs assisted by The General Atomic Company

The theory of the propagation of the bursting of a soap film from a linear origin shows that in the absence of surface relaxation the rim velocity cannot exceed the characteristic Culick's velocity of a rim without aureole. Experiments on radial bursting propagating from a point source indicated that higher velocities are observed. Numerical analysis of radial bursting shows that under some conditions Culick's velocity may be indeed exceeded but only by a few percent.

The study of the bursting of soap films can provide valuable information about both the equation of state of adsorbed monolayers at surface pressures and concentrations not otherwise accessible[2,3] and also about the kinetics of desorption on the submillisecond time scale.[4] The value of any interpretation of the experimental results depends, of course, on the accuracy of the experimental measurements and the validity of the theory used in their interpretation. An effort has been made therefore to analyze[5,6] a number of anomalies that have been encountered in these studies, and the present paper is the last in this series.

The theory of unidimensional bursting propagating from a line defect in a uniform sheet can be fully developed under the assumption that the surface tension is only dependent on surface shrinkage, i.e., that desorption is negligible during the short time involved.[8] This assumption is used throughout the present paper and, based on the work of ref 3, is believed to be applicable to most of the experimental studies available. The theory shows that the velocity of the rim of the hole cannot exceed a characteristic velocity u_c called Culick's velocity

$$u_c \equiv (2\sigma_0/\rho\delta_0)^{1/2} \quad (1)$$

where σ is the surface tension, ρ the density, δ the thickness of the film, and the subscript 0 indicates the condition of the undisturbed film. Culick's velocity is obtained when the film beyond the growing hole is completely undisturbed. When, as is in fact always the case, a region of shrinking film, the "aureole", precedes the hole, then it has been shown[8] that rim velocity has to be smaller than u_c.

On the other hand, experimental measurements on two-dimensional, radial bursting originating from a point

defect consistently showed[6,10] that when windage effects, i.e., the slowing down by the drag of the surrounding atmosphere, were eliminated or reduced, the rim velocity was slightly higher than u_c. As reported, the difference was within the limit of experimental errors but the fact that it was observed under very different conditions using two very different techniques made it credible.

The theory of radial bursting cannot be developed analytically to the same extent as that of unidimensional bursting so that no theorem about maximum rim velocity is available in this experimentally interesting case. Thus there is no real contradiction between theory and experiment but rather a disturbing area of ignorance. Numerical exploration of radial bursting seems to be the only way of clarifying this problem and the present paper is devoted to such an approach.

That rim velocity has to be equal to u_c when the aureole is nonexistent is a consequence of conservation of momentum. The existence of the aureole can, however, cause deviations. In the absence of desorption, with surface tension independent of time, there is no natural time constant for the system and velocities of all features, e.g., of any thickness, are constant.[8] It is convenient then to express velocities and positions in terms of Culick's velocity u_c. Thus

$$p = (r/t)/u_c \tag{2}$$

is the reduced velocity and position of a feature located at a radial distance r at time t. The aureole can then be characterized by the reduced thickness, or thickening, $\beta = \delta/\delta_0$, as a function of p. It is said to be self-similar.

Within the visible aureole the velocity of all features must increase with their reduced position. Otherwise the slower feature is overtaken by the faster one and a shock wave, i.e., an abrupt change of thickness, occurs.[8] The details of the thickness change within such a shock wave do not affect the calculations based on momentum changes, as long as the total width over which they take place is smaller than the uncertainty of the position of the shock wave. Furthermore, the same results apply to radial phenomena as long as this width is negligible compared to the radius of the shock. Hence the rim of the hole in radial bursting can be considered as a shock wave and on this basis it can be shown[2] that the limiting thickening $\beta_l = \delta_l/\delta_0$ satisfies the relation

$$\beta_l = 4I_l^2/p_l^2(\sigma_l/\sigma_0) \tag{3}$$

where I is the reduced amount of material per angular unit between the point considered and the center. Thus, I_l is the reduced amount of material in the rim per radian. I is conveniently obtained[8] by difference from the material within the visible film and aureole from a point p_0 in the undisturbed film and the point considered, i.e.

$$I = p_0^2/2 - \int_{p_0}^{p} p\beta \, dp \tag{4}$$

The limiting surface tension can be obtained[8] by integration of the local relation given by applying Newton's second law to a film element:

$$\frac{d\sigma/\sigma_0}{dp} = \frac{2I}{p}\left[1 - \frac{2I}{p^2\beta^2}\left(\beta + p\frac{d\beta}{dp}\right)\right] \tag{5}$$

which is eq 5.22 of ref 8 written in reduced units.

Thus, if the shape of the aureole, i.e., β as a function p, is known, one can calculate the value of σ by obtaining the value of I from eq 4 and the corresponding value of $d\sigma/dp$ from eq 5 at successive points and integrating the latter from p_0 where $\sigma = \sigma_0$ to p. Once the criterion of eq 3 is satisfied, the rim has been reached and thus its velocity obtained.

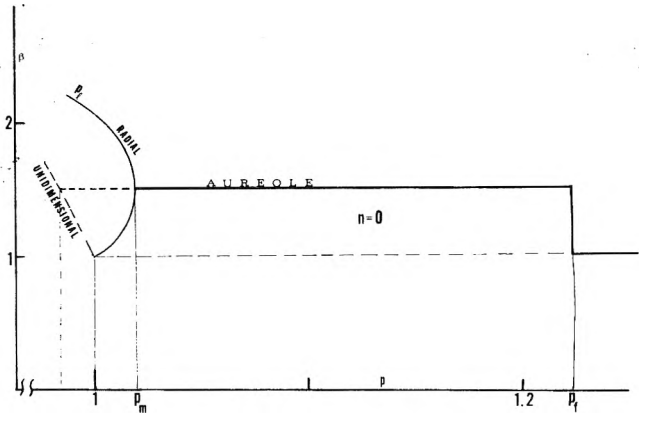

Figure 1. The locus of radial rim velocities for a flat aureole of varying thickness and fixed frontal velocity p_f. The locus reaches its maximum, p_m, for the aureole thickness shown. Dashed lines refer to the unidimensional case in which rim velocity decreases monotonically with thickness.

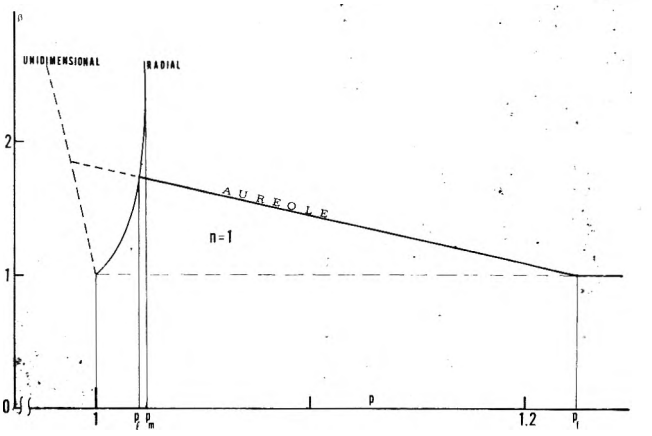

Figure 2. The locus of radial rim velocities for a linear aureole of varying slope and fixed frontal velocity p_f. The rim velocity p_l of the aureole shown is less than the maximum, p_m, of the locus. Dashed lines refer to the comparable unidimensional case.

Such a calculation can be made for experimentally obtained aureole profiles or for theoretical ones. The latter permits the varying of parameters to determine the factors affecting the rim velocity. Most of the results to be reported assumed a monomial aureole, i.e.

$$\beta = 1 + a(p_f - p)^n \tag{6}$$

where p_f is the frontal outer edge of the aureole, a determines its steepness, and n its curvature. The simplest case of a flat aureole (Figure 1) corresponds to $n = 0$. This is also the only one for which the rim velocity could be obtained by solving through successive approximations a closed expression.[11] For higher values of n including the linear aureole (Figure 2) numerical integration of eq 5 was required with step by step testing of eq 3.

The results are summarized in Figures 1–3. In all cases the rim velocity tended, as expected, to u_c as a approached zero, i.e., as the aureole vanished. In addition, the generalization that in the unidimensional case rim velocity cannot exceed u_c was confirmed as shown by the dotted lines in Figures 1 and 2. In the radial case, however, for small values of a, the rim velocity always exceeded u_c. At a certain value of a, a_m, rim velocity was maximum and for higher values of a it decreased. Thus there was a maximum rim velocity p_m for each value of p_f. This maximum depended on p_f, again tending to unity, i.e., to u_c, as p_f approached unity, i.e., as the aureole disappeared.

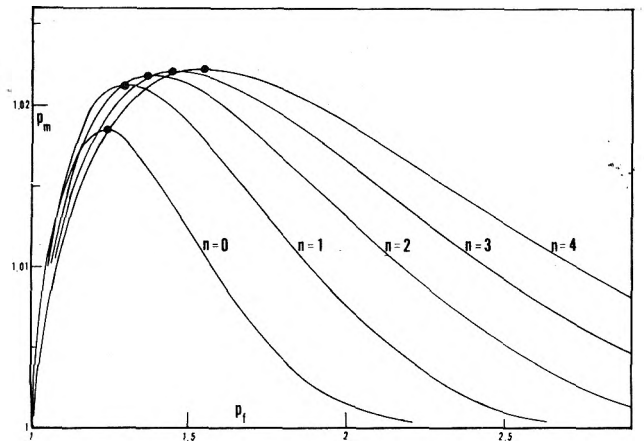

Figure 3. The locus of p_m, the maximum radial rim velocity for a given p_f, as a function of the p_f values for several values of the exponent for monomial aureoles defined by eq 6. The dots indicate the location of the maximum of each line. Note that the ordinate covers only 2.5% and that the maxima increase only slightly between $n = 2$ and 4.

It also tended to unity as p_f became large as shown in Figure 3. Hence, there was a maximum of p_m for every value of n. These maxima increased somewhat as n increased from 0 to 2 but after that the rise was very small. The maximum shifted to higher p_f values as n increased.

Thus, clearly the velocity of the rim of a radial aureole can exceed u_c. The magnitude of the difference is, however, rather small. The largest difference obtained in our calculations was less than 2.5% and from the trend of the values it seems unlikely that any other theoretical shape would give significantly higher ones. Neither the exponential shape nor a number of binomial ones have shown any marked increase. It should be noted that the shape of the aureole is determined by the variation of surface tension with shrinkage of the film as may be seen from eq 5. Hence, a rim velocity approaching the maximum value would require a special shape of the surface tension vs. shrinkage curve to give the necessary shape to the aureole. On a purely statistical basis, most real systems should give values below this.

A previously published experimental aureole, that of solution A, Figure 1 of ref 3, was fitted to the best significant polynomial expression and its rim velocity calculated for a number of assumed p_f values around the experimentally determined one. (The experimental uncertainty is larger in measuring absolute p values needed here than in the relative values involved in determining the aureole shape.) Rim velocities exceeding Culick's value were found with a maximum of $1.021u_c$ at the experimental p_f value of 1.50.

Thus, clearly theory and experiment both show that in radial self-similar bursting the rim velocity can exceed Culick's velocity u_c but only by a small amount. The higher values encountered in the present study are not far from those reported by McEntee and Mysels[10] who found for the thickest films an average excess of about 8% in u^2, i.e., about 2.8% in u over Culick's velocity. On the other hand, it is likely that any larger excesses, such as those seen in Figure 1 of ref 6, are likely to be due to experimental errors.

Acknowledgment. This work was begun and initial results obtained while the authors were members of the Research Department of R. J. Reynolds Industries in Winston-Salem, N.C.

References and Notes

(1) Presented in part before the Division of Colloid and Surface Chemistry at the 161st National Meeting of the American Chemical Society, Los Angeles, Calif., March 1971.
(2) G. Frens, K. J. Mysels, and B. R. Vijayendran, *Spec. Discuss. Faraday Soc.*, **1**, 12 (1970).
(3) B. R. Vijayendran, *J. Phys. Chem.*, **79**, 2501 (1975).
(4) A. T. Florence and G. Frens, *J. Phys. Chem.*, **76**, 3024 (1972).
(5) K. J. Mysels and A. T. Florence, *J. Phys. Chem.*, **78**, 234 (1974).
(6) K. J. Mysels and B. R. Vijayendran, *J. Phys. Chem.*, **77**, 1692 (1973). (For a different point of view, see ref 7.)
(7) G. Frens, *J. Phys. Chem.*, **78**, 1949 (1974).
(8) S. Frankel and K. J. Mysels, *J. Phys. Chem.*, **73**, 3028 (1969).
(9) F. E. C. Culick, *J. Appl. Phys.*, **31**, 1128 (1960).
(10) W. R. McEntee and K. J. Mysels, *J. Phys. Chem.*, **73**, 3018 (1969).
(11) This expression is

$$a^2p^4 + p^2[P(1.5a - 0.5 + a \ln p/p_f) - a] + 0.5P^2 = 0$$

where p represents p_1 and $P \equiv P_0(1 - a)$.

Electrochemistry of Chemisorbed Molecules. 5. Role of Nonaqueous Solvents in Ligand-Bridged Electrochemical Interconversion of Platinum Complexes[1]

Ross F. Lane*† and Arthur T. Hubbard†

Department of Chemistry, University of Hawaii, Honolulu, Hawaii 96822 *(Received August 9, 1976)*

Publication costs assisted by the National Science Foundation and the Petroleum Research Fund

Halide-bridged electrode reactions of complexes of Pt(IV) and Pt(II) proceed with difficulty or not at all in typical nonaqueous solvents. Thin layer voltammetric data are presented which demonstrate that dimethyl sulfoxide, acetonitrile, pyridine, sulfolane, and *p*-dioxane chemisorb irreversibly on Pt electrodes and markedly influence the rates of these reactions when examined in aqueous solutions. The dependence of the kinetics of the electron transfer process on surfactant coverage is shown to be quantitatively attributable to steric hindrance of the approach of the reactant to the electrode surface, and to electrostatic alteration of the (ϕ_2) potential and ionic concentrations at the reaction plane. Predominance of steric hindrance over electrostatic effects at high fractional converages of the organic surfactants accounts for the observed lack of reactivity in the nonaqueous electrolytes. Pretreatment of Pt surfaces with aqueous iodide provides electrodes which prevent adsorption of the organic solvents and allows the reactions to occur, suggesting their use for electrochemical investigations in strongly adsorbing aprotic media for which the influence of the compact region of the electrochemical double layer is pronounced.

Introduction

In a preliminary study[2] an attempt was made to exploit the relative inertness toward electrochemical reduction at platinum electrodes of aprotic solvents such as dimethyl sulfoxide, acetonitrile, propylene carbonate, dioxane, and dimethylformamide[3] for studies of the electrode reactions of platinum complexes.[4-12] For reasons that were not at first apparent the usual halide-assisted electrochemical interconversion of complexes of Pt(II) and Pt(IV) in aqueous electrolytes, eq 1, proceeded with difficulty or not

$$Pt^{II}L_4 + X^- + Y \underset{+e^-,\ fast}{\overset{-e^-,\ slow}{\rightleftharpoons}} [Pt^{III}L_4XY] \underset{+e^-,\ slow}{\overset{-e^-,\ fast}{\rightleftharpoons}} trans\text{-}Pt^{IV}L_4XY \quad (1)$$

($X^- = Cl^-, Br^-, I^-$; $Y = X^-, H_2O$; $L = X^-, Y, NR_3, CN^-, NO_2^-, SCN^-$)

at all in typical nonaqueous electrolytes. This difference in behavior is the subject of the present study.

Results and Discussion

Aqueous Electrolytes at Electrodes Treated with Nonaqueous Solvents. Experiments were carried out to determine the extent to which the electroinactivity of Pt(II) and Pt(IV) complexes in nonaqueous media was due to blocking of the compact layer by adsorbed solvent. Figure 1 shows current–potential curves for Pt electrodes in 1 M $HClO_4$ after rinsing with dilute aqueous solutions of typical nonaqueous solvent materials: acetonitrile, I; dimethyl sulfoxide (Me_2SO), II; sulfolane, III; *p*-dioxane, IV; pyridine, V; dimethylformamide, VI; propylene carbonate, VII; and acetic acid, VIII. The current–potential curve for the acetonitrile-treated Pt surface, Figure 1A, shows the typical features observed with surfactant-coated surfaces:[4] suppression of surface oxidation in the potential range from 0.4 to 0.8 V vs. NaCE, followed by a broad peak stemming from oxidation of the chemisorbed material, and

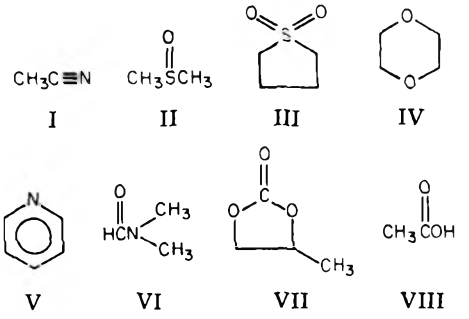

suppression of the small peaks occurring in the solvent reduction region from 0.0 to −0.3 V. Equally pronounced adsorption was observed for Me_2SO, sulfolane, and pyridine, but not for the others. Dimethylformamide decomposes in aqueous solutions to yield dimethylamine and carbon monoxide, eq 2, with the result that electrodes

$$HCN(CH_3)_2 \rightarrow NH(CH_3)_2 + CO \quad (2)$$

treated with its aqueous solutions acquire a layer of chemisorbed CO; accordingly, a peak is observed at 0.4 V vs. NaCE[9,13] for oxidation of adsorbed CO. Chemisorption was not observed for dimethylamine.

Fractional coverage of the surface by Me_2SO, acetonitrile, and pyridine has been determined by means of a procedure described in ref 4, 5, 6, and 9, in which the surfactant-treated surface is exposed to dilute aqueous KI and the density of unoccupied sites calculated from the I-coverage data subsequently obtained by oxidation of adsorbed iodine to dissolved IO_3^-, followed by thin layer coulometric reduction to I_2. The results appear in Table I.

Equations derived and tested as described in ref 4 and 5 are employed to compare the observed change in the electrode rate caused by adsorption of the surface-active solvent material with that calculated from the Gouy–Chapman–Stern theory of the double layer:

† Present address, Department of Chemistry, University of California, Santa Barbara, Calif. 93106.

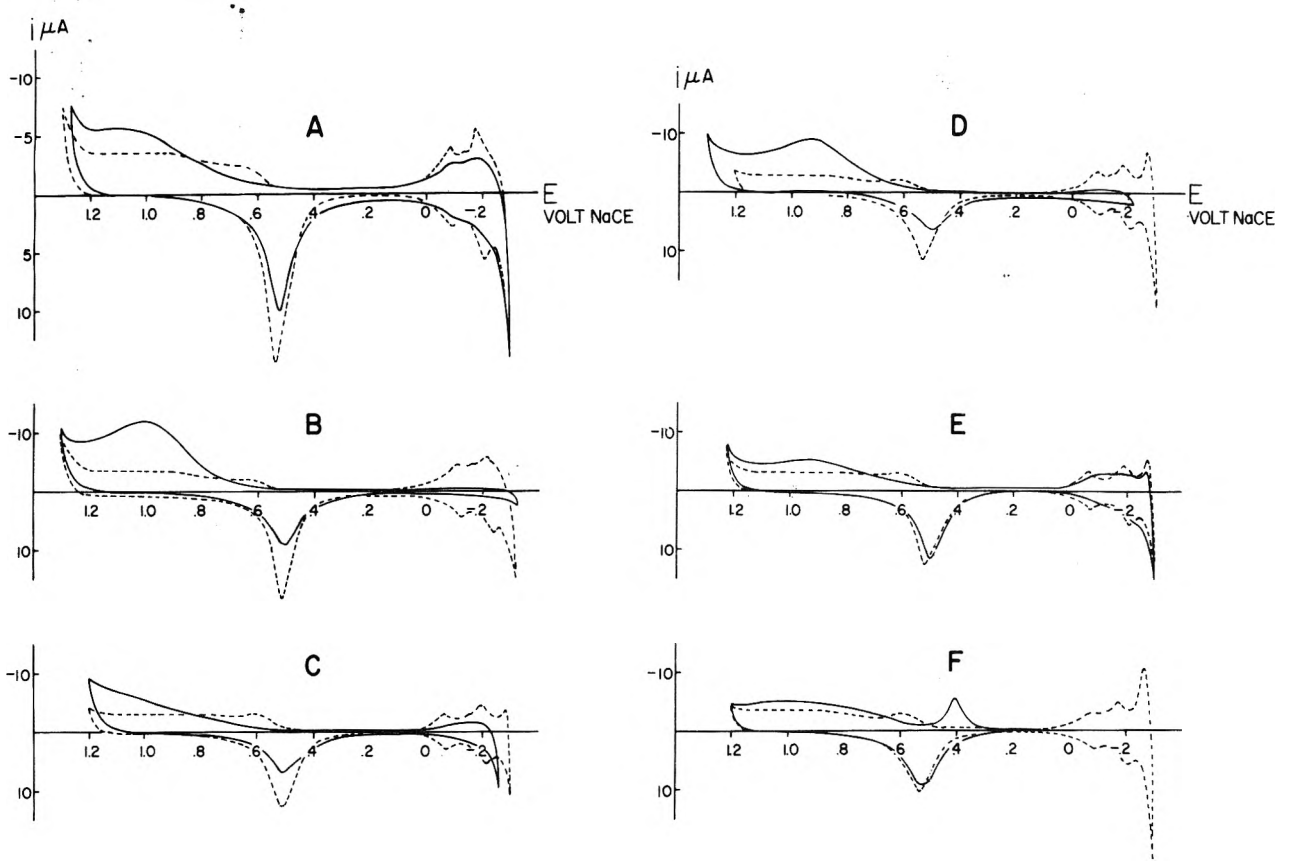

Figure 1. Thin layer current–potential curves for oxidation of chemisorbed nonaqueous solvents at a platinum electrode: (- - -) clean electrodes; (—) electrodes rinsed with aqueous solutions of organic solvents (A) acetonitrile, (B) dimethyl sulfoxide, (C) pyridine, (D) sulfolane, (E) *p*-dioxane, (F) dimethylformamide. The experimental conditions were as follows: The clean electrode was exposed for 3 min at open circuit to 0.1 mM aqueous organic solvent, followed by thorough rinsing with water and with pure supporting electrolyte. The supporting electrolyte was 1 M $HClO_4$. Thin layer volume, $V = 3.88$ μl; platinum electrode area, $A = 1.15$ cm^2; average solution layer thickness, $l = 33.7$ μm; rate of potential sweep, $|r| = 2.00$ mV s^{-1}; solution temperature, $T = 23 \pm 1$ °C.

TABLE I: Thin Layer Current–Potential Data for Complexes of Pt(II) and Pt(IV)[a]

Platinum complexes		Chemisorbed solvent	θ[b]	$_cE_p$, V	$_cE_p(s)$, V	$_ci_p$, μA	$_ci_p(s)$, μA	$_aE_p$, V	$_aE_p(s)$, V	$-_ai_p$, μA	$-_ai_p(s)$, μA
Pt(IV)	Pt(II)										
$Pt(NH_3)_5Cl^{3+}$	$Pt(NH_3)_4^{2+}$[c]	Me_2SO	0.69	0.28	0.14	17.5	16.0	0.48	0.59	17.0	14.0
		Acetonitrile	0.44	0.28	0.22	17.5	16.1	0.48	0.52	17.0	15.4
		Pyridine	0.54	0.28	0.17	17.5	16.2	0.48	0.56	17.0	14.5
$Pt(NH_3)_2(NO_2)_2Cl_2$	$Pt(NH_3)_2(NO_2)_2$	Me_2SO	0.69	0.43	0.38	13.7	13.2	0.66	0.67	14.0	12.9
		Acetonitrile	0.44	0.43	0.40	13.7	13.5	0.66	0.68	14.0	13.0
		Pyridine	0.54	0.43	0.41	13.7	13.3	0.66	0.67	14.0	13.0
$Pt(NO_2)_4Cl_2^{2-}$	$Pt(NO_2)_4^{2-}$[d]	Me_2SO	0.69	0.24	0.34	7.0	7.0	0.86	0.77	11.3	10.0
		Acetonitrile	0.44	0.24	0.30	7.0	6.7	0.86	0.83	11.3	10.3
		Pyridine	0.54	0.24	0.32	7.0	6.8	0.86	0.78	11.3	10.2

[a] Supporting electrolyte, 1 M $HClO_4$ + 10 mM NaCl; other experimental conditions were the same as Figure 1. [b] Values resulting from exposure of clean Pt electrodes to 1 mM aqueous solutions of organic solvents for 3 min. [c] Electrooxidation of $Pt(NH_3)_4^{2+}$ in 10 mM NaCl yields *trans*-$Pt(NH_3)_4Cl_2^{2+}$. [d] Electrooxidation of $Pt(NO_2)_4^{2-}$ in 10 mM NaCl yields *trans*-$Pt(NO_2)_4(H_2O)Cl^-$.

TABLE II: Rate Parameters Derived from Thin Layer Current–Potential Data[a]

Platinum complexes		Chemisorbed solvent	θ	$i_{23}(s)/i_{23}$	$\Delta_R\phi_2$ from eq 4, mV	$i_{43}(s)/i_{43}$	$\Delta_R\phi_2$ from eq 3, mV	$\Delta_R\phi_2$ from eq 5,[b] mV
Pt(IV)	Pt(II)							
$Pt(NH_3)_5Cl^{3+}$	$Pt(NH_3)_4^{2+}$	Me_2SO	0.69	0.87	18	0.007	28	26
		Acetonitrile	0.44	0.60	7	0.078	16	16
		Pyridine	0.54	0.91	13	0.019	26	21
$Pt(NH_3)_2(NO_2)_2Cl_2$	$Pt(NH_3)_2(NO_2)_2$	Me_2SO	0.69	0.28	26	0.20	28	26
		Acetonitrile	0.44	0.45	11	0.32	11	16
		Pyridine	0.54	0.40	19	0.44	29	21
$Pt(NO_2)_4Cl_2^{2-}$	$Pt(NO_2)_4^{2-}$[c]	Me_2SO	0.69	0.022	32	3.56	29	26
		Acetonitrile	0.44	0.12	17	1.74	17	16
		Pyridine	0.54	0.037	31	2.39	24	21

[a] The experimental conditions were the same as employed in Table I. [b] Values of Γ_{Cl^-} were taken from ref 5. [c] Oxidation of the chemisorbed solvents occurred to a certain extent during oxidation of this Pt(II) complex. The values determined for the oxidation reactions are thus less exact than those for the reduction processes.

$$\frac{i_{43}(s)}{i_{43}} = (1-\theta)^m\left[\exp\frac{F}{RT}(a_{43}-Z_4)\Delta_R\phi_2\right] \quad (3)$$

[reduction of Pt(IV)]

$$\frac{i_{23}(s)}{i_{23}} = (1-\theta)^m\ \exp\left\{\frac{F}{RT}[Z_2-(1-a_{23})]\Delta_R\phi_2\right\} \quad (4)$$

[oxidation of PtII)]

$$\Delta_R\phi_2 = \sum_j Z_j F({}_1\Gamma_j(s) - {}_1\Gamma_j)/{}_R C_d \quad (5)$$

where the symbols are as defined in the Appendix at the end of this article. In applying these equations it was assumed that the adsorbed surfactant interfered with adsorption of Cl^-, eq 6. The number of contiguous sites

$${}_1\Gamma_{Cl^-}(s) = (1-\theta)\,{}_1\Gamma_{Cl^-} \quad (6)$$

required by the activated complex, m, was taken to be 2, in line with previous results.[5] Typical thin layer current–potential data for the platinum complexes studied are summarized in Table I. The calculated and observed ratios, $\Delta_R\phi_2$, are given in Table II. The influence of surfactants on the electrode reaction rates is illustrated by the data in Figure 2, which show that the surfactants displace Cl^- which would otherwise have been adsorbed, and thus cause a positive shift in ${}_R\phi_2$, resulting, commonly, in an increase in the reaction rates of anionic complexes and a decrease in rates of cations for typical surfactant coverages. This behavior has been described in greater detail in ref 5, in which the surface active materials were olefins. Comparison of the results of Table II with previous kinetic data[5,9] indicates, as might be expected, that each nonaqueous solvent exhibits a kinetic influence on the electrode reactions characteristic of adsorption from solution in neutral form. Furthermore, the overall constancy of $\Delta_R\phi_2$ values implicates a general invariance in the site of the reaction plane with changes in the nature of the adsorbed materials or Pt complexes, consistent with previous observations.[5]

Since the reaction rates should approach zero as θ approaches unity, eq 3 and 4, it would be expected that very high coverages of surfactant would tend to prevent reaction regardless of the sign of reactant charge. Me_2SO, which adsorbs relatively strongly on clean Pt, shows this behavior, while the other surfactants do not, Figure 3. That the chemisorbed Me_2SO initially occupies all reactive sites at the Pt surface and thus constitutes a monolayer could be seen by exposing Me_2SO-treated surfaces to solutions of other surface active species and noting that the adsorption of these species was prevented. For instance, the adsorption of H is suppressed by the organic coating as is evident from the current–potential curves in Figure 4. Adsorption of iodide[6] is also prevented by similar pretreatment with Me_2SO. As a consequence, Me_2SO can be dismissed as a practical solvent for electrode reactions having surface involvement comparable to that in the reactions of Pt complexes.

Mixed Electrolytes at Electrodes Treated with Aqueous Iodide. It is clear from the foregoing results that the molecular characteristics of the compact region of the electrochemical double layer[14] are of primary importance to the course of Pt electrode reactions. A second aspect of the behavior of Pt complexes in nonaqueous media is the influence of the structure of the reactant in solution on the electrode reaction rate. In addition to solvolysis of the complexes to form new complexes in which the original ligands have been displaced by solvent molecules, a situation which is not of particular interest in the present context, the solvent influences the degree of ionization of

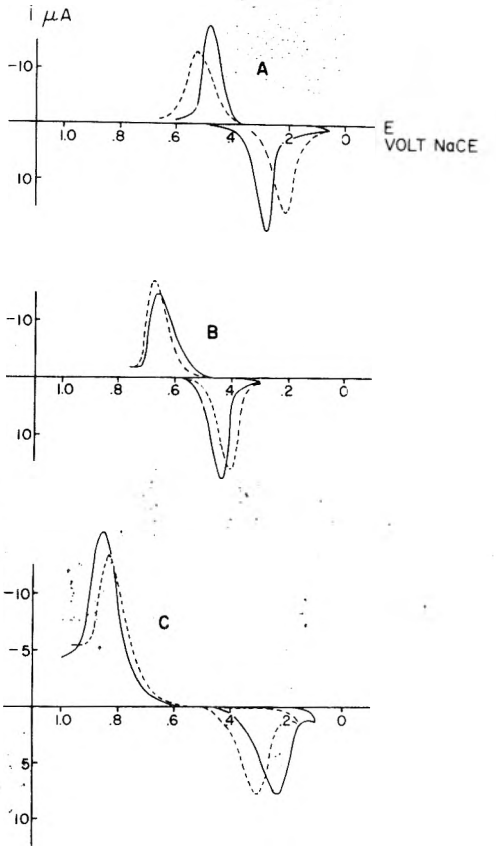

Figure 2. Cyclic thin layer current–potential curves for typical Pt(II) and Pt(IV) complexes at clean and acetonitrile-treated platinum electrodes: (—) clean electrodes; (- - -) electrodes containing chemisorbed CH_3CN. Reactant complexes: (A) $Pt(NH_3)_5Cl^{3+}$ and $Pt(NH_3)_4^{2+}$; (B) $Pt(NH_3)_2(NO_2)_2Cl_2$ and $Pt(NH_3)_2(NO_2)_2$; (C) *trans*-$Pt(NO_2)_4Cl_2^{2-}$ and $Pt(NO_2)_4^{2-}$. Reactant solutions initially contained 1 mM Pt(IV), 10 mM NaCl, and 1 M $HClO_4$. Other experimental conditions were as in Figure 1.

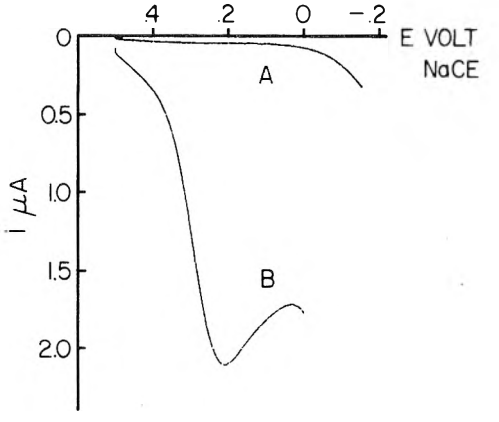

Figure 3. Linear potential sweep current–potential curves for electroreduction of *trans*-$Pt(NO_2)_4Cl_2^{2-}$ at a planar Pt electrode: (A) Me_2SO-coated electrode; (B) clean electrode. Reduction of the anionic complex is accelerated at lower fractional coverage of Me_2SO (see Table II). The experimental conditions were as follows: The reactant solution was 1.2 mM Pt(IV) in 1 M $HClO_4$, 10 mM NaCl. Scan rate = 20 mV s^{-1}. Chemisorption of Me_2SO was effected by exposing the clean electrode to pure Me_2SO for 10 min.

the reactant and supporting electrolyte. In order to separate the effects of changes taking place in the solution from those occurring in the compact layer, experiments were performed in which the Pt surface was treated with aqueous KI prior to use. Further study in nonaqueous solvents with I^--treated Pt surfaces was prompted by previous studies[5,6,9,11,15] in which it was shown that I^- forms

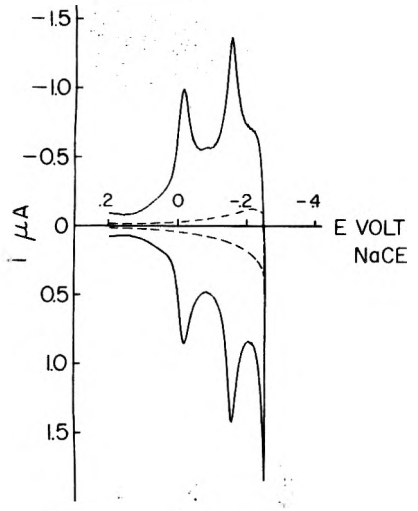

Figure 4. Prevention of H adsorption by chemisorbed Me_2SO: (- - -) clean electrode; (—) Me_2SO-coated electrode. The supporting electrolyte was 0.5 M H_2SO_4. Scan rate = 20 mV s^{-1}. Adsorption of Me_2SO was accomplished as in Figure 3.

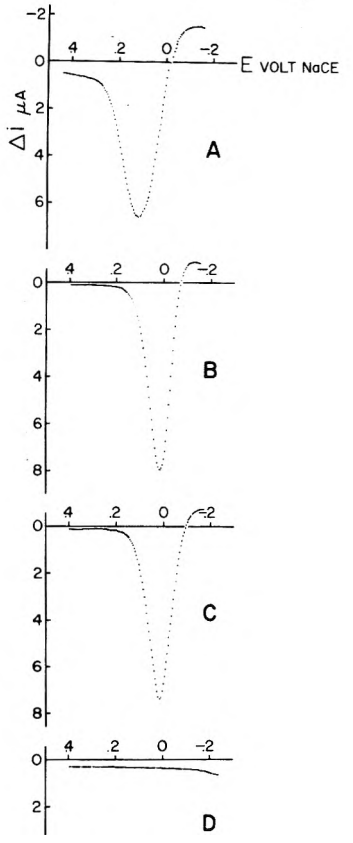

Figure 5. Differential double pulse voltammograms for electroreduction of $Pt(NH_3)_5Cl^{3+}$ at a planar Pt electrode: (A) clean electrode; (B) I^--treated electrode; (C) I^--treated electrode, exposed to neat Me_2SO for 10 min; (D) clean electrode, exposed to neat Me_2SO for 10 min. The experimental conditions were as follows: The reactant solution was 0.8 mM Pt(IV) in 0.5 M LiCl. Pulse amplitude, $\Delta E = -50$ mV; electrolysis time, $\Delta t = 15$ ms; scan rate = 5 mV s^{-1}.

a chemisorbed layer which prevented other species from adsorbing, yet was not, itself, reactive and did not interfere destructively with the electrode reactions. Thus by means of I^--treated Pt it appears possible to vary the composition of the solvent while avoiding appreciable change in compact layer properties.

Figure 5 shows differential double pulse voltammetric (DDPV) curves[15] for the reduction of $Pt(NH_3)_5Cl^{3+}$ in 0.5 M LiCl. Treatment of the Pt electrode with I^- shifts the

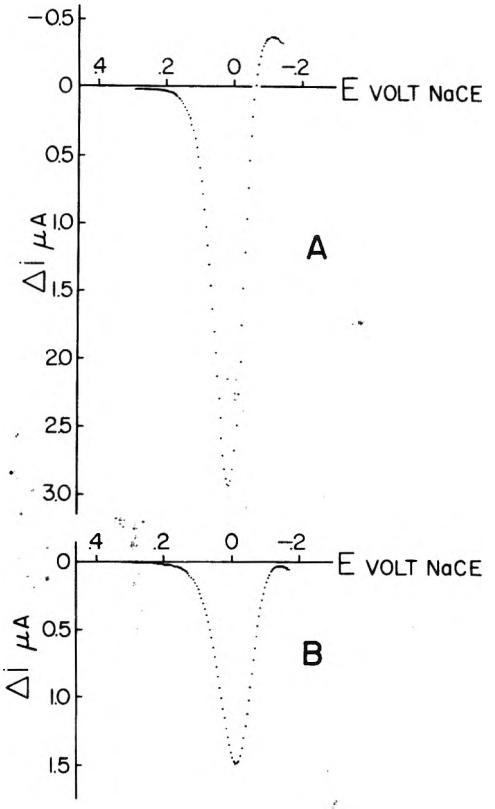

Figure 6. Differential double pulse voltammograms for reduction of $Pt(NH_3)_5Cl^{3+}$, I^--treated Pt electrode: (A) aqueous solution; (B) 70/30 v/v Me_2SO–H_2O mixture. Pt(IV) concentrations were (A) 0.30 mM, (B) 0.12 mM. The supporting electrolyte was 0.5 M LiCl. Other experimental conditions were as in Figure 5.

peak potential (E_p) to more negative values relative to the clean surface (curve B), because of electrostatic effects discussed elsewhere.[5,6,9,11] Of greater significance, however, is the fact that a Pt electrode treated with I^- and subsequently exposed to neat Me_2SO remains reactive toward the Pt complex (curve C) whereas exposure of the untreated electrode to Me_2SO renders it useless (curve D).

The influence of solvent composition on this electrode reaction rate is illustrated by the DDPV current–potential data presented in Figure 6. The observation is that the presence of Me_2SO in solution has little effect on the electron-transfer kinetics; for instance, the peak potentials (proportional to the heterogeneous charge transfer rate constant)[15,16] differ by only 30 mV when the solvent is varied from pure water to the 70/30 v/v Me_2SO–H_2O mixture and peak currents, i_p (normalized to Pt(IV) concentration), are in agreement to within experimental error. The dependence of reactivity on the nature of the solution composition is not nearly as striking as the variation of reactivity when Me_2SO is allowed access to the Pt surface (Table II). Such behavior suggests that the fundamental features of the halide-bridged reaction pathway, eq 1, persist in mixed solvents and that other factors, e.g., differences in solvation and ion pairing, probably are responsible for any reactivity variations. To be sure, solution–structure effects such as ion pairing between the Pt(IV) reactant and chloride ion may influence the observed rate but such effects do not account, of course, for the extreme decrease in rate caused by *chemisorbed* solvent materials.

Addition of Me_2SO to the electrolyte lowers the dielectric constant of the solution, thus influencing the potential, ϕ_2, of the diffuse double layer by altering the ionic strength of the solution. For small ϕ_2 potentials occurring in a large excess of supporting electrolyte:

$$_j\phi_2 \approx C/_jC_d(E - E_z) \quad (7)$$

as discussed in ref 5, 7, and 11. Experiments reported by others[17,18] for a complete range of various water–solvent mixtures indicate that this effect (±5%) is usually less than the experimental error in rate measurements in mixed solvents containing a large excess of supporting electrolyte.

Studies of Pt(II) electrooxidation reactions in Me_2SO–H_2O mixtures yielded results in general accord with those observed for Pt(IV) reduction, provided the Pt surfaces were pretreated with aqueous I^- prior to use.

Thus, modification of Pt surfaces by pretreatment with appropriate chemisorbing materials may be of practical advantage for applications when chemisorbing nonaqueous solvents are to be employed.

Experimental Section

The theory and practice of electrochemistry with thin layer cells has been reviewed recently[19] and equations of linear potential sweep voltammetry with thin layer cells have been presented for typical irreversible systems.[20] Details of electrode rate measurements by these experimental techniques have been described in recent publications dealing with platinum electrode kinetics.[4,5,8,9,11] The thin layer electrode design employed for these studies was described in ref 8.

Owing to the low solubility of the platinum complexes in the nonaqueous solutions, differential double pulse voltammetry[15] was employed for studies in mixed solvent systems. The acquisition of satisfactory current–potential curves in rather high resistance solutions and the enhancement in sensitivity to Faradaic processes by this technique have been discussed previously.[15,21] Construction of the platinum electrodes utilized in these studies, a platinum disk sealed in a borosilicate "soft" glass sleeve, has been described elsewhere.[15,22]

Electrode surface cleanliness is crucial in studies of this kind. Reproducible electrode surface pretreatment was accomplished by heating polycrystalline Pt surfaces to incandescence in an oxidizing gas–oxygen flame, with frequent quenching in 11 M $HClO_4$, immediately prior to use. Cyclic current–potential curves recorded in deaerated 1 M $HClO_4$ or 0.5 M H_2SO_4 from 0.2 to 1.3 to −0.3 and finally to 0.2 V (NaCE) served to complete the surface-cleaning process and to confirm the purity of the surface.[4,5,6,8]

In order to obtain reproducible surface coverage in various trials with the same surfactant, the clean electrode was exposed for exactly 180 s to an excess of a deaerated, freshly prepared solution of the surfactant in pure H_2O. In some cases, noted in the text, clean electrodes were exposed to the pure nonaqueous solvent for a predetermined time. The electrode was then rinsed with H_2O and with supporting electrolyte prior to use.

Reagent grade chemicals were used throughout. Platinum complexes used in this work were taken from samples described in ref 8. Matheson Coleman and Bell spectroquality grade acetonitrile was purified by the technique of Angerstein-Kozlowska et al.[23] Purification of propylene carbonate (Aldrich, 99%) and *p*-dioxane (Matheson Coleman and Bell, reagent grade) was as described by Mann.[24] Dimethylformamide (Mallinckrodt, ACS reagent), pyridine (Matheson Coleman and Bell, ACS reagent), acetic acid (Mallinckrodt, Analytical reagent) and sulfolane (Aldrich, 99+%) were used as received. Matheson Coleman and Bell spectroquality and reagent ACS grades of dimethyl sulfoxide were used interchangeably as received with similar results. All solutions were prepared with pyrolytically distilled H_2O[25] and deaerated with prepurified N_2 prior to and during use.

Operational amplifiers (Teledyne/Philbrick, Model 1026 with BQ-100 booster) were utilized in a conventional electrochemical circuit, designed with emphasis on low noise and high stability. Differential double pulse voltammetric data were obtained by means of a multipurpose electrochemical circuit based upon operational amplifiers and relays have mercury-wetted contacts. Copies of the circuit diagrams are available from the authors upon request. Potentials are reported with respect to a calomel reference electrode prepared with 1 M NaCl, denoted NaCE.

Acknowledgment. Acknowledgment is made to the donors of the Petroleum Research Fund, administered by the American Chemical Society, and to the National Science Foundation for support of this research.

Appendix. Notation

A	Electrode area, cm^2
α_{43}	Charge transfer coefficient of a Pt(IV)|Pt(III) couple (etc.)
C	Differential double layer capacitance, F cm^{-2}
C_d	Differential capacitance assignable to the "diffuse layer", F cm^{-2}
E	Electrode potential, V
$_aE_p$, $_cE_p$	Peak potential of positive or negative-going current–potential curve, respectively
E_z	Potential at which the electrode is uncharged
ΔE	Pulse amplitude, V
F	Faraday constant, C $equiv^{-1}$
$_1\Gamma_j$	Compact layer interfacial excess of ionic species j, mol cm^{-2}
θ	Fractional surface coverage of a surfactant
i	current, A
$_ai_p$, $_ci_p$	Peak current of positive or negative-going current–potential curve, respectively
Δi	Differential double pulse voltammetric current
m	Number of contiguous sites occupied by reactant in transition state
$_j\phi_2$	Potential at the plane of closest approach for species j, V
$\Delta_j\phi_2$	Change in ϕ_2 for species j caused by introduction of surfactant at constant potential
R	Gas constant, J mol^{-1} K^{-1}; as a subscript, R refers to "reactant"
r	Rate of potential scan, dE/dt, V s^{-1}
(s)	Indicates surfactant-coated electrode
T	Temperature, K
Δt	Differential double pulse voltammetric electrolysis time, s
V	Volume of thin layer cavity, cm^3
Z_j	Ionic valence of species j

References and Notes

(1) Articles I–IV in this series are ref 4, 5, 6, and 13.
(2) G. M. Tom and A. T. Hubbard, University of Hawaii, unpublished results.
(3) C. K. Mann and K. K. Barnes, "Electrochemical Reactions in Non-Aqueous Solvents", Marcel Dekker, New York, N.Y., 1970.
(4) R. F. Lane and A. T. Hubbard, *J. Phys. Chem.*, **77**, 1401 (1973).
(5) R. F. Lane and A. T. Hubbard, *J. Phys. Chem.*, **77**, 1411 (1973).
(6) R. F. Lane and A. T. Hubbard, *J. Phys. Chem.*, **79**, 808 (1975).
(7) C. N. Lai and A. T. Hubbard, *Inorg. Chem.*, **13**, 1199 (1974).
(8) C. N. Lai and A. T. Hubbard, *Inorg. Chem.*, **11**, 2081 (1972).
(9) A. L. Y. Lau and A. T. Hubbard, *J. Electroanal. Chem.*, **33**, 77 (1971).
(10) A. L. Y. Lau and A. T. Hubbard, *J. Electroanal. Chem.*, **24**, 237 (1970).
(11) J. R. Cushing and A. T. Hubbard, *J. Electroanal. Chem.*, **23**, 183 (1969).
(12) A. T. Hubbard and F. C. Anson, *Anal. Chem.*, **38**, 1887 (1966).
(13) H. W. Walker and A. T. Hubbard, *J. Phys. Chem.*, to be published.
(14) P. Delahay, "Double Layer and Electrode Kiretics", Interscience, New York, N.Y., 1965.

(15) R. F. Lane and A. T. Hubbard, *Anal. Chem.*, **48**, 1287 (1976).
(16) J. W. Dillard and K. W. Hanck, *Anal. Chem.*, **48**, 218 (1976).
(17) W. Jaenicke and P. H. Schweitzer, *Z. Phys. Chem. (Frankfurt am Main)*, **52**, 104 (1967).
(18) M. H. Miles and H. Gerischer, *J. Electrochem. Soc.*, **118**, 837 (1971).
(19) A. T. Hubbard, *Crit. Rev. Anal. Chem.*, **3**, 201 (1973).
(20) A. T. Hubbard, *J. Electroanal. Chem.*, **22**, 165 (1969).
(21) E. P. Parry and R. A. Osteryoung, *Anal. Chem.*, **37**, 1634 (1965).
(22) R. F. Lane, A. T. Hubbard, K. Fukunaga, and R. J. Blanchard, *Brain Res.*, **114**, 346 (1976).
(23) H. Angerstein-Kozlowska, B. MacDougall, and B. E. Conway, *J. Electroanal. Chem.*, **39**, 287 (1972).
(24) C. K. Mann in "Electroanalytical Chemistry", Vol. 3, A. J. Bard, Ed., Marcel Dekker, New York, N.Y., 1969.
(25) B. E. Conway, H. Angerstein-Kozlowska, W. B. A. Sharp, and E. E. Criddle, *Anal. Chem.*, **45**, 1331 (1973).

Adsorption of Argon on Sintered Tin Dioxide Analyzed by Several Methods

David C. Hinman and G. D. Halsey*

Department of Chemistry, University of Washington, Seattle, Washington 98195 *(Received November 8, 1976)*

Publication costs assisted by the National Aeronautics and Space Administration

Argon adsorption measurements are presented over a wide range of temperature and coverage on a series of three progressively sintered SnO_2 surfaces. These data are analyzed by mercury porosimetry, the BET method, the CAEDMON distribution analysis, and the Singleton–Halsey equation. Isosteric heats are computed, and the high-temperature virial expansion of the data presented. The advantages and disadvantages of each method are discussed with particular attention to the ability of physical adsorption to discriminate among surfaces beyond the measurement of surface area.

Introduction

Aside from intrinsic interest in the process of adsorption itself, physical adsorption has been used to investigate the exposed surfaces of solids for many years. The estimation of surface area and the analysis of pore-size distributions have become routine and important measurements. On specially selected or prepared surfaces, notably that of graphite, many other aspects of physical adsorption have been clarified, and other techniques of measurement suggested. It is the purpose here to explore and compare some of these other measurements on surfaces more typical of those usually encountered. We have studied the adsorption of argon on three progressively sintered tin oxide samples that have already been partially characterized by other measurements. These samples show varying degrees of heterogeneiety.

On surfaces which by reason of intrinsic structure or impurity are not homogeneous and uniform (homotattic) with respect to the adsorbed gas, adsorption measurements are qualitatively different from results on substances such as graphite. In particular, formation of regular layers of adsorbate is impeded, and the nature of the transition to bulk adsorbed phase is not clear.[1] It is the purpose of this paper to compare the effectiveness of various methods of measuring and presenting physical adsorption data over a relatively wide range of temperature and coverage.

Experimental Section

Materials and Method. The SnO_2 samples, which were obtained from Professor O. J. Whittemore, Jr., of the University of Washington, were prepared by mixing reagent-grade SnO_2 with a 50% (w/w) aqueous polyethylene glycol wax solution to about 30% wax. The samples were dried, pressed into pellets at 20 kpsi, heated at 450 °C to remove the wax, and sintered at a range of temperatures for 1 h. The wax was completely volatilized. The three samples used in this study, part of a program of interdisciplinary research in ceramic materials, were sintered at 600, 1000, and 1100 °C, and referred to as $SnO_2(600)$, $SnO_2(1000)$, and $SnO_2(1100)$. That the samples differ markedly in gross structure may be seen in Table I, which shows the results of a pore-size analysis by mercury porosimetry, supplied by Professor Whittemore.

TABLE I: Mercury Porosimetry Measurements

Sample	Pore volume, cm^3/g	Mid pore size, μm	90% pore size, μm	Area, m^2/g
$SnO_2(600)$	0.118	0.0636	0.0365–0.0871	7.75
$SnO_2(1000)$	0.118	0.0911	0.0700–0.108	5.35
$SnO_2(1100)$	0.120	0.121	0.0946–0.141	4.00

TABLE II: BET Analysis for SnO_2

Gas	T, K	c	V_m, $cm^3(STP)\ g^{-1}$	Molecular area, $Å^2$	A, $m^2\ g^{-1}$
			$SnO_2(600)$		
N_2	79.04	136	1.732	16.2	7.53
Ar	79.05	206	1.575	12.8	5.41
			$SnO_2(1000)$		
Ar	79.08	218	1.021	12.8	3.51
			$SnO_2(1100)$		
N_2	79.05	134	0.8257	16.2	3.59
Ar	79.05	207	0.7462	12.8	2.57

The neon, argon, and nitrogen used were supplied in glass flasks by Airco, with a stated purity of 99.998%.

Adsorption measurements were made in a high-precision volumetric adsorption apparatus suitable for measuring small adsorptions at high temperatures. The apparatus and procedure are described elsewhere.[1,2] The high-temperature adsorption measurements were made on samples of about 10 g each. Measurements were made on the same samples in the liquid nitrogen range, with the exception of the $SnO_2(1000)$ sample, for which a sample

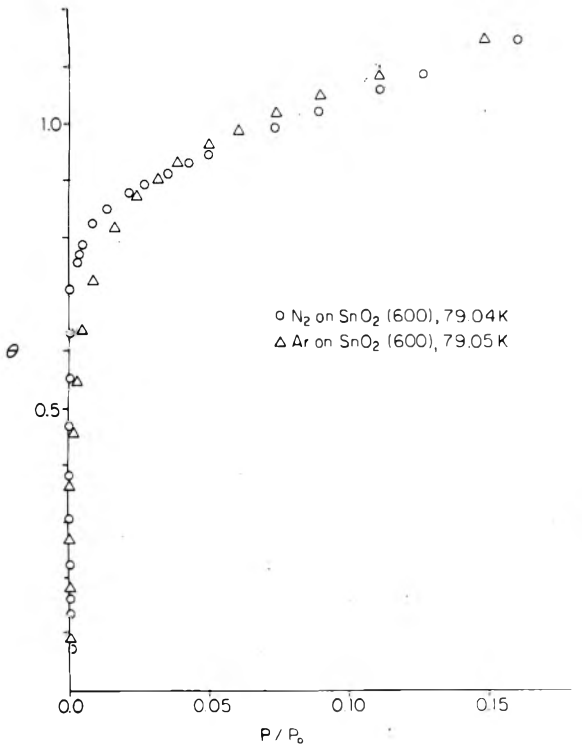

Figure 1. 79 K nitrogen and argon isotherms showing c values.

of about 7 g was substituted. The samples were encapsulated in Pyrex bulbs, treated with oxygen evaporated from the liquid for 2 h at 400 °C, then evacuated at that temperature to a residual pressure of less than 10^{-2} Torr. Dead-space measurements were made with neon.

BET Analysis

Argon isotherms were determined at 79 and 100 K for each sample, and nitrogen isotherms were determined at 79 K for the 600 and 1100 materials. BET analyses of the lower temperature data are shown in Table II. The c values and areas shown there were determined from BET plots in the relative pressure range 0.03–0.30. The plots were nonlinear below this range of pressures; in all cases the nitrogen isotherms lie closer to the axis than the argon isotherms in the first layer. In both cases where the comparison can be made, the monolayer volume for argon is about 10% less than for nitrogen, which combined with a smaller molecular area for argon yields a lower value for the determined surface area.

The much larger c values for argon are worthy of comment. Nitrogen, as is usually the case, is much more strongly adsorbed at low partial pressures. In the region below relative pressure 0.03, many BET slopes could be selected, but visual estimates of "point B" agree with the results obtained from the linear plots over the range mentioned above. When plotted as a function of θ and P/P_0, the experimental isotherms cross (Figure 1) and the result is the anomalous c values reported. Thus, the effective c value relates to isotherm behavior early in the second layer, and not to the initial behavior of the adsorption isotherm, as a naive examination of the BET equation theory would suggest.

Pore Volume Analysis

The relatively large pores revealed by mercury porosimetry (Table I) would allow the formation of at least 10 layers of adsorbed argon before capillary condensation would become possible. However, smaller pores not accessible to this technique can result in hysteresis in the

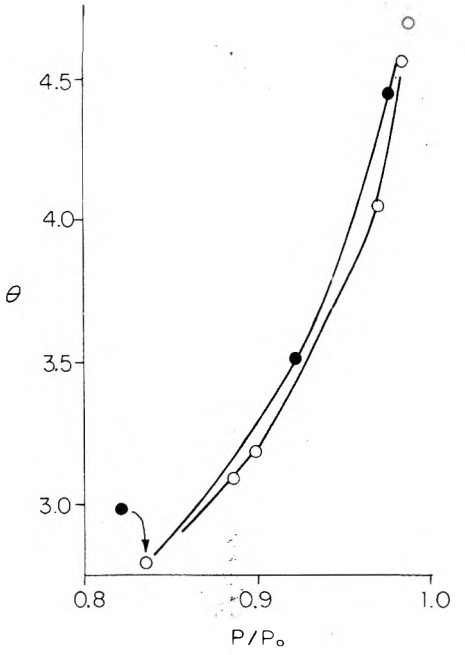

Figure 2. Hysteresis curve for Ar on SnO_2(600), 79 K. Solid points are desorption.

isotherms. Hysteresis loops appear in the Ar isotherms at 79 K on both SnO_2(600) and SnO_2(1100). No data were taken with descending pressure on the SnO_2(1000) sample. The loop in the SnO_2(600) isotherm closes at $P/P_0 \simeq 0.82$ (Figure 2), and the smaller loop in the SnO_2(1100) isotherm closes near to $P/P_0 = 0.90$. The effect was not large enough to allow a conventional pore-volume analysis, and in any other analysis of data in this region, the ascending branch of the isotherm was used.

The hysteresis qualitatively indicates, however, that for SnO_2(600) approximately 1% of the available surface is situated in small pores of the order of 100 Å radius, while the rest is in large pores revealed by mercury porosimetry. In the range measurable by adsorption, there is less pore volume in the SnO_2(1100) sample, and the pores are of larger size.

Isosteric Heats

The assembled argon data on the three adsorbents were used to obtain the isosteric heats, defined by the conventional formula

$$[\mathrm{d} \ln P/\mathrm{d}(1/RT)]_{\text{const } n_{\text{ads}}} = -q$$

At higher coverages, only the two Ar isotherms at 79 and 100 K were available; at the lowest coverages appropriate high temperature isotherms were used, and an extrapolation to zero coverage made. At intermediate coverages, various sets of data overlapped. The conflicting results in these intermediate ranges indicated that a ΔC_P correction or evaluation was not warranted, since the conflicts were of the order $R\Delta T$ between the high and low results. An absolute accuracy of ±50 deg or 100 cal is indicated.

The isosteric heats calculated for all three materials show a very rapid rise immediately from the zero-coverage intercept, followed by a monotonic decline through the first layer (Figures 3–5). In all three cases, the curves become less steep near $\theta = 0.2$, and more steep again near $\theta = 0.7$. For $\theta < 0.02$, the rise may be due to the presence of a number of sites of energy significantly higher than the remainder of the surface which are organized into patches large enough for positive cooperation to take place to an extent noticeable in the isosteric heat curves. If these sites

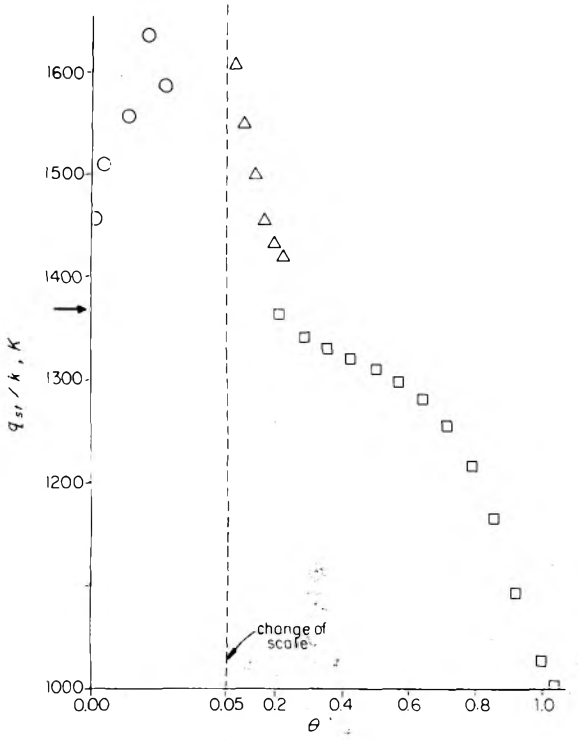

Figure 3. Isosteric heat vs. coverage for SnO_2(600). Arrow indicates zero-coverage intercept from extrapolation of high-temperature data. (O) indicates values derived from pairs of high-temperature isotherms. (△) indicates values from a Clausius–Clapeyron plot of high-temperature data. (□) indicates values from the two lowest temperature isotherms.

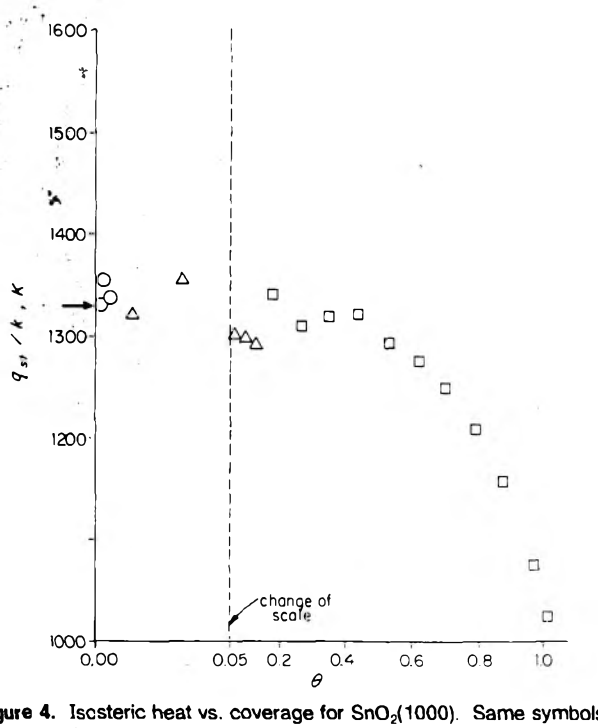

Figure 4. Isosteric heat vs. coverage for SnO_2(1000). Same symbols as Figure 3.

are nearly filled before adsorption commences on the rest of the surface, they will contribute to the isosteric heat curve a portion which reproduces the features observed in adsorption on a uniform surface with mobile adsorption,[3] compressed into a smaller coverage range according to their fraction on the surface.

It is also possible that a similar phenomenon takes place in the $0.2 < \theta < 0.7$ coverage region, although here adsorption is taking place on sites which are distributed over a range of energies, with the decline in the zero-coverage

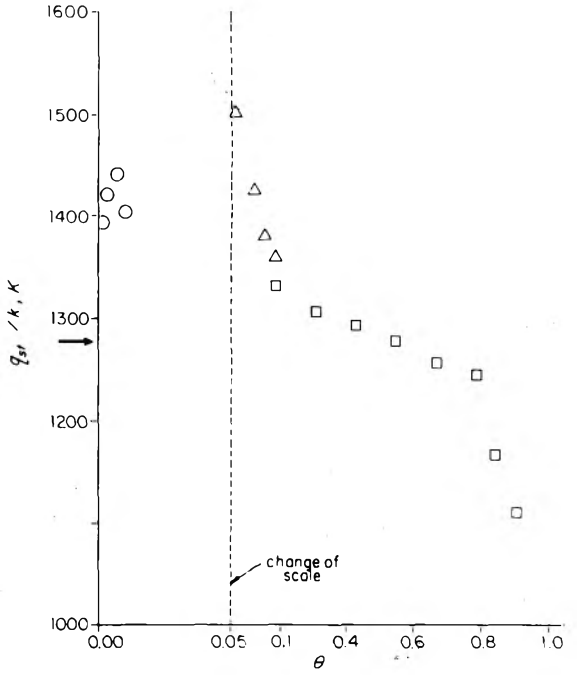

Figure 5. Isosteric heat vs. coverage for SnO_2(1100). Same symbols as Figure 3.

heat of adsorption overwhelming the cooperative effect.

Analysis by CAEDMON

The 79 and 100 K isotherms were analyzed by the CAEDMON model developed by Ross and Morrison.[4,5] In this analysis, the surface is divided up into a number of patches suitable for describing the distribution (20 in this case) which are energetically homogeneous and structureless. Each patch is characterized by an adsorption equilibrium constant, K, and the coverage determined from the patch isotherm at each of the pressure values of the data submitted for analysis. The two-dimensional virial equation of state is assumed to apply on the patches, with the adsorption isotherm derived from it by means of the Gibbs adsorption equation. The steric (area per molecule) and interaction energy parameters are taken from the bulk phase, and used to calculate the first two two-dimensional virial coefficients. Values for higher two-dimensional virial coefficients used were those calculated for a hard disk gas.

In the program, the range of values of $-RT \ln K$ (in kilocalories) is assigned from the data, and intermediate values are set at equal distance on an energy scale. The sum of squares of relative deviations of the calculated adsorption from the data points is minimized by adjusting the relative patch areas, f_A. We have used a modified version of the CAEDMON program which produces values of f_A normalized to unity. As a check, the data of Ross and Pultz[6] were analyzed by the modified program. The results were in substantial agreement with the distribution presented by Ross and Morrison.

Results from the fits of all three kinds of sample are quite similar, with a large peak near the high-energy end of the distribution and a relatively symmetrical bell-shaped peak centered 0.6 to 0.7 units of $RT \ln K$ lower (Figures 6 and 7). Each set of data also shows a final peak at lower energy still. Surface areas calculated from this analysis are shown in Table III. The argon areas are in constant ratio with the Ar BET areas for these samples, and are uniformly about 50% higher. The ratios of the N_2 areas to the corresponding N_2 BET areas agree much less well. Table III also presents values of $-RT \ln K'$, which contains the value of K at the maximum value of the central part

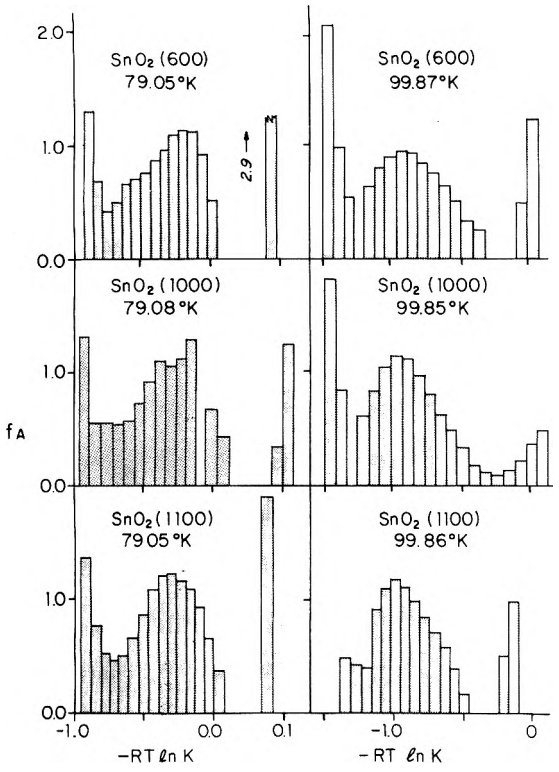

Figure 6. f_A vs. $-RT \ln K$ for Ar on SnO_2 from CAEDMON analysis.

TABLE III: CAEDMON Analysis

Sample	Adsorbate	T, K	CAEDMON area, $m^2\ g^{-1}$	$-RT \ln K'$,[a] kcal mol^{-1}
SnO_2(600)	Ar	79.05	7.93	−0.19
		99.87	8.76	−0.90
	N_2	79.04	13.67	−0.15
SnO_2(1000)	Ar	79.08	5.32	−0.95
		99.85	5.55	−0.95
SnO_2(1100)	Ar	79.05	3.90	−0.30
		99.86	4.18	−0.98
	N_2	79.05	8.26	−0.26

[a] $-RT \ln K'$ taken at maximum value of central part of distribution.

of the distribution function, and is thus a measure of the mean binding strength. There is in general a drift to slightly larger values of this parameter as the temperature of sintering increases.

Characteristics of CAEDMON

Since each CAEDMON distribution calculated here consists of a 20 point representation of a single low-temperature isotherm it will be unable to deal with whatever is absent from the source. In particular, in almost all isotherms of the "type II" form, the low coverage data (below $\theta \approx {}^1/_2$) will be up against the zero pressure axis and represented by a single point that defines an initial slope. If the isotherm is indeed not into a Henry's law region this point will define an arbitrary slope that will in turn give a "low coverage" peak at the lowest CAEDMON patch. This phenomenon is evident from the figures, and depends on the choice of data points.

At the other end of the isotherm, the second layer becomes a problem, and since the CAEDMON program is a first-layer-only analysis, arbitrary effects on the distribution will be introduced by the "cutoff" selected from the data. In turn, this choice produces a possibly spurious peak at the high-energy end of the distribution.

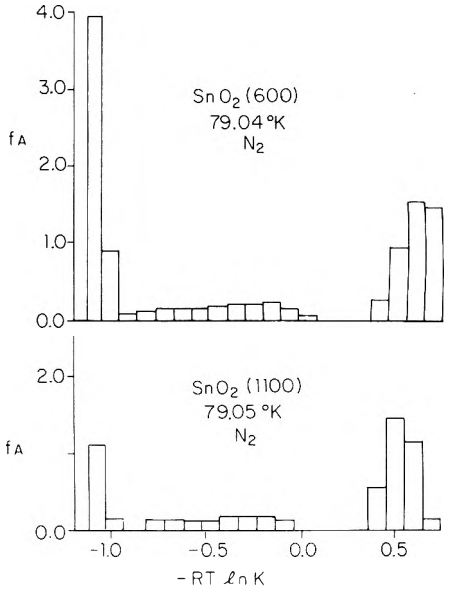

Figure 7. f_A vs. $-RT \ln K$ for N_2 on SnO_2 from CAEDMON analysis.

It is likely that the high values of the surface area calculated from these data result from the cutoff location.

The CAEDMON distributions for nitrogen show exaggerated peaks at the high-energy end when compared with argon, and a substantial peak at the low-energy end as well. Ignoring the low-energy peak as possibly due to the beginning of a second layer, the high-energy peak illustrates a strikingly different energy distribution for N_2 as determined by this method. That this large difference may be expected is apparent on consideration of Figure 1, which shows a much different behavior of N_2 in the first layer.

Furthermore, the theory is deficient for analysis of surfaces of this type in its assumptions. In the absence of chemical impurities, the changes in the potential at the surface are due to differences in surface geometry, either through densification of the surface atoms, or through changes in potential barriers across the surface. Calculations of $B_2^{(2D)}$, the second gas–solid virial coefficient, for various crystal lattices,[7] show these effects. The CAEDMON analysis uses values of $B_2^{(2D)}$ derived from unperturbed gas-phase values of the potential parameters, and cannot explicitly contain this type of geometrical information. For the SnO_2 surfaces studied here, measurements of the composite values of $B_2^{(2D)}$ show a qualitative difference between SnO_2(600) on the one hand, and the 1000 and 1100 samples on the other (see Table VII), for surfaces with nearly identical CAEDMON results.

CAEDMON Temperature Dependence

As an isothermal theory, CAEDMON produces a distribution in $-RT \ln K$, or essentially free energy. With distributions available at two temperatures, it should be possible with data of sufficient accuracy to produce a single distribution in U_0 for adsorption from the Gibbs–Helmholtz equation.

This can be done very simply for the most-numerous sites in the central peak if we assume that the simple form with constant coefficients

$$K = A \exp[-U_0/RT]$$

applies to the equilibrium constant. For all three of the samples studied the change in $(RT \ln K)_{max}$ on going from 79 to 100 K corresponds to an energy U_0/k equal to about 1550 ± 100 K. Data at more widely spaced temperatures might warrant more detailed analysis.

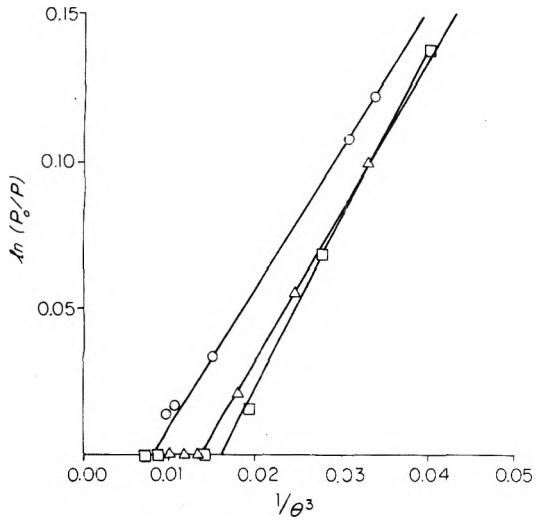

Figure 8. High-coverage limit of 79 K Ar data on SnO_2: (O) SnO_2(600); (Δ) SnO_2(1000); (□) SnO_2(1100).

TABLE IV: High-Coverage Analysis

Sample	E_1/k, K	θ_{max}
SnO_2(600)	365	5.20
SnO_2(1000)	401	4.19
SnO_2(1100)	461	3.96

It should be emphasized that this result, or the results of a more elaborate treatment of the same type, has no direct relation to the isosteric heat derived at the same coverage. The former are energy parameters in a statistical-mechanical model, and the latter the result of a differentiation of a thermally averaged enthalpy function, with no reference to individual sites or other model. With that said, U_0/k seems somewhat larger than would be suggested by a naive comparison with the isosteric heat curves.

High Relative Pressure Data

The high relative pressure ends of the lowest temperature Ar isotherms, $0.8 < \theta < 1.0$, diverge significantly from each other. This divergence may be analyzed on the basis of the equation of Singleton and Halsey[8] which is based on the slab model for adsorption, modified to take account of the incompatibility between the bulk lattices of the adsorbent and adsorbate. The isotherm at high coverages is given by the equation

$$RT \ln (P/P_0) \simeq -E_1/\theta^3 + w(1 - g)$$

The first term on the right represents the decay of adsorption energy with the number of layers adsorbed. The parameter E_1 is nominally the energy of adsorption in the first layer, but more properly is the long-range or inverse-cube component of that energy. The second term measures the lattice incompatibility in terms of the lateral interaction energy parameter w and the compatibility g. If the latter is unity, adsorption proceeds indefinitely, as saturation is approached.

If g is less than unity, the adsorption proceeds to a finite limit, θ_{max}. An upper adsorption limit is characteristic of many isotherms. Further condensation at saturation is into bulk crystals apart from (not wetting) the surface.[8] The data were analyzed according to this model by plotting $\ln (P_0/P)$ against $1/\theta^3$ for small values of the abscissa. These plots are shown in Figure 8, with the results of a least-squares analysis in Table IV.

All three isotherms show a finite upper limit for adsorption. The SnO_2 limit is significantly different from the samples sintered at higher temperature. As sintering progresses, the adsorbed layers appear to become less compatible with the underlying surface, and the long-range component of the adsorption energy becomes larger. The latter observation suggests that the surface region is less dense in the less sintered material. The effect of smaller pore size would operate in the opposite direction.[5]

TABLE V: B_{2s} and B_{3s} for Ar on SnO_2

T, K	B_{2s}, cm³	$s_{B_{2s}}$, cm³	$-B_{3s}$, cm⁶ mol⁻¹	$s_{B_{3s}}$, cm⁶ mol⁻¹
		SnO_2(600)		
152.10	1.2195	0.0109	64900	2800
166.13	0.5913	0.0026	22800	800
182.77	0.2703	0.0006	4640	160
201.22	0.1363	0.0005	1300	100
224.60	0.0696	0.0003	340	50
257.17	0.0334	0.0004		
300.35	0.0184	0.0003		
		SnO_2(1000)		
151.97	0.2649	0.0006	5500	140
166.06	0.1350	0.0004	1300	70
182.65	0.0705	0.0001	230	14
201.92	0.0402	0.0002	110	25
224.44	0.0221	0.0003		
256.84	0.0122	0.0004		
308.74	0.0056	0.0002		
		SnO_2(1100)		
151.97	0.3664	0.0013	12600	340
166.05	0.1754	0.0003	3040	66
182.61	0.0870	0.0002	652	31
202.01	0.0456	0.0001	201	21
224.38	0.0244	0.0004		
257.11	0.0123	0.0003		
300.26	0.0065	0.0002		

High-Temperature Data

Argon isotherms were measured at nine temperatures between 130 and 300 K. Only the seven highest temperature isotherms for each sample had clearly defined linear regions near the origins of their excess volume plots, and only these were used for extracting values of the first two gas–solid virial coefficients as described by Freeman.[10] Values of these coefficients, the first two in the equation

$$n_{ads} = B_{2s}(P/RT) + B_{3s}(P/RT)^2 + B_{4s}(P/RT)^3 + \ldots$$

are listed in Table V, along with their standard deviations (s) calculated from least-squares fits.

Values for the second gas–solid virial coefficient, B_{2s}, were fitted to an inverse-cube attractive potential model for a uniform structureless solid as a first approximation,[11] with an inverse ninth-power and a hard-sphere repulsion. These surfaces are very likely heterogeneous; the high-temperature models used for analysis of the heterogeneity were those of Pierotti and Thomas,[12] which contain a Gaussian distribution for the site energies with standard deviation U, and the dual attractive power model of the present authors.[1] The latter models seek to extract a correct value of the limiting long-range energy for calculating the surface area. The results are summarized in Table VI.

Raw two-dimensional second virial coefficients were calculated from B_{2s} and B_{3s} according to the formula[13] (Table VII)

$$B_2^{(2D)}/A = -B_{3s}/2B_{2s}^2$$

These coefficients were used to calculate lateral interaction energies (ϵ'), steric parameters (σ), and the surface area

TABLE VI: Parameters from Least-Squares Fits of B_{2s} vs. $1/T$

Model	E^*/k, K	$10^3 Az_0$, cm³	α or U	$\sigma(\ln Az_0)$	A, m² g⁻¹	z_0, Å	z^*, Å
			SnO_2(600)				
Unif, +3-inf	1585	0.981		0.0314	4.00	2.45	
Unif, +3-9	1450	0.418		0.0467	2.28	1.84	2.21
+3-inf-gauss.	1498	1.112	150 K	0.0298	4.46	2.50	
+3-9-gauss.	1087	0.839	300 K	0.0349	4.15	2.02	2.43
+3+4-inf	1585	0.981	0	0.0314	4.00	2.45	
+3+6-inf	1000	1.305	0.589	0.0306	4.57	2.86	
+3+8-inf	900	1.558	0.775	0.0294	5.27	2.96	
			SnO_2(1000)				
Unif, +3-inf	1426	0.531		0.0338	2.09	2.54	
Unif, +3-9	1286	0.248		0.0178	1.30	1.91	2.29
+3-inf-gauss.	1426	0.531	0	0.0338	2.09	2.54	
+3-9-gauss.	1286	0.248	0	0.0178	1.30	1.91	2.29
			SnO_2(1100)				
Unif, +3-inf	1518	0.426		0.0044	1.72	2.48	
Unif, +3-9	1382	0.188		0.0181	1.01	1.86	2.23
+3-inf-gauss.	1518	0.426	0	0.0044	1.72	2.48	
+3-9-gauss.	1222	0.256	200 K	0.0094	1.32	1.94	2.33
+3+4-inf	1518	0.426	0	0.0044	1.72	2.48	
+3+6-inf	1600	0.409	−0.052	0.0040	1.68	2.44	
+3+8-inf	1750	0.366	−0.142	0.0031	1.54	2.37	

Constants Used in Kirkwood-Müller Formula

	SnO_2	Ar
Polarizability, cm³ × 10^{24}	4.43[a]	1.63[b]
Magnetic susceptibility,[c] × 10^{29}	6.81[c]	3.24[d]

[a] "Handbook of Chemistry and Physics", 49th ed, Weast, Ed., Chemical Rubber Company, Cleveland, Ohio, 1968. [b] H. Margenau, *J. Chem. Phys.*, 6, 896 (1938). [c] Magnetic susceptibility determined by Mr. E. R. Byrd, University of Washington. [d] K. E. Mann, *Z. Phys.*, 98, 548 (1936).

TABLE VII: Lateral Interaction Parameters for Ar on SnO_2

T, K	$10^{-4}B_2^{(2D)}/A$ uniform	$10^{-4}B_2^{(2D)}/A$ gauss.-patch	$10^{-4}B_2^{(2D)}/A$ gauss.-random	$B_2^{(2D)}/\sigma^2$ gauss.-patch	$B_2^{(2D)}/\sigma^2$ gauss.-random
		SnO_2(600)			
152.10	2.18	0.824	2.18	0.225	0.469
166.13	3.26	1.44	3.26	0.394	0.701
182.77	3.18	1.62	3.18	0.443	0.684
201.22	3.50	2.01	3.50	0.550	0.753
224.60	3.51	2.25	3.51	0.615	0.775
		SnO_2(1000)			
151.97	3.92	3.92	3.92		
166.06	3.57	3.57	3.57		
182.65	2.31	2.31	2.31		
201.92	3.40	3.40	3.40		
		SnO_2(1100)			
151.97	4.69	4.69	4.69		
166.05	4.94	4.94	4.94		
182.61	4.31	4.31	4.31		
202.01	4.83	4.83	4.83		

Model	ϵ'/k, K	σ, Å	A, m² g⁻¹	
Gauss.-patch	83	3.51	2.03	SnO_2(600)
Gauss.-random	64	3.58	1.66	
Hard sphere	$0 < \epsilon'/k < 25$	3.40	3.31	SnO_2(1000)
Hard sphere	$0 < \epsilon'/k < 25$	3.40	2.33	SnO_2(1100)

(A) according to the model for a uniform surface due to Barker and Everett.[13] Pierotti and Thomas[12] have used the Gaussian model for B_{2s} described above and the two calculable limiting cases of random and patchwise site–pair distributions on a heterogeneous surface to calculate from the raw coefficients values of $B_2^{(2D)}$ suitable for these surfaces. The values of $B_2^{(2D)}/A$ for SnO_2(1000) and SnO_2(1100) are virtually constant over the temperature range studied, and will not fit these models. Values for these coefficients and the parameters derived from them are shown in Table VII. Parameters for the fit for SnO_2(600) are taken from the +3-inf-Gaussian model in Table VI. In the case of the other two samples, $B_2^{(2D)}/A$ varies so little with temperature that all that can be said is that the points represented are far out on the repulsive limb of the virial coefficient where $B_2^{(2D)}$ does not vary significantly with temperature. Here we can place only an upper limit on ϵ'/k. We have been forced to use a hard-sphere $B_2^{(2D)}$ and the uncorrected bulk steric factor to calculate an area.

Comparison of Results

The isosteric heats show the most structure and, viewed uncritically, characterize any surface uniquely. Given, however, the large experimental uncertainty, evident in our data by the misfit between several sets of data, most

of this structure is within the limits of error. One feature distinguished the $SnO_2(600)$ from the higher temperature samples; the initial cooperative rise in the heat is substantially greater and that on the strongest sites, the argon–argon interaction, is most effective on the less-sintered material.

Beyond the initial heat and its slope, there is no useful theory of the isosteric heat; it is notoriously misleading to make intuitive interpretations of these curves. Some early calculations for cooperative adsorption on patchwise-heterogeneous[14] and random-heterogeneous[15] surfaces have been made, in the direction of synthesis of hypothetical curves, but no analysis of experimental curves appears to be available.

The CAEDMON analysis is promising, but does little to distinguish the three samples studied here. With change of adsorbate from argon to nitrogen a striking difference is encountered, however. The argon distributions have the expected bell shape characteristic of site energies distributed around a most probable value; the nitrogen distributions are bimodal. The first or lowest energy peak corresponds to the strong adsorption encountered in the isotherms and discussed in connection with the BET analysis. The widely displaced peak in the vicinity of the monolayer corresponds to the stronger adsorption and higher c value of argon relative to nitrogen.

The poorer agreement of the CAEDMON and the BET areas in the case of nitrogen is probably connected with the nature of the nitrogen energy distribution. One of the peaks for the nitrogen case is mixed in with the artificial peak caused by the arbitrary choice of the highest data point and the end of the monolayer region. The problem could have been avoided by choosing the CAEDMON data so that the areas found agreed with the previously determined BET areas, by a trial-and-error procedure.

The logical extension of the theory to the multilayer region, and to the temperature dependent or energy-distribution form for the results, seems indicated. In order to establish contact with experimental isosteric heats, a theory for the heat capacity of a patchwise heterogeneous adsorbed phase is required. This is available for the case of Langmuir-patchwise adsorption[16] but not where a more realistic isotherm is employed, as is the case with the CAEDMON analysis. This isotherm itself could be made even more realistic with the provision of an interaction energy between ad-atoms that depended on the underlying structure and the binding energy.[14] The only arbitrary element of the model would then be the patchwise hypothesis for the energy distribution.

The Singleton-Halsey plots of the high temperature data reveal interesting differences among the samples. The results reinforce the contention that cooperative adsorption is facilitated on the less-sintered material, or that the argon bulk structure is relatively more compatible with the underlying structure in this material. Also, the impression that the samples become more dense as sintering progresses is compatible with the decrease of the small pores noted.

The high-temperature gas–solid virial coefficient analysis is quite disappointing. Although the $SnO_2(600)$ data can be fit better by a variety of models incorporating heterogeneity, the degree of improvement as measured by the standard deviation is probably insignificant. The analysis of B_{2s} fails to reveal any difference between the samples by itself. A more sophisticated analysis of more extensive data, such as the methods of Pierotti et al.,[17] that takes account of possible saturation effects on high energy sites, might reveal more deatil. For systematic investigation of a variety of solids the effort involved might be unjustified. However, the 3-8-inf assignment (Table VII) for $SnO_2(600)$ is strongly reinforced by the low E_1 values that result from the Singleton–Halsey plot.

Again, the B_{3s} analysis shows a definite distinction between the $SnO_2(600)$ and the other samples. Here quantitative evidence for the relative facility of Ar–Ar interaction is available, to confirm the qualitative inference from the isosteric heat curves. Although these two results are based on the same data, the two-dimensional Barker–Everett treatment is clearly a more informative way to present the data.

Description of the Sintering Process

The sintering process for SnO_2 which takes place at constant volume, involves the growth of macropores and the disappearance of micropores. Densification of the material near the surface proceeds along with pore-size growth. The structural changes that accompany this densification produce an incompatible crystal lattice that impedes attractive interaction between adsorbed argon atoms.

Acknowledgment. We are indebted to Professor V. Schomaker for many discussions, and to the Tartar Fund for financial assistance. The work was partially supported by National Aeronautics and Space Administration Grant NGL 48-002-004 to the University of Washington for "interdisciplinary research on the nature and properties of ceramic materials".

Supplementary Material Available: Tables of isotherm data (7 pages). Ordering information is available on any current masthead page.

References and Notes

(1) D. C. Hinman and G. D. Halsey, *J. Chem. Phys.*, **64**, 3353 (1976).
(2) D. C. Hinman, Ph.D. Thesis, University of Washington, 1975.
(3) J. R. Sams, Jr., G. Constabaris, and G. D. Halsey, Jr., *J. Phys. Chem.*, **66**, 2154 (1962).
(4) I. D. Morrison, Ph.D. Thesis, Rensselaer Polytechnic Institute, 1975.
(5) S. Ross and I. D. Morrison, *Surface Sci.*, **52**, 103 (1975).
(6) S. Ross and W. W. Pultz, *J. Colloid Sci.*, **13**, 397 (1958).
(7) W. A. Steele, "The Interaction of Gases with Solid Surfaces", Pergamon Press, Oxford, England, 1974, Chapter IV.
(8) J. H. Singleton and G. D. Halsey, Jr., *Can. J. Chem.*, **33**, 184 (1955).
(9) W. A. Steele and G. D. Halsey, Jr., *J. Phys. Chem.*, **59**, 57 (1955).
(10) M. P. Freeman and G. D. Halsey, Jr., *J. Phys. Chem.*, **59**, 181 (1955).
(11) W. A. Steele and G. D. Halsey, Jr., *J. Chem. Phys.*, **22**, 979 (1954).
(12) R. A. Pierotti and H. E. Thomas in "Surface and Colloid Science", Vol. 4, E. Matijevic, Ed., Wiley, New York, N.Y., 1971, p 93.
(13) J. A. Barker and D. H. Everett, *Trans. Faraday Soc.*, **58**, 1608 (1962).
(14) W. M. Champion and G. D. Halsey Jr., *J. Am. Chem. Soc.*, **76**, 974 (1954).
(15) T. L. Hill, *J. Chem. Phys.*, **17**, 762 (1949).
(16) N. N. Roy and G. D. Halsey, *J. Low Temp. Phys.*, **4**, 231 (1971).
(17) H. E. Thomas, R. N. Ramsey, and R. A. Pierotti, *J. Chem. Phys.*, **59**, 6163 (1973).

High Energy States of the Trivalent Rare Earths

R. C. Ropp* and B. Carroll

Chemistry Department, Rutgers University, Newark, New Jersey 07102 *(Received November 12, 1976)*

There are three possible energy processes involving change in electronic states for the trivalent rare earths in oxygen-dominated hosts. These are intrashell (4f–4f), intershell (4f–5d), and charge transfer (CT) transitions. It is possible to differentiate between these processes on the basis of band width and number of components present even though they overlap over a wide range of energies. Several examples are given and present results are compared to theoretical and experimental results in the literature. It is concluded that whereas the 5d bands probably follow predicted trends in oxygen-dominated hosts, the CT bands show some deviation. The energy of individual charge transfer states appears to be predicted on the nature of the matrix in which the rare earth is incorporated, as exemplified by Pr^{3+} in borate compared to phosphate.

Introduction

The trivalent rare earths, Ln^{3+}, exhibit three types of spectra in absorption and one in fluorescence. The spectra can be related to changes in electronic states among the 4f electrons. These energy processes include intrashell transitions (4f–4f), intershell (4f–5d) transitions, and charge transfer transitions, an energy process involving change in virtual electron cloud density from the vicinity of the ligands to that of the metal ion.

The 4f multiplets comprise the lowest energy state of Ln^{3+} ions. Narrow line groups are seen in absorption and luminescence. These are caused by transitions between 4f levels, split into Stark states by the crystal field. Because of the strong spin–orbit coupling and small radius of the 4f electrons, which are buried beneath closed shells of $5s^2$ and $5p^6$ electrons, the crystal field has minor influence on the energy position of the line groups. Indeed, about the only observable effect upon these line groups is the difference in individual line strengths (transitions between Stark states) as a function of symmetry.[1] Thus the 4f–4f transitions are found at their specific characteristic energies and with characteristic half-widths of 5–30 Å. On the other hand, intershell transitions and charge transfer transitions (hereafter called 5d and CT transitions, respectively) produce broad bands in absorption whose energy positions are dependent upon the neighboring atoms and the cation site symmetry of the lattice. The width of the absorption bands is caused by the Franck–Condon principle acting on differing electron configurations in the ground and excited states wherein the equilibrium internuclear distances are different. In general the equilibrium radius of the excited state is larger than those of the $5s^2$–$5p^6$ electron shells and the excited state is perturbed by the crystal field. Because these three energy states (i.e., 4f, 5d, and CT) appear in absorption at increasingly higher energies, but only one type of luminescence appears (i.e., 4f) it is safe to say that all three states are coupled, the 4f state being the lowest in energy.

A considerable amount of prior investigation into the relative energy positions of these three processes has taken place in the past. Dieke and co-workers[2] were probably the first to establish the relation of the 4f ground state levels and their adjoining J-level multiplets. Dieke also showed that the 4f states, 5d states, and CT states overlap considerably in energy.

Jørgensen[3-6] also addressed himself to this problem and using appropriate atomic parameters, derived two equations, one for 5d transitions, and the other for CT transitions. These equations show the relative energy positions among the several rare earths. As will be seen below, an energy minimum is expected at Ce and Tb for 5d states and at Eu and Yb for CT states.

Loh[7,8] studied the lowest energy 5d absorption bands for 11 of the 14 rare earths in CaF_2. The correspondence of his 5d band energy positions and those calculated from Jørgensen's equation (with 18 000 cm^{-1} subtracted) was remarkable. However, the CT bands were not observed, as would be expected for a matrix containing fluoride, a nonpolarizable anion with high electronegativity. Nugent et al.[9,10] studied both the CT and 5d absorption bands in nonaqueous solutions such as anhydrous ethanol and acetonitrile. In that case, both types of absorption bands appeared within the same energy region. These authors differentiated between 5d and CT bands on the basis of half-width of the bands. The 5d bands characteristically had half-widths of 800–1400 cm^{-1} whereas those of the CT bands were 1600–2400 cm^{-1}.

Actually, none of these authors had specifically considered the major difference between 5d and CT transition spectra. For 5d transitions, the 5d state will be split by the crystal field into components (t_{2g} and e_g for octahedral and tetragonal symmetry). However, the CT transition will show only *one* broad band. As an example,[17] the orthovanadate ion, VO_4^{3-}, exhibits a CT band at about 37 000 cm^{-1}. Dahl et al.[11] calculated the molecular orbital (MO) diagram for this complex. The highest lying MO of the ground state is $3t_2$ which is derived primarily from p orbitals of the surrounding oxygen atoms. The first excited state is $3a_1$ which is derived from the 4s orbitals of vanadium.[18] The transition involves flow of charge along the bond where the electron cloud density increases in the vicinity of the metal ion. The mechanism can be represented as

$$V^{5+}O_n^{n(2-)} \rightleftharpoons [V^{4+}O_n^{n(2-)+1}]^*$$

or

$$\pi \rightarrow 4s^*$$

where the asterisk represents the excited state. Only one band[19] usually occurs in CT transitions, and only those metal ions having an accessible lower valence state will exhibit the CT transition.

The present paper deals with the identification and classification of 5d and CT bands of Ln^{3+} in oxygen-dominated hosts. This problem has been studiously avoided heretofore because of the attendent experimental difficulties. In order to differentiate between 4f, 5d, and CT absorption bands, one requires resolution of at least 5 Å in the absorption spectrum. If a single crystal were available, this requirement would present no problem. However, for the most part, only powders could be easily obtained. It was not until the development of a high-

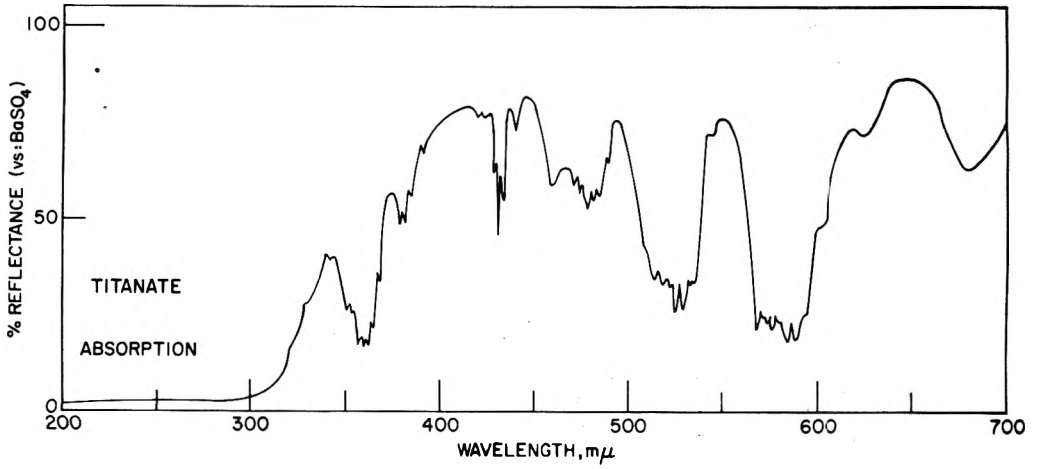

Figure 1. Reflectance spectrum of $Nd_2Ti_2O_7$.

resolution powder reflectance spectrophotometer[12] that the problem could be solved. As has been noted,[1] powder reflectance spectra have been obtained with estimated resolutions in the ultraviolet region of the spectrum of 1–2 Å.

Experimental Section

All materials were prepared by coprecipitation methods. For titanates and zirconates, the tetrachlorides were dissolved at 0 °C in $LnCl_3$ solution. Oxalic acid was added and a coprecipitated oxalate was formed by adding NH_4OH to increase the pH while heating the solution to about 80 °C. The coprecipitate was then fired at elevated temperatures to form the desired titanate or zirconate. Varying the ratio of Ln^{3+} to $TiCl_4$ or $ZrCl_4$ in solution prior to precipitation gave fired products whose composition and crystal structure followed the original ratios of cations in solution. In this way it was very easy to prepare all of the titanate and zirconate compounds, as illustrated for Nd^{3+}: 2:1 Nd_2TiO_5, 1:1 $Nd_2Ti_2O_7$, 4:3 $Nd_2(Ti_3O_6)_3$, 1:1 $Nd_2Zr_2O_7$; yields in most cases were above 95%.

For $LnPO_4$ and $LnBO_3$ compounds, H_3PO_4 and H_3BO_3 were employed. Ln^{3+} solutions were added slowly to a hot (80 °C) H_3PO_4 solution to precipitate a *crystalline* $LnPO_4$ compound, whose degree of hydration varied according to ratios of reagents, temperature of precipitation, and concentration of reagents. The details will be given in a subsequent report.[13] When Ln^{3+} and H_3BO_3 solutions are prepared, a precipitate does not form until the pH of the solution is raised by addition of NH_4OH. The crystallinity and degree of hydration of the product was not dependent upon the temperature of precipitation as in the case of the phosphates. The product was usually $LnBO_3 \cdot 2H_2O$. Yields ranged between 90 and 95% in both cases. The precipitated phosphates and borates were then fired to form a dehydrated product. All fired products were identified by standard x-ray diffraction techniques.

There are two general approaches one can take in preparing powders for measurement of the high energy bands of Ln^{3+}. In one method, a solid solution of $LnXO_n$ and MXO_n can be formed or the pure $LnXO_n$ compound can be used directly. The latter method proved to be more useful. Two other factors are equally important: (a) to obtain a spectrally transparent host and (b) to be sure that any broad band observed is due to the rare earth and not to some other factor. For the latter, this is the most easily achieved by preparing all of the rare earth compounds within a given system and comparing spectra for common features. If, for example, all rare earth titanates of a given structure and stoichiometry (e.g., $Ln_2Ti_2O_7$) had a common reflection band of the same general shape and position in energy, one is safe in assigning this band to titanate groups. For the former factor, if the band is not due to the cation (i.e., rare earth) or the anion (i.e., titanate), then perhaps lattice defects could be the culprit. For this reason, the materials were carefully prepared by the indicated methods which were chosen in order to minimize this possibility.

Results

The measurement range of the instrument[12] was limited to 1750–8000 Å. Within this range, one will observe most of the 4f bands, the lowest energy 5d band components, or the CT band, depending upon which of the two are present in the spectrum. If one broad band is present in the spectrum then the other will not appear within the instrumental measurement range, but will be found at much higher energies.[14]

Effect of Anion on Spectra. The selection of the proper anion, X, in the general compound, $LnXO_n$, is difficult. A survey of possible rare earth compounds soon revealed that most of these would not be suitable because of excessive absorption of the anion. For example, the oxides, Ln_2O_3, are not suitable since they show edge absorptions[20] near 2300 Å, irrespective of the rare earth.[15]

The halides of lanthanides are hygroscopic, the carbonates are difficult to prepare, as are the nitrates in stoichiometric form, and the chalcogenides have a band gap of only a few electron volts and so are strongly absorbing across the entire measured spectrum.

The complete series of titanates were prepared, e.g., $Ln_2Ti_2O_7$ as well as the zirconates, $Ln_2Zr_2O_7$. All of the measured spectra exhibited the broad band at >3000 Å (shown in Figure 1 for $Nd_2Ti_2O_7$ and Figure 2 for $Er_2Zr_2O_7$). The shapes of these bands allowed positive identification of the anion absorption. This illustrates the fact that most of the transition metals as anions exhibit broad absorption bands in the ultraviolet region of the spectrum and so are not suitable as hosts for measurement of the high energy states of lanthanides.

Fortunately, two systems proved to be sufficiently transparent in the ultraviolet so as to allow detection and identification of the broad Ln^{3+} absorption bands. These were:

Structure	Cation site symmetry
$LnPO_4$ Xenotime tetragonal	D_{2d}
Monazite monoclinic	C_1
$LnBO_3$ Hexagonal	D_{3d}

Although bands due to borate appeared in all spectra

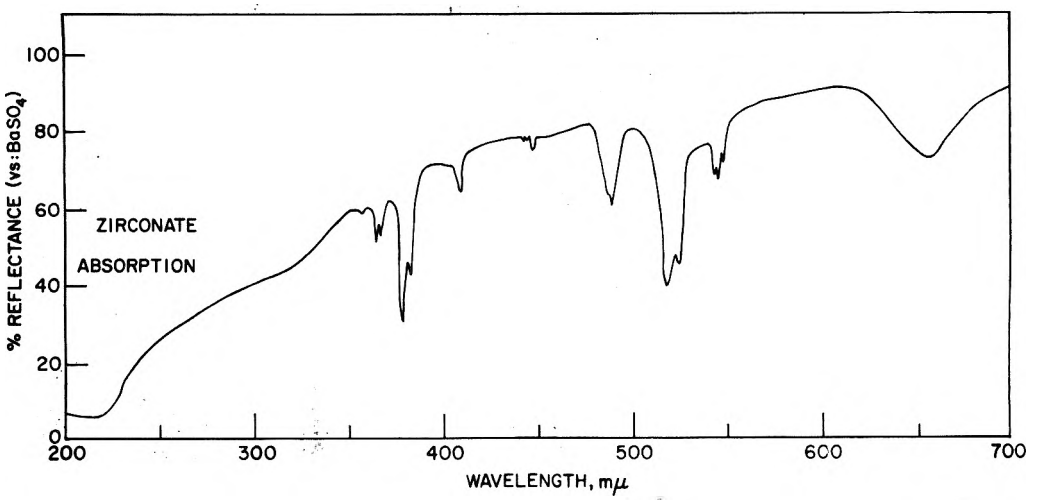

Figure 2. Reflectance spectrum of $Er_2Zr_2O_7$.

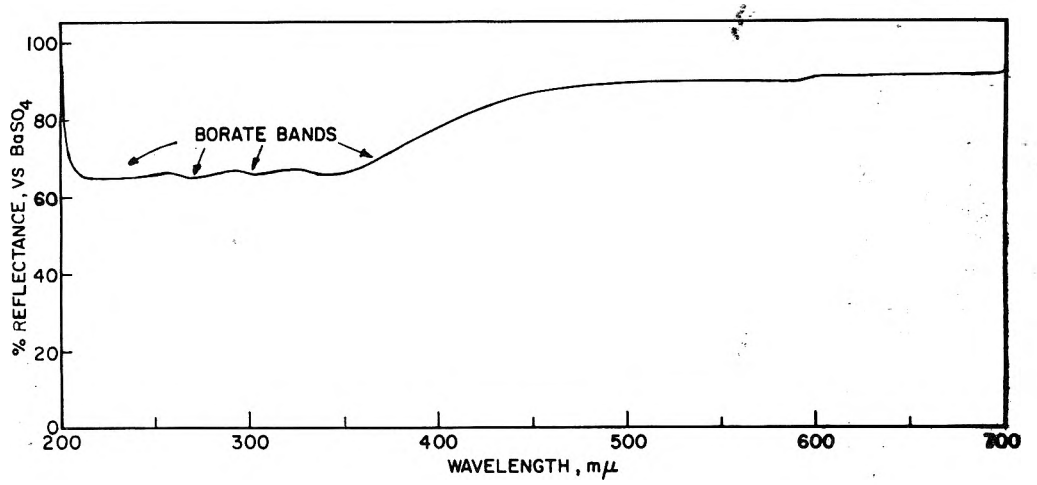

Figure 3. Reflectance spectrum of YBO_3.

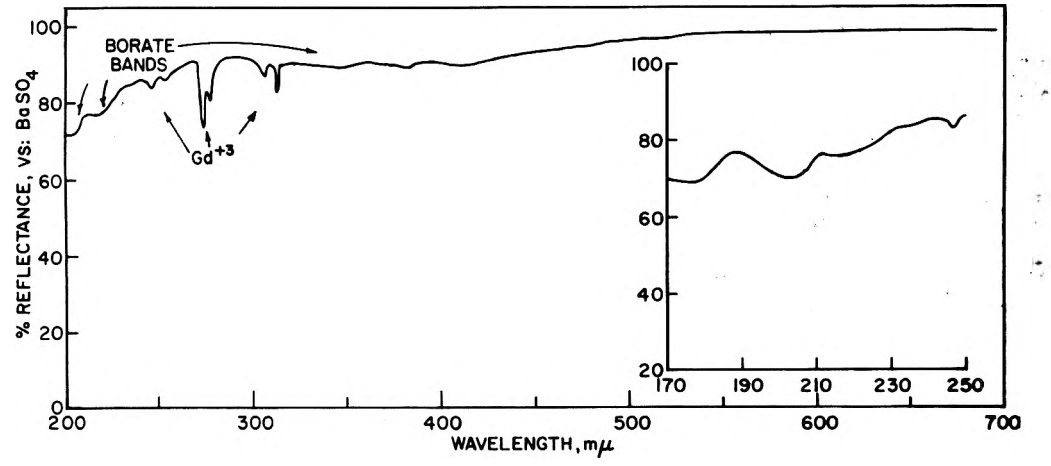

Figure 4. Reflectance spectrum of $GdBO_3$.

between 1700 and 3000 Å, they were sufficiently weak to permit the use of $LnBO_3$ compounds. The ion, Y^{3+}, has a closed-electron-shell structure and has no observable absorption in the near ultraviolet. Figure 3 shows the reflectance spectrum of YBO_3 with the weak borate bands clearly evident. A similar spectrum for $GdBO_3$ is shown in Figure 4 where the borate bands are seen as weak absorptions (~15% as 1-R) at 1750, 2050, 2150, 2300, 3000, and 3400 Å. The 4f transitions of Gd^{3+} are also indicated at 2500, 2750, and 3100 Å. These transitions occur from the $^8S_{7/2}$ ground state to the ^6D_j, ^6I_j, and ^6P_j multiplets, respectively.

The phosphate band appears below about 1850 Å.[16] This limited the measurement range of the orthophosphate compounds from about 1900 to 8000 Å. The phosphate band is a strongly absorbing broad band which peaks at about 1700 Å. As will be shown, comparison of both borate and phosphate reflectance spectra allowed unequivocal identification of the nature of the broad rare earth band which appears in absorption.

Relative Positions of Energy Processes. The several trivalent lanthanides are expected to vary considerably in the energy positions of their 5d and CT bands as n in $4f^n$ is increased monotonically. Figure 5 shows a plot of data

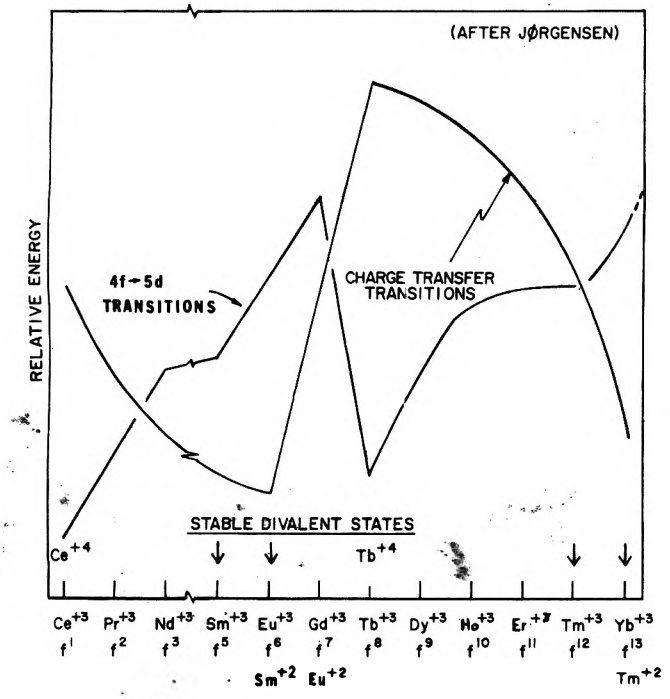

Figure 5. Relative positions of energy processes.

calculated from Jørgensen's[3-6] equations for both the 5d and CT transitions.[21]

The 5d transition curve shows minima at Ce^{3+} and Tb^{3+} and maxima at Gd^{3+} and Lu^{3+}. In contrast, the CT transition curve shows minima at Eu^{3+} and Yb^{3+} and maxima at Ce^{3+} and Tb^{3+}. All of the other rare earths are intermediate to these values. A summary of this data is shown in Table I. There seems to be a correlation between tetravalent states and 5d transitions as well as divalent states and CT transitions.

TABLE I: Comparison of Known Oxidation States and Transitions Expected

Transition	Energy state		Known oxidation states
	Lowest	Highest	
$4f \rightarrow 5d^*$	Ce	Eu, Gd	Ce^{3+}, Ce^{4+}
	Tb	Yb, Lu	Tb^{3+}, Tb^{4+}
$\pi \rightarrow 4f^*$	Eu	Ce	Eu^{2+}, Eu^{3+}
	Yb	Tb	Yb^{2+}, Yb^{3+}

Powder Reflectance Spectra of Trivalent Lanthanides. La^{3+} $4f^0$. This rare earth has no 4f electrons[22] yet it exhibits a well defined CT band centered at about 2050 Å for $LaBO_3$, as shown in Figure 6. The half-width of the band is about 600 Å. The presence of a CT band for La^{3+} indicates that this ion has considerable divalent character. The spectrum of $LaPO_4$ was similar except that only the edge of the band could be measured due to the proximity of the phosphate band.

Ce^{3+} $4f^1$. This ion is expected to show 5d bands and the spectra obtained confirm this as shown in Figure 7 for $CePO_4$. There are four components present and their average width is about 600 Å.[23] Since $CeBO_3$ proved difficult to prepare, no spectra were obtainable.

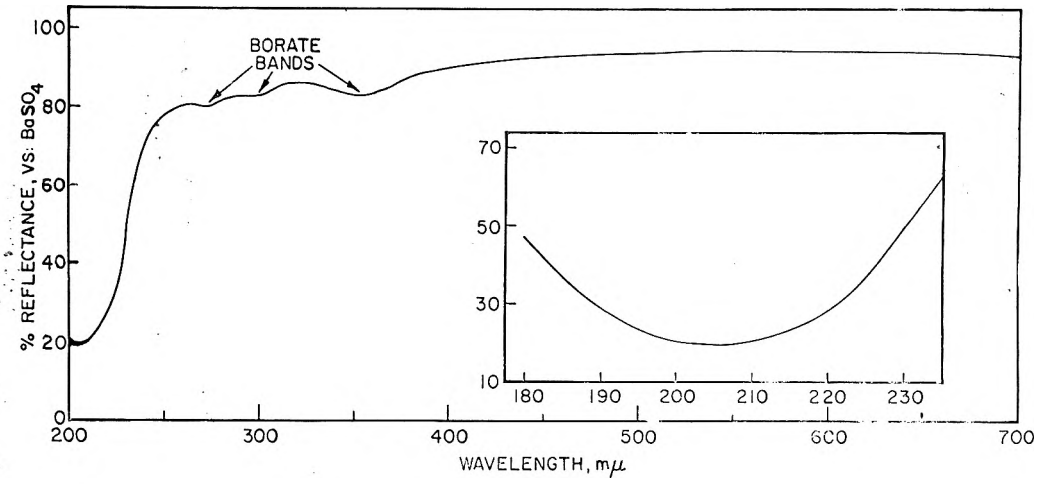

Figure 6. Reflectance spectrum of $LaBO_3$.

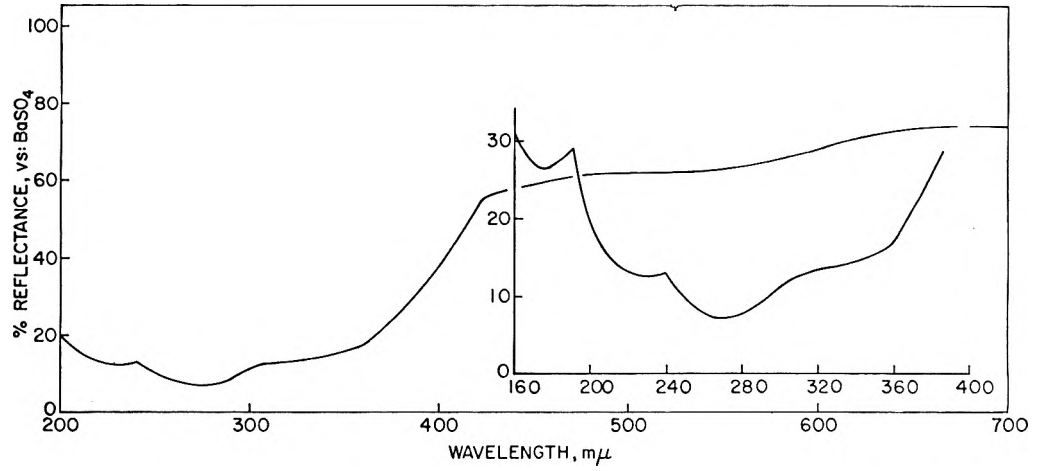

Figure 7. Reflectance spectrum of $CePO_4$.

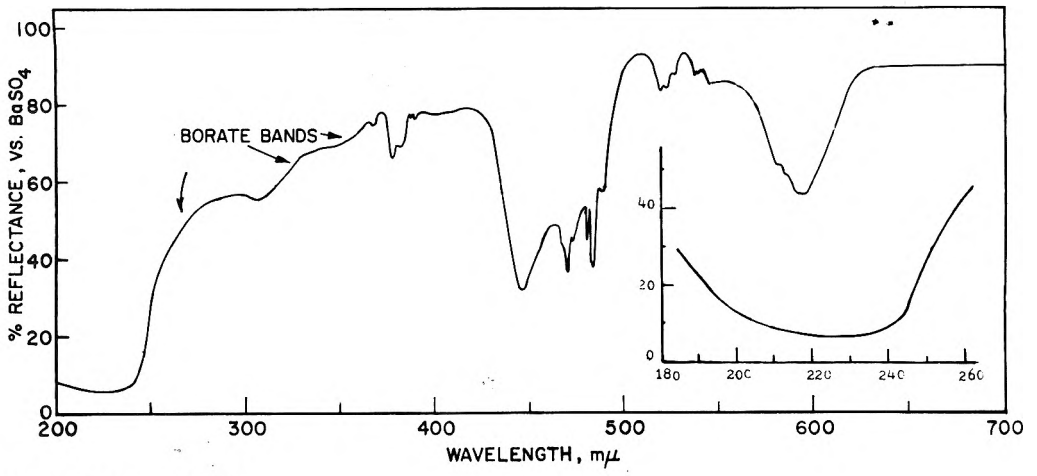

Figure 8. Reflectance spectrum of $PrBO_3$.

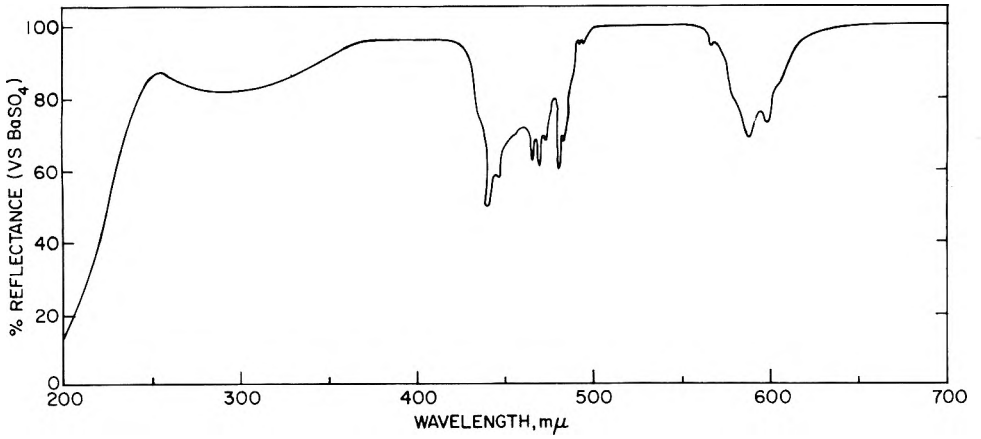

Figure 9. Reflectance spectrum of $PrPO_4$.

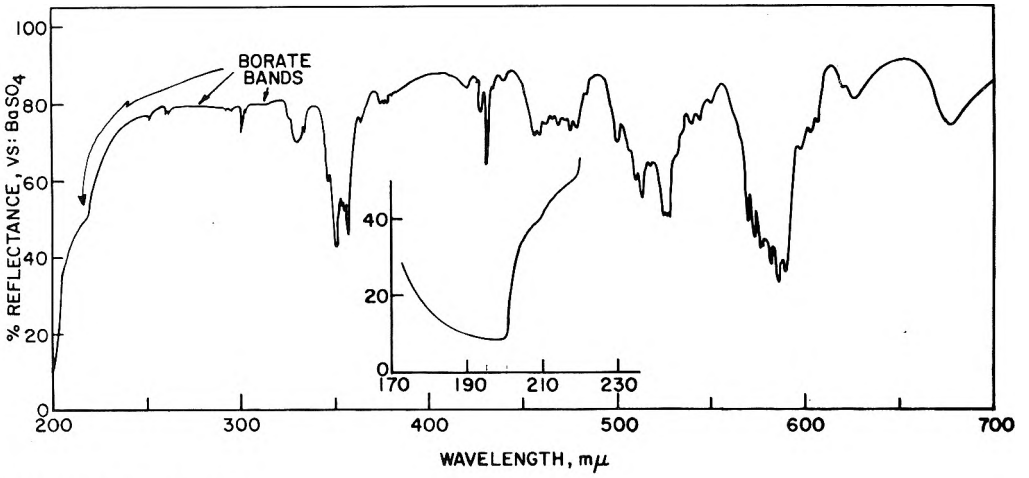

Figure 10. Reflectance spectrum of $NdBO_3$.

Pr^{3+} $4f^2$. This rare earth should exhibit 5d states because it has a well-defined tetravalent state but, as is evident from Figure 8 for $PrBO_3$ and Figure 9 for $PrPO_4$, the CT band is prominent. The half-widths are 600 and 500 Å, respectively. Note that the 4f bands are very broad. The half-width of the 4f transitions ranges between 25 and 150 Å, some five times greater than the average value of 5–30 Å for the other rare earths.[24]

Nd^{3+} $4f^3$. This ion was expected to show 5d states because a tetravalent state is known but the divalent state is not. Nevertheless, a single band is evident in Figure 10, peaking at about 1950 Å with a half-width of 200 Å. This CT band is considerably different from those shown for Pr^{3+}, or for Sm^{3+}, given below. Although $NdPO_4$ was measured, only a side band at 1900 Å, superimposed on the major phosphate band, was observed.

Sm^{3+} $4f^5$. This ion is expected to manifest a CT band since samarium has a well-defined divalent state. The spectra of Figure 11 for $SmPO_4$ and Figure 12 for $SmBO_3$ confirm this. The CT band for $SmPO_4$ peaks at 1900 Å with a half-width of 400 Å whereas that for $SmBO_3$ peaks at 1950 Å with a half-width of 800 Å.

Eu^{3+} $4f^6$. This rare earth also has a well-defined divalent state and the spectra of the trivalent ion are easily classified as CT bands. The CT band of $EuPO_4$ peaks at 2300 Å with a half-width of 800 Å (see Figure 13) whereas the

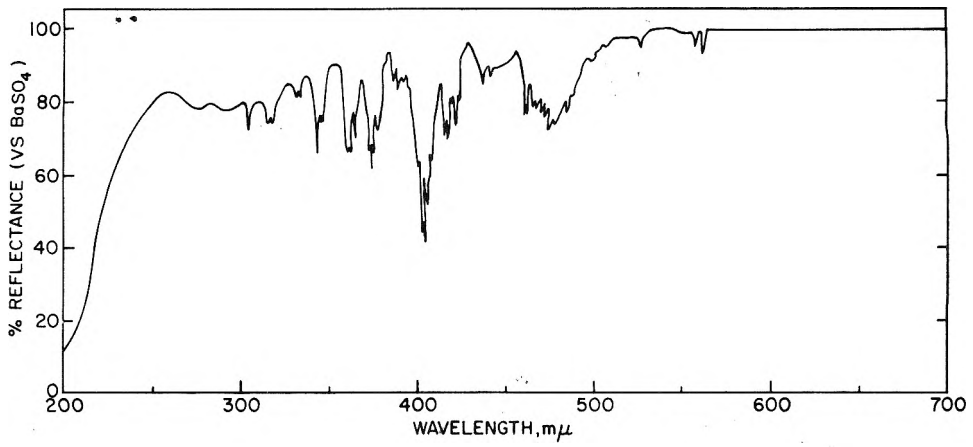

Figure 11. Reflectance spectrum of $SmPO_4$.

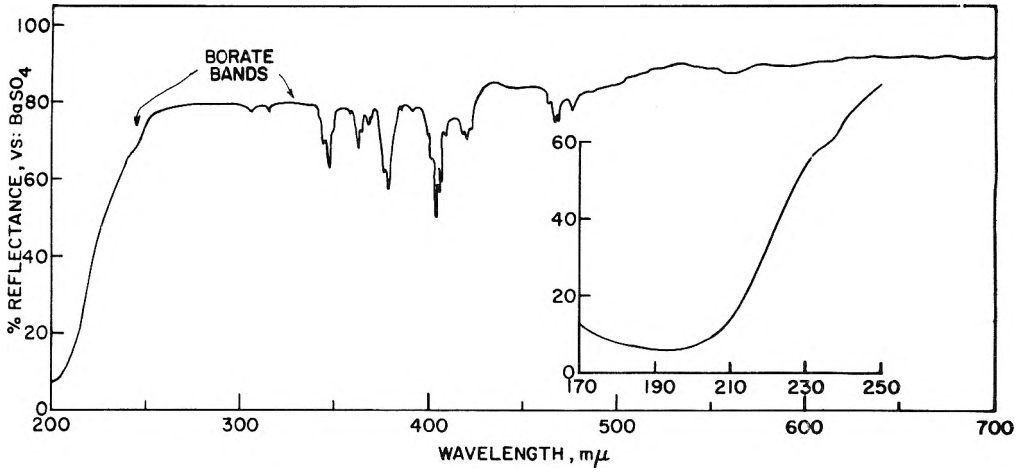

Figure 12. Reflectance spectrum of $SmBO_3$.

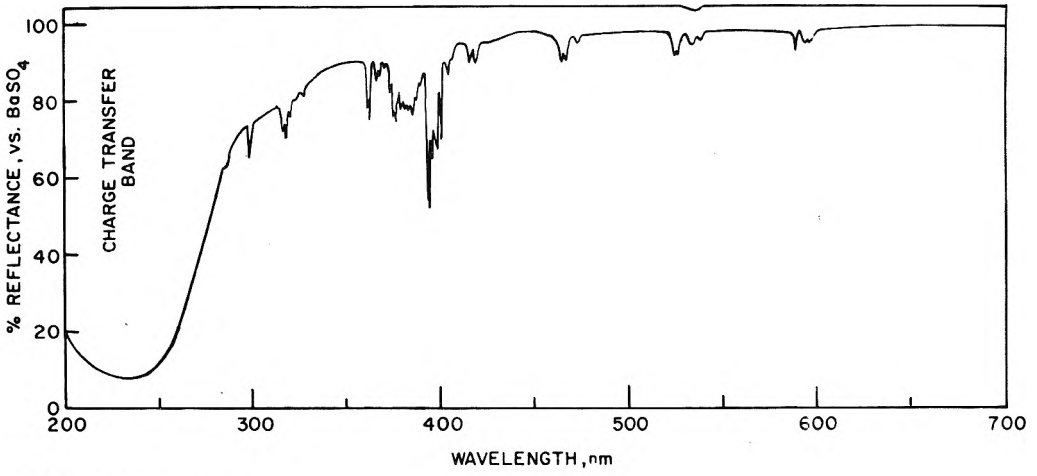

Figure 13. Reflectance spectrum of $EuPO_4$.

CT band of $EuBO_3$ peaks at 2250 Å with a half-width of 1000 Å (see Figure 14). These bands are the widest of all those CT bands observed for the rare earths.

Gd^{3+} $4f^7$. The spectra for this ion were inconclusive. No evidence of either 5d or CT transitions was observed (see Figure 4).

Tb^{3+} $4f^8$. The spectra of this ion were very interesting. Since terbium has a well-defined tetravalent state, 5d bands would be expected. There are five components apparent in Figure 15 for $TbBO_3$, indicating 5d transitions. One is tempted to compare these to the five crystal field splittings ($3t_{2g}$ and $2e_g$) expected for a 5d level. The band at 2700 Å for $TbBO_3$ appears to be similar to that at 2300 Å in $TbPO_4$ (see Figure 16). The other higher energy component is masked by the phosphate band. This is an example of a crystal field shift of the 5d bands. The half-widths of these individual components are about 100 Å in both cases.

There was a band in the $TbPO_4$ spectrum at about 2600 Å with a half-width of 90 Å, which was initially believed to be one of the 5d field components. However, it did not have the appearance and shape of the other 5d components. When a series of powder compositions were prepared, $1 - xYPO_4 \cdot xTbPO_4$, where x was varied from 0.05 to 1.00, and the spectra were measured, it was found that the band intensity at 2600 Å was dependent upon Tb^{3+}

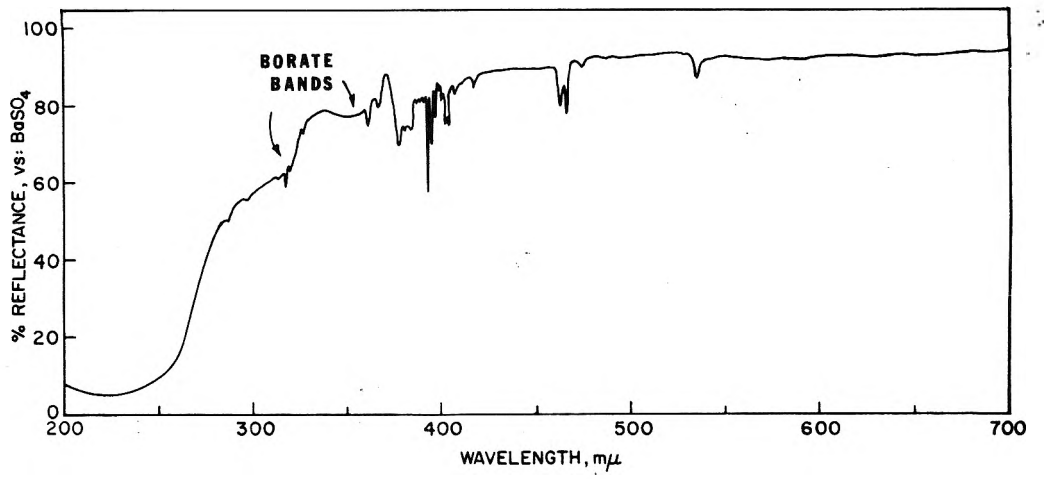

Figure 14. Reflectance spectrum of $EuBO_3$.

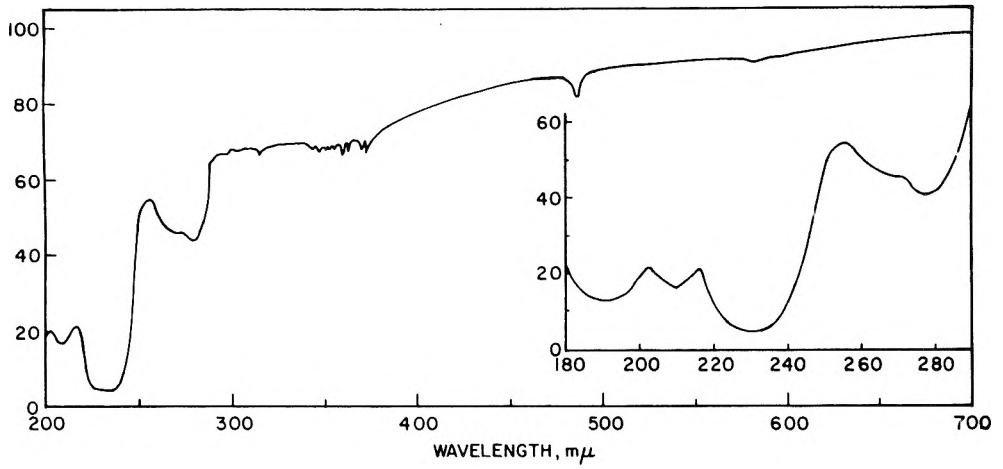

Figure 15. Reflectance spectrum of $TbBO_3$.

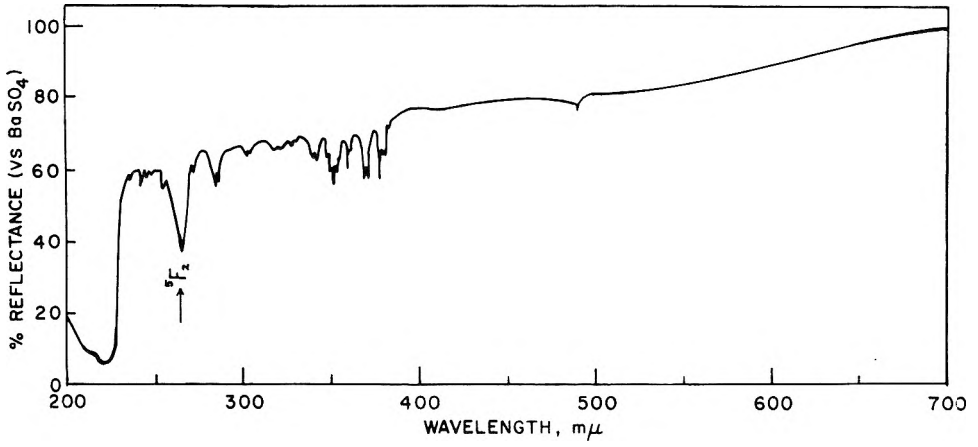

Figure 16. Reflectance spectrum of $TbPO_4$.

concentration, although the 5d components at 2300 Å maintained about the same relative intensity. It appears that the 2600-Å band is of 4f origin.[25] The transition was identified as $^7F_6 \rightarrow {}^5F_2$. As x approaches one in the above formula, the reflectance spectrum changes from narrow lines (~15 Å in half-width) to a single broad 4f band of intermediate intensity. The other 4f line multiplets remain about the same in intensity. This behavior of the $^5F_2$ multiplet indicates that an interaction of neighboring Tb^{3+} ions occurs as x approaches one in the above formula and that this perturbation has a major effect upon the intensity of this line multiplet.

Dy^{3+} $4f^9$. This ion also has a stable tetravalent state and 5d bands are expected to be observed. For $DyPO_4$, no such bands were observed. However, the crystal field effect is strong enough in $DyBO_3$ so that 5d components are observed at the extreme edge of the measured range of the spectrum, as shown in Figure 17. The half-widths of the components are about 50 Å. These bands are the narrowest 5d bands measured, for all of the lanthanides.

Ho^{3+} $4f^{10}$. The spectra of this ion were inconclusive. No broad bands were observed within the measurement range of the instrument.

Er^{3+} $4f^{11}$. The spectra of this ion were also inconclusive.

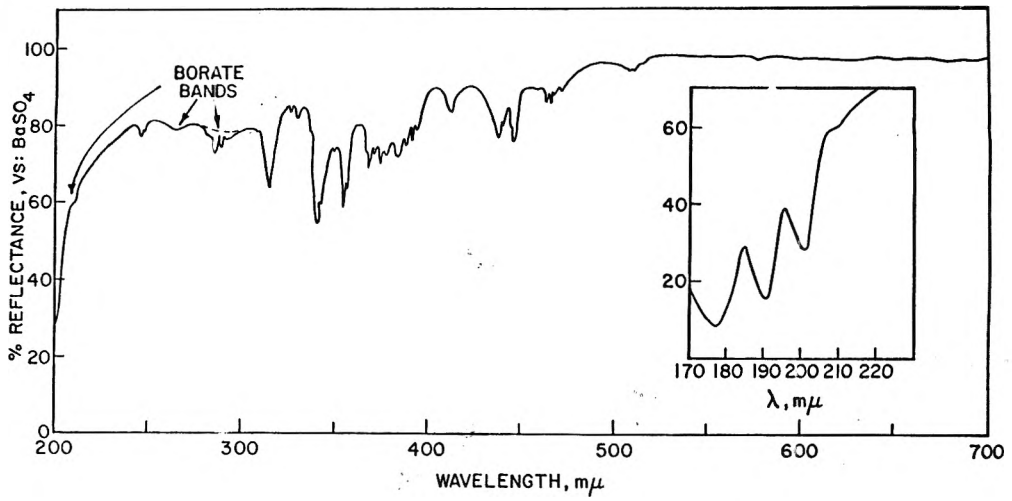

Figure 17. Reflectance spectrum of $DyBO_3$.

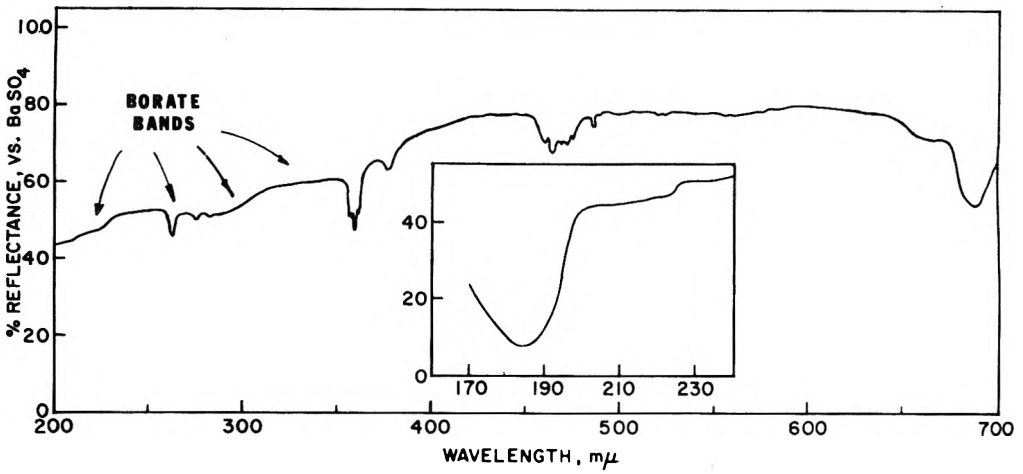

Figure 18. Reflectance spectrum of $TmBO_3$.

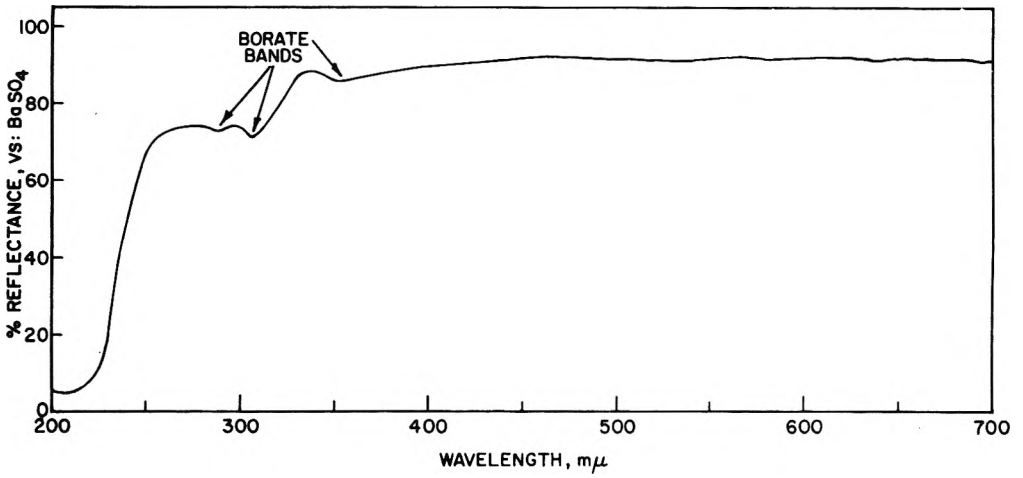

Figure 19. Reflectance spectrum of $YbBO_3$.

Tm^{3+} $4f^{12}$. Since this rare earth has a well-defined divalent state, a CT band is expected to be a prominent feature in the spectra. While a broad band was observed in the $TmBO_3$ spectrum (see Figure 18) none was seen in the $TmPO_4$ spectrum, possibly because the phosphate band was prominent at about 1850 Å. The band observed in Figure 18 appears to be a CT band with a half-width of about 200 Å.

Yb^{3+} $4f^{13}$. This rare earth, with a well-defined divalent state, produced powder reflectance spectra which contained broad bands easily classified as CT bands as shown in Figure 19 for $YbBO_3$ and Figure 20 for $YbPO_4$. Whereas the former is a very broad band with a half-width of about 500 Å, the latter is rather narrow with a half-width of about 100 Å.

Discussion

As a result of high-resolution reflectance measurements, spectral data have been obtained that appear to be in accordance with predictions made by Jørgensen with the exception of Pr^{3+} which appears to be out of line. As may be seen in Figure 5 and Table I, a *smooth* progression in

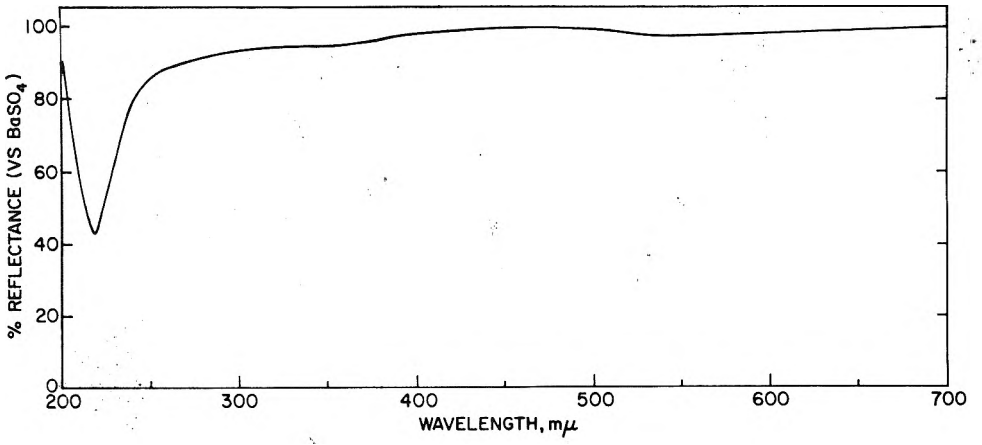

Figure 20. Reflectance spectrum of $YbPO_4$.

TABLE II: Lanthanides for which Charge Transfer Bands Were Observed and Their Band Widths

	Phosphate		Borate			
Cation	$\lambda_{1/2}$, Å	Peak energy, eV	$\lambda_{1/2}$, Å	Peak energy, eV	Expected band (after Jørgensen)	No. of bands obsd per spectrum
Eu^{3+}	800	5.39	1000	5.51	CT	1
Sm^{3+}	400	6.51	800	6.36	CT	1
Yb^{3+}	100	5.71	500	6.06	CT	1
Pr^{3+}	500	6.54	600	5.39	5d	1
La^{3+}	Side band		600	6.04	None	1
Nd^{3+}	Side band		200	6.47	5d	1
Tm^{3+}	Not obsd		200	6.70	CT	1

TABLE III: Lanthanides for which 5d States Were Observed and Their Band Widths

	Phosphate		Borate			
Cation	$\lambda_{1/2}$, Å	Peak energy, eV	$\lambda_{1/2}$, Å	Peak energy, eV	Expected band	No. of bands obsd per spectrum
Ce^{3+}	600	3.71	Not obtained		5d	4
Tb^{3+}	100	5.54	100	4.47	5d	5
Dy^{3+}	Not obsd		50	6.14	5d	3

CT state energies is expected, with maxima at Ce^{3+} ($4f^1$) and Tb^{3+} ($4f^8$) and minima at Eu^{3+} ($4f^6$) and Yb^{3+} ($4f^{13}$). The opposite is expected for 5d band energies. Experimentally, prior workers[7-9] have demonstrated a smooth progression in 5d state energies of Ln^{3+} ions in a matrix of CaF_2.

In the present work, using a phosphate or borate as a matrix, CT bands were observed for most of the rare earths. However, the observed energies did not follow a smooth progression with numbers of 4f electrons. Table II shows the lanthanides for which CT bands were observed along with their half-widths and the energy of the peak in electron volts.

An arrangement can be given in the form of a spectrochemical series in order of ascending energy:

Phosphates: $Eu^{3+} < Yb^{3+} < Sm^{3+} < Pr^{3+}$

Borates: $Pr^{3+} < Eu^{3+} < La^{3+} < Yb^{3+} < Sm^{3+} < Nd^{3+} < Tm^{3+}$

It is notable that Pr^{3+} appears at the top of one series and the bottom of the other. However, the CT bands of rare earths in a phosphate matrix do not hold the same relationship to one another as to those observed for the borate series. These series should relate to the reduction potential of the divalent state. Indeed, Nugent et al. have made extensive comparisons between their data and the standard II–III reduction potential. Whereas their values for the CT band in nonaqueous solvents ranged between 3.2 and 5.5 eV, our values for oxygen-dominated hosts fall between 5.4 and 6.7 eV.

TABLE IV: Stable Valence States of the Rare Earths in Phosphate and Borate Hosts

4f electrons	Valence state according to type of spectrum obsd		
	CT.	Y^{3+}	5d
$4f^0$	La^{2+}	La^{3+}	
$4f^1$		Ce^{3+}	$-Ce^{4+}$
$4f^2$	Pr^{2+}	Pr^{3+}	
$4f^3$	Nd^{2+}	Nd^{3+}	
$4f^5$	Sm^{2+}	Sm^{3+}	
$4f^6$	Eu^{2+}	Eu^{3+}	
$4f^7$		Gd^{3+}	
$4f^8$		Tb^{3+}	$-Tb^{4+}$
$4f^9$		Dy^{3+}	$-Dy^{4+}$
$4f^{10}$		Ho^{3+}	
$4f^{11}$		Er^{3+}	
$4f^{12}$	Tm^{2+}	Tm	
$4f^{13}$	Yb^{2+}	Yb^{3+}	

A comparison of the 5d bands observed is shown in Table III. Note that the half-widths varies from 50 to 600 Å. By comparing these data to those in Table II it can be seen that the primary difference between 5d and CT bands is not the width of the band, but the number of bands present. The present data are not sufficient to be able to make comparisons between these measured 5d bands and the trend predicted by Jørgensen. His predictions have been shown to be correct for halide hosts. If they are indeed applicable to oxygen-dominated hosts, then it is easy to account for the Er^{3+} and Ho^{3+} spectra. The 5d bands of these rare earths probably lie at an energy higher than 1700 Å and so were not measured.

One final comparison can be made in terms of the stable valence states of each rare earth, as deduced from the type of spectrum observed. This is shown in Table IV. The rare earths which deviate from expected values derived from the prior literature are La, Pr, and Nd.

Summary

(1) Charge transfer bands of rare earths in oxygen-dominated hosts follow the trend predicted by Jørgensen with few exceptions.

(2) Several ions exhibit CT bands in phosphate and borate hosts rather than the expected 5d states.

(3) Band width is not the criterion for identification of 5d or CT bands but rather the number of crystal field components present.

Acknowledgment. The authors wish to thank Professor Mme. F. Gaume of the University of Lyon for the valuable suggestions concerning the interpretation of our data. Many of these have been incorporated into this paper.

References and Notes

(1) R. C. Ropp and B. Carroll, *J. Phys. Chem.*, **77**, 339 (1973).
(2) G. H. Dieke and H. M. Crosswhite, *Appl. Opt.*, **2**, 657 (1963). See also "Spectra and Energy Levels of Rare Earth Ions in Crystals", Interscience, New York, N.Y., 1968.
(3) C. K. Jørgensen, *Mol. Phys.*, **5**, 271 (1962).
(4) C. K. Jørgensen, *Solid State Phys.*, **13**, 375 (1962).
(5) C. K. Jørgensen, *J. Inorg. Nucl. Chem.*, **24**, 1587 (1962).
(6) C. K. Jørgensen, *Proc.* 5th Rare Earth Res. *Conf.*, Ames, Iowa (1965).
(7) E. Loh, *Phys. Rev.*, **154**, 270 (1967).
(8) E. Loh, *Phys. Rev.*, **158**, 273 (1967).
(9) L. J. Nugent, R. D. Baybarz, J. L. Burnett, and J. L. Ryen, *J. Inorg. Nucl. Chem.*, **33**, 2503 (1971).
(10) L. J. Nugent, R. D. Baybary, and J. L. Ryan, *J. Phys. Chem.*, **77**, 1523 (1973).
(11) J. P. Dahl and H. Johansen, *Theor. Chim. Acta*, **11**, 26 (1968).
(12) R. C. Ropp, Ph.D. Thesis, Rutgers University, Newark, N.J., 1971.
(13) R. C. Ropp and B. Carroll, to be submitted for publication.
(14) C. K. Jørgensen, private communication.
(15) C. K. Jørgensen, R. Pappalardo, and E. Ritterhaus, *Z. Naturforsch. A*, **19**, 424 (1964); **20**, 54 (1965).
(16) M. Halman and I. Platner, *J. Chem. Soc.*, 3386 (1964).
(17) We chose orthovanadate as an example because it has been well characterized. Although VO_4^{3-} is an anion, it clearly represents the probable situation for the rare earths wherein the charge transfer centers involve a central complex of the trivalent metal ion with nearest neighbor oxygen atoms of the lattice structure.
(18) In a review by A. Muller et al. (*Struct. Bonding*, **14**, 23 (1973)), it is suggested that the first charge transfer transition is O_{2p} $(t_1) \rightarrow V_{3d}$ (e).
(19) It is not trivial that the CT center gives only one band. Several levels are found in molecular orbital calculations, but generally they are too closely spaced except for one large energy gap which gives rise to the CT band.
(20) This is not a maximum but an edge depending upon grain size.
(21) It is implicit that if the CT band is lowest for a given rare earth in a given host, then the 5d bands will appear at higher energies, and vice-versa. The CT band energies depend primarily upon local symmetries around the central rare earth, whereas the 5d states are directly affected by the crystal field strength of the host at the cation site. Thus the cross-over points of the two curves depend upon the nature of the host. In fluorides (nonpolarizable), they are far apart (ref 7 and 8) whereas in oxygen-dominated hosts (polarized), they are much closer. The latter situation is illustrated in Figure 5.
(22) Although a CT band is indicated for these lanthanum compounds, it is difficult to compare its energy to those of other rare earths. The 4f orbital in lanthanum is not pure but has a mixed character 4f–5d (it is the same for cerium). Thus La has an apart position in the energy scheme.
(23) The half-widths given are a mean value in all cases.
(24) In Figure 8, the 4f band in $PrBO_3$ at 3600 Å cannot be due to Pr^{3+}, because no energy levels exist in this region for Pr^{3+}. Most likely it is due to a low level Nd^{3+} impurity. For reasons that are not clear, this 4f band does not appear in the $PrPO_4$ spectrum (see Figure 9), although the same raw material, Pr_6O_{11}, was used in preparing both compounds.
(25) Professor Gaume (University of Lyon, France) has suggested that this line is due to an ion pair because of the effect of concentration on intensity. As the Tb concentration increases in $Y_{1-x}Tb_xPO_4$, the relative intensity ratios between the 5d components and the 4f levels remain about constant, whereas only the one line intensity increases with concentration. Its energy position allows one to consider it as a $4f^n$ transition.

Low Temperature Luminescence Properties of Some Ortho-Substituted Anilides

Marie-Paule Pileni and René Santus*

Laboratoire de Biophysique, Muséum National d'Histoire Naturelle, 61, Rue Buffon-75005, Paris, France *(Received October 29, 1976)*

Publication costs assisted by the Muséum National d'Histoire Naturelle

The synthesis of various ortho-substituted anilides makes it possible to confirm that the abnormally red-shifted fluorescence (λ_{max} 510 nm) observed at room or low temperature can be attributed to an excited state proton transfer between the formamido group and the carbonyl of the side chain on the benzene ring situated ortho to one another. This excited state proton transfer is very sensitive to the presence of inorganic ions. All derivatives display dual phosphorescence emissions in polar or nonpolar solvents. Addition of a relatively low salt concentration results in a dramatic increase in the phosphorescence quantum yield. At low temperature, the acetyl 2′-acetanilide derivative shows anomalous phosphorescence properties. The phosphorescence excitation spectra critically depend upon the hydrogen bond forming ability of the solvent.

Introduction

For some time now, we have been interested in the understanding of the photosensitizing properties of *N*-formylkynurenine (FK), a tryptophan UV photooxidation product and its major metabolite.[1-3] As photochemistry is a consequence of photophysical events, it was important to study the FK photophysics. During the course of a preceding study[4] we found that the FK luminescence properties were rather unusual. A proton transfer in the first excited singlet state has been proposed in order to account for the large fluorescence Stokes shift which is observed in nonpolar solvents. This excited state proton transfer was thought to be caused by an intramolecular hydrogen bond between the hydrogen of the formamido group and the *o*-carbonyl of the side chain as shown by NMR spectroscopy.[5] The occurrence of an excited state proton transfer was confirmed by the room temperature fluorescence studies on some ortho-substituted anilides[6] which are FK parent compounds.

At low temperature, in addition to the abnormally red-shifted fluorescence attributed to the excited state proton transfer, a dual phosphorescence emission was

observed whose characteristics were dependent upon the hydrogen bonding ability of the solvent and/or the structure of the side chain situated ortho to the formamido group on the benzene ring.

The synthesis of various anilides derivatives differently substituted on the amide group leads to compounds which also possess quite interesting low temperature luminescence properties. In this paper we describe these luminescence properties and we show that they are not only greatly influenced by the substituent on the amide group but also by the solvent polarity and its hydrogen bonding ability. We also show that intra- or intermolecular hydrogen bond formation which modifies the low temperature luminescence properties of ortho-substituted anilides (and of aromatic carbonyl compounds in general[7]) is very sensitive to the presence of a rather low salt concentration.

Experimental Section

The ortho-substituted anilides under investigation in the present study can be represented as

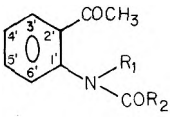

Compound I ($R_1 = R_2 = H$) has been prepared according to the method given in ref 1. Compound II ($R_1 = H$, $R_2 = CH_3$) was synthesized according to the standard fashion[8] while compounds III ($R_1 = CH_3$, $R_2 = H$) and IV ($R_1 = R_2 = CH_3$) have been prepared by formylation or acetylation of *N*-methylacetyl-2'-acetophenone according to the method outlined in ref 9. Purification was done by two or three successive chromatographies on Sephadex G 10 using water or pH 7 phosphate buffer (10^{-2} M) as eluent (for compounds I, III, and IV) or on biogel P2 (compound II). Solid samples were obtained by extracting a given compound from water by hexane. Their purity was checked either by gas chromatography or mass spectroscopy and their structural formulae were confirmed by NMR spectroscopy.[9]

The solvents used for spectrophotometry or luminescence measurements were of the best available grade (Merck spectroquality reagents). Ethylene glycol was a Fluka product. Water was first deionized, once distilled, and then evaporated using a quartz still.

Absorption measurements were performed using a Beckman DK-U spectrophotometer. Luminescence excitation or emission spectra (uncorrected) were recorded at 77 K using a modified Aminco-Bowman spectrofluorophosphorimeter.[10] Phosphorescence lifetimes were determined from CRO traces obtained with a Tektronix 5103N oscilloscope. EPR spectra of the triplet state of some derivatives were obtained through the use of a Varian E_9 EPR spectrometer equipped with an optical cavity.

Results and Discussion

I. *Fluorescence Spectroscopy.* (a) *A Summary of Optical Absorption Properties.* The room temperature optical absorption spectra[4,6] show that the four anilides under study can be classified into two groups depending upon the presence (compounds I and II) or absence of an intramolecular hydrogen bond between the N-H and the o-carbonyl of the side chain (see general formulae in the Experimental Section). The $S_0 \rightarrow S_1$ transition is located at $\lambda_{max} \sim 320$ nm for I and II or $\lambda_{max} \sim 290$ nm (for III and IV) and has a strong $n\pi^*$ character although the molar extinction coefficient (~ 3000 M^{-1} cm^{-1}) is too large for a pure $n\pi^*$ transition.

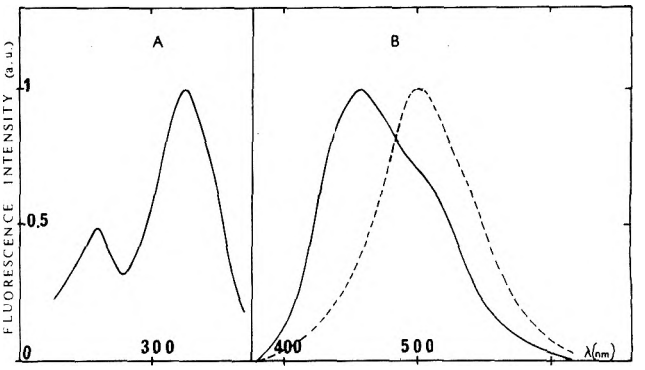

Figure 1. (A) Fluorescence excitation spectrum of compound II (2×10^{-4} M) in isopentane or in isopentane + 2% 2-propanol. (B) Corresponding fluorescence emission spectrum: (——) in isopentane; (- - - -) in isopentane + 2% 2-propanol. Temperature 77 K, excitation wavelength 290 or 320 nm.

Mixing with other states, such as $\pi\pi^*$ or CT states, has been proposed in order to explain the high ϵ values.[6]

(b) *Low Temperature Fluorescence Studies. Compound I.* There is only one fluorescence (λ_{max} 510 nm) whatever the solvent:water–ethylene glycol 1:1 vol (WEG) or ethanol–water 95:5 vol (hereafter called ethanol) mixture, isopentane, methylcyclohexane.

This fluorescence emission is quenched by adding $CaCl_2$ in water or ethanol (see below). We have characterized the 510-nm fluorescence as belonging to the species formed by transfer of the formamido NH proton to the 2' carbonyl.[4]

As already noted in ref 4, it is very surprising that no fluorescence emission can be detected at short wavelength. Thus a detailed study of the temperature effect on the fluorescence quantum yield would be of great interest. However, both the low fluorescence quantum yield and the low sensitivity of the fluorimeter equipped with the variable temperature setup preclude such a study.

Compound II. This compound presents some rather unexpected fluorescence properties with respect to other ortho-substituted anilides under study in the present investigation.

At 77 K in isopentane (Figure 1) one observes a fluorescence at λ_{max} 460 nm and a shoulder at 510 nm. However this fluorescence spectrum is rather different from the one obtained at room temperature.[6] The temperature evolution of the fluorescence spectrum (Figure 2) and intensity (at 460 and 510 nm) (Figure 3) clearly shows that two emitting species are involved in the fluorescence emission both having the same excitation spectrum (see below). Moreover in the temperature range 300–200 K, the Arrhenius plots for the 460- and 510-nm emissions lead to different activation energies (2 and 4 kcal mol^{-1}, respectively) which confirms this hypothesis. It is worth noting that the 510-nm fluorescence intensity corresponding to the excited state proton transfer remains constant below 120 K which corresponds to the isopentane vitreous transition temperature. This probably arises from the fact the vitreous state blocks the acetamido group in a given conformation and the proton transfer is no longer a temperature-dependent process.

Addition of 2% 2-propanol, a well-known H bond forming solvent, leads to the disappearance of the 460-nm fluorescence in parallel to an increase in the 510-nm emission. Accordingly in alcoholic solvents we only observe the 510-nm fluorescence (Figure 1).

In all solvents so far investigated, the uncorrected fluorescence excitation spectrum resembles the optical absorption spectrum (two excitation bands with maxi-

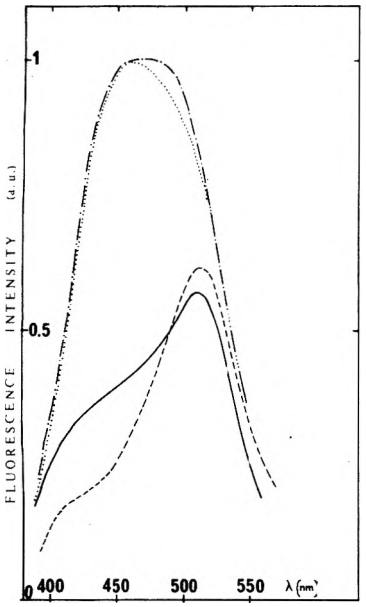

Figure 2. Temperature evolution of compound II fluorescence emission spectrum in isopentane: (——) T = 295 K, sensitivity × 200; (- - - -) T = 200 K, sensitivity × 20; (· · · · ·) T = 120 K, sensitivity × 1; (– · – · –) T = 80 K, sensitivity × 1. Excitation wavelength 320 nm, concentration 1.5 × 10^{-4} M.

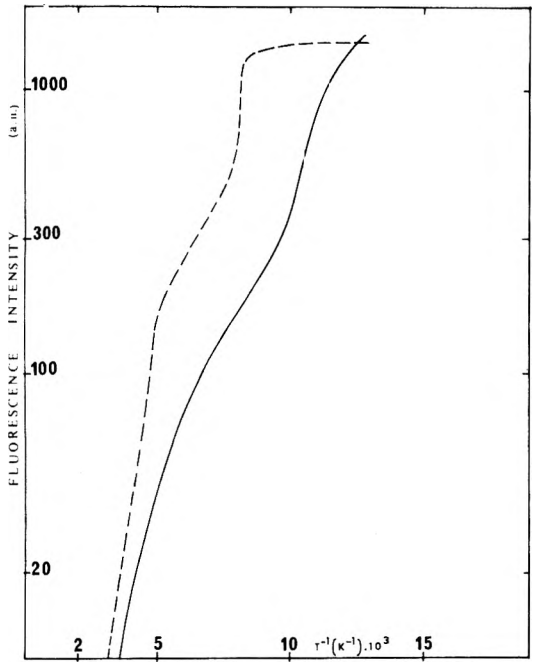

Figure 3. Arrhenius plots of the temperature evolution of the fluorescence intensity measured at 460 (——) or 510 nm (- - - -) in isopentane. The solute was compound II (1.5 × 10^{-4}), excitation wavelength 320 nm.

mums at 260 and 320 nm). It does not depend upon the solvent and is concentration independent. The latter point confirms that no impurity problems are involved in these particular emission properties.

The fluorescence properties observed in isopentane can be understood in view of the NMR results which suggest that, in nonpolar solvents, three species are in equilibrium. They also show that the intramolecular hydrogen bonding between the amide proton and the o-carbonyl forces the amide group to be coplanar with the benzene ring allowing the H_6' proton to interact with the amide carbonyl.[5] In other words the H_6' proton can be in a deshielding region of the carbonyl of the amide group. In compound II, the energy difference between the rotamers is increased by the

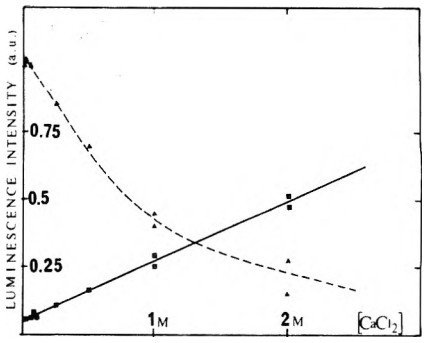

Figure 4. Variation of the fluorescence intensity (measured at 510 nm) (- - - - -) and of the phosphorescence intensity (measured at 455 nm) (——) as a function of calcium chloride concentration in ethanol at 77 K. The solute was compound II (2 × 10^{-4} M); excitation wavelengths were 280 or 320 nm (——), 320 nm (- - -).

steric interaction brought by the methyl group and this H_6'–carbonyl interaction is favored.[5] However, Gribble and Bousquet report that this preferential conformation is greatly perturbed by the hydrogen bonding ability of the solvent (the greater its hydrogen bonding ability the less the deshielding effect for H_6'). The effect of 2% 2-propanol on the low temperature fluorescence spectrum in isopentane is probably due to intramolecular hydrogen bond formation between the carbonyl of the amide group and 2-propanol molecules. As shown by the NMR results[5] this hydrogen bond formation causes drastic changes in the weak H_6'–carbonyl interaction which may result in the quenching of the 460-nm fluorescence.

Compound I which is the formamido derivative shows no composite fluorescence spectrum in isopentane since, in this case, the steric hindrance for rotation around the C–N bond is unlikely as shown by molecular models and the H_6'–carbonyl interaction is not favored.

Special attention must be devoted to the effect of increasing the $CaCl_2$ concentration on the 510-nm fluorescence intensity obtained in ethanolic solutions of II (or I). In Figure 4 is reported the 510-nm fluorescence intensity evolution in ethanol as a function of the $CaCl_2$ concentration. It is obvious that $[CaCl_2] > 0.1$ M appreciably quenches the 510-nm fluorescence. At this $CaCl_2$ concentration, the average distance between chromophore molecules and inorganic ions is estimated to be ~1.2 nm. One may suggest that neighboring strongly basic Cl^- ions act as traps for the reversible proton transfer via short-range Coulombic interactions. As the room temperature optical absorption spectrum of the anilides is totally independent of the $CaCl_2$ concentration up to $[CaCl_2] = 4$ M we may assume that there is no complex formation between ortho-substituted anilides and Ca^{2+} ions. Furthermore it must be noted that Ca^{2+} ions are generally known as poorly complexing ions. They only form complexes with strong complexing agents such as EDTA.

In addition we will see below that adding calcium chloride has striking effects on the phosphorescence emission. This may indicate that other explanations may prevail to account for the observed effects on the 510-nm fluorescence inhibition.

Compounds III and IV have no detectable fluorescence emission whatever the solvent. This is similar to the room temperature results and consistent with the excited state proton transfer hypothesis.[4]

II. *Phosphorescence Spectroscopy.* (a) *General Spectral Properties.* Table I shows that the phosphorescence emission is shifted to the red in going from polar to nonpolar solvent for all compounds under investigation. As the solvent polarity decreases one observes

TABLE I: Phosphorescence Emission λ_{max} (nm) in Various Solvents[a] at 77 K

Compd	4 M $CaCl_2$ in EtOH or water	WEG	MeOH, EtOH, 2-PrOH	Isopentane
I	440	440	450	490
II	455	460	460	500
III	440	450	460	470
IV	445	465	480	490

[a] MeOH = methanol, EtOH = ethanol, 2-PrOH = 2-propanol. Phosphorescence spectra have been recorded using a phosphoroscope. Solute concentration: [I] = [II] = 2 × 10^{-4} M, [III] = [IV] = 5 × 10^{-4} M. Excitation wavelengths = 320 nm for I and II, and 290 nm for III and IV.

TABLE II: Relative Phosphorescence Quantum Yield in Various Solvents[a]

Compd	4 M $CaCl_2$ in water	WEG	Alcohols	Isopentane
I	1	0.30	0.02	0.02
II	1	0.30	0.02	0.02
III	1	0.76	0.35	0.03
IV	1	0.75	0.34	0.02

[a] Temperature, excitation wavelengths, and concentration conditions are the same as in Table I.

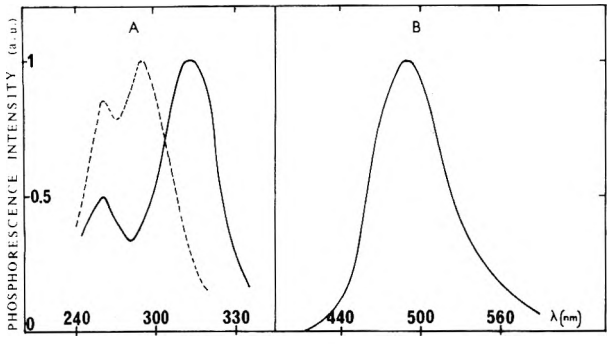

Figure 5. (A) Phosphorescence excitation spectrum of compounds I (2 × 10^{-4} M) (——) and IV (5 × 10^{-4} M) (- - - -) in isopentane at 77 K; observation wavelength 490 nm. (B) Corresponding phosphorescence spectrum of I and IV in isopentane at 77 K; excitation wavelength 290 or 320 nm.

a reduction in the phosphorescence quantum yield (Table II).

The phosphorescence excitation spectra of I, III, and IV resembles their optical absorption spectra with two distinct maximums at λ_{max} 320 and 260 nm (for I) and λ_{max} 290 and 260 nm (for III and IV) (Figure 5). As reported for *N*-formylkynurenine derivatives[4] the phosphorescence quantum yield of I and III is wavelength dependent while that of compound IV remains apparently constant. The wavelength dependence is deduced from the comparison of excitation and absorption spectra in various solvents (see ref 4).

(b) *Some Special Properties of Compound II.* As far as compound II is concerned, examination of its phosphorescence excitation and emission spectra in various solvents shows some interesting properties.

In an "inert" nonpolar solvent (isopentane) its phosphorescence maximum is located at 500 nm while its phosphorescence excitation spectrum looks like the optical absorption spectra with two maximums at 320 and 260 nm (Figure 6). It thus seems reasonable to associate the 460-nm fluorescence (see above) with this phosphorescence. Addition of 2% 2-propanol (in volume) to the isopentane

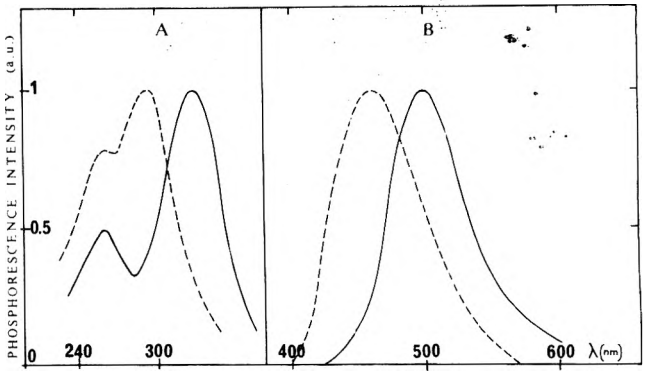

Figure 6. (A) Compound II phosphorescence excitation spectrum in isopentane (——) and isopentane + 2% 2-propanol (- - - -); observation wavelengths 500 nm (——) and 460 nm (- - - -); solute concentration 2 × 10^{-4} M; temperature 77 K. (B) Corresponding phosphorescence spectrum in isopentane (——) or isopentane + 2% 2-propanol (- - - -); excitation wavelengths 320 nm (——) or 290 nm (- - - -).

solution leads to a blue shift in the phosphorescence excitation spectrum (Figure 6) in contrast to the *fluorescence* excitation spectrum which shows no change upon 2-propanol addition. The same phosphorescence excitation spectrum is observed in ethanol or WEG. In ethanol except at high concentration, this phosphorescence excitation spectrum is concentration independent (5×10^{-5} M < *C* < 8×10^{-4} M) and is somewhat similar to the one observed with compounds III and IV where intramolecular hydrogen bond formation has been inhibited by methylating the acetamido or formamido group ($N-CH_3$ derivatives). Beside steric hindrance considerations, the replacement of the hydrogen (formamido derivative) by a methyl group (acetamido derivative) may favor the formation of complexes between alcohol molecules and the amide group because the small donor character of the methyl group should increase the negative charge on the amide carbonyl oxygen and its ability to form hydrogen bonds with hydroxyl-containing solvents.

It must be noted that the occurrence of two different excitation spectra for the fluorescence and the phosphorescence emission of compound II is not very surprising. Since addition of 2% 2-propanol leads to a *fluorescence* emission peaking at 510 nm it is reasonable to admit that no phosphorescence emission can be associated with excited state proton transfer. The 460-nm phosphorescence emission observed in isopentane + 2% 2-propanol (or alcoholic solvents) (Figure 6) must be attributed to the complexed species obtained via intermolecular hydrogen bond formation with alcohol molecules. As already suggested by Callis and Wilson[11] in order to explain the emission properties of Michler's ketone, the study of the luminescence properties of aromatic carbonyls is a way of investigating their microenvironment. It is likely that several emitting species are present in the vitreous solution leading to complex phosphorescence spectra which may be resolved into separate emissions (Michler's ketone) or not (the present case). The sensitivity of the luminescence technique makes it possible to detect them, even is small amounts, by studying luminescence excitation spectra.

The effect of microenvironment on the phosphorescence emission properties of compound II can be also shown using calcium chloride as a perturbent. The presence of $\sim 10^{-2}$ M $CaCl_2$ in ethanol (or WEG) induces a *blue* shift of the phosphorescence emission spectrum and dramatic changes in the phosphorescence excitation spectrum which progressively shifts to the *red* (Figure 7). Under the same conditions, as indicated above, the room temperature

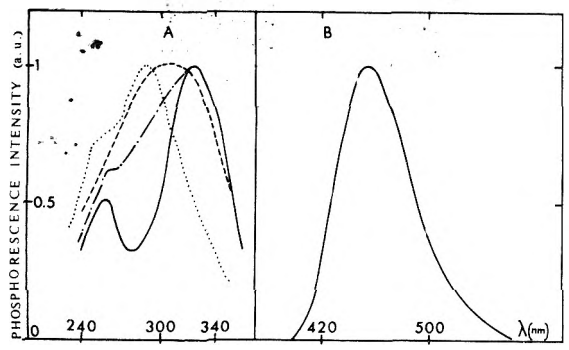

Figure 7. (A) Compound II phosphorescence excitation spectrum in ethanol at 77 K as a function of the $CaCl_2$ concentration; observation wavelength 455 nm; solute concentration 2×10^{-4} M: $0 < [CaCl_2] \leq 1.25 \times 10^{-2}$ M (· · · · ·); $[CaCl_2] = 2.5 \times 10^{-2}$ M (- - - -); $[CaCl_2] = 5 \times 10^{-2}$ M (– · – · –); 0.1 M $< [CaCl_2] <$ 4 M (——). (B) Corresponding phosphorescence spectrum in the $[CaCl_2]$ range 0–4 M; excitation wavelengths 290 nm (· · · · · ·), 290 or 320 nm (- - - - -) (– · – · –) (——).

optical absorption spectrum shows no change upon calcium chloride addition. Finally, the phosphorescence excitation spectrum at $[CaCl_2] \geq 1$ M is the same as the one observed in isopentane (Figure 6). These spectral changes are accompanied by a large increase in the phosphorescence quantum yield (Figure 4). This is also true for I, III, and IV (see Table II). This effect resulting in an increase in the phosphorescence quantum yield is somewhat similar to the room temperature results obtained by Busel et al.[12] on the fluorescence of indoles. These authors observed that, in strongly alkaline solution, salt addition increases the indole fluorescence quantum yield. They attributed this effect to a partial desolvation of the chromophore molecules because the inorganic ions may "tie up" solvent molecules responsible for fluorescence quenching. It was also suggested that inorganic ions polarize solvent molecules constituting the solvation shell near the chromophore and thus change the efficiency of reversible photochemical events or charge transfer between the solvent and the excited chromophore.

The low temperature luminescence study on compound II clearly indicates that the presence of calcium chloride inhibits excited state proton transfer and, at least partially, complex formation between solvent molecules and II. The large phosphorescence quantum yield increase may thus be due, in part, to the quenching of excited state proton transfer since it is known that excited state proton transfers are a source of nonradiative deactivation pathways.[13] However, compounds III and IV which exhibit no excited state proton transfer show some phosphorescence yield enhancement upon $CaCl_2$ addition (note in Table II the much higher relative phosphorescence yield for III and IV in WEG or alcohols). The fact that in ethanol–1 M $CaCl_2$ the phosphorescence excitation spectrum looks like the one observed in isopentane is in favor of a "partial" desolvation of the chromophore. However, such a "desolvation" cannot account for the observed increase in the phosphorescence quantum yield for the latter is rather low in isopentane (see Table II) where solvation is expected to be very weak. ESR experiments performed with randomly oriented triplet molecules of compounds I and II in ethanol indicate that the zero field splitting parameter $D^* = (D^2 + 3E^2)^{1/2}$[14] is very sensitive to the presence of $CaCl_2$ (see Table III). The increase in the D^* value in going from ethanol to ethanol–1 M $CaCl_2$ is in keeping with the inhibition of anilide–solvent complex formation by $CaCl_2$ since the smaller the D^* the greater the electron delocalization in the triplet state. Of course this interpretation is valid if one rules out the

TABLE III: Zero field Splitting Parameter D^* of the Triplet State of Compound II (10^{-3} M) in Ethanol as a Function of the Calcium Chloride Concentration[a]

$CaCl_2$ concn M	D^*
0	0.097 14
5×10^{-4}	0.114 30
1	0.115 54

[a] Temperature 77 K, excitation wavelengths ⩾250 nm. The relative uncertainty is ⩽5%.

TABLE IV: Lifetimes Characterizing the Dual Phosphorescence Emissions of Compounds I, II, III, and IV[a]

	τ_1, ms	τ_2, ms
I	100	500
II	60	500
III	<20	100
IV	<20	125

[a] See text. Temperature, excitation wavelength, and concentration conditions are the same as in Table I.

possibility of complex formation between Ca^{2+} and anilides (see section I,b). Complex formation might explain several things: (1) enhancement of phosphorescence, possibly by a "heavy atom effect"; (2) prevention of H transfer; (3) shifting phosphorescence excitation spectrum (Figure 7); (4) increased ZFS (Table II).

(c) *Lifetime Measurement.* For all ortho-substituted anilide derivatives, the phosphorescence decay kinetics can be decomposed into two exponential stages (see Table IV and ref 4). This results is not surprising in itself for many aromatic carbonyls exhibit anomalous phosphorescence decay kinetics.[15,16] The lifetimes are practically solvent independent for a given compound, however, the short-lived component is almost inhibited in the presence of calcium chloride.

The mechanism of anomalous low temperature phosphorescences in aromatic carbonyls is still open to question. Griffin[17] explained these properties in terms of coexistent $n\pi^*$, $\pi\pi^*$, and CT triplet states. However, since the molecular relaxation time is $\sim 10^{-12}$ s[18] this explanation seems unlikely.[11] It seems more probable that anomalous phosphorescence decays occur because the solute molecules are surrounded by different types of environments.[11]

As far as the present study is concerned, the presence of various molecular species can be rather well established using NMR data or phosphorescence spectral characteristics. As shown above, in alcoholic solvents, intermolecular bond formation occurs with probably all derivatives leading to different emitting species, at high concentration ($\geq 8 \times 10^{-4}$ M) aggregation may also occur (see above) which should complicate the matter further.

In nonpolar solvents, NMR results[5] indicate that compounds I or II exist as three isomeric species whose concentration depends upon the amide group substituent (see above). Accordingly, NMR data regarding III and IV show that there exist two rotameric forms which coalesce at about 80 °C.[9]

From Table IV, it can be seen that the phosphorescence lifetimes are much smaller for III or IV than for I and II. In the former compounds it seems reasonable to assume that the shortest lifetime corresponds to a $n\pi^*$ triplet state while the longest would be a $\pi\pi^*$ triplet state. One must remember that although the $S_0 \rightarrow S_1$ transition is $n\pi^*$ in nature (in view of the solvent effects) the molar extinction coefficient are too high for a pure $n\pi^*$ transition and thus mixing with $\pi\pi^*$ or CT states is probable.[6] This means that at the triplet level we should expect that a $\pi\pi^*$ state

lies above, but close to, a $n\pi^*$ one. However *inter*molecular hydrogen bonding or *intra*molecular interaction may change the relative position of both triplets and then the emitting triplet state could be of $\pi\pi^*$ nature. As far as compounds III and IV are concerned, it must be noted that in isopentane the singlet–triplet splitting (ΔE_{ST}) is quite large for $n\pi^*$ states ($\sim$11 000 cm^{-1}). As generally assumed[14] the magnitude of ΔE_{ST} parallels the overlap density of the nonbonding oxygen orbital and the π^* molecular orbital. In other words, the smaller the charge transfer which accompanies $n\pi^*$ transitions the greater the ΔE_{ST} value. One may tentatively suggest that the presence of a substituted amide group considerably affects the *o*-carbonyl oxygen electronegativity. However there is additional evidence that compounds III and IV have $n\pi^*$ triplet states for room temperature laser flash photolysis studies[9] indicate that these triplet states are efficiently quenched by 2-propanol or ethanol which support their $n\pi^*$ character.[19] On the other hand, compound I or II triplet state does not react with alcohol molecules which is in agreement with their $\pi\pi^*$ character as evidenced by their long lifetime at low temperature.

Conclusion

The low temperature luminescence of the acetyl formanilides or acetyl acetanilides under study displays some interesting features. As other carbonyl compounds, their luminescence properties are very sensitive to their microenvironment and dual phosphorescence emissions are observed due to the presence of solute molecules in different solvation and/or conformational states.

The acetyl 2′-acetanilide derivative is particularly interesting in view of the extreme sensitivity of its fluorescence emission and phosphorescence excitation spectra to intermolecular interaction with hydroxylic solvent molecules. This sensitivity suggests that it might be used as a luminescent probe for testing microenvironments in macromolecules (proteins for instance).

It is worth pointing out the large increase in the phosphorescence quantum yield of all studied compounds upon salt addition in ethanol solutions. This salt effect is believed to be due to the perturbation of the solvation shell of the phosphorescence solute molecules by the inorganic ions. Since salt addition has been also shown to increase the fluorescence yield of other aromatic compounds at room temperature,[12] this effect is probably of general significance and deserves further interest.

Acknowledgment. It is a pleasure to thank Drs. Tatischeff and Klein (Institut du Radium, Paris) for making it possible to use their variable temperature setup. We also wish to express our gratitude to Dr. Chachaty (C.E.N., Saclay) for his help in the ESR experiments.

References and Notes

(1) P. Walrant and R. Santus, *Photochem. Photobiol.*, **19**, 101 (1974).
(2) P. Walrant and R. Santus, *Photochem. Photobiol.*, **20**, 455 (1974).
(3) P. Walrant, R. Santus, and M. Charlier, *Photochem. Photobiol.*, **24**, 13 (1976).
(4) M. P. Pileni, P. Walrant, and R. Santus, *J. Phys. Chem.*, **80**, 1804 (1976).
(5) G. W. Gribble and F. P. Bousquet, *Tetrahedron*, **27**, 3785 (1971).
(6) M. P. Pileni, P. Walrant, and R. Santus, *Chem. Phys. Lett.*, **42**, 89 (1976).
(7) G. Porter and P. Suppan, *Trans. Faraday Soc.*, **62**, 3375 (1967).
(8) N. D. Cheronis and J. B. Entrikin, "Semimicro Qualitative Organic Analysis", Interscience, New York, N.Y., 1957.
(9) M. Giraud, M. P. Pileni, A. Valla, and R. Santus, *J. Chim. Phys.*, in press.
(10) M. Aubailly, M. Bazin, and R. Santus, *Chem. Phys.*, **2**, 203 (1973).
(11) P. R. Callis and R. W. Wilson, *Chem. Phys. Lett.*, **13**, 417 (1972).
(12) E. P. Busel, T. L. Bushueva, and E. A. Burshtein, *Opt. Spectrosc. (Engl. Trans.)*, **32**, 158 (1972).
(13) H. Shizuka, K. Matsui, T. Okamura, and I. Tanaka, *J. Phys. Chem.*, **79**, 2731 (1975).
(14) S. P. McGlynn, T. Azumi, and M. Kinoshita in "Molecular Spectroscopy of the Triplet State", Prentice-Hall, Englewood Cliffs, N.J., 1969.
(15) Y. Tanimoto, N. Hirota, and S. Nagakura, *Bull. Chem. Soc. Jpn.*, **48**, 41 (1975).
(16) N. C. Yang and S. Murov, *J. Chem. Phys.*, **45**, 4358 (1966).
(17) R. N. Griffin, *Photochem. Photobiol.*, **7**, 159 (1968).
(18) P. M. Rentzepis, *Chem. Phys. Lett.*, **3**, 717 (1969).
(19) T. S. Godfrey, G. Porter, and P. Suppan, *Discuss Faraday Soc.*, **39**, 194 (1965).

A Sodium-23 Nuclear Magnetic Resonance Study of the Exchange Kinetics of Na^+ with 2,2,2-Cryptate Complexes in Water, Ethylenediamine, Tetrahydrofuran, and Pyridine

Joseph M. Ceraso, Patrick B. Smith, J. Steven Landers, and James L. Dye*

Department of Chemistry, Michigan State University, East Lansing, Michigan 48823 *(Received November 4, 1976)*

Publication costs assisted by the U.S. Energy Research and Development Administration

The measurement conditions and data treatment used to obtain accurate rate constants and activation energies from ^{23}Na pulsed Fourier transform data are described in detail. Application is made to the exchange of Na^+ between the free state and the complex with 2,2,2-cryptand in four solvents. The exchange proceeds via dissociation of the complex. Activation enthalpies of 12.3, 13.6, 13.8, and 16.1 kcal mol^{-1} and activation entropies of −7.6, −12.6, −8.1, and +5.3 cal mol^{-1} deg^{-1} were obtained for the release of Na^+ from the 2,2,2-cryptate complex in ethylenediamine, pyridine, tetrahydrofuran, and water, respectively.

Introduction

Macrocyclic polyethers (crown ethers), first synthesized by Pedersen,[1] and macroheterobicyclic diamines (cryptands) first synthesized by Lehn et al.[2] form very stable complexes with alkali metal and alkaline earth metal cations. X-Ray structure determination of cryptate complexes formed from the macrobicyclic hexaoxadiamine $N(CH_2CH_2OCH_2CH_2OCH_2CH_2)_3N$, ($C_{222}$), 1, and alkali metal salts show that the alkali metal cation is contained within the central cavity of the ligand.[3,4] Association

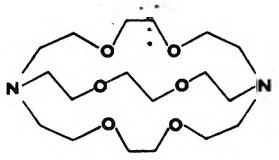

1

constants for complex formation between many of the synthetic complexing agents of both the crown and cryptand class and a variety of metal salts are known for aqueous solutions.[2,5-13] Except for association constants in methanol, very few thermodynamic or rate data have been obtained in nonaqueous solvents. Some rate data exist for the exchange of metal ions between solvated and bound sites.[13,14-24] Exchange rates at the coalescence temperature were reported from ^1H NMR studies on D_2O solutions which contain C_{222} and half the stoichiometric amount of alkali metal salt.[14] From these results it was clear that sodium cation exchange should be slow enough to be observed directly by using ^{23}Na NMR. Ceraso and Dye[19] investigated the kinetics of complexation reactions of Na^+C_{222} cryptates in ethylenediamine (EDA) solutions by using ^{23}Na NMR techniques. Their work is the first example of sodium cation exchange which is slow enough to exhibit clearly defined separate signals for two environments. Cahen et al.[23] studied the Li^+–cryptate exchange kinetics in water and in several nonaqueous solvents. Cryptands smaller than C_{222} were used. Recently, Loyola, Wilkins, and Pizer[13] measured the kinetics of complexation of Ca^{2+} by three cryptands by using a stopped-flow technique. The kinetics of complexation of crown ethers with sodium and potassium cations have been studied in several solvents by using ^{23}Na and ^{39}K NMR line shape analysis.[15,20,24] Since for the crown case the chemical shift between the free and bound site is negligible compared to the ^{23}Na and ^{39}K line width of the bound site and since the line width for the bound site is extremely broad, these experiments only gave one apparent resonance. Under these conditions, it was possible to reduce the complete line shape expression for two site chemical exchange to a single Lorentzian line shape function. This is a special case of the general treatment to be discussed later.

In this paper we report a detailed analysis of the temperature dependence of sodium ion exchange in the presence of C_{222} in H_2O, EDA, tetrahydrofuran (THF), and pyridine (py) solutions. Line shapes are calculated from the exact expression (derived from the Bloch equations) for general two site exchange of uncoupled spins. The calculated line shapes are fitted to the experimentally observed line shapes with the aid of a generalized weighted non-linear least-squares program.[25]

We have chosen to use the ^{23}Na pulsed Fourier transform (FT) technique because the advantages over continuous wave NMR techniques are threefold: (1) no modulation distortion occurs; (2) no saturation broadening occurs; and (3) signal averaging is accomplished in a much shorter time period. Despite the low sensitivity of ^{23}Na NMR compared to that of ^1H NMR, its use has two major advantages over ^1H NMR: (1) the chemical shift range of sodium nuclei is much greater than that of protons and (2) deuterated solvents are not required.

Experimental Section

C_{222} used in this work was synthesized by a modification of the method of Dietrich, Lehn, and Sauvage.[2,6] EDA was purified by fractional freezing followed by distillation from Na–K alloy.[27] Tetrahydrofuran (THF) was dried over CaH_2 and distilled from a mixture of NaK and benzophenone. Pyridine was refluxed over granulated barium oxide and then fractionally distilled in a nitrogen atmosphere. Water was of conductance quality. Reagent grade NaBr, NaI, and $NaPh_4B$ were dried and used without further purification.

Samples were prepared in a drybox or glove bag under an inert atmosphere of dry nitrogen or argon. Thin-wall high-resolution NMR tubes (10-mm o.d.) purchased from Wilmad Glass Co. were modified by placing a standard ground glass joint at the open end to provide an air-tight seal.

Measurements were made at 15.87 MHz with a home-built, single-coil, multi-nuclear pulse spectrometer, which employed a Varian DA-60 magnet and console. A small external probe which contained doped water (line width $\approx$ 4 Hz) was constructed and placed 1.5 to 2.5 cm from the sample. The Varian proton lock circuitry was used to lock the magnetic field. In this manner, the maximum drift was less than 6 Hz during an 8-h period. Samples were referenced to saturated aqueous NaCl at 25 °C by the substitution method. Experiments were controlled by a 1080 Nicolet computer which was coupled to a Diablo magnetic disk system. Temperature was measured with a calibrated Doric digital thermocouple to within ±1 °C.

Free induction decays were stored on a magnetic disk. The digital data were Fourier transformed without applying smoothing or exponential weighting. The transformed data were punched onto paper tape and then onto standard keypunch cards for treatment with a CDC 6500 computer.

General Features of ^{23}Na NMR. The sodium nucleus has a spin $I = 3/2$ and it possesses a quadrupole moment (Q = 0.10 b).[28] As with most nuclei of spin >1/2, the dominant relaxation mechanism is quadrupolar and occurs through molecular reorientation of the solvent. The quadrupole relaxation rate for a nucleus in the motionally narrowed limit ($\omega\tau_c << 1$) is given by[29]

$$\frac{1}{T} = \frac{3}{40}\frac{2I+3}{I^2(2I-1)}\left(1+\frac{\eta^2}{3}\right)\left(\frac{eQ}{\hbar}\frac{\partial^2 V}{\partial Z'^2}\right)^2\tau_c \qquad (1)$$

where I is the spin of the nucleus, η is the asymmetry parameter (η = 0 for a symmetric field gradient), Q is the quadrupole moment of the nucleus, $\partial^2V/\partial Z'^2$ is the Z component of the electric field gradient at the nucleus produced by solvent fluctuations, and τ_c is the correlation time which characterizes these fluctuations. For solutions ($\omega\tau_c << 1$), $T_1 = T_2$, the resonance line shape is Lorentzian and the line width $\Delta\nu^{1/2}$ (full-width at half-height in Hz) $= 1/\pi T_1$. The information obtained from the line width contains the product $[(eQ/h)(\partial^2V/\partial Z'^2)]^2\tau_c$. When τ_c can be derived from other measurements, the field gradient $\partial^2V/\partial Z'^2$ can be evaluated.[21] For a simple process one would expect that $\tau_c = A'e^{-E_r/RT}$[28] where E_r is an activation energy for solvent reorganization. If the value of the quadrupolar coupling constant $[(eQ/h)(\partial^2V/\partial Z'^2)]$ is assumed not to change with temperature, then the relaxation process will vary exponentially as a function of temperature. This behavior is observed for H_2O, EDA, and THF but not for py.

For many monodentate liquids the infinitely dilute sodium line width varies from 4 to 30 Hz at 25 °C. When the cation is placed in an environment which does not have cubic symmetry, such as within the cavity of an 18-crown-6 polyether in solution, the line width increases by large amounts (approximately 25 times the free cation line width in methylamine, for example). This increase is caused by

TABLE I: Selected Chemical Shifts of Free and Cryptated Sodium Ions in Several Solvents

Concn, M	Temp, °C	Solvent	$\delta(Na_s^+$ vs. $Na^+_{\infty dil,H_2O})$
0.2 NaI	21.2	H_2O	−0.1
0.2 Na^+C,I^-	25.0	H_2O	+8.6
0.6 Na^+Br^-	26.3	EDA	−13.7
0.3 Na^+C,Br^-	26.6	EDA	+10.7
0.4 $NaPh_4B^-$	25.7	THF	+7.5
0.2 Na^+C,Ph_4B^-	25.1	THF	+12.0
0.2 $Na^+Ph_4B^-$	22.6	py	−0.9
0.2 $Na^+Ph_4B^-$	25.5	py	+12.4

the asymmetry of the electric field at the sodium nucleus because of the planar structure of 18-crown-6. When a bicyclic ligand such as C_{222} is used, the Na^+C_{222} line width is <100 Hz at 25 °C, indicating that the electric field produced by C_{222} is much more symmetric than that produced by crown complexes.

Solvated cations undergo large paramagnetic shifts from the gaseous cations.[33] Changes in the diamagnetic shielding constant σ_D as a function of solvent are expected to be small compared to changes in the paramagnetic shielding constant σ_P.[34,35] The change in total shielding σ_T for Na^+ (at infinite dilution) in H_2O vs. Na gas is −60.5 ppm (σ_T gaseous atom = 0),[33] whereas σ_T for Na^+ gas vs. Na gas is calculated to be only −5.1 ppm.[36] Solvent interaction with the cation introduces angular momentum into the wave function and causes a paramagnetic shift. For sodium, the magnitude of the chemical shift has been shown to correlate well with the Gutmann donor number of the solvent.[30,31] The Gutmann donor number of a solvent is a measure of its strength as a Lewis base.[32] The solvent effect upon chemical shift occurs primarily in the first solvation or coordination layer of the sodium cation. Because of this, the chemical shifts of Na^+C_{222} (and Li^+C_{211}) are nearly independent of solvent, whereas those of Na_s^+ are strongly solvent dependent (see Table I).

Determination and Interpretation of the Line Shape Function. The Bloch equations which describe the motion of the x and y components of magnetization in the rotating frame can be modified to include chemical exchange.[37,38] The solutions for slow passage conditions and for transient conditions have been shown to form a Fourier transform pair.[39,40] The shape function, adapted for our case of Fourier transform spectroscopy, may be written as

$$G(\omega) = K\{I \cos(\theta_0 + \theta') - R \sin(\theta_0 + \theta')\} + C \quad (2)$$

$$I = \frac{SU + TV}{S^2 + T^2}; \qquad R = \frac{UT - SV}{S^2 + T^2} \quad (3)$$

$$S = \frac{P_A}{T_{2A}} + \frac{P_B}{T_{2B}} + \frac{\tau}{T_{2A}T_{2B}} - \tau(\omega_A + \Delta - \omega)(\omega_B + \Delta - \omega) \quad (4)$$

$$U = 1 + \tau\left(\frac{P_B}{T_{2A}} + \frac{P_A}{T_{2B}}\right) \quad (5)$$

$$T = P_A\omega_A + P_B\omega_B + \Delta - \omega + \tau\left(\frac{\omega_A + \Delta - \omega}{T_{2B}} + \frac{\omega_B + \Delta - \omega}{T_{2A}}\right) \quad (6)$$

$$V = \tau[P_B\omega_A + P_A\omega_B + \Delta - \omega] \quad (7)$$

$$\tau = \frac{\tau_A\tau_B}{\tau_A + \tau_B} \quad (8)$$

$$P_A = \frac{\tau_A}{\tau_A + \tau_B}; \qquad P_B = \frac{\tau_B}{\tau_A + \tau_B} \quad (9)$$

where I represents the absorption mode line shape and R represents the dispersion mode line shape. ω_A, ω_B and T_{2A}, T_{2B} are the Larmor frequencies and transverse relaxation times of sites A and B in the absence of exchange. P_A and P_B are the relative populations in sites A and B. The other terms are defined below. Equation 2 predicts the line shape throughout the entire range of exchange from the slow limit to the fast limit.

In order to evaluate exchange times (τ) through application of eq 2, we must first obtain information about the Larmor frequencies and transverse relaxation times for sites A and B in the absence of exchange. (A denotes a solvated sodium cation and B denotes a cryptated sodium cation.) In addition, the populations, P_A and P_B, for exchanging systems must also be known. In many studies of systems which undergo two-site chemical exchange, ^1H and ^{13}C NMR line shape analysis is used to obtain τ values. In some studies the assumption $1/T_{2A} = 1/T_{2B} = 0$ is made. This assumption is not justified for sodium since the transverse relaxation times are usually much smaller than those of ^1H or ^{13}C and contribute significantly to the observed NMR line shapes.

Since the equilibrium constant (K_a) for complex formation between Na^+ and C_{222} is large ($K_a > 10^3$) in all solvents used and at all temperatures, P_A and P_B are directly determined from the mole ratios of C_{222} and sodium salt added to solution.

To obtain ω_A, ω_B, T_{2A}, and T_{2B} in the absence of exchange, two solutions in each solvent were prepared. The first contained sodium salt with no C_{222} and the second contained equimolar sodium salt and C_{222}. Since K_a is large, the second solution contained only bound sodium cations. Chemical exchange is absent since no unbound sites are available. The ^{23}Na NMR of each of these solutions was studied as a function of temperature (see Table I). All experimental line shapes were Lorentzian within experimental error. The values of ω and T_2 were determined in each case by fitting a Lorentzian line to the observed signal. Complete characterization of the Lorentzian signal obtained by the Fourier transform NMR technique requires the determination of six parameters. These are the amplitude, K, the Larmor frequency, ω_0, the line width parameter, T_2, the height of the baseline, C, the zero-order phase correction, θ_0, and the first-order phase correction, θ'. The zero-order phase correction is independent of frequency and determines the contribution of dispersion and absorption mode signals to the observed line shape. The first-order phase correction varies linearly with frequency (and hence channel number, j) according to $\theta' = \theta_1(j/N)$ in which N is the total number of channels in the spectrum and θ_1 is the total change in phase over the entire spectrum. In terms of these parameters, the intensity is given as a function of frequency by

$$G(\omega) = \frac{KT_2}{1 + T_2^2(\omega_0 - \omega)^2}\{\cos(\theta_0 + \theta') - T_2(\omega_0 - \omega)\sin(\theta_0 + \theta')\} + C \quad (10)$$

Commonly, the phase parameters and the baseline position are instrumentally adjusted by visual inspection so that one obtains a symmetric absorption-mode signal with a zero baseline. The value of θ_1 is constant for given instrument settings and may be accurately determined by measuring the signal from a reference sample at several different magnetic field settings which span the entire frequency range to be used. Once θ_1 is evaluated in this way it does not change from sample to sample and was therefore not used as an adjustable parameter. By contrast, θ_0 is influenced not only by instrument settings, but

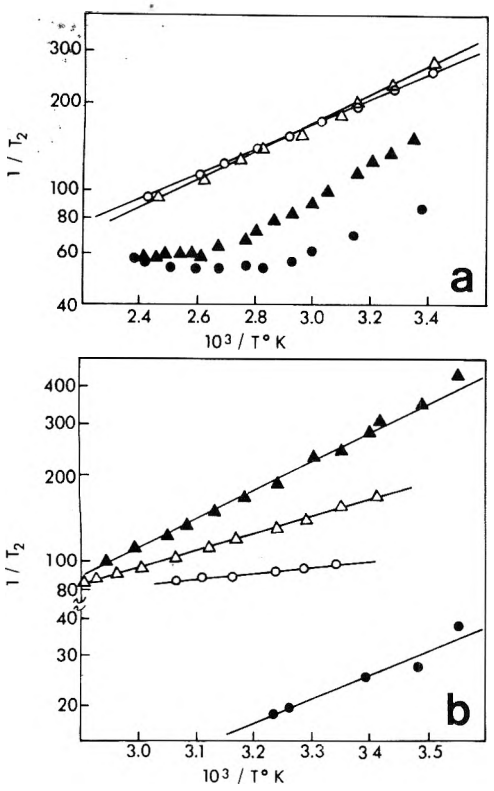

Figure 1. Reciprocal transverse relaxation times for free and complexed Na^-: (a) O, free Na^+ in EDA; Δ, complexed Na^+ in EDA; ●, free Na^+ in py, ▲, complexed Na^+ in py; (b) O, free Na^+ in THF; Δ, complexed Na^- in THF; ●, free Na^+ in H_2O; ▲, complexed Na^+ in H_2O.

also by sample position, temperature, etc., and therefore it must be adjusted for each sample.

Since the parameters must always be adjusted (either numerically or instrumentally), we have chosen to evaluate all parameters except θ_1 by fitting the Lorentzian equation (10) to the observed spectrum by a non-linear least-squares procedure. The equation fit the data within experimental error and with random residuals. Figure 1 shows semilog plots of the observed relaxation rates (corrected for inhomogeneities) vs. reciprocal absolute temperature. Straight lines are observed for THF, EDA, and H_2O solutions but not for py solutions. The origin of the deviation from a straight line for py solutions is unknown but it might be caused by changes in contact ion-pair formation with temperature or changes in the quadrupole coupling constant. In any event, direct determination of the parameters for the nonexchanging case should yield reliable data for treatment of exchange.

The Larmor frequencies show only a slight dependence upon temperature ($\lesssim$1 ppm over the entire temperature range studied for each solvent). The value of ω at any temperature between those examined was determined by graphical interpolation. A sample of saturated aqueous sodium chloride at 25 °C was used as an external reference for both chemical shift and line width calibrations. Line width contributions from magnetic field inhomogeneities ranged from 2 to 6 Hz and were for all cases except aqueous solutions a small fraction of the measured width. Inhomogeneous line broadening varied from one set of experiments to the next. The inhomogeneous contribution to the line width was determined for each set of experiments by using an aqueous reference sample with a known natural relaxation time according to

$$(1/T_2)_{\text{inhom}} = (1/T_2)_{\text{obsd}} - (1/T_2)_{\text{nat}}$$

This value was then added to the previously determined value of $(1/T_2)_{\text{nat}}$ for each of the sites so that the values of $1/T_{2A}$ and $1/T_{2B}$ used in eq 2 included both the natural contribution to the line width and the inhomogeneous contribution.

The evaluation of the exchange time, τ, by application of eq 2 requires the determination of six parameters. These are the amplitude, K, baseline position, C, zero-order phase correction, θ_0, first-order phase correction, θ', frequency shift, Δ, and exchange time, τ. Again, the first-order phase correction was directly measured for each set of instrumental settings. Five parameters were adjusted to obtain the best fit of eq 2 to the observed data. The frequency shift parameter, Δ, was introduced because of experimental difficulties with referencing *absolute* frequencies from one set of data to the next. The *relative* chemical shifts at the two sites were not adjusted. The errors in precise referencing of one set of data to another were caused by the method of exernal referencing. If an internal reference in each sample and an internal lock had been employed, there would be no need for the correction term Δ. This frequency shift parameter allows the absolute frequency in eq 2 to shift, without changing the shape of the function. The average absolute value of Δ was found to be 0.37 ppm.

The mean lifetime, τ, together with P_A and P_B, contains all of the kinetics information. For each spectrum analyzed, 90 to 99 data points were used to determine τ. The program used (KINFIT)[25] gave complete statistical information about the fit to the data, including standard deviation estimates for each of the parameters and the multiple correlation coefficient, which gives a measure of the coupling of each parameter to all of the others. Coupling between τ and the other four parameters was lowest at intermediate rates of exchange ($\tau \approx \sqrt{2}/(\omega_A - \omega_B)$). This is expected, since τ has its greatest influence upon the line shape in the intermediate region of exchange.

Results and Discussion

Many sources of systematic error can arise when the Fourier transform NMR technique is used. These can cause distortion of the observed line shapes. Some sources are pulse feed-through, the first-order phase correction, and narrow-band audio filtering. The effects that they produce can sometimes be eliminated instrumentally and/or the calculated line shape can be modified to include these effects. For example, our calculated NMR line shapes included the first-order phase correction. It is not at all obvious by inspection of the spectra what first-order phase correction is needed. This is because a single line spectrum can be phased to appear as an absorption mode signal by using only the zero-order phase correction. Even in the case of a broad doublet, the spectrum can be visually phased to an apparent absorption mode signal without using a first-order phase correction. By contrast, ^{13}C NMR spectra usually exhibit many narrow lines which span the entire frequency range sampled. In this case visual evaluation of the first-order phase correction is easily made. The first-order phase correction will have its maximum effect on the line shape for an exchanging system at the slow exchange limit (low temperatures), where the spectral intensities are spread out over a broad frequency range.

Failure to make such a correction usually gives only small differences between the calculated and observed line shapes. In addition, as shown in Figure 2, straight line Arrhenius plots result in either case, but with different activation energies. The experimental data are the same for both sets of calculations shown in Figure 2 but the τ values were evaluated with and without first-order phase correction. This shows that failure to make the proper

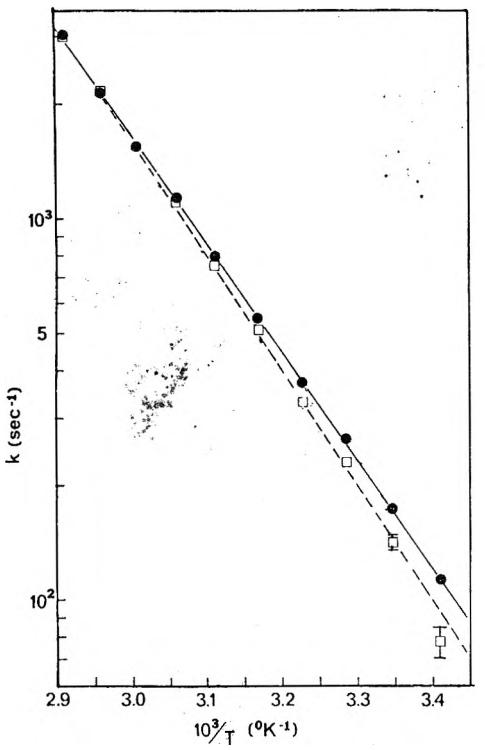

Figure 2. Arrhenius plot of k (rate of release of Na^+ from C_{222}) for a solution of 0.15 M C_{222} and 0.6 M NaBr in EDA: □, no first-order phase correction; ●, first-order phase corrected.

first-order phase correction might not be readily apparent but it can have a pronounced effect on the accuracy of the results. In this particular case, neglect of the θ' correction gives an 8% error in the calculated activation energy.

Two possible mechanisms of exchange were considered. The first (I) is given by

$$[C_{222}] + [Na^+] \underset{k_{-1}}{\overset{k_1}{\rightleftharpoons}} [Na^+C_{222}] \qquad (11)$$

and assumes exchange proceeds through a dissociation-association process. The second mechanism (II), given by

$$^*[Na^+] + [Na^+C_{222}] \overset{k_2}{\rightleftharpoons} ^*[Na^+C_{222}] + [Na^+] \qquad (12)$$

is bimolecular and also represents the overall exchange process. Results of Lehn et al.[14] combined with those of Ceraso and Dye[19] indicated a preference for mechanism I, but mechanism II was not disproved. For the reaction of C_{222} with Ca^{2+} in H_2O, mechanism II was found to be unimportant and kinetics data were consistent with mechanism I.[13] The complexation of certain crown polyethers with sodium ions proceeds via mechanism I.[15,20,24] To determine which mechanism is more consistent with the data at all temperatures, we examined the concentration dependence of τ. Three solutions (EDA 1, 2, 3), each containing 0.6 M NaBr but with variable amounts of C_{222} (0.15, 0.30, and 0.45 M, respectively) were examined. Figure 3 illustrates some of the experimental data obtained as a function of temperature for these three solutions.

Mechanism I predicts a dependence of τ upon the relative population of site A while mechanism II predicts a dependence of τ upon the inverse total concentration of sodium ion. The variation of τ with p_A at fixed total $[Na^+]$ shows that mechanism II is not applicable. Table II gives the calculated activation energies for each solution from the best fit of an Arrhenius activation expression to the data.

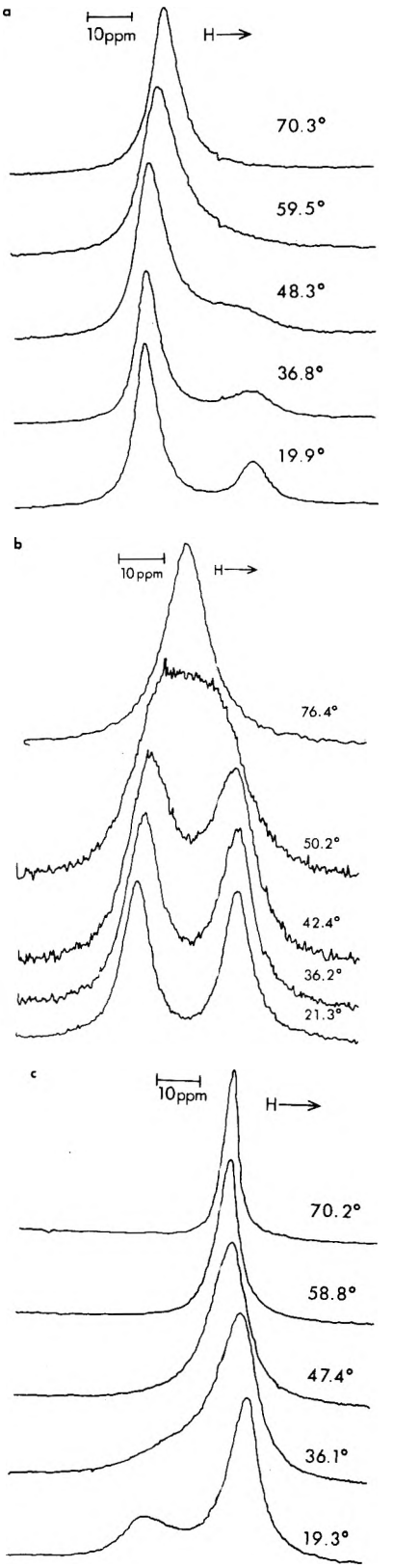

Figure 3. Spectra at various temperatures for solutions of Na^+ with C_{222} in EDA: (a) EDA1, 0.15 M C_{222} and 0.6 M NaBr, $P_A = 0.25$; (b) EDA2, 0.30 M C_{222} and 0.6 M NaBr, $P_A = 0.50$; (c) EDA3, 0.45 M C_{222} and 0.6 M NaBr, $P_A = 0.75$.

Activation energy plots, log k_{-1} vs. $1/T$, are shown in Figure 2 for EDA and in Figure 4 for H_2O, py, and THF. Activation energies, rate constants (k_{-1}), and values of $\Delta H_0^{\ddagger}$, $\Delta S_0^{\ddagger}$, and $\Delta G_0^{\ddagger}$ for the release of Na^+ from the cryptate are given in Table II. Rate constants were calculated from τ values by assuming that the pathway of sodium ion exchange for H_2O, py, and THF solutions also

TABLE II: Exchange Rates and Thermodynamic Parameters of Sodium Cryptate Exchange in Various Solvents

Solvent	k_{-1}, s^{-1} (298 K)	$\Delta H_0^{\ddagger}$, kcal mol^{-1}	$\Delta S_0^{\ddagger}$, cal K^{-1} mol^{-1}	$\Delta G_0^{\ddagger}$, kcal mol^{-1} (298 K)
py	1.14 (0.09)[a]	13.6 (0.2)	−12.6 (0.6)	17.374 (0.004)
THF	8.03 (0.27)	13.8 (0.2)	−8.1 (0.6)	16.22 (0.02)
H_2O	147.4 (2.6)	16.1 (0.2)	+5.3 (0.8)	14.49 (0.01)
EDA1	169.4 (1.8)	12.37 (0.08)	+6.9 (0.3)	14.43 (0.01)
EDA2	150.5 (6.9)	12.4 (0.3)	−7.0 (1.0)	14.48 (0.03)
EDA3	175.2 (5.8)	12.1 (0.2)	−7.8 (0.6)	14.39 (0.02)
EDA av	165.0 (4.9)	12.3 (0.2)	−7.6 (0.6)	14.44 (0.02)

[a] Standard deviation.

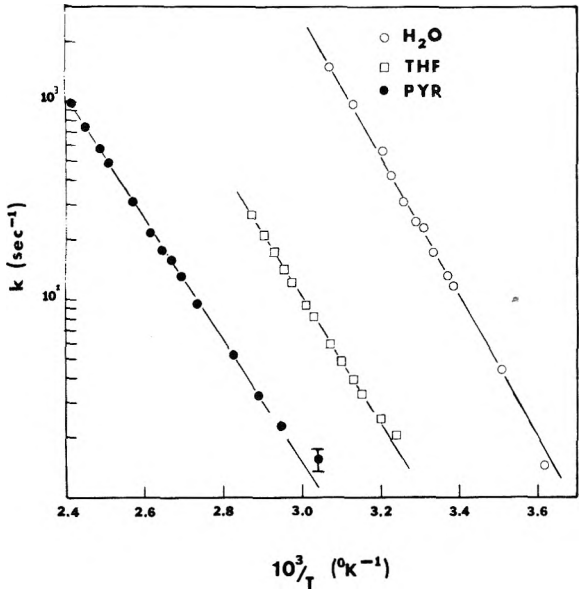

Figure 4. Arrhenius plots of k (rate of release of Na^+ from C_{222}) vs. $1/T$ for solutions in H_2O, THF, and py.

proceeds via mechanism I. The free energy of activation is directly determined from k_{-1} and therefore has the smallest standard deviation.

The average value of the activation energy for EDA solutions (12.9 ± 0.2 kcal) is in good agreement with the value of 12.2 ± 1.1 kcal obtained by Ceraso and Dye[19] by continuous wave ^{23}Na NMR techniques. For aqueous solutions, the forward rate of association, k_1, calculated from k_{-1} and the association constant is 1.2×10^6 M^{-1} s^{-1}. A value of $k_{-1} = 27$ s^{-1} is reported for sodium ion release from C_{222} in D_2O solutions at 3 ± 4 °C[14] and is in fair agreement with our calculated value of 16 s^{-1} at 3 °C for sodium ion release into H_2O.

The activation energies depend upon the solvent used. A variation in activation energy with solvent for Li–cryptate decomplexation has been reported by Cahen et al.[23] They observe a rough correlation between the activation energy for release of the lithium cation from the cryptand and the donicity of the solvent as expressed by the Gutmann donor number. As the solvent donor number increased, the activation energy for release of Li^+ from the cryptate complex also increased. In the present case this trend is not observed (the donor numbers for THF, H_2O, py, and EDA are 20.0, 33.0, 33.1, and 55.0, respectively). For both lithium and sodium, the exchange rate in py solution is very much slower than the corresponding rates in H_2O solution. By contrast Schori et al.[15,20] found activation energies for the release of Na^+ ion from several crown ethers to be independent of solvent (to within ±1 kcal). They suggest the energy barrier to exchange may be determined by the barrier for a conformational twist of a crown molecule. However, their data are restricted to three solvents with very similar donicities.

The positive entropy of activation for H_2O solutions probably indicates solvent participation in the transition state. Values for entropies of transfer ΔS_{tr} of univalent electrolytes from water to other solvents indicate a standard partial molar entropy of the cation in water which is higher than in other solvents[41] (after corrections have been made for differences in dielectric constants). This has been attributed to extensive structure breaking of bulk water when an ionic solution is formed.[41] The more positive value for $\Delta S_0^{\ddagger}$ in water than in nonaqueous solvents is therefore a strong indication that the solvent participates in the transition state. A similar effect was noted in the case of lithium.[23]

Acknowledgment. This research was supported by the United States Energy Research and Development Administration under Contract No. EY-76-S-02-0958.

References and Notes

(1) C. J. Pedersen, *J. Am. Chem. Soc.*, **89**, 7017 (1967).
(2) B. Dietrich, J. M. Lehn, and J. P. Sauvage, *Tetrahedron Lett.*, 2885, 2889 (1969).
(3) P. D. Moras and R. Weiss, *Acta Crystallogr., Sect. B*, **29**, 396, 400 (1973).
(4) P. D. Moras, B. Metz, and R. Weiss, *Acta Crystallogr., Sect. B*, **29**, 383, 388 (1973).
(5) C. J. Pedersen and H. K. Frensdorff, *Angew. Chem.*, **84**, 16 (1972).
(6) J. Cheney, J. M. Lehn, J. P. Sauvage, and M. E. Stubbs, *J. Chem. Soc., Chem. Commun.*, 1100 (1972).
(7) J. M. Lehn, *Struct. Bonding (Berlin)*, **16**, 1 (1973).
(8) R. M. Izatt, D. J. Eatough, and J. J. Christensen, *Struct. Bonding (Berlin)*, **16**, 161 (1973).
(9) J. J. Christensen, D. J. Eatough, and R. M. Izatt, *Chem. Rev.*, **74**, 351 (1974).
(10) Y. M. Cahen, J. L. Dye, and A. I. Popov, *J. Phys. Chem.*, **79**, 1289 (1975).
(11) J. M. Lehn and J. P. Sauvage, *J. Am. Chem. Soc.*, **97**, 6700 (1975).
(12) G. Anderegg, *Helv. Chim. Acta*, **58**, 1218 (1975).
(13) V. M. Loyola, R. G. Wilkins, and R. Pizer, *J. Am. Chem. Soc.*, **97**, 7382 (1975).
(14) J. M. Lehn, J. P. Sauvage, and B. Dietrich, *J. Am. Chem. Soc.*, **92**, 2916 (1970).
(15) E. Shchori, J. Jagur-Grodzinski, Z. Luz, and M. Shporer, *J. Am. Chem. Soc.*, **93**, 7133 (1971).
(16) D. H. Haynes, B. C. Pressman, and A. Kowalsky, *Biochemistry*, **10**, 852 (1971).
(17) D. H. Haynes, *FEBS Lett.*, **20**, 221 (1972).
(18) P. B. Chock, *Proc. Natl. Acad. Sci. USA*, **69**, 1939 (1972).
(19) J. M. Ceraso and J. L. Dye, *J. Am. Chem. Soc.*, **95**, 4432 (1973).
(20) E. Shchori, J. Jagur-Grodzinski, and M. Shporer, *J. Am. Chem. Soc.*, **95**, 3842 (1973).
(21) J. P. Kintzinger and J. M. Lehn, *J. Am. Chem. Soc.*, **96**, 3313 (1974).
(22) J. M. Lehn and M. E. Stubbs, *J. Am. Chem. Soc.*, **96**, 4011 (1974).
(23) Y. M. Cahen, J. L. Dye, and A. I. Popov, *J. Phys. Chem.*, **79**, 1292 (1975).
(24) M. Shporer and Z. Luz, *J. Am. Chem. Soc.*, 97, 665 (1975).
(25) V. A. Nicely and J. L. Dye, *J. Chem. Educ.*, 48 (1971).
(26) J. L. Dye, M. T. Lok, F. J. Tehan, J. M. Ceraso, and K. J. Voorhees, *J. Org. Chem.*, **28**, 1773 (1973).
(27) M. G. DeBacker, Ph.D. Thesis, Michigan State University, 1970.
(28) C. Deverell, *Prog. Nucl. Magn. Reson. Spectrosc.*, **4**, 278 (1969).
(29) A. Abragam, "The Principles of Nuclear Magnetism", Oxford University Press, London, 1961.
(30) R. H. Erlich and A. I. Popov, *J. Am. Chem. Soc.*, **93**, 5620 (1971).
(31) M. Herlem and A. I. Popov, *J. Am. Chem. Soc.*, **94**, 1431 (1972).
(32) V. Gutmann and E. Wychera, *Inorg. Nucl. Chem. Lett.*, **2**, 257 (1966).
(33) A. Beckmann, K. D. Boklen, and D. Elke, *Z. Phys.*, **270**, 173 (1974).
(34) A. Saika and C. P. Slichter, *J. Chem. Phys.*, **22**, 26 (1954).
(35) C. Deverell, *Mol. Phys.*, **16**, 491 (1969).
(36) C. Melli and S. Fraga, *Theor. Chim. Acta*, **5**, 275 (1966).

(37) H. S. Gutowsky, D. W. McCall, and C. P. Slichter, *J. Chem. Phys.*, **21**, 279 (1953).
(38) H. M. McConnell, *J. Chem. Phys.*, **28**, 430 (1958).
(39) D. E. Woessner, *J. Chem. Phys.*, **35**, 41 (1961).
(40) R. K. Gupta, T. P. Pitner, and R. Wasylishen, *J. Magn. Reson.*, **13**, 383 (1974).
(41) B. G. Cox, G. R. Hedwig, A. J. Parker, and D. W. Watts, *Aust. J. Chem.*, **27**, 477 (1974).

Electron Spin Resonance and Optical Electron Spin Resonance Studies of Alkali Metals–Tetrahydrofuran Solutions in the Presence of Dicyclohexyl 18-Crown-6[1]

Abraham Friedenberg[2] and Haim Levanon*[3]

Department of Physical Chemistry, The Hebrew University, Jerusalem, Israel and Radiation Laboratory and Department of Chemistry, University of Notre Dame, Notre Dame, Indiana 46556 *(Received June 23, 1976; Revised Manuscript Received February 7, 1977)*

Publication costs assisted by the Division of Physical Research, U.S. Energy Research and Development Administration

An ESR and ESR–optical study of M–THF (M = K, Rb, Cs) solutions in the presence of dicyclohexyl 18-crown-6, CR, is presented. In K–THF solutions at room temperature, the ESR signal intensity of the photoelectrons passes through a maximum at [CR] $\simeq 10^{-3}$ M. The monomer radicals, K·, exhibit an optimum ESR signal-to-noise ratio at [CR] $\simeq 10^{-5}$ M. In solutions which are not illuminated the ESR signal intensity of the dark solvated electrons increases monotonously with CR concentration (up to $\sim 10^{-3}$ M), whereas its line width is almost unaffected ($\sim$180 mG) retaining its Lorentzian line shape. Above 10^{-3} M CR the ESR line width becomes very narrow ($\sim$15 mG). Contrary to the case of potassium, the ESR line width of the solvated electron in Rb–THF systems is increased significantly on addition of CR. This observation is interpreted in terms of an exchange process of the type e + $RbCR^+$, e $\rightleftarrows$ $RbCR^+$, e + e. The rate constant for this exchange is 3×10^8 M^{-1} s^{-1}. The recombination process of the photoelectrons in M–THF systems follows a pseudo-first-order kinetics which depends on the CR concentration. This reaction is interpreted in terms of two competitive reactions, e + M^+ $\rightarrow$ M· and e + MCR^+ $\rightarrow$ e, MCR^+. An activation energy for this recombination process is found to be in the range of 2–8 kcal/mol for low and high CR concentrations, respectively.

A. Introduction

The introduction of the organic macrocyclic molecules such as crown ethers, CR, as complexing agents of alkali-metals cations, opened many interesting possibilities in the study of the blue solutions of alkali metals dissolved in ethers and amines.[4-6] Thus, by monitoring the CR concentrations, it is possible to control the elementary processes

$$2M_s \rightleftarrows M^+ + M^-$$

$$M^+ + CR \rightleftarrows MCR^+$$

It was shown by Dye and co-workers that in some cases, where the solutions consisted mainly of M^- and MCR^+, the salt M^+CRM^- could be precipitated and identified.[7]

It is generally accepted that, in addition to the anion and cation, there are also present in these solutions the solvated electron and the monomer radical. Regarding other species, there is experimental and theoretical evidence for the existence of e_2, M_2, and ion pairs between the electron and the cation or the solvent (e, M^+) or (M^+, S^-), respectively.[8-11]

Solutions of alkali metals in amines have been extensively investigated by optical and magnetic resonance techniques.[6,12,13] Regarding ethers as solvents, these have mainly been subjected to optical[4,14] and, to a lesser extent, magnetic resonance experiments.[15] The main difficulty in the latter experiments is the relatively low solubility of alkali metals in ethers.

In a recent communication,[16] we reported some preliminary results on the behavior of the photoelectrons and monomer radicals upon light excitation in the presence of low CR concentrations in M–THF solutions (M = K, Rb). The purpose of the present work is to study the solutions of alkali metals over a wide range of CR concentrations by employing the technique of ESR and ESR–optical spectroscopy.

In section C-I we describe in detail the behavior of the dark electrons and photoelectrons in K–CR–THF solutions. We find that the yield of the photoelectrons increases with CR concentrations (up to $\sim 10^{-3}$ M) and also on lowering the temperature. The monomer radical concentration, on the other hand, is affected only over a narrow range of temperatures and CR concentrations.

Although the ESR line shape and line width are hardly affected on changing the CR concentration up to $\sim 10^{-3}$ M in K–THF solutions, we find at high CR concentration a substantial change of the ESR line shape which is followed by a very narrow line width of the solvated electron due to exchange narrowing process. Unlike potassium, we find that the line width of the solvated electron in Rb–THF solutions is broadened with the CR concentration. This is analyzed in terms of exchange phenomenon. These effects are described in section C-II.

In section C-III, we describe the kinetics associated with the photoelectrons as a function of the CR concentration. Over almost the entire range of temperatures and CR concentrations we find a pseudo-first-order behavior for the recombination process of the photoelectrons. These observations are found in K–THF, Rb–THF, and Cs–THF systems.

The effect of spin polarization reported previously[16] was observed in all the systems described above and will be discussed elsewhere.

B. Experimental Section

Dry solvents, prior to sample preparations, were prepared as described previously in the literature.[14,17] Di-

cyclohexyl 18-crown-6, CR, was purchased from Aldrich Chemicals and was used with no further purification. Rubidium and cesium were purchased from Fluka in 1-g ampules, and were divided into four capillary tubes of 3 mm i.d. under high vacuum. Each of these tubes was sealed off and was used separately. Alkali metal solutions were prepared on a vacuum line in two stages: (i) distillation of the alkali metal through a glass side arm, divided by constrictions, into the main glass tubing apparatus. On such an apparatus an ESR pyrex tube and an optical cell were attached; (ii) distillation of the dry solvent into the main tube whose volume was calibrated previously. This compartment was sealed off after a few freeze–thaw cycles. For additional details on sample preparation, the reader is referred to previous publications.[17] When CR was used, an additional pyrex glass compartment, separated by a break seal, was attached to the main glass tubing apparatus. The concentration of CR was governed by first dissolving a known amount of CR in DME solution. This solution served as a stock of CR from which a known volume was transferred into the separated compartment. The DME was evacuated, leaving behind only the oily CR. After an experiment was performed on the CR free compartment, the seal was broken and CR was added to the solution. In this way, two experiments with different CR concentrations could be performed.

Before sample preparation, the glass apparatus was rinsed with a detergent, followed by several rinses with triple distilled water. Finally it was rinsed with analytical acetone, degassed, and heated on a vacuum line for several minutes. It should be noted, however, that the stability of the solutions is markedly affected by the handling of the glass apparatus prior to the distillation processes.[9,15] All experiments were performed immediately after sample preparation. After 12 h the samples were discarded.

Optical measurements were performed at room temperature on a Cary-14 spectrophotometer. The optical path lengths of the cells varied from 1 to 10 mm, depending on the concentration of CR.

ESR measurements were carried out on a Varian E-12 spectrometer equipped with 100, 10, and 1 kHz field modulation units. The temperature of the samples in the ESR cavity was controlled by using a standard N_2 flow system. The temperatures were measured using a copper–constantan thermocouple. Part of the experiments have been performed on a noncommercial ESR spectrometer with 10-kHz field modulation.[18]

The exciting light source was a high-pressure xenon arc (150 W), which was modulated electronically. The experimental procedure for time averaging of the ESR signal intensity, and for phase sensitive detection coupled to the modulated light frequency, was performed as described in previous studies.[19] Irradiation of the sample solutions was in situ in the ESR cavity using Corning cutoff filters.

The signal intensity of the ESR lines was determined by employing the expression for the relative line intensity $\sum_i \Delta H_i^2 h_i$, where ΔH is the measured peak-to-peak separation in the absorption derivative of the susceptibility, h is the signal height from peak to peak, and the summation is over the hyperfine components. The relative intensities were always normalized to the same experimental setup of the ESR spectrometer.

C. Results and Discussion

I. *K–THF Solutions at Low CR Concentrations.* When potassium metal is dissolved under high vacuum in THF at room temperature, a colorless solution results. The solution turns into pale blue on rigorous shaking at low temperatures while keeping the solvent in contact with the metal. Once the solution turns to pale blue, the color persists for several hours also at room temperature.

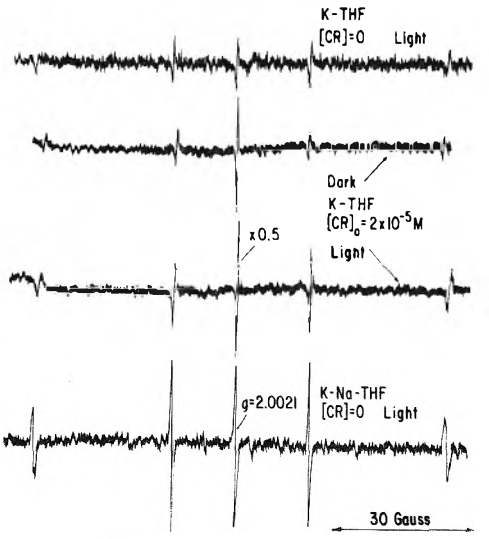

Figure 1. ESR spectra of the solvated electron e (g = 2.0021), and of the monomer radical K· at 293 K. The experimental conditions at which the spectra were recorded are indicated on each trace. Light spectra were recorded when the ESR sample was irradiated (in situ) with all wavelengths above 650 nm.

At room temperature, the paramagnetic species which is normally observed by ESR is the solvated electron, whereas the monomer radical in many cases escapes detection. Upon irradiation of the sample at a wavelength which corresponds to the absorption peak of K^- (900 nm), the photoelectron, e, and the monomer radical, K·, are expected to be observed by ESR according to the reaction

$$K^- \xrightarrow{h\nu} K\cdot + e \qquad (I.1)$$

ESR detection of the monomer radical as described by eq I.1 depends strongly upon the experimental conditions. In particular, the way of sample preparations is the main factor responsible for the success or failure to obtain the monomer radical. For example, we found that it is of extreme importance that the solution should come in contact with a highly active metal mirror. To test this, we dissolved a liquid alloy of Na–K, which is known to be highly active, in a THF solution. When the sample was irradiated continuously with all wavelengths above 650 nm, both the solvated electron, e, and the monomer radical, K·, could be observed easily. Nevertheless, under these experimental conditions, we could not observe the monomer radical in a reasonable signal-to-noise ratio when the ESR spectrum was taken under dark conditions. In Figure 1 we present four ESR spectra taken at two different concentrations of CR, both in dark and light. As a comparison the ESR spectrum of K–Na–THF solution is also given (bottom trace).

In the presence of small amounts of CR in K–THF solutions, we have invariably observed the ESR signal due to the monomer, both in the dark and in the light. Apparently, the introduction of small amounts of CR initiates the dissociation of the metal in the nonpolar solvent. Figure 2 shows the dependence of the signal intensity of the monomer radical and the solvated electron vs. $[CR]_0$ (concentration of added CR). On increasing $[CR]_0$ the ESR signal of the monomer first increased then after passing through a maximum it started to decrease and finally disappeared at about 10^{-4} M of $[CR]_0$ (cf. triangles in Figure 2). At the same time the intensity of the color increased monotonously with $[CR]_0$ at all concentrations

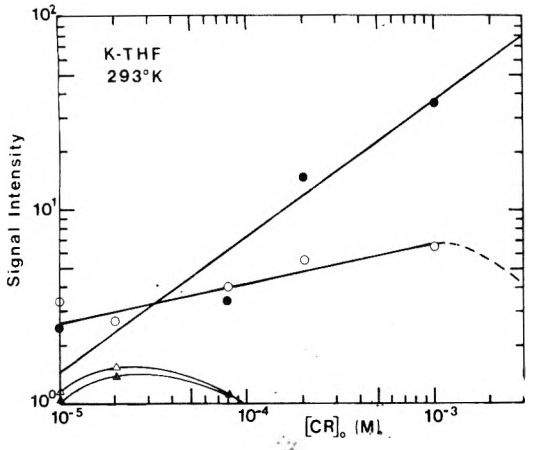

Figure 2. ESR signal intensities of the solvated electron (circles) and of the monomer radical (triangles) as a function of the $[CR]_0$ (concentration of CR added). Full circles and triangles are the experimental intensities measured under dark conditions. Open circles and triangles are the corresponding intensities measured under light irradiation conditions, after subtracting the dark contribution. The dashed curve indicates that above 10^{-3} M of added CR the signal intensity is reduced.

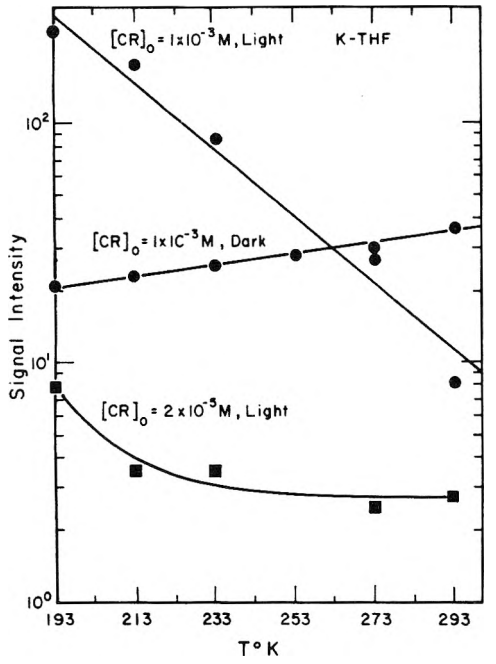

Figure 3. ESR signal intensity of the solvated electron at two CR concentrations in light and dark conditions as a function of the temperature. The experimental conditions are indicated on each line.

of CR studied. At room temperature the ESR signal intensity in the dark always increased with increasing $[CR]_0$ whereas in the light it showed a maximum at about 10^{-3} M CR. In this range of CR concentrations, the ESR line shape was Lorentzian and its line width remained constant (180 mG). It was saturated by microwave power at about 2 mW.

Figure 3 shows the temperature dependence of the ESR signal intensities of the solvated electron at two CR concentrations. For the low CR concentration, the signal intensity in the dark was too small to be drawn to scale. Also, it is worth noting that the difference in the signal intensities at low temperatures exceeds almost two orders of magnitude, whereas at high temperatures both signal intensities are of the same order or magnitude. The monomer radicals (observed in the range of $0 < [CR] < 10^{-4}$ M) escaped ESR detection at temperatures below 230 K.

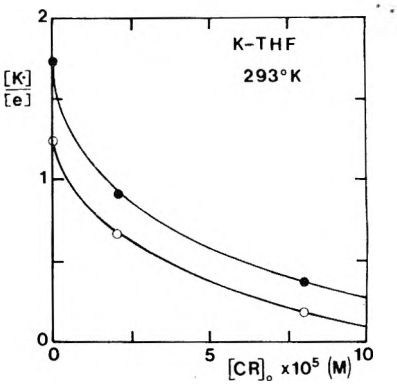

Figure 4. The ratio $R = [K\cdot]/[e]$ as a function of $[CR]_0$. Open and full circles are the experimental points measured under dark and light conditions, respectively.

The dominant equilibria in nonpolar solvents are[6,15]

$$2M_S \underset{k_2}{\overset{k_1}{\rightleftarrows}} M^+ + M^- \qquad k_1/k_2 = K_1 \tag{I.2}$$

$$M^- \underset{k_4}{\overset{k_3}{\rightleftarrows}} M\cdot + e^- \qquad k_3/k_4 = K_2 \tag{I.3}$$

$$M\cdot \underset{k_6}{\overset{k_5}{\rightleftarrows}} M^+ + e^- \qquad k_5/k_6 = K_3 \tag{I.4}$$

$$M^+ + CR \underset{k_8}{\overset{k_7}{\rightleftarrows}} MCR^+ \qquad k_7/k_8 = K_4 \tag{I.5}$$

The overall reaction may be summed up as

$$2M_S + CR \rightleftarrows 2e^- + M^+ + MCR^+ \rightleftarrows M^- + MCR^+ \tag{I.6}$$

Thus, excess of CR will shift (I.6) to the right to give solvated electrons, M^-, and to a lesser extent M^+ and M·. This is reflected experimentally by increasing the solvated electron concentration and the intensification of the blue color of the solution. The latter was verified by monitoring the absorption peak due to the anion, K^-, at 900 nm, on increasing the CR concentration.

Alternatively, one can consider the ratio $[K\cdot]/[e]$ which in terms of (I.3) and (I.5) can be expressed as

$$R = \frac{[K\cdot]}{[e]} = \frac{k_6}{k_5}[M^+] = \frac{K_3^{-1}[M^+]_0}{1 + K_4[CR]} \tag{I.7}$$

where

$$[M^+]_0 = [M^+] + [MCR^+]$$

Since $K_4 \simeq 10^9$ M^{-1},[5] the product $K_4[CR]$ will start to affect R at very low concentrations of free CR, i.e., at $[CR] > 10^{-9}$ M. We thus expect R to decrease upon increasing the CR concentration. Figure 4 shows the experimental results of R vs. CR added at room temperature.[20] From the experimental value of R at $[CR] = 0$ (lower trace), and taking K_3[15] as 5×10^5 M^{-1} we estimated the solubility of K^+ (and K^-) in THF as $\sim 5 \times 10^{-6}$ M in accord with optical determination.[21] This value is reasonable if it is compared to the reported value of 5×10^{-4} M in DME at 193 K.[15]

The experimental observation that the monomer radicals are not detected at higher CR concentration than 10^{-4} M is conspicuous and warrants some remarks. From eq I.2 and I.4, one should expect that the monomer concentration in a metal saturated solution should be independent of the CR concentration, i.e, $[K\cdot]$ = constant. This is in contradiction to ESR measurements (cf. Figure 2) and also to previous observations that the monomer radical at high CR concentration escapes detection.[6] For example, the monomer radical in K–diethyl ether solution could be

observed only in the presence of CR (5×10^{-3} M).[22] Such a discrepancy may be interpreted in terms of earlier suggestions[9] that part of the monomer radicals escape ESR detection due to ion-pair formation which exchange with the monomeric species. In view of the photoelectron kinetics (section III) we propose that in addition to (e, K^+) at low CR concentrations, there exists also (e, KCR^+) at high CR concentrations. Both species have a broad ESR signal which is covered by the solvated electron signal. Inspection of the ESR spectra shown in Figure 1 supports evidence for such a dynamic process. It is evident that the signal amplitudes of the inner hyperfine components exceed the corresponding outer components. (This phenomenon should not be confused with spin polarization.)[16] Regarding Rb–THF and Cs–THF systems, the monomer radicals in the former system could be observed in a poor signal-to-noise ratio having a hyperfine splitting A = 150 G.

II. *K–THF and Rb–THF Solutions at High CR Concentrations.* A further increase of CR (up to 0.1 M) results in a deep blue color of K–CR–THF system, giving rise to a suspension type solution. When this solution is inserted immediately after its preparation into the spectrometer's cavity at room temperature, a single ESR line appears. Its line shape depends strongly on the sample tube diameter. In a ~3-mm i.d. tube, the line shape of the first derivative spectrum is anomalous and is very similar to the ESR spectrum reported by Acrivos and co-workers[23] for Pb–Na–NH_3 solutions. Such a spectrum is characterized by its broad wings and a very sharp break between the peaks of the first derivative spectrum. In an ~0.5-mm i.d. tube, the ESR spectrum, although distorted by the inhomogeneity of the magnetic field, has a normal line shape and the peak-to-peak separation is 12 mG. The line shape and width change gradually with time, giving rise to a broader spectrum with a line width of 40–60 mG. After a 24-h period, the line width reaches a constant value of about 180 mG, retaining its normal Lorentzian line shape. The variation in time of the ESR line shape and width were always accompanied with a change in the solution from a suspension type into an homogeneous one.

Apparently, the anomalous line shape having an extremely narrow line width originates from an experimental artifact due to the shift of the klystron frequency by the strong and narrow resonance itself.[24] By reducing the sample volume the anomalous behavior disappeared. Also, when the AFC was turned off and the ESR spectrum was recorded using the large diameter sample, a normal line shape was obtained which was somewhat broadened (30 mG).

As mentioned above, very narrow ESR lines have been observed in Na–NH_3 systems (dilute and concentrated solutions),[23-25] where a fast exchange mechanism leads to a narrowing process. Such a mechanism may account for the narrow ESR lines in K–CR–THF solutions.

The same experiment was carried out with Rb–THF in the presence of excess CR. Unlike potassium, the line width due to the solvated electron broadened appreciably on increasing the CR concentration and was saturated at relatively high microwave power (2–30 mW) for low and high CR concentration, respectively. Figure 5 shows the ESR line width of the solvated electron (peak to peak in the first derivative curve) vs. the CR concentration added, in a Rb–THF solution at 213 K. Comparing this observation to that discussed above for the K–CR–THF solution, it seems unlikely from the increasing of the line width with addition of CR that a spin exchange process between the solvated electrons may account for the ESR

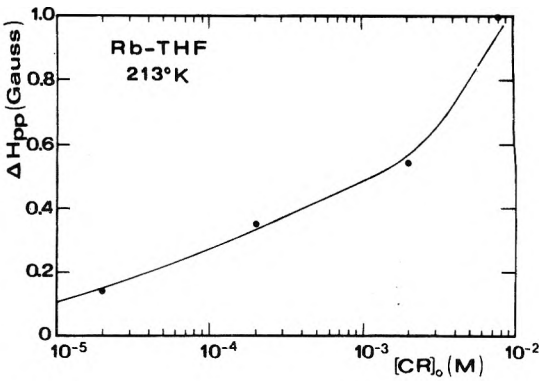

Figure 5. ESR peak-to-peak line width, ΔH_{pp}, vs. $[CR]_0$.

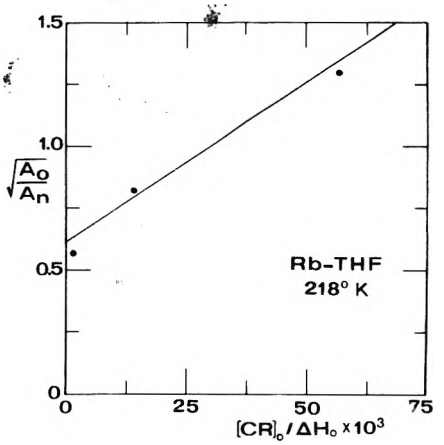

Figure 6. Plot of $(A_0/A_n)^{1/2}$ vs. $[CR]_0/\Delta H_0$ corresponding to the solvated electron in Rb–THF solutions. The variables A_0 and A_n are the normalized ESR signal amplitudes at $[CR]_0 = 0$ and different $[CR]_0$, respectively; ΔH_0 (140 mG) is the peak-to-peak line width of the solvated electron at $[CR]_0 = 0$ (for cetails see ref 26).

line broadening. Neither a spin exchange of the type

$$e\uparrow + Rb^+, e\downarrow \rightleftarrows e\downarrow + Rb^+, e\uparrow \qquad (II.1)$$

since the $[Rb^+]$ decreases on increasing the CR concentration.

Hence, either of the following exchange processes may account for the line broadening:

$$e\uparrow + RbCR^+, e\downarrow \rightleftarrows e\downarrow + RbCR^+, e\uparrow \qquad (II.2)$$

or

$$e + RbCR^+, e \rightleftarrows RbCR^+, e + e \qquad (II.3)$$

Assuming that $[CR]_0 \simeq [RbCR^+]$ we calculated the second-order rate constant for the exchange process k_{ex} following Ward and Weissman.[26] From the slope S in Figure 6 we have $k_{ex} = \sqrt{3} \times \pi \times 2.8 \times 10^6 \times S \simeq 3 \times 10^8$ M^{-1} s^{-1}. This value is smaller than the diffusion controlled rate. On the other hand, this value seems to be too high for the large cation transfer. It is likely that both processes contribute to the broadening effect.

III. *Kinetics of the Photoelectrons.* Inspection of Figures 1 and 3 shows that strong photo-ESR signals are observed on decreasing the temperature and increasing the CR concentration. Employing pulse light excitation, we have followed the temporal behavior of the ESR signal intensity on varying the CR concentration and temperature. Typical kinetic curves are shown in Figure 7. These were taken under different conditions as indicated on each trace. Except for the high temperature region, all of the kinetic curves follow a pseudo-first-order recombination process. The effect of increasing the CR concentration on the observed first-order rate constant is analogous to that

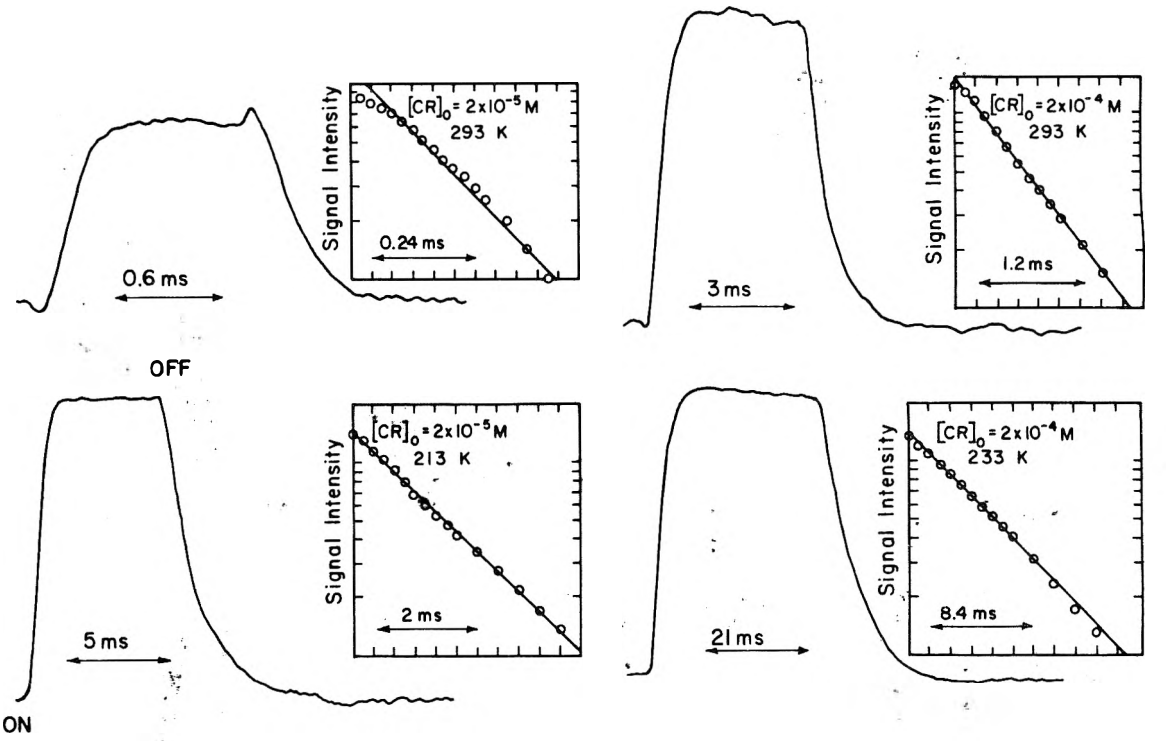

Figure 7. ESR decay curves of the photoelectron in K–CR–THF solutions at two CR concentrations at different temperatures. Inserted are first-order plots as described in the text (cf. eq I.4, III.1, and III.2). The distance between the ON and OFF is the duration of the light pulse.

TABLE I: Pseudo-First-Order Rate Constants k^{obsd} at 213 K (s^{-1}) and Activation Energies ΔH (kcal/mol) for Potassium, Rubidium, and Cesium in THF at Different CR Concentrations

$[CR]_0$, M	k_K^{obsd}	ΔH_K	k_{Rb}^{obsd}	ΔH_{Rb}	k_{Cs}^{obsd}	ΔH_{Cs}
0	400	2-4	1470	2-3	3100	1-2
2×10^{-5}	480	2-4	147	3-4	1470	1-2
2×10^{-4}	30	5-6	173	3-4	1470	3-4
1×10^{-3}	6	7-8				

of decreasing the temperature.

To account for these observations, we propose the occurrence of the process (see also section I):

$$e + KCR^+ \xrightarrow{k_9} e, KCR^+ \qquad (III.1)$$

in addition to

$$e + K^+ \xrightarrow{k_6} K\cdot \text{ (or } e, K^+) \qquad (I.4)$$

These two processes lead to a pseudo-first-order decay rate k^{obsd} given by

$$k^{obsd} = [M^+]_0 \left\{ \frac{k_6 + k_9 K_4 [CR]}{1 + K_4 [CR]} \right\} \qquad (III.2)$$

where k^{obsd} is the observed pseudo-first-order rate constant. Figure 8 shows plots of k^{obsd} vs. $[CR]_0$ at 233 and 293 K. It follows from (III.2) that when $[CR]_0 = 0$, it is possible to determine k_6, provided that $[M^+]_0$ is known. In section C-I we have estimated the solubility of potassium in THF at room temperature ($[M^+]_0 \simeq 5 \times 10^{-6}$ M). The observed rate constant at room temperature at $[CR]_0 = 0$ was found to be $k^{obsd} = 4.0 \times 10^3$ s^{-1}. This value gives rise to $k_6 \simeq 8 \times 10^8$ M^{-1} s^{-1}. The rate constant lies close to the diffusion-controlled limit, in agreement with previous reports.[15] The other limit of eq III.2 enables us to estimate k_9. When $[CR]_0$ is in excess we have

$$k^{obsd} = [M^+]_0 k_9 \qquad (III.3)$$

Assuming that $[CR]_0 \simeq [M^+]_0$, we calculated k_9 to be $\sim 10 \times 10^6$ M^{-1} s^{-1} at room temperature. We measured the activation energies for the electron recombination at

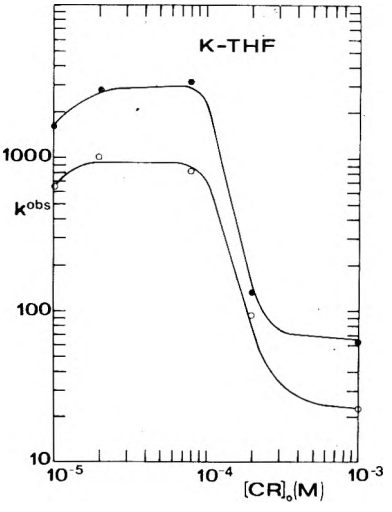

Figure 8. Plots of k^{obsd} vs. $[CR]_0$ at 293 K (full circles) and at 233 K (open circles). For definition of k^{obsd}, see eq III.2 in the text.

various CR concentrations, assuming a first-order process. The calculated activation energies lie between 2.0 and 8.0 kcal/mol for low (10^{-5} M) and high (10^{-3} M) CR concentrations, respectively. Considering the fact that the solubility of potassium metal in DME is greater than in THF, these results fit those reported by Glarum and Marshall.[15] The results of a series of experiments with potassium, rubidium, and cesium are summarized in Table I.

It has been observed that at high CR concentrations ($[CR]_0 > 10^{-3}$ M) and at low temperatures the kinetics of

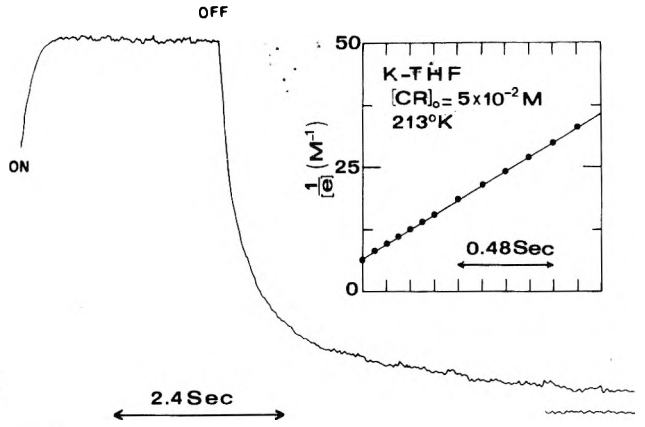

Figure 9. ESR decay curve of the photoelectron at 213 K and $[CR]_0 = 5 \times 10^{-2}$ M. Inserted is a second-order plot. The concentration of the electron was determined by comparing the observed signal intensity to standard solution of DPPH in benzene.

recombination deviates from first order (at high temperatures the photoelectron concentration is very low). The experimental observation (cf. Figure 3) that the photo-ESR signal intensity increases on decreasing the temperature, despite the fact that the dark ESR signal decreases, may be interpreted in terms of an additional reaction under these conditions.

$$e + e \underset{k_{11}}{\overset{k_{10}}{\rightleftarrows}} e_2 \qquad \text{(III.4)}$$

On decreasing the temperature equilibrium III.4 shifts to the right, resulting in a decrease of the dark ESR signal intensity.

The strong enhancement of the ESR signal intensity upon irradiation is probably due to the photodissociation of the dielectron. Figure 9 shows a decay curve of the ESR signal intensity of the photoelectron in a K–THF solution at 213 K in the presence of $[CR]_0 = 5 \times 10^{-2}$ M. The decay follows a second-order reaction.[27] The rate constant from a second-order plot (insert in Figure 9) has been calculated as 2.4×10^5 M^{-1} s^{-1}.

Acknowledgment. The valuable comments of the referees are highly acknowledged.

References and Notes

(1) This work was partially supported by a grant from U.S–Israel Binational Science Foundation (BSF), Jerusalem, Israel, and by the Radiation Laboratory of the University of Notre Dame (operated under contract with the U.S. Energy Research and Development Administration). This is Document No. NDRL-1712.
(2) Hebrew University, Jerusalem. In partial fulfillment of the requirements for a M.Sc. thesis to be submitted October, 1976.
(3) University of Notre Dame. On leave from the Hebrew University, Jerusalem.
(4) M. T. Lok, F. J. Tehan, and J. L. Dye, *J. Phys. Chem.*, **76**, 2975 (1972).
(5) J. L. Dye, C. W. Andrews, and S. E. Mathews, *J. Phys. Chem.*, **79**, 3065 (1975).
(6) J. L. Dye in "Electrons in Fluids", J. Jortner and C. R. Kestner, Ed., Springer-Verlag, West Berlin, 1973, p 77.
(7) F. J. Tehan, B. L. Barnett, and J. L. Dye, *J. Am. Chem. Soc.*, **96**, 7203 (1974).
(8) J. L. Dye, M. G. DeBacker, J. A. Eyre, and L. M. Dorfman, *J. Phys. Chem.*, **76**, 839 (1972).
(9) T. R. Tuttle, Jr., *J. Phys. Chem.*, **79**, 3071 (1975), and a private communication.
(10) J. W. Fletcher and W. A. Seddon, *J. Phys. Chem.*, **79**, 3055 (1975).
(11) S. Golden, *J. Phys. Chem.*, **79**, 2887 (1975).
(12) R. Catterall and P. Edwards, *J. Phys. Chem.*, **79**, 3010 (1975).
(13) A. Gaathon and M. Ottolenghi, *Isr. J. Chem.*, **8**, 165 (1970).
(14) J. Eloranta and H. Linschitz, *J. Chem. Phys.*, **38**, 2214 (1963).
(15) S. H. Glarum and J. H. Marshall, *J. Chem. Phys.*, **52**, 5555 (1970).
(16) A. Friedenberg and H. Levanon, *Chem. Phys. Lett.*, **41**, 84 (1976).
(17) T. R. Tuttle, Jr., and S. I. Weissman, *J. Am. Chem. Soc.*, **80**, 5342 (1958).
(18) R. W. Fessenden, *J. Chem. Phys.*, **48**, 3725 (1968).
(19) H. Levanon and S. I. Weissman, *Isr. J. Chem.*, **10**, 1 (1972).
(20) Notice that the lower curve in Figure 4 was obtained after many unsuccessful attempts to observe the monomer radical in solutions free of CR.
(21) R. Catterall, J. Slater, and M. C. R. Symons in "Metal-Ammonia Solutions", J. J. Lagowski and M. J. Sienko, Ed., Butterworths, London, 1969, p 329.
(22) J. L. Dye, M. G. DeBacker, and V. A. Nicely, *J. Am. Chem. Soc.*, **92**, 5226 (1970).
(23) J. V. Acrivos, J. Azebu, and S. Farmer in ref 21, p 145; J. V. Acvivos and J. Azebu, *J. Magn. Reson.*, **4**, 1 (1971).
(24) S. I. Weissman and T. R. Tuttle, private communication.
(25) C. A. Hutchison, Jr., and R. C. Pastor, *J. Chem. Phys.*, **21**, 1959 (1953).
(26) R. L. Ward and S. I. Weissman, *J. Am. Chem. Soc.*, **79**, 2086 (1957).
(27) Note that at this CR concentration the ESR spectrum recorded immediately after sample preparation shows the anomalous line shape as described in section C-II. This kinetic curve was taken after the ESR signal gained a normal Lorentzian line shape ($\Delta H \simeq 180$ mG).

A Theoretical Study of Li_2H. 2. Correlation Diagram, and Collinear Reactions of H with Li_2 and Li with LiH in Ground and Excited States†

Walter B. England,* Nora H. Sabelli,‡ Arnold C. Wahl,

Chemistry Division, Argonne National Laboratory, Argonne, Illinois 60439

and Arnold Karo

Lawrence Livermore Laboratory, Livermore, California 94550 *(Received September 3, 1976)*

Publication costs assisted by Argonne National Laboratory and Lawrence Livermore Laboratory

A SCF correlation diagram is reported for low-lying linear and bent states of Li_2H. SCF potential curves are computed for the collinear reactions H + Li_2 and Li + LiH. These are related to the earlier study of C_{2v} and collinear paths. Charge transfer is found to be important in all of the lowest states, and reactive charge transfer cones are discussed. Estimated electron-jump Li_2H geometries are given. It is suggested that the reaction of Li with LiH may produce the as yet unobserved Li_2H molecule.

1. Introduction

The reactions

$$H + Li_2 = Li_2H = LiH + Li \quad (1)$$

are prototypes for beam reactions of hydrogen with alkali metal dimers.[1] Although theoretically predicted to be bound by ~20 kcal/mol,[2,3] Li_2H has not been observed. The computed potential curves[2,3] imply that any Li_2H formed during the collision of H and Li_2 will be short-lived and difficult to observe. Charge transfer in broadside (C_{2v}) and near broadside (C_s) collisions of H with Li_2 is the dominant reaction mechanism[1-3] involved in the beams. Siegbahn and Schaefer[2] studied the ground surface of Li_2H in detail, and were the first to demonstrate the presence of a reactive charge transfer cone ab initio. Our previous ab initio work[3] surveyed excited state broadside reaction paths, and found that charge transfer occurred on all low-lying reactive surfaces.

In this work we demonstrate that similar reactive cones exist in all low-lying ionic surfaces. A correlation diagram is reported which connects two linear geometries of Li_2H via C_s and C_{2v} geometry intermediates. Potential energy curves are computed for the linear ($C_{\infty v}$) approach of H to Li_2. This is the opposite of the C_{2v} path and is least favorable for charge transfer. Electron jump regions are determined from the potential curves, and charge transfer from Li_2 to H is characterized.

Potential energy curves are also reported for collinear path reactions of Li with LiH. A reactive cone, i.e., a fairly broad range of geometries, centered on the broadside approach, which favor reaction by means of a HLi_2 charge transfer complex, exists for collisions of Li with the H^- end of ground state LiH. These collisions appear to have a good chance of yielding Li_2H. Reactions of Li with excited electronic states of LiH involve covalent intermediates. These favor Li approach to the Li end of the molecule.

2. Correlation Diagram for Li_2H

The correlation diagram (CD) connecting doublet electronic states between linear and bent Li_2H geometries is shown on Figure 1. The left-hand molecule, HLiLi, is given genealogical LiH and Li_2 orbital labels that qualitatively describe its valency. For example, the valency of the lowest state, $H^2\sigma_g$, is qualitatively a doubly occupied LiH charge transfer, or ionic, orbital centered on $H(H^2)$, and a singly occupied Li_2 σ valence orbital (σ_g). The right-hand molecule, LiHLi, is given genealogical LiH and Li orbital labels that approximately describe its valence structure. For example, the electronic structure of the lowest state, $H^2$2s, is qualitatively a doubly occupied LiH charge transfer orbital (H^2) and a singly occupied Li 2s orbital (2s). The states of the two bent Li_2H molecules shown in the center of the CD are labeled with irreducible representations of the C_s and C_{2v} symmetry groups. Note that similar Σ and Π labels for the left- and right-hand $C_{\infty v}$ molecules can be easily extracted from the orbital labels.

The energy of each state shown on the CD is listed in Table I. All were computed with the SCF LCAO–MO model[4-6] and the BISON–MC program.[7] The basis set was documented in our previous paper,[3] and gives SCF energies $\lesssim$0.002 au above the known Hartree–Fock limits. The SCF model suffices because the processes we are probing involve rearranging, but not breaking, chemical bonds. In this case the SCF model properly describes dissociation.

The dotted state levels on the CD represent estimates of actual SCF energies, which either could not be computed because of variational collapse to lower states having the same symmetry, or were not converged because an estimate was suitable for present purposes. In the cases of three open shells, $H\sigma_g\sigma_u$, $H\sigma_g\pi_u$, etc., only the lowest doublets are reported. The higher energy doublets behave similarly.

The states are connected diabatically. This was possible because the character of the orbitals could be followed. For example, the $H^2\sigma_g$ and the lowest A′ orbitals show a clear genealogy. In one case the genealogy is not obvious. The connections, lowest A_1 to $H^2$2s and lowest B_2 to H^2p_σ, could be reversed. Further discussion will be given in a future paper.[8]

All ionic states are more stable when H is near two Li centers. Thus $H^2\pi_g$, $H^2\pi_u$, $H^2\sigma_u$, and $H^2\sigma_g$ all are more stable in the C_s, C_{2v}, and right-hand linear geometries. The energies are comparable in all three geometries, but the C_{2v} states usually lie lowest. The C_{2v} geometry is near the minimum energy geometry of ground state Li_2H.[2] The C_s geometry is near the edge of the ground surface reactive cone.[2] The CD therefore indicates that the ground and excited charge transfer surfaces behave similarly. The

† Work performed under the auspices of the United States Energy Research and Development Administration.

‡ Visiting Scientist from Computer Center, University of Illinois at Chicago Circle.

TABLE I: Computed SCF Energies (in au) for the Li_2H Correlation Diagram[a]

H-Li-Li		C_s		C_{2v}		Li-H-Li	
$H\sigma_g\pi_u$	−15.3083	A′	−15.2619	B_1	~−15.295	$H\pi 2s$	−15.2663
$H\sigma_g\sigma_u$	−15.3263	A′	−15.2811	B_2	~−15.305	$H3\sigma 2s$	−15.3057
$H^2\pi_g$	~−15.25	A″	−15.3479	A_2	−15.3565	$H^2\pi$	−15.3646
$H^2\pi_u$	−15.3372	A″	−15.3976	B_1	−15.4057	$H^2 2p_\pi$	−15.3954
$H^2\sigma_u$	−15.3464	A′	−15.4128	B_2	−15.4217	$H^2 2p_\sigma$	~−15.40
$H^2\sigma_g$	−15.4228	A′	−15.4445	A_1	−15.4516	$H^2 2s$	−15.4372

[a] The labels are described in the text and the geometries are shown on Figure 1.

TABLE II: Linear HLi_2 SCF Energies in au[a]

	H + Li-Li′ (bond length = 5.07 au)			H-Li (bond length = 3 au) + Li′			
	HLi = 7.5	HLi = 5	HLi = 4	LiLi′ = 6	LiLi′ = 7.5	LiLi′ = 10	
$H\sigma_g^2$	−15.3702	−15.3701	−15.3707				
$H^2\sigma_g$	−15.3208	−15.3747	−15.4023	−15.4229	−15.4227	−15.4197	$H^2 2s$
$H^2\sigma_u$	−15.2265	−15.2844	−15.3153	−15.3464	−15.3556		$H^2 2p_\sigma$
$H^2\pi_u$	−15.2222	−15.2795	−15.3104	−15.3372	−15.3435	−15.3474	$H^2 2p_\pi$
$H^2\pi_g$	−15.1363	−15.1809	−15.2069		−15.2343		$H^2\pi$
$H\sigma_g\sigma_u$	−15.3412	−15.3366	−15.3328	−15.3263	−15.3305	−15.3320	$H3\sigma 2s$
$H\sigma_g\pi_u$	−15.3241	−15.3241	−15.3231	−15.3083	−15.2974	−15.2903	$H\pi 2s$

[a] The HLi and LiLi′ distances are in au. The labels are described in the text.

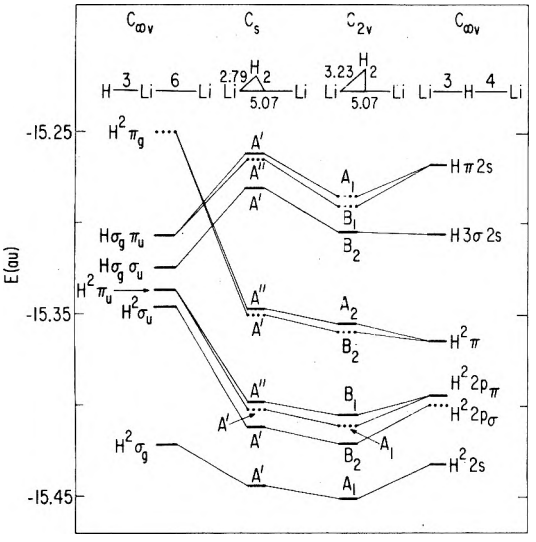

Figure 1. SCF correlation diagram for Li_2H.

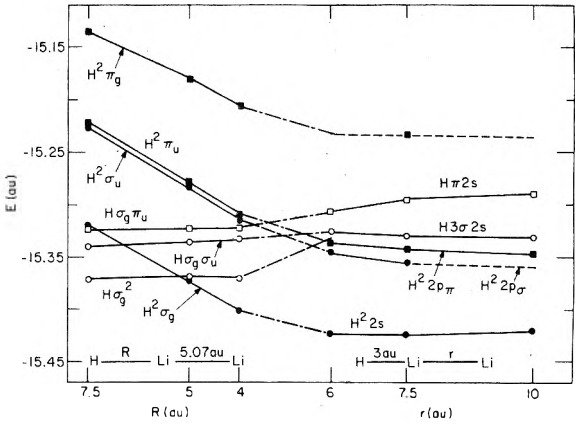

Figure 2. SCF potential curves for $H + Li_2 = Li_2H = LiH + Li$. Circles denote Σ^+ symmetry and squares denote Π symmetry. Shaded symbols indicate charge transfer.

covalent states $H\sigma_g\sigma_u$ and $H\sigma_g\pi_u$ show "barriers" to bent geometries. (Since geometries were not optimized, the "barrier" magnitudes may be too large.) It is consequently expected that chemical reactions of H with Li_2 proceed through charge transfer intermediates.

3. Linear Path Reactions of H with Li_2

Potential energies along various cuts through the collinear potential energy surfaces are shown on Figure 2. The left side of the figure describes an H atom incident on equilibrium bond length Li_2. The right side describes Li atom incident on equilibrium bond length LiH. The two paths are connected by the dashed-dotted lines in the center of the figure. The use of the dashed-dotted symbol signifies that bond lengths were not optimized to make the connections. (Optimization would provide a smooth potential joining the two paths.)

The potential curves on Figure 2 were computed with the SCF model, as was described in the preceding section. The dashed curves are SCF estimates, also as was described in the preceding section. All computed energy values are reported in Table II. The left- and right-hand row labels $H^2\sigma_g$, $H^2 2s$, etc. in Table II are the same as for Figure 1, and are arranged according to the diabatic connections on Figure 2.

The curve labeling on Figure 2 is the same one used for Figure 1. Σ states are plotted with circles and Π states are plotted with squares. Shaded symbols are used for charge transfer curves. Each curve shown has doublet spin symmetry. In the case of the three open-shell covalent curves $H\sigma_g\sigma_u$, $H\sigma_g\pi_u$, etc., only the lowest energy doublet is shown. It was found in paper I[3] that the higher energy doublet curves are approximately parallel to the corresponding lower energy doublets. The corresponding quartet curves are likewise approximately parallel to the doublet curves shown on Figure 2, but lie slightly lower in energy.[3]

The charge transfer curves describe H^- approaching Li_2^+. As H^- comes nearer to Li_2^+, the energy is of course significantly lowered. The covalent curves describe H approaching neutral Li_2 and become higher in energy as H nears Li_2. Both sets of curve characteristics are similar to the findings along the C_{2v} path.[3] However, there are two related qualitative differences between the linear and C_{2v} curves. First, the ionic C_{2v} curves are substantially lower in energy, as can be seen from the CD of Figure 1. All cross several C_{2v} covalent curves, and most show minima.[3] None of the linear path ionic curves show minima, and only the lowest curve crosses linear path covalent curves. Second, the linear path covalent curves are less repulsive than the C_{2v} path covalent curves. This factor likewise moves the ionic and covalent curve crossings

TABLE III: Linear and C_{2v} Electron-Jump Geometries[a]

Ionic curve	Covalent curve	Collinear path R_{HLi}, au	C_{2v} path symmetry	C_{2v} path R_{HLi}, au	Intersection energy, au
$H^2\sigma_g$	$H\sigma_g^2$	5.2	A_1	5.6	−15.37
$H^2\sigma_g$	$H\sigma_g\sigma_u$	~4	B_2	5.2	−15.33
$H^2\pi_u$	$H\sigma_g\pi_u$	~4	$A_1(B_1)$	4.7 (5.2)	~−15.24
$H^2\pi_g$	$H\sigma_u\pi_u$	~3	$B_2(A_2)$	4.3 (6.1)	~−15.24

[a] The Li_2 bond length is 5.07 au in both cases. R_{HLi} for the collinear path is the distance between H and the nearest Li atom.

to shorter HLi distances along the linear path.

Qualitative interpretations can be given. The ionic C_{2v} curves are lower in energy because H^- interacts equally with two "half-charged" positive Li ions. The covalent C_{2v} curves are higher in energy because the H atom valence electron is forced into the "center" of the covalent bonding region of the Li_2 molecule.

4. Charge Transfer from Li_2 to H

Electron jumps occur where diabatic ionic and covalent surfaces cross.[2,9,10] We shall approximate the electron jump as the crossing point of diabatically connected SCF ionic and covalent curves. Linear path and C_{2v} path electron jump geometries are listed in Table III. The geometries listed describe the points where charge is transferred from equilibrium bond length Li_2 to the incident H atom. Other Li_2 bond lengths are of interest and in some cases may be more realistic for approximating the charge transfer. Likely candidates would be bond lengths corresponding to SCF energy minima of the several covalent Li_2 asymptotes. However, with many states involved, extensive geometry optimization is really required. Rather than undertake this, we use the equilibrium Li_2 bond length in the belief that this will give a useful overall characterization of charge transfer processes in Li_2H.

The curve labels in Table III describe the ionic and covalent surfaces that are involved in the electron jumps. For example, in row 1 of Table III, the ionic curve is $H^2\sigma_g$ and the covalent curve is $H\sigma_g^2$. These two curves intersect at R_{HLi} = 5.2 au along the linear path, and at R_{HLi} = 5.6 au along the C_{2v} path. The intersection energy is approximately −15.37 au in both cases.

The R_{HLi} are larger on the C_{2v} path for all cases listed in Table III. The intersection energies are roughly the same for each path. This is because in Li_2H rapidly varying SCF ionic curves cross slowly varying SCF covalent curves. The covalent curves essentially describe asymptote states. For example, the intersection between $H^2\sigma_g$ and $H\sigma_g^2$ occurs at the computed SCF energy[3] of −15.3702 au for the $Li_2(^1\Sigma_g^+)$ + $H(^2S)$ asymptotes. The R_{HLi} are expected to be largest on the C_{2v} path, because in Li_2H the C_{2v} ionic curves are ultimately most stable, and hence are the first to cross the covalent curves.

It should be mentioned that in Li_2H ionic curves may cross several covalent curves. For example, $H\sigma_g\sigma_u$ and $H^2\sigma_g$ intersect before $H\sigma_g\sigma_u$ and $H^2\sigma_u$ intersect, so the $H\sigma_g\sigma_u$ surface can lead to ground surface Li_2H. The situation clearly becomes complicated. If desired, many of the other intersections can be estimated from the present results, and those of paper I.[3]

The characterization of reactive portions of the surface is illustrated by SCF computations for the ground surface reactive cone. The SCF curves are shown on Figure 3. Different curves correspond to different angles θ of incident $H(^2S)$ on equilibrium bond length $Li_2(^1\Sigma_g^+)$. The SCF asymptote energies computed with our basis and equilibrium bond lengths are plotted as horizontal dashed lines.

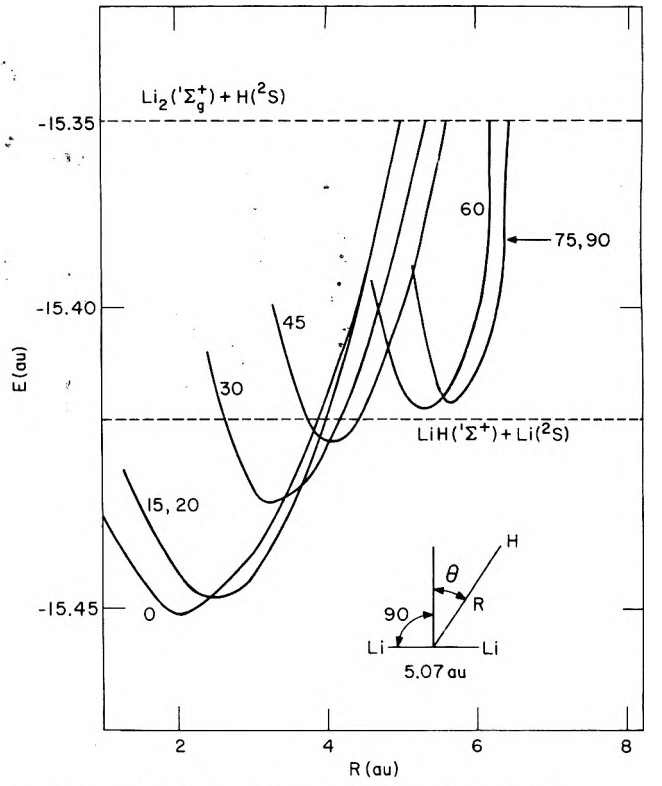

Figure 3. SCF ground surface reactive conditions for Li_2H.

The intersection of each curve with the upper horizontal line corresponds to the electron jump from $H\sigma_g^2$ to $H^2\sigma_g$. (The points of intersection for θ = 60° and θ = 75° are estimates, but should be reasonably accurate.)

The minima for the θ = 0, 15, and 20° curves are the same to ~2 kcal/mol. All three lie ~12 kcal/mol below the minimum of the θ = 30° curve, and ~20 kcal/mol below the minimum of the θ = 45° curve. This is the reactive cone. Angles much beyond θ = 45° do not produce stable Li_2H relative to $LiH(^1\Sigma^+)$ + $Li(^2S)$. The θ = 60, 75, and 90° curves are all much alike, so the linear reaction path gives a good description of this portion of the surface.

It seems reasonable to assume that overall the charge transfer curves for excited surfaces of Li_2H are similar to those shown on Figure 3 for the ground surface. This is supported by the previous discussion of the CD and the collinear and C_{2v} paths.[3] We have sketched on Figure 4 cuts of the charge transfer surface which describe the covalent $H\sigma_g\sigma_u$ and ionic $H^2\sigma_u$ surface crossing. The θ = 90° curve was drawn using the energies in Table II. The θ = 0° curve was drawn from the SCF energies reported in ref 3. The θ = 15° minimum was taken from the C_s column of row $H^2\sigma_u$ in Table I. The remaining curves were estimated from Figure 3, invoking the assumption that the overall features of charge transfer are similar for the two cases. It should be noted that the upper asymptote line uses the SCF energy computed with R = 5.07 au, the equilibrium bond length of ground state Li_2.

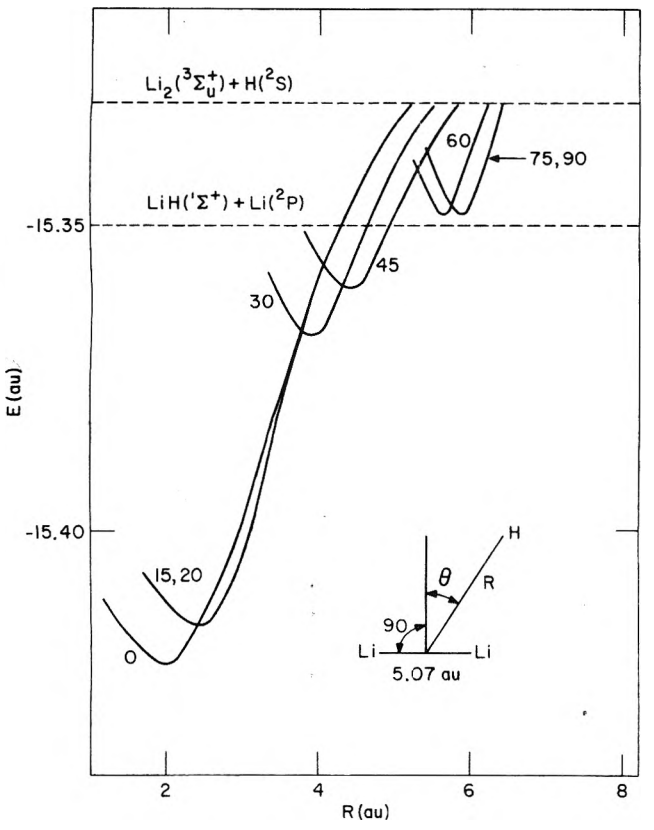

Figure 4. Qualitative reactive cone for the first excited surface of Li_2H. The $\vartheta = 90°$ curve was drawn using the energies in Table II. The $\theta = 0°$ curve was drawn using the SCF energies of ref 3. The $\theta = 15°$ minimum was taken from the C_s column of row $H^2\sigma_u$ in Table I. Remaining curves were estimated, based on the assumption that their overall features should be similar to the corresponding curves shown on Figure 3.

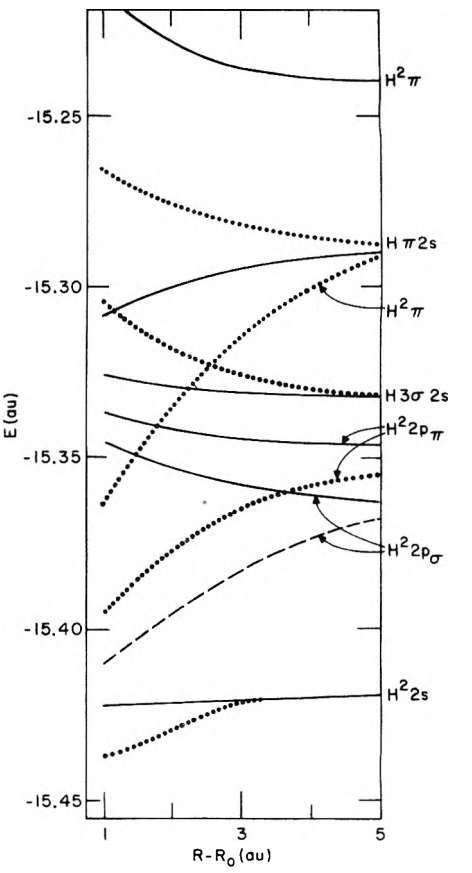

Figure 5. Comparison of SCF potential curves describing Li_2H formation from the collinear reactions Li → HLi (dotted curves) and Li → LiH (solid curves). For the dotted curves, $R_0 = 3.0$ au and R is the distance between H and the incident Li. For the solid curves, $R_0 = 5.07$ au and R is the Li–Li distance. In both cases the LiH bond length is fixed at 3.0 au.

5. Reactions of Li with LiH

SCF potential curves for a collinear reaction of Li with LiH are shown on Figure 5. The LiH bond length is frozen at the equilibrium value, 3 au. The solid curves represent Li approaching the Li atom end of LiH, and the dotted lines represent Li approaching the H atom end of LiH. The dashed curve is an estimate of the variationally collapsed SCF curve. The abscissa ($R - R_0$) is the deviation from the appropriate diatomic molecule equilibrium bond length. When Li approaches the Li end of LiH (solid curves), R is the distance between Li atoms, and $R_0 = 5.07$ au, the equilibrium Li_2 bond length. When Li approaches the H end of LiH (dotted curves), R is the distance between the incoming Li atom and the H atom, and $R_0 = 3$ au, the equilibrium LiH bond length. The curve labels are the same as described for Figure 1.

A striking feature on Figure 5 is the large separation between the solid and dotted $H^2\pi$ curves. This arises from charge transfer of the type LiH^-Li^+, which is much more stable when Li^+ approaches the H^- end of the molecule. We have found similar charge transfer in the $H^2 2p_\sigma$ curves. This will be discussed fully in a future publication.[8]

Reactions involving ionic states of LiH with Li favor a Li approach to the H^- end of the molecule. The CD on Figure 2 shows that C_s paths are energetically more favorable than linear paths. Nevertheless, even linear paths lead to stable Li_2H, as can be seen from Figure 5. If Li′ is the incident atom, this means that there is a reactive cone about the LiLi′ axis for reactions of Li′ with the H^- end of LiH. Judging from the CD, the range of HLiLi′ angles (relative to the LiLi′ axis) subtended by the cone is more than 40°. It can therefore be expected to have dynamical significance.[3]

The reactions

$$Li(^2S) + LiH(^1\Sigma^+) = Li_2H(^2A_1) \quad (2)$$

$$Li(^2P_\Sigma) + LiH(^1\Sigma^+) = Li_2H(^2B_2) \quad (3)$$

$$Li(^2P_\Pi) + LiH(^1\Sigma^+) = Li_2H(^2A_1, {}^2B_1) \quad (4)$$

are predicted to be exothermic by ~20 kcal/mol. The same prediction for (2) was made by Siegbahn and Schaefer.[2] This is insufficient energy to open the product channels

$$Li_2H(^2A_1) = Li_2(^1\Sigma_g^+) + H(^2S) \quad (5)$$

$$Li_2H(^2B_2) = Li_2(^{1,3}\Sigma_u^+) + H(^2S) \quad (6)$$

$$Li_2H(^2A_1, {}^2B_2) = Li_2(^{1,3}\Pi_u) + H(^2S) \quad (7)$$

We have previously given qualitative paths for reactions of H with Li_2.[3] These paths are smooth and apparently provide easy access to LiH + Li channels. Consequently, allowing Li to react with LiH as in (2)–(4) may be a better way to obtain Li_2H, which at present has not been observed.

Consider collinear reactions of Li with LiH in a covalent state ($H3\sigma 2s$ and $H\pi 2s$ on Figure 5). Figure 5 shows that the Li atom approach to the Li end of LiH is preferred. This is reasonable since covalent states of Li_2H are unstable relative to $H(^2S) + Li_2(^{1,3}\Sigma_u^+, {}^{1,3}\Pi_u)$.[3] Approach of Li to the Li end of LiH (covalent state) leads directly to the H + Li_2 products.

It should be pointed out that the bound Σ^+ and Π states of LiH have equilibrium bond lengths around 5 au,[11-13] significantly larger than the frozen value of 3 au used on Figure 5. Consequences of this can be estimated from the energies reported in Table II. For both $H3\sigma 2s$ and $H\pi 2s$,

the HLi = 5 au energy (corresponding to a LiH bond length of 5 au in linear HLi–Li) is lower than the LiLi′ = 6 au energy (corresponding to a LiH bond length of 3 au in linear HLi–Li) by ~7 kcal/mol. This energy difference is almost the same as the energy difference between the 5 and 3 au bond length energies of the covalent Σ^+ and Π states of LiH.[11-13] Therefore, the estimated effect of using the 3 au LiH bond lengths is an upward shift of the solid LiH $H3\sigma 2s$ and $H\pi 2s$ curves on Figure 5 by ~7 kcal/mol. This is perhaps reasonable because the excited states of LiH have broad wells, and the energy is somewhat insensitive to bond length changes.

References and Notes

(1) Y. T. Lee, R. J. Gordon, and D. R. Herschbach, *J. Chem. Phys.*, **54**, 2410 (1971).
(2) P. Siegbahn and H. F. Shaefer, *J. Chem. Phys.*, **62**, 3488 (1975).
(3) W. B. England, N. H. Sabelli, and A. C. Wahl, *J. Chem. Phys.*, **63**, 4596 (1975).
(4) C. C. J. Roothaan, *Rev. Mod. Phys.*, **23**, 69 (1951).
(5) C. C. J. Roothaan, *Rev. Mod. Phys.*, **32**, 179 (1960).
(6) C. C. J. Roothaan and P. S. Bagus in "Methods in Computational Physics", Vol. 2, B. Alder, S. Fernbach, and M. Rotenberg, Ed., Academic Press, New York, N.Y., 1963.
(7) G. Das and A. C. Wahl, "BISONMC: A Fortran Computational System for MCSCF Calculations on Atoms, Diatoms and Polyatoms", Argonne National Laboratory Report ANL-7955, 1972.
(8) W. B. England, N. Sabelli, and A. C. Wahl, to be submitted for publication.
(9) J. L. Magee, *J. Chem. Phys.*, **8**, 687 (1940).
(10) F. T. Smith, *Phys. Rev.*, **179**, 111 (1969).
(11) G. Herzberg, "Spectra of Diatomic Molecules", 2nd ed, Van Nostrand, Princeton, N.J., 1950.
(12) K. K. Docken and J. Hinze, *J. Chem. Phys.*, **57**, 4928 (1972).
(13) K. K. Docken, Ph.D. Dissertation, The University of Chicago, 1972.

The Combination of Molecular Covolume and Frictional Coefficient to Determine the Shape and Axial Ratio of a Rigid Macromolecule. Studies on Ovalbumin

P. D. Jeffrey, L. W. Nichol,* D. R. Turner,

Department of Physical Biochemistry, John Curtin School of Medical Research, Australian National University, Canberra, A.C.T. 2601, Australia

and D. J. Winzor

Department of Biochemistry, University of Queensland, St. Lucia, Queensland 4067, Australia

(Received September 7, 1976)

A function ψ is formulated as $U_{22}\eta^3/N(f_2^H)^3$, where N is Avogadro's number, U_{22} is the effective covolume of a noninteracting macromolecule, f_2^H its translational frictional coefficient, and η is the viscosity of the medium used for determination of these experimental quantities. Theory is presented to show that ψ is an explicit function of the axial ratio of oblate and prolate ellipsoids of revolution (or their limiting case, a sphere). Plots of ψ is relation are presented for the oblate and prolate cases: these curves diverge in a manner such that a particular value of ψ defines uniquely the geometry of the ellipsoid and, therefore, they offer advantage over analogous plots which correlate only hydrodynamic parameters. It follows that, provided a macromolecule in solution may be assumed to behave as such an ellipsoid, a potential means is available for defining its geometry without assumption concerning the degree of hydration. This potential is explored with results obtained for ovalbumin at pH 4.59 and 7.50, where the net charge borne by the protein is, respectively, zero and −14. Particular emphasis is given to the determination of U_{22} from the concentration dependence of activity coefficients obtained from sedimentation equilibrium results by the recently developed $\Omega(r)$ analysis. Correlation of mean values of the parameters defining ψ indicates that ovalbumin behaves in solution as a prolate ellipsoid of revolution with axial ratio 2.5:1 and degree of hydration 0.37 g/g. It is stressed, however, that this interpretation is based on best estimates of the parameters: the results also permit assessment of experimental errors and thus comment on likely limitations of the approach.

It is well established that determination of the frictional ratio of a single, noninteracting macromolecule is not sufficient to define its shape,[1-6] except in special cases.[7] Thus, in general, the contour diagram presented by Oncley[1] shows that a choice remains between a prolate and an oblate ellipsoid each of specified axial ratio, even when a degree of hydration has been assumed. In an attempt to overcome this ambiguity, frictional ratios and intrinsic viscosity were combined,[2-4] an example being the determination of the β parameter of Scheraga and Mandelkern.[2] This parameter, however, is almost completely insensitive to variation in axial ratio for oblate ellipsoids and, moreover, with experimental uncertainty can only be used to distinguish between prolate and oblate cases for extremely asymmetric molecules. The major use of the β parameter has therefore been in molecular weight determinations.[8,9] Other combinations of hydrodynamic parameters, such as the intrinsic viscosity and the coefficient of the concentration dependence of the reciprocal sedimentation coefficient, have also been discussed[10,11] as indices of relative asymmetry. One purpose of the present work is to explore the possibility that a different type of combination, that of the translational frictional coefficient with the covolume of the macromolecule deduced from the concentration dependence of its activity coefficient, might provide a more sensitive means of delineating between oblate and prolate ellipsoids and of determining the relevant axial ratio without initial specification of the degree of hydration. Theory is presented showing that this combination of parameters does indeed lead to a function, ψ, capable both of experimental determination and of independent formulation in terms of axial ratio. Moreover,

the dependence of ψ on axial ratio is such that distinction between prolate and oblate ellipsoids of any axial ratio is possible in principle.

Basic to the experimental determination of the ψ function and its potential practical use is a sufficiently precise determination of the concentration dependence of the activity coefficient. The second aspect of this work is concerned with the presentation of a method of evaluating activity coefficients from sedimentation equilibrium results utilizing the recently developed $\Omega(r)$ analysis.[12,13] The method is illustrated with sedimentation equilibrium results obtained with ovalbumin at its isoelectric point (pH 4.59) and at pH 7.50. Comment is then made on the asymmetry and hydration of ovalbumin predicted on the basis of the ψ function. As ovalbumin is not markedly asymmetric,[14,15] it provides a suitable test system for assessing the likely limitations of the present approach.

Theory

Determination of Activity Coefficients and Effective Covolumes from Sedimentation Equilibrium. Consider the sedimentation equilibrium of a solution of a single, noninteracting macromolecule, denoted by subscript 2, which has been predialyzed against buffer, the dialyzate being used in the reference channel.[16] The experimental record at equilibrium may be formulated as a plot of the weight concentration $c_2(r)$ vs. radial distance r with the use of the specific refractive increment (Rayleigh interference optics) or the extinction coefficient (absorption optics) both proportionality constants being referred to the anhydrous concentration scale (g/L). On the other hand, the thermodynamic description of the equilibrium distribution is in terms of the activity, which is usually defined in terms of an infinitely dilute reference state and of weight-based concentrations.[17,18] The expression relating $a_2(r)$, the activity of macromolecular solute at any radial distance r, to $a_2(r_F)$, its activity at any reference radial distance r_F, is

$$a_2(r) = a_2(r_F) \exp\{M_2^U(1 - \bar{v}_2^U\rho)\omega^2(r^2 - r_F^2)/2RT\} \quad (1)$$

where ρ is the solution density, ω the angular velocity, R the gas constant, and T the temperature; M_2^U and $\bar{v}_2^U$ denote, respectively, the unsolvated molecular weight and partial specific volume. It is implicit in eq 1 that $M_2^U(1 - \bar{v}_2^U\rho)$ has been assumed constant, and hence its value may be determined from the limiting slope, d ln $c_2(r)$/dr^2, as $c_2(r) \to 0$ in a sedimentation equilibrium experiment of the meniscus-depletion design.[19] Moreover, when required, M_2^U may be evaluated using the apparent specific volume based on density measurements and an unsolvated solute concentration scale as an independent estimate of $\bar{v}_2^U$. As noted by Casassa and Eisenberg,[16] the value of M_2^U so obtained refers to the molecular weight of macroion plus counterions required for electrical neutrality.

It is now possible to select a reference point (r_F, $c_2(r_F)$) in any sedimentation equilibrium distribution and thereby to formulate values of $\Omega_2(r)$, defined previously[12,13] as

$$\Omega_2(r) = c_2(r) \exp\{M_2^U(1 - \bar{v}_2^U\rho)\omega^2(r_F^2 - r^2)/2RT\}/c_2(r_F) \quad (2a)$$

Application of eq 1 and l'Hôpital's rule reveals that the extrapolated value of a plot of $\Omega_2(r)$ vs. $c_2(r)$ is given by[12,13]

$$\lim_{c_2(r) \to 0} \Omega_2(r) = a_2(r_F)/c_2(r_F) = y_2(r_F) \quad (2b)$$

where $y_2(r_F)$ is the activity coefficient at r_F. Moreover, since combination of eq 1 and 2a shows that $\Omega_2(r) = c_2(r)a_2(r_F)/c_2(r_F)a_2(r) = y_2(r_F)c_2(r)/a_2(r)$, it follows that

$$y_2(r) = y_2(r_F)/\Omega_2(r) \quad (2c)$$

The results of a series of sedimentation equilibrium experiments may therefore be correlated as a plot of ln $y_2(r)$ vs. $c_2(r)/M_2^U$. Following previous formulations,[17,20-22] we may write

$$\ln y_2(r) = (\alpha_{22}c_2(r)/M_2^U) + \text{higher terms} \quad (3)$$

where $c_2(r)/M_2^U$ is the molar concentration, which has been substituted for the molal concentration. The value of α_{22} (M^{-1}), the apparent second virial coefficient from sedimentation equilibrium referring to the macromolecule as it exists in solution, may be determined as the limiting slope of the plot as $c_2(r)/M_2^U \to 0$. Least-squares regression fit of the experimental points may be used to aid the determination of this slope. It might be noted that α_{22} is related to B, the second virial coefficient employed in osmometry, by the expression $\alpha_{22} = 2B(M_2^U)^2$.

Ogston and Winzor[22] in their eq 12 have identified α_{22} as

$$\alpha_{22} = U_{22} + (Z^2/2I) \quad (4)$$

where U_{22} and Z_2 are respectively the effective covolume and net charge of the macromolecule and I is the ionic strength of the uniunivalent supporting electrolyte. Indeed eq 4 is formally identical with eq 34 of Scatchard[23] with the final term of the latter equation neglected: this omission is justified for studies performed at the isoelectric point where $Z_2 = 0$ and no Gibbs–Donnan effect operates. Moreover, it will be shown later that this final term is often likely to be of negligible magnitude in relation to experimental values of α_{22} found when Z_2 is nonzero. Provided that Z_2 is known, the use of the $\Omega_2(r)$ analysis of sedimentation equilibrium results in conjunction with eq 4 permits evaluation of U_{22}. U_{22} has been termed an *effective* covolume to emphasize that we are equating U_{22} with Scatchard's[23] β_{22}, which includes other factors as well as the true excluded volume. We are thus assuming that the contributions of these additional factors can be taken into account by employing an operationally defined covolume[24] that may differ from the true excluded volume. Some support for the use of this operationally defined U_{22} for the covolume of globular proteins is provided by the agreement observed between the Stokes radius of hemoglobin derived from velocity sedimentation and the effective covolume radius deduced from osmometry.[25]

The effective covolume defined by eq 3 and 4 refers to the hydrated macromolecule since it is determined from an experimentally measured value of α_{22}. In this connection, we note that values of $\Omega_2(r)$ and $y_2(r)$ defined by eq 2a and 2c, respectively, remain virtually unaltered if the hydrated particle is considered in a conceptual sense, because $M_2^U(1 - \bar{v}_2^U\rho) = M_2^H(1 - \bar{v}_2^H\rho)$ provided ρ approximates to the reciprocal of the solvent partial specific volume, v_1. Thus the plot of ln $y_2(r)$ vs. the molar concentration ($c_2^U/M_2^U = c_2^H/M_2^H$) is essentially unchanged by considering consistently either the hydrated or the anhydrous situations and, indeed, in the limit $c_2(r) \to 0$, where α_{22} is determined, the formulations become identical.

The ψ Function. In order to proceed, it is now necessary to write an expression relating U_{22} to the geometrical factors that dictate the shape of the entity whose effective covolume has been found experimentally. To this end the commonly used practice[1,2,6,9,14,15] will be adopted of assuming that this entity may be represented as a prolate or oblate ellipsoid of revolution (or their limiting case, a sphere). On this basis, U_{22} is related to the axial ratio by an expression common to both prolate and oblate ellipsoids[26-28]

$$U_{22} = NV_2^{H}\left\{2 + \frac{3}{2}\left(1 + \frac{\sin^{-1}\epsilon}{\epsilon(1-\epsilon^2)^{1/2}}\right)\left(1 + \frac{1-\epsilon^2}{2\epsilon}\ln\frac{1+\epsilon}{1-\epsilon}\right)\right\} \quad (5a)$$

$$\epsilon^2 = 1 - (b^2/a^2) \quad (5b)$$

where N is Avogadro's number, V_2^{H} is the volume (in L) of a molecule whose effective covolume is U_{22} (M^{-1}), and ϵ is the eccentricity, a dimensionless quantity related to the axial ratio a/b, as defined in eq 5b. The convention is adopted for both prolate and oblate ellipsoids that a is the major semi-axis and b the minor semi-axis, such that $a/b \geq 1$ and hence $0 \leq \epsilon < 1$ for both cases. When $\epsilon = 0$ (a sphere) eq 5a becomes $U_{22} = 32N\pi r^3/3$ since the limits as $\epsilon \rightarrow 0$ of $\sin^{-1}\epsilon/\epsilon$ and of $(1/2\epsilon)\ln\{(1+\epsilon)/(1-\epsilon)\}$ are unity; this is in accord with the established[15] self-covolume of a sphere, $4\pi(r+r)^3/3$.

Inspection of eq 5a shows that an explicit expression is required for V_2^{H} (for both prolate and oblate cases) in terms of ϵ. This may be done in the following steps. First, the required volumes V_2^{H} and the frictional coefficients, f_2^{0}, of spheres of the same volume are given by[14]

$$V_2^{H} = 4\pi ab^2/3; \quad f_2^{0} = 6\pi\eta(ab^2)^{1/3} \quad \text{(prolate)} \quad (6a)$$

$$V_2^{H} = 4\pi a^2 b/3; \quad f_2^{0} = 6\pi\eta(a^2 b)^{1/3} \quad \text{(oblate)} \quad (6b)$$

where η is the viscosity of the medium used for the determination of U_{22}. Secondly, the frictional ratios of the hydrated ellipsoids have been given in terms of the axial ratios[14,15,29,30] and become on rearrangement using eq 5b

$$f_2^{H}/f_2^{0} = 2\epsilon/[(1-\epsilon^2)^{1/3}\ln\{(1+\epsilon)/(1-\epsilon)\}] \quad \text{(prolate)} \quad (7a)$$

$$f_2^{H}/f_2^{0} = \epsilon/[(1-\epsilon^2)^{1/6}\sin^{-1}\epsilon] \quad \text{(oblate)} \quad (7b)$$

Eliminating f_2^{0} between eq 6 and 7 gives

$$V_2^{H} = \frac{4\pi(f_2^{H})^3(1-\epsilon^2)\{\ln[(1+\epsilon)/(1-\epsilon)]\}^3}{3(6\pi\eta)^3(2\epsilon)^3} \quad \text{(prolate)} \quad (8a)$$

$$V_2^{H} = \frac{4\pi(f_2^{H})^3(\sin^{-1}\epsilon)^3(1-\epsilon^2)^{1/2}}{3(6\pi\eta)^3\epsilon^3} \quad \text{(oblate)} \quad (8b)$$

which are the required expressions. Equations 8a and (separately) 8b may now be combined with eq 5a to yield

$$\psi = \frac{\left\{2 + \frac{3}{2}\left(1 + \frac{\sin^{-1}\epsilon}{\epsilon(1-\epsilon^2)^{1/2}}\right)\left(1 + \frac{1-\epsilon^2}{2\epsilon}\times\ln\frac{1+\epsilon}{1-\epsilon}\right)\right\}\{1-\epsilon^2\}\left\{\ln\frac{1+\epsilon}{1-\epsilon}\right\}^3}{1296\pi^2\epsilon^3} \quad \text{(prolate)} \quad (9a)$$

$$\psi = \frac{\left\{2 + \frac{3}{2}\left(1 + \frac{\sin^{-1}\epsilon}{\epsilon(1-\epsilon^2)^{1/2}}\right)\left(1 + \frac{1-\epsilon^2}{2\epsilon}\times\ln\frac{1+\epsilon}{1-\epsilon}\right)\right\}\{\sin^{-1}\epsilon\}^3(1-\epsilon^2)^{1/2}}{162\pi^2\epsilon^3} \quad \text{(oblate)} \quad (9b)$$

where

$$\psi = U_{22}\eta^3/N(f_2^{H})^3 \quad (9c)$$

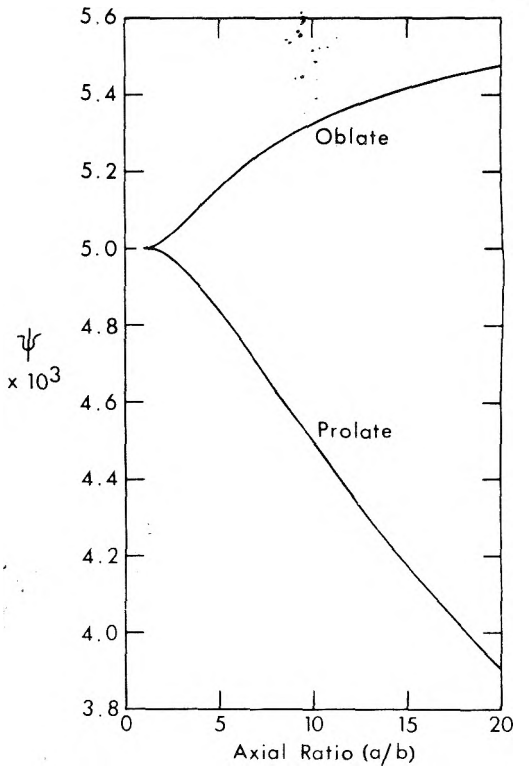

Figure 1. A theoretical plot of the ψ function for prolate ellipsoids (eq 9a) and oblate ellipsoids of revolution (eq 9b) as a function of the axial ratio a/b, related to the eccentricity by eq 5b.

Values of ϵ in the permitted range were used to calculate from eq 9a and 9b values of ψ and from eq 5b the corresponding values of the axial ratio. These calculated values are plotted in Figure 1 and it is noted that the range could readily be extended, if required. The two curves shown in Figure 1 have the same value of ψ when $a/b \rightarrow 1$ (sphere), this common value being $8/162\pi^2$ as may readily be shown by applying limit arguments to eq 9a and 9b. For values of $a/b > 1$, it is clear not only that the curves for the prolate and oblate cases diverge, but also that a unique value of ψ is associated with a unique axial ratio for a specified ellipsoid. This behavior may be contrasted with the analogous plot of the β parameter defined by Scheraga and Mandelkern.[2] Equation 9c stresses that ψ may be obtained as an experimental quantity, the evaluation of U_{22} and η having already been outlined. The remaining quantity requiring comment is f_2^{H}, the translational frictional coefficient of the entity whose effective covolume is U_{22}. This quantity may be found from

$$f_2^{H} = \frac{M_2^{H}(1-\bar{v}_2^{H}\rho)}{Ns_2^{0}} = \frac{M_2^{U}(1-v_2^{U}\rho)}{Ns_2^{0}}; \quad \lim_{c_2 \rightarrow 0}\rho = 1/v_1 \quad (10)$$

where s_2^{0} is the value of the sedimentation coefficient at infinite dilution, determined by extrapolation of values found in the same buffer and at the same temperature as used for the determination of U_{22}. Again it is noted that $M_2^{U}(1-\bar{v}_2^{U}\rho)$ is needed and is available from a sedimentation equilibrium experiment of the meniscus-depletion design.[19]

Four further points require comment. First, no assumption has to this point been made concerning the degree of hydration nor (if this is nonzero) to the disposition of the "bound" water except that the hydrated entity has been described as an exact ellipsoid of revolution.

Secondly, it is implicit in the joint use of f_2^H and U_{22}, via the ψ function, that the hydrated entity behaves as the same ellipsoid in both velocity and equilibrium sedimentation performed in the same environment. A similar point has been queried[9] when correlation is made of intrinsic viscosity and sedimentation velocity results obtained under different shearing stress. There are, of course, differences between sedimentation velocity and sedimentation equilibrium; but nevertheless (and especially for relatively rigid and impenetrable molecules[22]) the queried identity would appear to have equal justification in the present context. Thirdly, although the theoretical treatment has shown that a particular value of ψ defines a unique geometry, it is not suggested that ψ will be without uncertainty when experimentally determined; this point will be examined further after the presentation of experimental results. Finally, since the method outlined for the evaluation of α_{22} applies only to monodisperse systems (defined by a single value of $M_2^U(1 - \bar{v}_2^U\rho)$), precautions should be taken to ensure that the solute being examined is homogeneous with respect to molecular weight.

Experimental Section

Materials. Two buffers were employed in this work: pH 4.59 (0.01 M sodium acetate, 0.01 M acetic acid, 0.15 M sodium chloride, 0.001 M EDTA), ionic strength 0.16, η_{20} = 0.010 16 P, ρ_{20} = 1.0057 g/mL; and pH 7.50 (0.01 M sodium diethylbarbiturate, 0.02 M diethylbarbituric acid, 0.09 M sodium chloride), ionic strength 0.10, η_{20} = 0.010 27 P, ρ_{20} = 1.0032 g/mL. Ovalbumin (Sigma, salt-free, crystallized and lyophilized) in the appropriate buffer was subjected to gel chromatography on Sephadex G-100 (Pharmacia), the fraction at the peak maximum being used after suitable dilution for sedimentation experiments. All such experiments employed fresh samples and were preceded by exhaustive dialysis (using prewashed 18/32 Visking tubing) against the relevant buffer.[16] Protein concentrations were measured spectrophotometrically at 280 nm using an extinction coefficient[31] of 6.6 ($E^{1\%}_{1cm}$) and checked refractometrically.

Sedimentation Experiments. Sedimentation velocity experiments were performed at 60 000 rpm and 20 ± 0.1 °C in a Spinco Model E ultracentrifuge employing schlieren optics. Duplicate experiments 48 h apart (exceeding the maximum time required to complete a sedimentation equilibrium experiment) at both pH 4.59 and 7.50 revealed that the protein remained homogeneous. In this connection it is noted that previous workers[32,33] had reported aggregation of ovalbumin in metal centerpieces near the isoelectric point (pH 4.59); the effect was obviated in the present work by including EDTA in the isoelectric buffer and by avoiding contact of the protein solutions with metal surfaces. To this end, Kel-F and carbon-filled centerpieces were used in sedimentation velocity and equilibrium experiments, respectively. The measured sedimentation coefficients at each pH fitted within 1% the relationship $s_{20,w} = (3.42 - 0.026c_2)S$, with $0.1 < c_2$ (g/L) < 10, reported by Creeth and Winzor.[34] The corresponding s_2^0 value (at 20 °C in buffer, appropriate to this work) was 3.81 ± 0.03S (for both buffers), found by employing the standard correction[14] and a partial specific volume, $\bar{v}_2^U$, of 0.7479 mL/g.[35]

In sedimentation equilibrium experiments equal amounts by weight of the fluorocarbon FC43 (0.04 g) and protein solution and its equilibrium dialyzate (0.1 or 0.2 g) were placed in the respective sectors of a double-sector cell. In control experiments at both pH values no interaction between the FC43 and protein solutions was detected. In experiments where the method of overspeeding[36] was employed to shorten the time required to approach equilibrium, the initial velocity was 1.4 times the final value; overspeeding and total times were calculated from Figure 4 of Howlett and Nichol.[37] Details of experimental parameters for each sedimentation equilibrium experiment are reported in the text. Rayleigh interference optics were used to record the equilibrium distributions which were measured according to the method of Richards et al.[38] with a Nikon microcomparator. Results are presented in terms of a concentration scale in Rayleigh interference fringes $J_2(r)$; conversion to a weight concentration scale is effected by noting that 1 g/L of ovalbumin corresponds to 4.00 fringes using the cell path length of 1.2 cm, a wavelength of 5461 Å (employed in this work) and the anhydrous specific refractive increment of 0.001 82 dL/g for ovalbumin.[39]

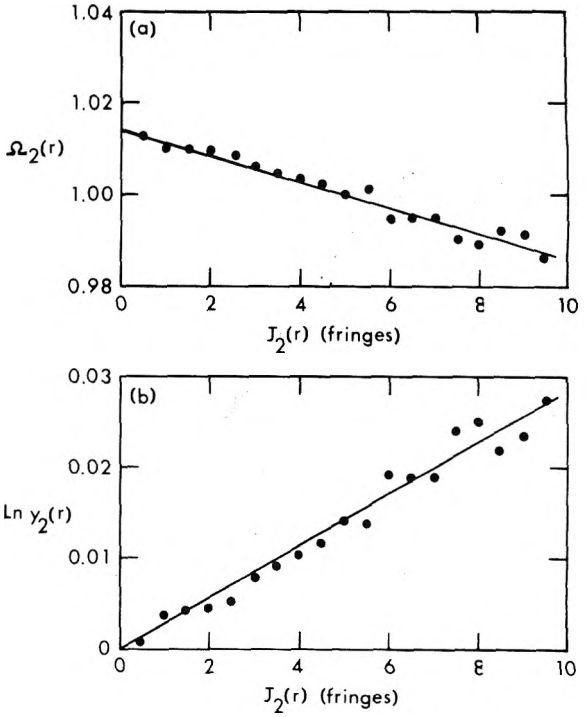

Figure 2. Results pertaining to the sedimentation equilibrium of ovalbumin at ionic strength 0.16, 20 °C, and pH 4.59, the isoelectric point. Experimental details are given in the text. (a) A plot of $\Omega_2(r)$ defined by eq 2a vs. $J_2(r)$, the concentration in fringes. Experimental points are denoted by ● and the solid line was obtained by least-squares regression; (b) the corresponding values of ln $y_2(r)$ found using eq 2c vs. $J_2(r)$. The solid line describes the relation ln $y_2(r) = 0.0028J_2(r)$.

Results and Discussion

Studies on Isoelectric Ovalbumin. Figure 2 presents results pertaining to a sedimentation equilibrium experiment conducted at pH 4.59 with intial loading concentration of ovalbumin of 0.36 g/L, angular velocity of 20 000 rpm, and column height of 0.5842 cm. The experiment was run for 36 h and was of the meniscus-depletion design,[19] evaluation of the limiting slope d ln $c_2(r)/d(r^2)$ as $c_2(r) \rightarrow 0$ giving a value of 45 000 for M_2^U, in agreement with previous findings.[40] This value of the molecular weight and a partial specific volume of 0.7479 mL/g[35] were used in all calculations. Figure 2a was constructed using eq 2a and the reference point r_F = 7.1000 cm, $J_2(r_F)$ = 5 fringes. The extrapolated value of 1.014 was determined by least-squares regression and equals, according to eq 2b, $y_2(r_F)$. Equation 2c was then employed to calculate $y_2(r)$ as a function of $J_2(r)$, leading to the results plotted in Figure 2b. By least-squares regression these results are

described by $\ln y_2(r) = 0.0028 \pm 0.0001 J_2(r)$, the slope corresponding to a value of $5.0 \pm 0.2 \times 10^5$ mL/mol for α_{22} defined in eq 3; clearly, up to a concentration of 2.5 g/L ($J_2(r) = 10$) effects of higher virial coefficients were within experimental error. Since under these conditions Z_2, the net charge borne by ovalbumin, is close to zero, this value of α_{22} equals the effective covolume U_{22} (eq 4). The corresponding value of f_2^H calculated from eq 10 is $5.60 \pm 0.05 \times 10^{-8}$ g/s.

Using the mean values of U_{22} and f_2^H together with the reported η of 0.010 16 P leads by eq 9c to a value of $4.9_7 \times 10^{-3}$ for the ψ function. Interpolation of this mean value in Figure 1 reveals that ovalbumin in the defined environment behaves as a prolate ellipsoid with axial ratio a/b of 2.5:1. Comment on the uncertainty in interpretation due to experimental error follows after presentation of further results. It could be noted immediately, however, that this axial ratio corresponds to an eccentricity ϵ of 0.92 and yields via eq 8 a value of 8.3×10^{-23} L for V_2^H. If the standard relations[15] $M_2^H = M_2^U(1 + w)$, $\bar{v}_2^H = (\bar{v}_2^U + w v_1)/(1 + w)$, and $V_2^H = M_2^H \bar{v}_2^H / N$, are combined, the last relation not being without question,[2,9] we obtain

$$w = (N V_2^H - M_2^U \bar{v}_2^U)/M_2^U v_1 \qquad (11)$$

where w is the number of grams of solvent bound per gram of dry solute. It follows that the apparent value of w is 0.37 g/g, which is within the range generally accepted for globular proteins.[15]

Studies of Ovalbumin at pH 7.5. Two further sedimentation equilibrium experiments were performed, both at pH 7.50. The first utilized an initial loading concentration of 0.98 g/L with column height 0.2858 cm and was conducted at a final angular velocity of 17 000 rpm after initial overspeeding.[36,37] The total time to reach equilibrium was 20 h and $J_2(r)$ at the meniscus was 0.70 fringes. Figure 3a was constructed in an analogous manner to Figure 2a using the reference point $r_F = 7.0485$ cm, $J_2(r_F) = 5$ fringes. It is immediately apparent that the slope as $J_2(r) \to 0$ in Figure 3a is greater than that in Figure 2a, as is the ordinate intercept; in this instance $y_2(r_F) = 1.043$. Moreover, in contrast to Figure 2a, the plot in Figure 3a deviates from linearity in the vicinity of $J_2(r)$ of 8 fringes. This is manifested as a slight deviation from linearity in the plot of $\ln y_2(r)$ vs. $J_2(r)$ calculated using eq 2c and shown in Figure 3b. The deviation (albeit slight) reflects the operation of higher order terms in eq 3, an interpretation supported by the results of the second experiment, conducted over a higher total concentration range, and also shown in Figure 3b. This second experiment at pH 7.5 was conducted with an initial loading concentration of 5.87 g/L, a column height of 0.2782 cm, final angular velocity after overspeeding of 10 000 rpm, total equilibrium time of 21 h, and led to $J_2(r)$ at the meniscus of 14.50 fringes; a reference point of $r_F = 7.0248$ cm, $J_2(r_F) = 25.5$ fringes was used to compute the $\Omega_2(r)$ plot leading to the results shown in Figure 3b. Least-squares regression fit of all results shown in Figure 3b to the quadratic

$$\ln y_2(r) = (\alpha_{22} c_2(r)/M_2^U) + (\theta_{22} c_2^2(r)/M_2^U)^2 \qquad (12)$$

lead to values of $\alpha_{22} = 14.9 \times 10^5$ mL/mol and $\theta_{22} = -2.1 \times 10^{12}$ mL^2 mol^{-2}. While the latter value of the third virial coefficient must be regarded as apparent, it does not significantly influence the value of the limiting slope d $\ln y_2(r)/dc_2(r)$ as $c_2(r) \to 0$ applicable to the determination of α_{22} in the present analysis. It is, however, of interest to note that if the low range of $c_2(r)$ was not accessible (in osmotic pressure studies, for example), an erroneous apparent limiting slope affected by θ_{22} may be assigned,

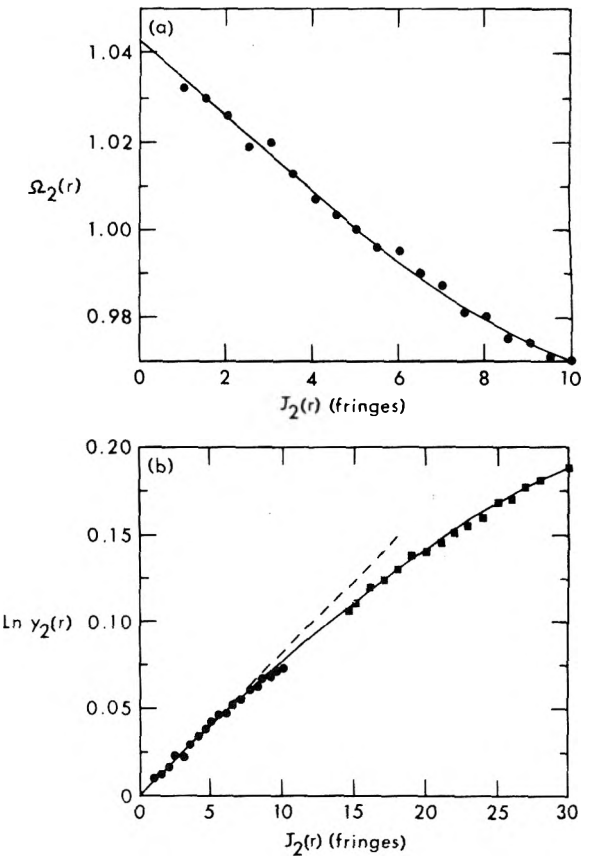

Figure 3. Sedimentation equilibrium results obtained with ovalbumin at ionic strength 0.1, 20 °C, and pH 7.50. (a) A plot of $\Omega_2(r)$ vs. $J_2(r)$ for the experiment conducted with $\omega = 17\,000$ rpm (further details in text). The solid line represents an attempt to average the experimental data (●). (b) Corresponding values (●) of $\ln y_2(r)$ vs. $J_2(r)$ and similar values (■) found in a separate experiment conducted with $\omega = 10\,000$ rpm. The solid curve is described by eq 12, while the broken line is the limiting tangent predicted with $U_{22} = 5.0 \times 10^5$ mL/mol and $Z_2 = -14.0$.

leading to an underestimate of α_{22}.

The correlation of α_{22} measured at pH 7.50 with the covolume U_{22}, and hence the ψ function, requires discussion of the net charge Z_2 borne by ovalbumin in this environment both with respect to the second term appearing in eq 4 and the neglected term appearing in eq 34 of Scatchard.[23]

Charge on Ovalbumin at pH 7.5. From the pH-titration data of Cannan et al.,[41] 14 equiv of OH^- per mol are required to adjust isoionic ovalbumin (pH 4.98) to pH 7.8, a further 4 equiv of H^+ per mol being required to titrate the isoionic solution to pH 4.59, the isoelectric point in 0.1I buffers. On the basis of these data and the additional assumption of no changes in ion binding, Longsworth[42] considered the net charge at pH 7.8 to be −18. However, Carr[43] has detected the binding of 4 chloride ions per mol of ovalbumin at pH 5 which are not present at pH 6; he has also found no evidence of cation binding at neutral pH.[44] Consequently, Longsworth's estimate of −18 for the charge on ovalbumin at pH 7.8 becomes −14 when allowance is made for the change in chloride binding. Since the state of ionization of ovalbumin varies little between pH 7.5 and 7.8 (ref 41), it follows that, within the ability to interpret pH-titration data, a charge of −14 is indicated for ovalbumin at pH 7.5.

At variance with this conclusion is the report[34] of a charge of −10.7 for ovalbumin in 0.1I buffer, pH 8.5, the estimate being based on δ-boundary elimination[45] in moving boundary electrophoresis. However, this procedure required the calculation of the Kohlrausch regulating

function[46] $\sum m_i Z_i/u_i$ (where m_i denotes the molarity of ion i with charge Z_i and mobility u_i). In the earlier report[34] the measured mobility of ovalbumin at 1 °C was coupled with values of u_i for the three buffer ions that were corrected from 0 to 1 °C, a potential source of error in the summation required to calculate the regulating function. This correction can be obviated by using the mobility-pH data of Longsworth,[42] which refer to the migration of ovalbumin at 0 °C. Coupling of the value of -6.0×10^{-5} $cm^2\ s^{-1}\ V^{-1}$ with the buffer ion mobilities (also at 0 °C) reported by Alberty[47] leads to an estimate of −14.2 for the charge on ovalbumin at pH 8.5. On the basis of the ratio of mobilities at pH 7.5 and 8.5 the charge at pH 7.5 is −14.0, in agreement with the value obtained from pH-titration data after correction for chloride binding.

Neglect of the Solvent–Solute Term in Eq 4. As noted earlier, eq 4 is formally identical with eq 34 of Scatchard[23] with the macromolecule–salt interaction term omitted. Such interaction may be expressed[23] as the product of two factors, the first (from eq 14–21 of Tanford[15]) being approximately $Z_2^4 m_2^2/16I^2$, where m_2 is the protein molarity and I the ionic strength of the uniunivalent electrolyte used as dialyzate. In regard to the second factor $((2/I) + \beta_{33})$, an approximate value of β_{33} may be obtained from the empirical relationship presented by Scatchard et al.[48] for sodium chloride at 25 °C. With $Z_2 = -14.0$, $I = 0.1$, and $m_2 = 1.7 \times 10^{-4}$ M (an extreme value in relation to Figure 3b) the neglected term assumes a magnitude of 0.001×10^5 mL/mol, which is certainly negligible in relation to the value of 14.9×10^5 mL/mol found for α_{22} at pH 7.5.

Correlation of U_{22} from Studies at pH 4.59 and 7.5. On the basis of $U_{22} = 5.0 \times 10^5$ mL/mol (the observed value at pH 4.59) and $Z_2 = -14.0$, the magnitude of α_{22} predicted by eq 4 for ovalbumin at pH 7.5 is 14.8×10^5 mL/mol. This value, which is represented in Figure 3b by the broken line, is in excellent agreement with the experimentally determined α_{22} of 14.9×10^5 mL/mol. Thus the experiments at pH 7.5 confirm the estimate (from studies at pH 4.59) of 5.0×10^5 mL/mol for the covolume U_{22} of ovalbumin.

Evaluation of the Uncertainty in ψ. With the reported standard errors in U_{22} and f_2^H, the standard error in ψ has been calculated[49] as $\pm 0.24 \times 10^{-3}$. The ψ range of $4.97 \pm 0.24 \times 10^{-3}$ for ovalbumin, when considered together with eq 11, indicates oblate and prolate ellipsoids with axial ratios approximately 5:1 and $w = 0$ as the possible extremes in interpretation. It seems fair to point out, however, that other methods of analysis[2,11] have used only mean values of the required parameters. Moreover, the error envelope assessed in this study suggests that distinction between prolate and oblate models would pose little difficulty in the investigation of more asymmetric molecules (axial ratio greater than 5:1). In this sense the use of the ψ function offers advantage over earlier treatments.[1,2,11] The major potential source of error in the present procedure is the assumption that the operationally defined U_{22} represents the true covolume. In this respect the method cannot possibly be applied to all macromolecules, since adoption of the present approach with a flexible polymer under Θ conditions would yield a value of zero for the effective covolume. However, the earlier result with hemoglobin[25] and the observed identity of U_{22} for ovalbumin in two buffers with different pH lend support to the assumption at least for globular proteins.

Evaluation of Activity Coefficients. Finally, it should be noted that this investigation has provided data on the activity coefficients of ovalbumin under two sets of conditions (Figure 2b and Figure 3b). By so doing, this study has illustrated a method which may find general application in determining this basic thermodynamic quantity for solutions of a variety of homogeneous, noninteracting solutes.

References and Notes

(1) J. L. Oncley, *Ann. N.Y. Acad. Sci.*, **41**, 121 (1941).
(2) H. A. Scheraga and L. Mandelkern, *J. Am. Chem. Soc.*, **75**, 179 (1953).
(3) C. Sadron, *Prog. Biophys. Biophys. Chem.*, **3**, 237 (1953).
(4) A. G. Ogston, *Trans. Faraday Soc.*, **49**, 1481 (1953).
(5) J. T. Edsall, "The Proteins", Vol 1B, H. Neurath and K. Bailey, Ed., Academic Press, New York, N.Y., 1953, p 549.
(6) H. K. Schachman, "Ultracentrifugation in Biochemistry", Academic Press, New York, N.Y. 1959.
(7) M. A. Lauffer, *J. Am. Chem. Soc.*, **66**, 1138 (1944).
(8) A. Holtzer and S. Lowey, *Biopolymers*, **1**, 497 (1963).
(9) J. T. Yang, *Adv. Protein Chem.*, **16**, 323 (1961).
(10) M. Wales and K. E. Van Holde, *J. Polym. Sci.*, **14**, 81 (1954).
(11) J. M. Creeth and C. G. Knight, *Biochim. Biophys. Acta*, **102**, 549 (1965).
(12) B. K. Milthorpe, P. D. Jeffrey, and L. W. Nichol, *Biophys. Chem.*, **3**, 169 (1975).
(13) L. W. Nichol, P. D. Jeffrey, and B. K. Milthorpe, *Biophys. Chem.*, **4**, 259 (1976).
(14) T. Svedberg and K. O. Pedersen, "The Ultracentrifuge", Oxford University Press, London, 1940.
(15) C. Tanford, "Physical Chemistry of Macromolecules", Wiley, New York, N.Y., 1961.
(16) E. F. Casassa and H. Eisenberg, *Adv. Protein Chem.*, **19**, 237 (1964).
(17) H. Fujita, "Mathematical Theory of Sedimentation Analysis", Academic Press, New York, N.Y., 1962.
(18) R. H. Haschemeyer and W. F. Bowers, *Biochemistry*, **9**, 435 (1970).
(19) D. A. Yphantis, *Biochemistry*, **3**, 297 (1964).
(20) J. W. Williams, K. E. Van Holde, R. L. Baldwin, and H. Fujita, *Chem. Rev.*, **58**, 715 (1958).
(21) H. Fujita, "Foundation of Ultracentrifugal Analysis", Wiley-Interscience, New York, N.Y., 1975
(22) A. G. Ogston and D. J. Winzor, *J. Phys. Chem.*, **79**, 2496 (1975).
(23) G. Scatchard, *J. Am. Chem. Soc.*, **68**, 2315 (1946).
(24) P. J. Flory, "Principles of Polymer Chemistry", Cornell University Press, Ithaca, N.Y., 1953.
(25) P. A. Baghurst, L. W. Nichol, A. G. Ogston, and D. J. Winzor, *Biochem. J.*, **147**, 575 (1975).
(26) A. Isihara, *J. Chem. Phys.*, **18**, 1446 (1950).
(27) L. W. Nichol, P. D. Jeffrey, and D. J. Winzor, *J. Phys. Chem.*, **80**, 648 (1976).
(28) J. O. Hirschfelder, C. F. Curtis, and R. B. Bird, "Molecular Theory of Gases and Liquids", Wiley, New York, N.Y., 1954.
(29) F. Perrin, *J. Phys. Radium*, **7**, 1 (1936).
(30) R. O. Herzog, R. Illig, and H. Kudar, *Z. Phys. Chem.*, **A167**, 329 (1933).
(31) J. L. Crammer and A. Neuberger, *Biochem. J.*, **37**, 302 (1943).
(32) J. M. Creeth, L. W. Nichol, and D. J. Winzor, *J. Phys. Chem.*, **62**, 1546 (1958).
(33) J. A. Gordon and M. Ottesen, *Biochim. Biophys. Acta*, **75**, 453 (1963).
(34) J. M. Creeth and D. J Winzor, *Biochem. J.*, **83**, 566 (1962).
(35) M. O. Dayhoff, G. E. Perlmann, and D. A. MacInnes, *J. Am. Chem. Soc.*, **74**, 2515 (1952).
(36) P. E. Hexner, L. E. Radford, and J. W. Beams, *Proc. Natl. Acad. Sci. USA*, **47**, 1848 (1961).
(37) G. J. Howlett and L. W. Nichol, *J. Phys. Chem.*, **76**, 2740 (1972).
(38) E. G. Richards, D. C. Teller, and H. K. Schachman, *Biochemistry*, **7**, 1054 (1968).
(39) M. Halwer, G. C. Nutting, and B. A. Brice, *J. Am. Chem Soc.*, **73**, 2786 (1951).
(40) H. L. Fevold, *Adv. Protein Chem.*, **6**, 187 (1951).
(41) R. K. Cannan, A. Kibrick, and A. H. Palmer, *Ann. N.Y. Acad. Sci.*, **41**, 243 (1941).
(42) L. G. Longsworth, *Ann. N.Y. Acad. Sci.*, **41**, 267 (1941).
(43) C. W. Carr, *Arch. Biochem. Biophys.*, **46**, 417 (1953)
(44) C. W. Carr, *Arch. Biochem. Biophys.*, **62**, 476 (1956)
(45) P. A. Charlwood, *Biochem. J.*, **46**, 312 (1950).
(46) F. Kohlrausch, *Ann. Phys. (Leipzig)*, **62**, 209 (1897).
(47) R. A. Alberty, *J. Chem. Ed.*, **25**, 426 (1948).
(48) G. Scatchard, A. C. Batchelder, and A. Brown, *J. Am. Chem. Soc.*, **68**, 2320 (1946).
(49) C. G. Paradine and B. H. P. Rivett, "Statistical Methods for Technologists", English Universities Press, London, 1960.

Transmission Methods in Dielectric Time Domain Spectroscopy

B. Gestblom and E. Noreland*

Institute of Physics, University of Uppsala, Box 530, S-751 21 Uppsala, Sweden *(Received October 12, 1976)*

Publication costs assisted by the Institute of Physics, University of Uppsala

It is shown how transmission methods can be used in dielectric time domain spectroscopy (TDS) for the evaluation of permittivities over a large frequency range. Graphs, which show the transmission coefficients under different conditions, are given, and compared with those for the corresponding reflection methods hitherto used in TDS. The transmission methods are applied to the study of 1-butanol and chlorobenzene and comparison is made with results from reflection measurements. The permittivities were studied up to 10 GHz. The results show that transmission methods offer an attractive alternative to the reflection methods over the total frequency range within reach in TDS. Direct time domain evaluation of dielectric parameters from thin sample transmission data is illustrated for 1-butanol.

Introduction

In dielectric time domain spectroscopy (TDS) the dielectric properties of a sample are determined by its response to an electric pulse with very short rising time.[1] The pulse is generated by a tunnel diode and the incident pulse and its response, which are transmitted in a coaxial line, are monitored with a sampling oscilloscope. The method most frequently used is to study the first reflection $r(t)$ of the incident pulse $v(t)$.[2] The sample should here be sufficiently long to allow the reflected pulse to reach a steady state before multiple reflections reach the sampling system. This method may be called the single reflection method. Fourier transformation

$$F(\omega) = \int_{-\infty}^{\infty} f(t)e^{-j\omega t}\,dt \tag{1}$$

of the two pulses give the reflection coefficient in the frequency domain

$$\rho = \frac{R(\omega)}{V(\omega)} = \frac{1 - \epsilon^{*1/2}}{1 + \epsilon^{*1/2}} \tag{2}$$

from which the complex permittivity $\epsilon^* = \epsilon' - j\epsilon''$ may be calculated.

An alternative approach is to study the totally reflected pulse, including all multiply reflected contributions from a sample of short length.[3] The permittivity can in this case be determined from the solution of the transcendental equation for the reflection coefficient

$$S_{11}(\omega) = \frac{R(\omega)}{V(\omega)} = \rho\frac{1 - \exp\left[\frac{-j2\omega l}{c}\epsilon^{*1/2}\right]}{1 - \rho^2\exp\left[\frac{-j2\omega l}{c}\epsilon^{*1/2}\right]} \tag{3}$$

Here c is the speed of light and l is the length of the sample.

This equation has also been used as a basis for thin sample approximations, $|\omega l\epsilon^{*1/2}/c| << 1$, in which case expansions of the exponentials can be made which give simpler equations for the permittivity ϵ^* as a function of the reflection coefficient.[4] Equation 3 is valid for the case that the sample is placed in the coaxial line, with a matched 50-Ω termination. Alternative total reflection coefficients are obtained for the cases when the sample is terminating an open ended coaxial line[5] or placed against a short circuit.[6]

A severe problem in evaluation of the Fourier transforms for the reflection methods is to determine a common time reference point for the incident pulse and reflected pulse. A timing error Δt will cause a phase error in the Fourier transform of $\omega\Delta t$. Since the phase shift, e.g., in the single reflection coefficient ρ, only varies with a few degrees with varying permittivity, it is realized that for frequencies ≥1 GHz the timing error cannot be allowed to exceed a few picoseconds.

An alternative to the reflection methods is obtained by studying the pulses transmitted through a sample. The direct approach here is to study the first transmitted pulse through a long sample, the single transmission method, or the totally transmitted pulse through a short sample, the total transmission method. The transmission coefficient ratio method[7] uses the ratio of the transforms of the singly transmitted pulses through two samples of different length.

The transmission methods create larger phase shift in the transmission coefficients than what is achieved for the reflection coefficients in the reflection methods. Errors in the phase of the experimental transmission coefficients due to inaccuracies in the time reference procedure should therefore be less severe than for the corresponding reflection methods, implying that the TDS transmission methods should offer an attractive alternative to the TDS reflection methods in determination of permittivities. It is the purpose of this paper to show how the single and total transmission measurements can be made and to compare results and accuracies with the corresponding reflection methods.

Single Transmission

In the frequency domain the single transmission coefficient for a signal of frequency ω through a dielectric sample of length l is given by[1]

$$T(\omega) = \frac{4\epsilon^{*1/2}}{(1 + \epsilon^{*1/2})^2}\exp\left[\frac{-j\omega l}{c}\epsilon^{*1/2}\right] \tag{4}$$

In TDS the pulse transmitted through the sample of length l, $r(t)$, is compared to the incident pulse transmitted through the same length of air-filled coaxial line, $v(t)$. The pulses should be time referenced to a common origin. This means that the single transmission coefficient to be used for TDS is given by

$$T_s(\omega) = \frac{R(\omega)}{V(\omega)} = \frac{4\epsilon^{*1/2}}{(1 + \epsilon^{*1/2})^2} \times \exp\left[\frac{-j\omega l}{c}(\epsilon^{*1/2} - 1)\right] \tag{5}$$

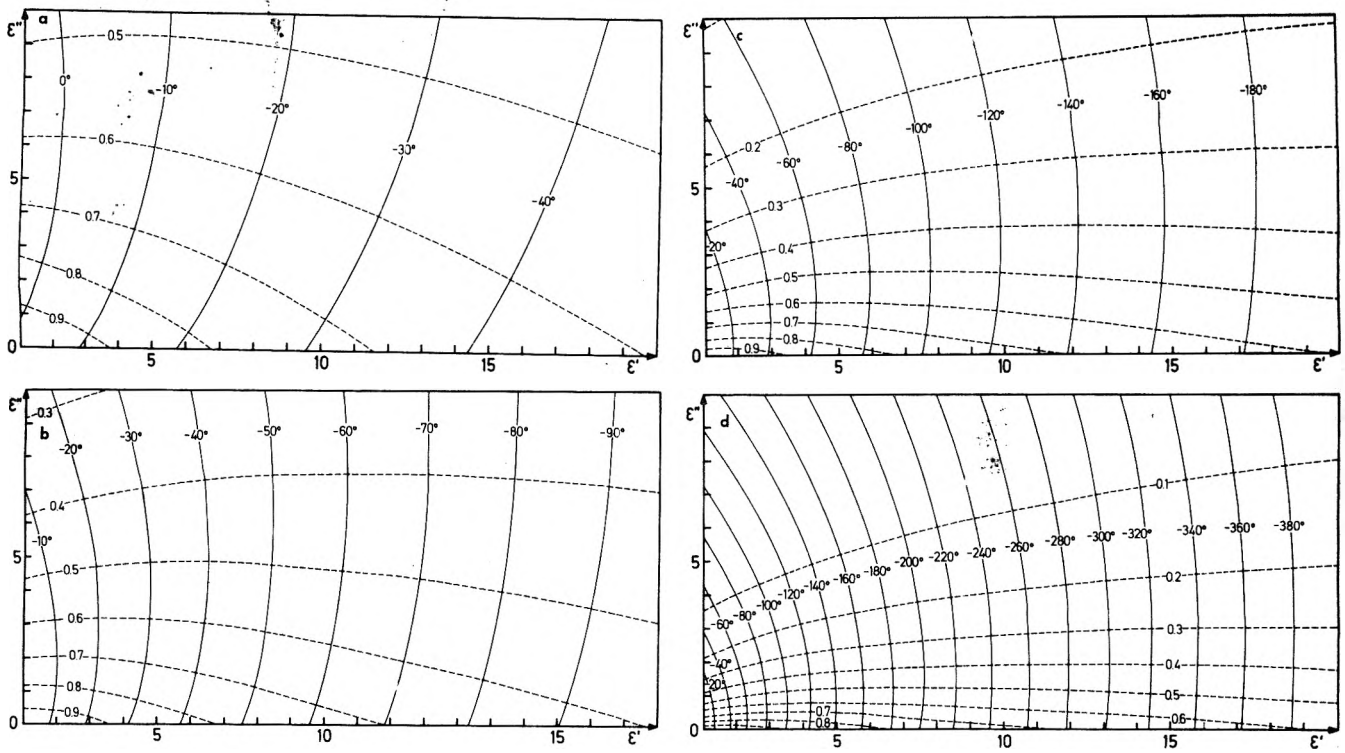

Figure 1. Equitransmission lines from the single transmission coefficient T_s for different values of $\omega l/c$. Lines representing constant amplitude are broken while the full lines show constant phase of T_s; (a) $\omega l/c = 0.25$; (b) $\omega l/c = 0.50$; (c) $\omega l/c = 1.00$; (d) $\omega l/c = 2.00$.

It is immediately seen that the exponential term will create a large phase shift in the transmission coefficient. This is due to the extra travel time for the pulse to be transmitted through the sample. Even a nondispersive medium would introduce a phase shift of $-(\omega l/c)(\epsilon_\infty^{1/2} - 1)$ in the transmission coefficient, but this phase shift is further increased for the ϵ^* complex. The exponential term also implies a strong absorption of power at higher frequencies for long sample lengths leading to small transmission coefficients. This means that the single transmission method is limited to lower frequencies for which $T_s(\omega) \gtrsim 5\%$.

The rise time of the first transmitted pulse depends on the relaxation time of the sample. The sample must relax and the first transmitted pulse reach a steady state before multiply transmitted pulses arrive at the sampler. This requires that $\epsilon_s^{1/2} < 3\epsilon_\infty^{1/2}$, since the first multiply transmitted high frequency components, which propagate fastest through the sample, should not overtake the low frequency components propagating with speed $c/\epsilon_s^{1/2}$.

To visualize the meaning of eq 5 equitransmission lines have been calculated for different values of $\omega l/c$. These are shown in Figure 1, where the lines are drawn in the ϵ', ϵ'' plane, for which the amplitude and phase of the transmission coefficient T_s have constant values. Equiphase and equiamplitude lines are orthogonal. This is a consequence of the fact that eq 5 defines a conformal mapping of a set of circles and radii, defining the equiamplitude and equiphase lines in the complex ϵ', ϵ'' plane. From the diagrams in Figure 1 rough values for ϵ^* can be deduced from a given transmission coefficient. Of importance also is that resulting inaccuracies in ϵ^* due to an error in the phase or amplitude of the transmission coefficient can be estimated. The single transmission diagrams clearly illustrate that large phase shifts are created in the transmission coefficient T_s. This implies that timing errors will not have a serious effect on the calculated permittivities. Consider for instance the case of transmission through a 30-cm long sample, for which

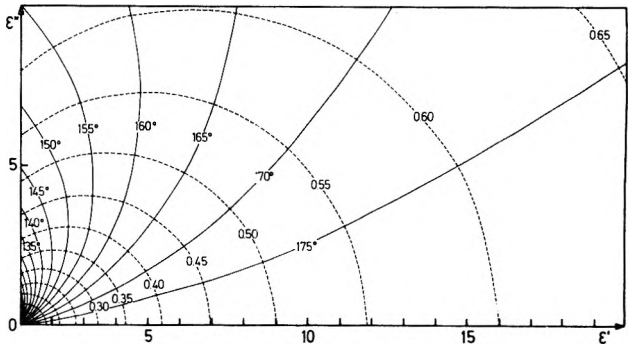

Figure 2. Equireflection lines from the single reflection coefficient ρ. Lines representing constant amplitude are broken while the full lines show constant phase of ρ.

$\epsilon^* = 10 - 7.5j$ at a frequency 320 MHz. An error as large as 20 ps in the time referencing will lead to a phase error of 2.3° in the transmission coefficient. As seen from the relevant diagram, where $\omega l/c = 2.0$, this large timing error will give $\Delta\epsilon' < 0.1$ and $\Delta\epsilon'' << 0.1$.

For comparison with the single reflection method, similar equireflection lines have been calculated from eq 2 and are given in Figure 2. For a nondispersive medium, for which $\epsilon'' = 0$, the reflection coefficient ρ should be negative, giving a phase angle of 180°. For a dispersive medium, which can be described by a Cole–Cole plot in the diagram, it is seen that the additional phase change can hardly exceed 20°. The diagram clearly shows how a phase error in the reflection coefficient, due to a timing error, will influence the calculated permittivity. Consider for instance again the case that the permittivity $\epsilon^* = 10 - 7.5j$ at 320 MHz. A timing uncertainty of 5 ps will give a phase uncertainty of ~0.6° giving $\Delta\epsilon' \simeq \Delta\epsilon'' \simeq 0.3$. The timing error will have much more serious consequences at higher frequencies since the phase error grows linearly with frequency. At 3 GHz for instance the same timing uncertainty will give a phase error of ~5° leading to large errors in calculated permittivities.

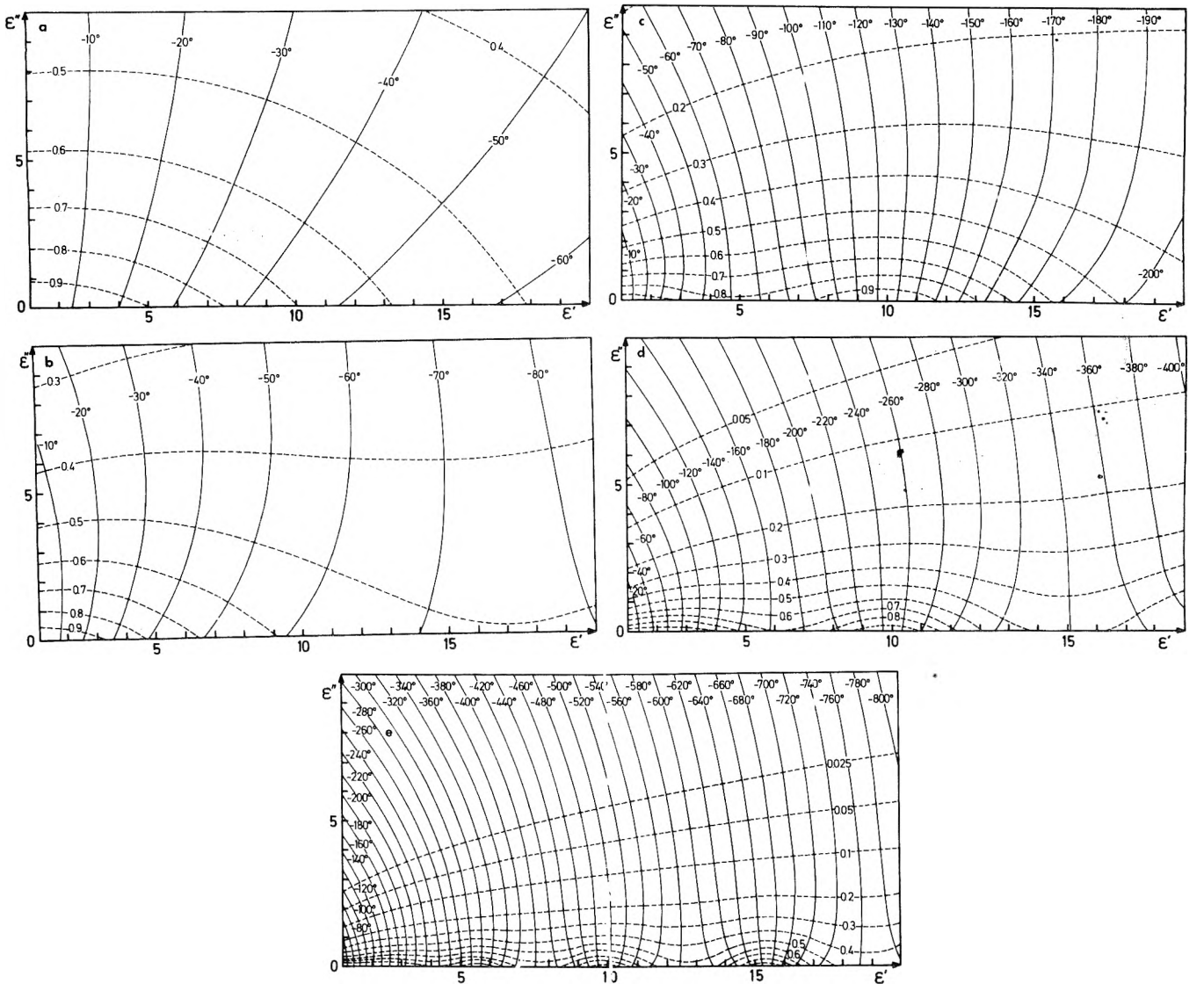

Figure 3. Equitransmission lines from the total transmission coefficient T_t for different values of $\omega l/c$. Lines representing constant amplitude are broken while the full lines show constant phase of T_t: (a) $\omega l/c = 0.25$; (b) $\omega l/c = 0.50$; (c) $\omega l/c = 1.00$; (d) $\omega l/c = 2.00$; (e) $\omega l/c = 4.00$.

The comparison between the single transmission and single reflection method would lead to the conclusion that the relaxed requirement on the time referencing accuracy, makes the transmission method an attractive alternative to reflection measurements. The disadvantage is that the strong absorption of power at higher frequencies makes the method frequency limited.

Total Transmission

In order to use transmission methods at higher frequencies the sample length has to be shortened in order to allow sufficient power to be transmitted through the sample. This means that one has to study the totally, multiply transmitted pulse. On the other hand the sample length should be long enough to create sufficiently large phase shifts in the transmission coefficient for the time referencing inaccuracy not to become an unmanageable problem. The total transmission coefficient at frequency ω through a sample of length l is given by[1]

$$S_{21} = \frac{(1-\rho^2)\exp\left[\frac{-j\omega l}{c}\epsilon^{*1/2}\right]}{1-\rho^2\exp\left[\frac{-j2\omega l}{c}\epsilon^{*1/2}\right]} \qquad (6)$$

In TDS this transmitted pulse $r(t)$ should be compared to the incident pulse $v(t)$ transmitted through the same cable length of air and we obtain the total transmission coefficient

$$T_t(\omega) = \frac{R(\omega)}{V(\omega)} = \frac{(1-\rho^2)\exp\left[\frac{-j\omega l}{c}(\epsilon^{*1/2}-1)\right]}{1-\rho^2\exp\left[\frac{-j2\omega l}{c}\epsilon^{*1/2}\right]} \qquad (7)$$

The implications of this equation are best visualized by diagrams of equitransmission lines for different values of $\omega l/c$. These are shcwn in Figure 3. It can be seen that large phase shifts are introduced and that substantial fractions of the power are transmitted through the sample also at high frequencies. To see the influence of a time referencing error, consider the case of a dielectric with $\epsilon^* = 3 - 1.5j$ at 3 GHz with sample length of 3.2 cm. The diagram, for which $\omega l/c = 2.0$, is relevant. A timing error of 10 ps will introduce a phase error of $\sim 10°$ giving an uncertainty in the permittivity of $\Delta\epsilon' \leq 0.3$ while ϵ'' is hardly affected. To achieve the same accuracy with the single reflection method the phase error has to be smaller than $\sim 2.5°$ requiring a time referencing uncertainty $\Delta t \leq 2.5$ ps!

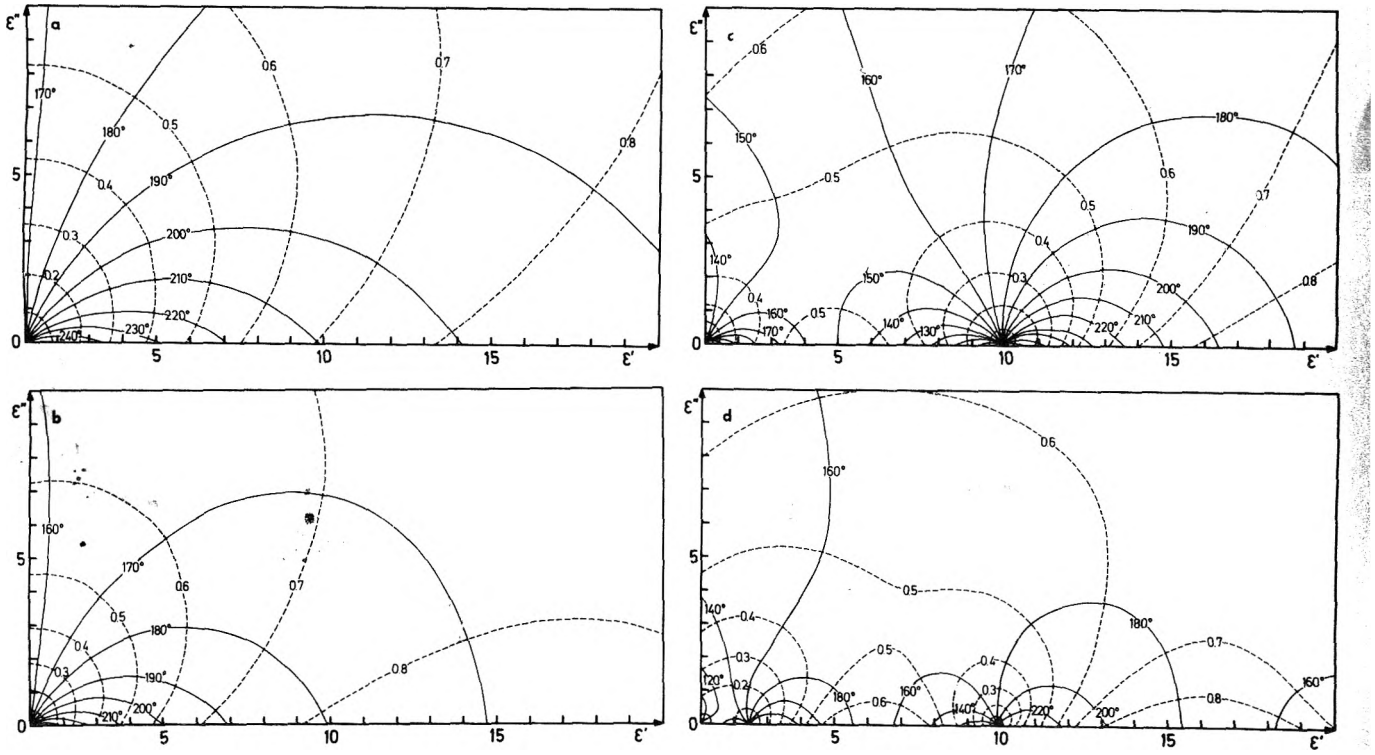

Figure 4. Equireflection lines from the total reflection coefficient S_{11}. Lines representing constant amplitude are broken while the full lines show constant phase of S_{11}: (a) $\omega l/c = 0.25$; (b) $\omega l/c = 0.50$; (c) $\omega l/c = 1.00$; (d) $\omega l/c = 2.00$.

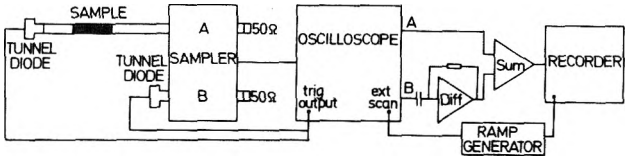

Figure 5. Experimental setup for transmission measurements using a dual-channel sampling oscilloscope.

The diagrams in Figure 3 show that for the higher values of $\omega l/c$, and a given value for the total transmission coefficient, multiple solutions of eq 7 exist. The algorithm used to find the solution of this equation has to be written in such a manner that all solutions are identified. Some of them can then be rejected on physical reasons, e.g., ϵ^* should vary continuosly with changing ω.

To compare the total transmission method with the total reflection method, equireflection lines have been calculated from eq 3 for different values of $\omega l/c$. These are shown in Figure 4. The curves at higher frequency show a very irregular pattern and the reflection coefficient is very sensitive to phase errors in large regions of the ϵ', ϵ'' plane. It can also be seen that small errors in the amplitude of the reflection coefficient will cause large errors in the calculated permittivity. The total reflection method thus compares unfavorably with the total transmission method and gives an accuracy in the result which strongly depends on the region of the ϵ', ϵ'' plane used.

Experimental Section

The experimental setup used for transmission measurements is shown in Figure 5.

A dual-channel sampling oscilloscope, HP 1811 A, was used. Two step pulse generators are triggered from the same triggering pulse taken from the oscilloscope. The step pulse in channel B gives the time reference point necessary in the Fourier transform procedures. This reference pulse can be displaced from the pulse to be studied in channel A by introducing a delay cable in the triggering circuit of suitable length and by varying the relative triggering levels of the two channels.

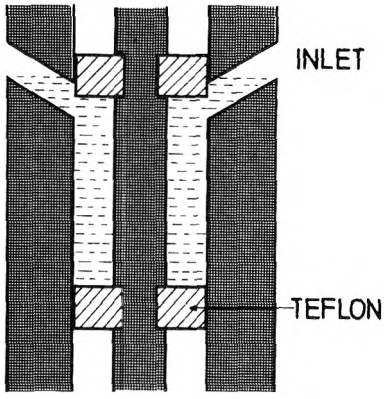

Figure 6. The 2.7-cm sample cell for total transmission and reflection measurements.

The oscilloscope is modified to allow the external sweep of the time base, in this case from a ramp voltage generator. The output from channel B is derivated in a differentiating circuit, which will cause the reference pulse to appear as a narrow spike. This spike is added to the pulse to be studied from channel A in a summing amplifier and displayed on an X–Y recorder. This setup has the advantage that the two channels are locked to each other through the common triggering pulse and long term drifts or shifts in the time base of the oscilloscope will not influence the time referencing point. The two channel system can be used also if an automatic data acquisition system is available, except that the differentiator can be deleted and the step pulse in B used directly as a time reference.

The measuring cell for total transmission measurements is shown in Figure 6. The teflon beads are dimensioned to give impedance match and a minimum of spurious reflections in the measuring cell. Holes of diameter 1 mm are drilled in the coaxial line to allow the injection of the studied liquid through a syringe, without disassembling the coaxial line. For the single transmission and reflection

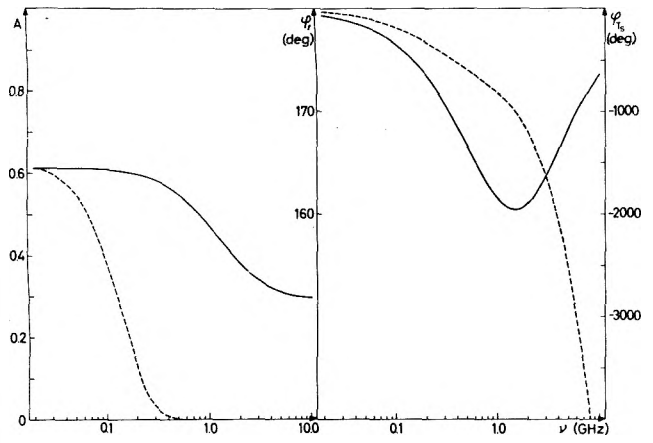

Figure 7. Amplitude A and phase φ of single reflection ρ (full lines) and single transmission T_s coefficients (broken lines) for a Debye model dielectric with $\epsilon_s = 17.3$, $\epsilon_\infty = 3.3$, and $\tau = 460$ ps. Sample length $l = 50$ cm.

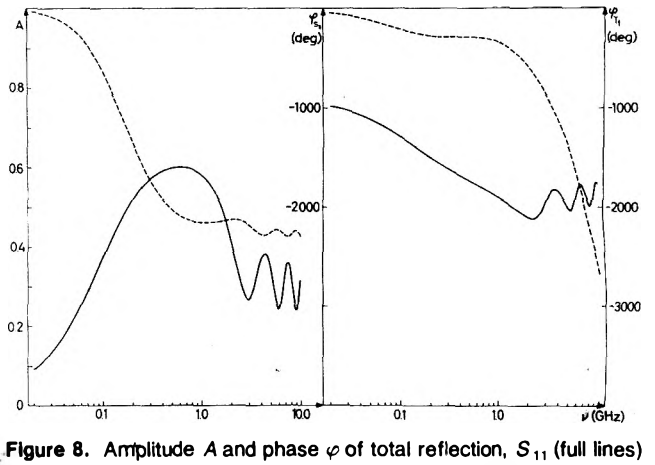

Figure 8. Amplitude A and phase φ of total reflection, S_{11} (full lines) and total transmission T_l (broken lines) coefficients for a Debye model dielectric with $\epsilon_s = 17.3$, $\epsilon_\infty = 3.3$, and $\tau = 460$ ps. Sample length $l = 2.7$ cm.

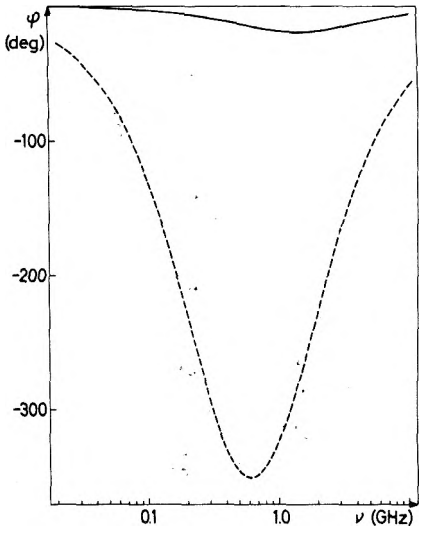

Figure 9. Phase of single reflection coefficient ρ in Figure 7 corrected by 180° (full line) and phase of single transmission coefficient T_s in Figure 7 corrected by $(\omega l/c)(3.3^{1/2} - 1)$ (broken line).

measurements a 50-cm long coaxial cable was manufactured to allow the study of liquids with longer relaxation times.

In the measurements the pulse transmitted through the empty cell is first recorded. The studied liquid is then injected and the transmitted pulse recorded under otherwise unchanged conditions. Since no digital data acquisition system was available, the recorded curves were digitized manually. No averaging over several scans could consequently be performed. The relative stability of the two pulses indicates that the accuracy of the time referencing procedure used in the transmission measurements is better than 10 ps.

The Fourier transformations were done by the Samulon formula, which has been shown to be accurate up to frequencies of the order of 10 GHz for sampling densities of 20 ps.[8] To solve the transcendental eq 3, 5, or 7 a program was written which by a step by step procedure locates an interval on the ϵ' axis, inside which the real part of the complex equation has a solution. The computer then traces the line in the complex ϵ', ϵ'' plane, where the real part of the equation is satisfied. At some point this line will intersect another line in the complex plane for which the imaginary part of the equation is satisfied. This intersection point defines the solution.[9]

Results

As a test case we have applied the various TDS methods discussed above to 1-butanol. An estimate of the transmission and reflection coefficients to be expected can be obtained by assuming that butanol behaves like a Debye dielectric with

$$\epsilon' = \epsilon_\infty + \frac{\epsilon_s - \epsilon_\infty}{1 + \omega^2\tau^2}$$
$$\epsilon'' = \frac{(\epsilon_s - \epsilon_\infty)\omega\tau}{1 + \omega^2\tau^2} \qquad (8)$$

and feed these expressions into eq 2, 3, 5, or 7. Assuming $\tau = 460$ ps, $\epsilon_s = 17.3$, $\epsilon_\infty = 3.3$, the sample lengths $l = 50$ cm for single transmission and $l = 2.7$ cm for total transmission and reflection the appropriate coefficients have been calculated and are presented in Figures 7 and 8.

In the case of single reflection even an undispersive medium causes a phase shift of 180° in the reflection coefficient. To bring out the part of the phase which is due to the fact that the liquid is polar, this constant phase shift of 180° should be subtracted as shown in Figure 9. It is readily seen that the dispersion introduces a phase shift of less than 20°. In the case of single transmission even a nondispersive medium will introduce a phase shift of $-(\omega l/c)(\epsilon_\infty^{1/2} - 1)$ in the transmission coefficient, due to the time delay the pulse suffers in passing through the medium. To bring out the phase shift due to the dispersion of the medium this factor should then be subtracted from the total phase shift. The result is included in Figure 9. This diagram clearly shows the relaxed demands on the time referencing procedure and phase determination in the single transmission method compared to the single reflection method. Figure 7 on the other hand shows the limited frequency region of the single transmission method. At frequencies of the order of a few hundred megahertz the amplitude of the transmission coefficient drops to a few percent and accurate determinations of the permittivities for higher frequencies cannot be expected.

In the limit $\omega \to 0$ the single transmission coefficient is given by $T_s = 4\epsilon_s^{1/2}/(1 + \epsilon_s^{1/2})^2$ which can readily be solved for ϵ_s. The static permittivity can also be obtained directly in the time domain from the first transmitted pulse. For low frequencies the incident pulse can be regarded as an ideal step pulse of height v_0, in which case we obtain

$$\lim_{t\to\infty} r(t)/v_0 = \lim_{\omega\to 0} T_s(\omega) = \frac{4\epsilon_s^{1/2}}{(1 + \epsilon_s^{1/2})^2}$$

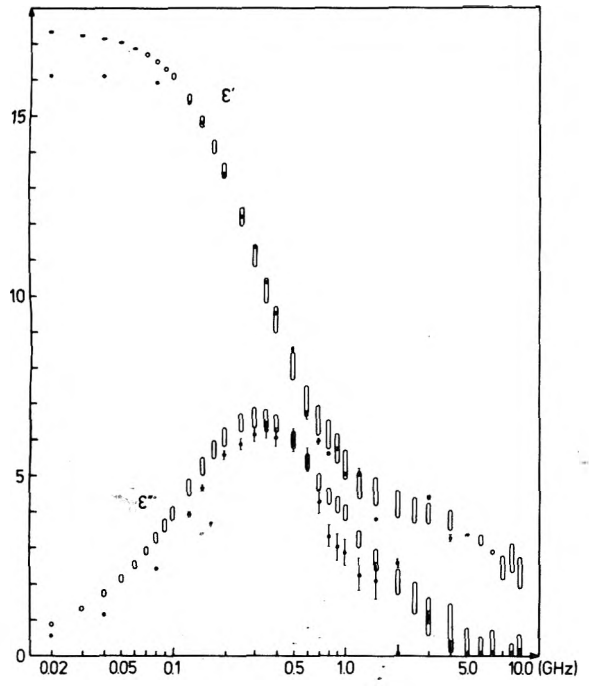

Figure 10. Permittivity of 1-butanol from the single and total reflection measurements. Total reflection results are illustrated by dots with a vertical bar showing the displacement of permittivities obtained by varying the time origin ±5 ps. Single reflection results are illustrated by "ellipses" giving the span of the permittivity on varying the time origin ±5 ps.

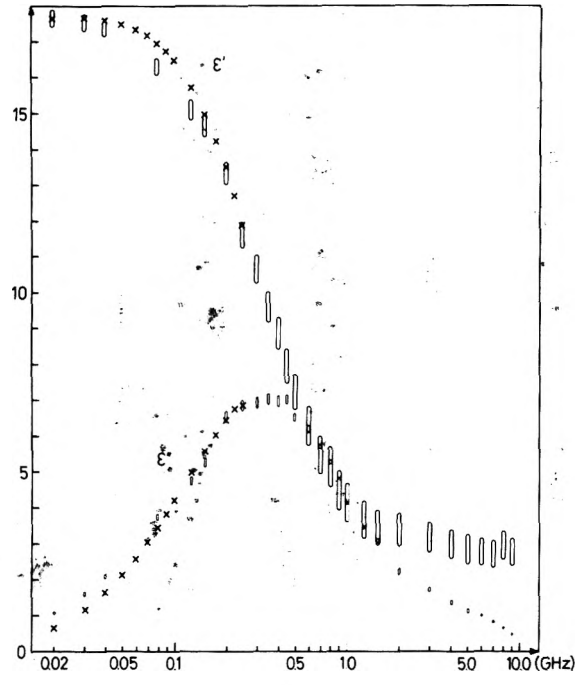

Figure 11. Permittivity of 1-butanol from the single and total transmission measurements. Single transmission results are illustrated by crosses. Displacements of the permittivities obtained by varying the time origin ±10 ps are in this case too small to be illustrated. Total transmission results are illustrated by "ellipses" giving the span of the permittivity on varying the time origin ±10 ps.

Figure 8 shows how the total reflection coefficient undergoes rather strong oscillations both in amplitude and phase at higher frequencies. The low reflection coefficient appears at frequencies for which standing waves are set up in the sample. These oscillations can be noticed also in the transmission coefficient but are much smaller here.

The resulting permittivities from measurements with the two reflection and two transmission methods are shown

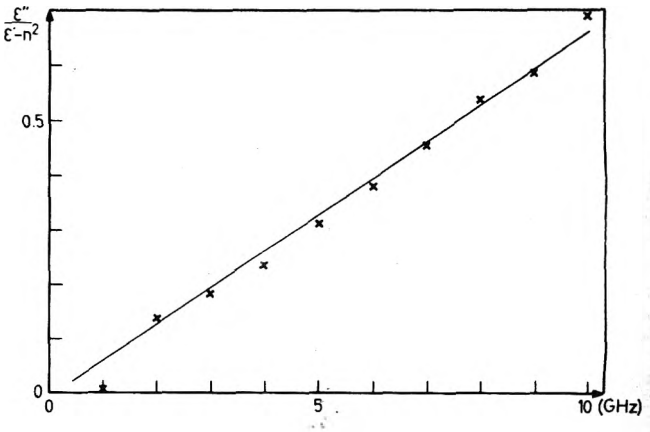

Figure 12. The ratio $\epsilon''/(\epsilon' - 2.3)$ as a function of frequency for chlorobenzene using permittivity values from the total transmission measurement.

in Figures 10 and 11. Displacements of permittivity values for a change in time reference are illustrated. The time referencing uncertainty has been estimated to ±5 ps for the reflection methods and ±10 ps for the transmission methods. The time referencing for the transmission methods was as described above while the intercept of the extrapolated base line and initial rise of the pulse was used in the reflection methods.[1]

Figure 10 gives the result of the single and total reflection measurements. The permittivity data from the total reflection measurement shows a large scattering at frequencies >1 GHz, and no change in the time referencing point gives an improvement.

The single reflection results are systematically displaced, even giving negative ϵ'' values at high frequencies. This is due to an error in the time reference point, since a shift of 5 ps will give permittivity values in better agreement with a Debye model for butanol. This illustrates that the time reference procedure in the reflection measurements cannot be considered satisfactory if reliable results at higher frequencies are wanted. One is then referred to time referencing through an indirect route, using data from other measurements.[7]

The results from the transmission measurements are given in Figure 11. The total and single transmission data differ at lower frequencies. The single transmission data should be more accurate here. The total transmission method gives good results at higher frequencies and it is seen that the ϵ'' values are rather unsensitive to time referencing error. To cover as large a frequency range as possible the single transmission and total transmission methods should therefore be combined.

A fit of the combined transmission data in Figure 11 to a Debye model gives a relaxation time of 0.47 ns. The time referencing error in the single reflection measurement leads to a much poorer fit to the Debye model and no value of τ is quoted.

To test the total transmission method on a liquid with shorter relaxation time, and lower permittivity, chlorobenzene has also been studied. The relaxation time is here of the order of 10 ps which means that within the range of 10 GHz only part of the dispersion curve can be determined, not even reaching the maximum of the absorption. A 27-mm cell was used. The result is shown in Figure 12. Here a plot is given of $\epsilon''/(\epsilon' - \epsilon_\infty)$ as a function of ω for frequencies from 1 to 10 GHz. For a Debye dielectric, obeying eq 8, this plot should give a straight line, with a slope equal to the relaxation time τ. In the plot in Figure 12, $\epsilon_\infty = n^2 = 2.3$ was used, and the slope of the line gives a relaxation time $\tau = 11$ ps in good agreement with

literature values.[10]

Thin Sample Transmission

Fellner-Feldegg[4] has shown how thin samples can be used in reflection measurements to achieve the relaxation time directly from the time dependence of the reflected pulse. The time domain analysis of reflection from thin samples has been extended by Cole,[11] who showed how the dielectric response function may be calculated from the time integral and self-convolution of the reflections produced.

If the total transmission coefficient as expressed in eq 7 is expanded, under the thin sample condition $|(\omega l/c)\epsilon^{*1/2}| << 1$, we obtain the transmission coefficient

$$T_{\text{thin}} = 1 + \frac{j\omega l}{2c} - \frac{j\omega l}{2c}\epsilon^* \tag{9}$$

If we study the difference $d(t)$ of the pulse transmitted through the thin sample $r(t)$ and the pulse transmitted through the same empty cell $v(t)$ and solve for the permittivity ϵ^* we obtain

$$\epsilon^* = \frac{D(\omega)2c}{V(\omega)j\omega l} + 1 \tag{10}$$

The decay function of the dielectric $\phi(t)$, which gives the normalized decay of the polarization when a steady macroscopic electric field is removed from the medium, is related to the complex permittivity by[12]

$$\frac{\epsilon^* - \epsilon_\infty}{\epsilon_s - \epsilon_\infty} = -\int_{-\infty}^{\infty} \frac{d\phi}{dt} \exp(-j\omega t)\, dt \tag{11}$$

where

$$d\phi/dt = 0 \text{ for } t \leq 0$$

Inverting this transform, the decay function can be calculated from the permittivity by

$$\frac{d\phi(t)}{dt} = -\frac{1}{2\pi}\int_{-\infty}^{\infty} \frac{\epsilon^* - \epsilon_\infty}{\epsilon_s - \epsilon_\infty} \exp(j\omega t)\, d\omega \tag{12}$$

Insertion of eq 9 gives, if δ functions are deleted

$$\frac{d\phi(t)}{dt} \propto \int_{-\infty}^{\infty} \frac{D(\omega)}{V(\omega)\, j\omega} \exp(j\omega t)\, d\omega \tag{13}$$

If the incident pulse $v(t)$ is assumed to be a perfect step pulse its transform $V(\omega)$ is proportional to $1/j\omega$. This implies that

$$d\phi(t)/dt \propto d(t) \tag{14}$$

where $d(t)$ is the difference in the time domain between the two pulses. The above relation is only appropriate for times much larger than the rise time of the incident pulse, where the assumption of an ideal step pulse is valid.

In the case of a Debye dielectric $\phi(t) = \exp(-t/\tau)$ where τ is the macroscopic relaxation time. The slope of the logarithmic plot of $d(t)$ should in such a case give the relaxation time. The relaxation time of butanol was obtained from the study of the transmission of the pulse through a sample of thickness 1 mm, where the thin sample expansion should be an excellent approximation for all frequencies of interest. The difference between the incident and transmitted pulse $d(t)$ is plotted in Figure 13. The slope of this curve gives a relaxation time of 0.51 ns in good agreement with the time measured with other methods.

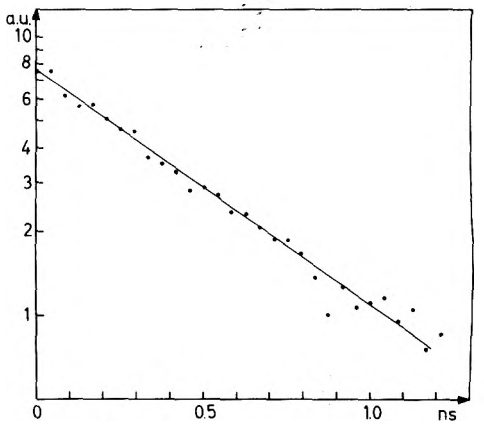

Figure 13. Difference between incident and transmitted pulse through a 1-mm sample of 1-butanol.

Conclusion

The theoretical and experimental results show that the single and total transmission methods offer an attractive alternative to the reflection methods. At low frequencies the single transmission should be the most accurate method. The dual channel time referencing procedure is sufficiently accurate to lead to more reliable permittivity data at higher frequencies using the total transmission method than what can normally be expected from the single reflection method. The total transmission method has also been shown to be applicable to dielectrics with lower permittivity and shorter relaxation time than what has hitherto been the subject of reflection TDS measurements. The total reflection method seems very unsatisfactory for certain frequency and permittivity regions, some small inaccuracies in the experimental data will cause large errors in calculated permittivities. It can be expected that the use of an automatic data acquisition system should improve the accuracy in the results that can be achieved with the described transmission methods. Such a system should also give a possibility to extend the frequency range.

Acknowledgment. Financial support from the Swedish Natural Science Research Council is gratefully acknowledged.

References and Notes

(1) For a review, see M. J. C. van Gemert, *Philips Res. Rep.*, **28**, 530 (1973).
(2) H. Fellner-Feldegg, *J. Phys. Chem.*, **73**, 616 (1969).
(3) A. H. Clark, P. A. Quickenden, and A. Suggett, *J. Chem. Soc., Faraday Trans. 2*, **70**, 1847 (1974).
(4) H. Fellner-Feldegg, *J. Phys. Chem.*, **76**, 2116 (1972).
(5) R. H. Cole, *J. Phys. Chem.*, **79**, 1469 (1975).
(6) G. P. de Loor, M. J. C. van Gemert, and H. Gravestyn, *Chem. Phys. Lett.*, **181**, 295 (1973).
(7) H. W. Loeb, G. M. Young, P. A. Quickenden, and A. Suggett, *Ber. Bunsenges. Phys. Chem.*, **75**, 1155 (1971).
(8) B. Gestblom and E. Noreland, *J. Phys. Chem.*, **80**, 1631 (1976).
(9) R. W. Hamming, "Numerical Methods for Scientists and Engineers", McGraw-Hill, New York, N.Y., 1962.
(10) N. E. Hill, W. E. Vaughan, A. H. Price, and M. Davies, "Dielectric Properties and Molecular Behavior", Van Nostrand, London, 1969.
(11) R. H. Cole, *J. Phys. Chem.*, **79**, 1459 (1975).
(12) G. Williams, *Chem. Rev.*, **72**, 55 (1972).

Quadrupole Relaxation of Chloride Ion, and of Perchlorate and Other Tetrahedral Ions in Aqueous Solution

Pétur Reimarsson,* Håkan Wennerström, Sven Engström, and Björn Lindman

Physical Chemistry 2, Chemical Center, P.O.B. 740, S-220 07 Lund, Sweden *(Received December 17, 1976)*

The ^{35}Cl and ^{37}Cl nuclear magnetic relaxation of the chloride and perchlorate ions has been investigated for simple aqueous electrolyte solutions. The infinite dilution relaxation rates obtained by extrapolation are compared with Hertz's electrostatic theory of ion quadrupole relaxation. Good agreement between experiment and theory is obtained for the chloride ion. For nuclei at symmetry sites in tetrahedral or octahedral ions a more elaborate analysis is required. Thus distortion of the ion from tetrahedral or octahedral symmetry may create sizable electric field gradients and, furthermore, the Sternheimer antishielding terms must take into account that not only an external electric field gradient, but also an external electric field can produce field gradients at the nucleus. Indeed, the latter effect is found to be considerable for the ammonium ion. Using calculated antishielding factors, the ^{14}N relaxation of the aqueous ammonium ion is found to agree closely with Hertz's theory. A discussion of the quadrupole relaxation of other symmetrical polyatomic ions is presented and it is found that for the case of the perchlorate ion, as well as for other ions, the electric field induced field gradient may have a marked influence on the relaxation.

Introduction

There has been a rapid growth in the physicochemical and biological applications of Cl^- nuclear magnetic relaxation[1] and, recently, considerable interest in studies of the ^{35}Cl (and ^{37}Cl) relaxation of the ClO_4^- ion has arisen.[1-6] The majority of these studies has been concerned with determination of ^{35}Cl line widths and only in a few cases[1,2,7-9] have direct determinations of the relaxation times been performed. These studies were concerned with protein solutions and then it is essential to determine both T_1 and T_2 as the extreme narrowing approximation generally is inappropriate. On the other hand, no direct determinations of T_1 and T_2 of Cl^- and ClO_4^- ions in simple electrolyte solutions have been reported. This is unfortunate both from a theoretical point of view and in the applications where detailed knowledge of a simple reference situation is lacking. The present investigation is concerned with providing precise relaxation data of the Cl^- and ClO_4^- ions for simple aqueous electrolyte solutions. Thus we consider the infinite dilution relaxation rates, the activation energies of relaxation, the solvent H/D and ion $^{35}Cl/^{37}Cl$ isotope effects, as well as the concentration dependence of the relaxation. The results are compared with Hertz's electrostatic theory of ion quadrupole relaxation[10-12] which has been very successful in accounting for experimental relaxation results for many monoatomic ions.[1,13,14] In particular, the relaxation behavior of the ClO_4^- ion is considered in some detail and possible origins of the fluctuating electric field gradients are considered. The results for ClO_4^- are also compared with relaxation data for the central nucleus in IO_4^-, NH_4^+, and $(CH_3)_4N^+$. Finally, a theoretical discussion of Sternheimer shielding in tetrahedral and octahedral systems is presented.

Experimental Section

The ^{35}Cl and ^{37}Cl relaxation times were measured at 8.82 and 7.34 MHz, respectively, on a Bruker BKr 322 s spectrometer with home-made probes.

The longitudinal relaxation times were measured using a 180–τ–90 pulse sequence and the transverse relaxation times by means of the Meiboom-Gill modification of the Carr-Purcell sequence. All signals were averaged with a Varian 1024 CAT time averaging computer to obtain a S/N ratio of at least 10:1.

Each reported relaxation time is the average of at least two independent measurements and the resulting errors are estimated to be about 10% or less.

The probe temperature was maintained by a stream of dry, thermostated nitrogen gas and is accurate to ±0.5 K.

All chemicals are of finest grade available and were used without further purification.

Chloride Ion Relaxation

Chloride ion relaxation data for aqueous NaCl solutions are illustrated in Figures 1 and 2. The concentration dependence of the relaxation can be seen to be weak. The infinite dilution ^{35}Cl values of $1/T_1$ and $1/T_2$ are found to be 25 s^{-1} at 25 °C which is considerably smaller than values given in the literature on the basis of line width studies (reviewed in ref 1). For the ratio $[1/T_1(^{35}Cl)]/[1/T_1(^{37}Cl)]$ we obtain 1.55 which agrees well with the expected ratio (1.61) for the case of predominant quadrupole relaxation. The ratio of the ^{35}Cl relaxation rates in D_2O and H_2O solutions is found to be 1.17 ± 0.08 which correlates well with previous findings for monoatomic ions and with the H/D isotope effect in water molecular motion (cf. discussion in ref 1). The Arrhenius activation energy of $^{35}Cl^-$ relaxation is obtained to be 11.4 kJ/mol in the range 276–361 K for a 1 M NaCl solution. In view of the weak concentration dependence this value may be expected to represent to a good approximation the activation energy of the relaxation due to ion–solvent interactions. The value obtained is somewhat smaller than the activation energy of a water molecule rotation in the hydration sphere of Cl^- which was deduced from water proton relaxation studies.[15]

Good support for the applicability of the electrostatic model developed by Hertz[10-12] in a wide range of situations has now been collected.[1] Following Hertz,[11] the infinite dilution relaxation rate may, for a spin-3/2 nucleus such as ^{35}Cl or ^{37}Cl, be written

$$\frac{1}{T_1} = \frac{8\pi^3}{5}\left(\frac{eQ}{h}\right)^2 (\mu(1 + \gamma_\infty)P)^2 \frac{C_s\tau_s}{r_0^5} \quad (1)$$

Here eQ is the nuclear electric quadrupole moment, μ the solvent electric dipole moment, $1 + \gamma_\infty$ the Sternheimer antishielding factor, P a polarization factor, C_s the solvent concentration, τ_s the solvent correlation time, and r_0 the

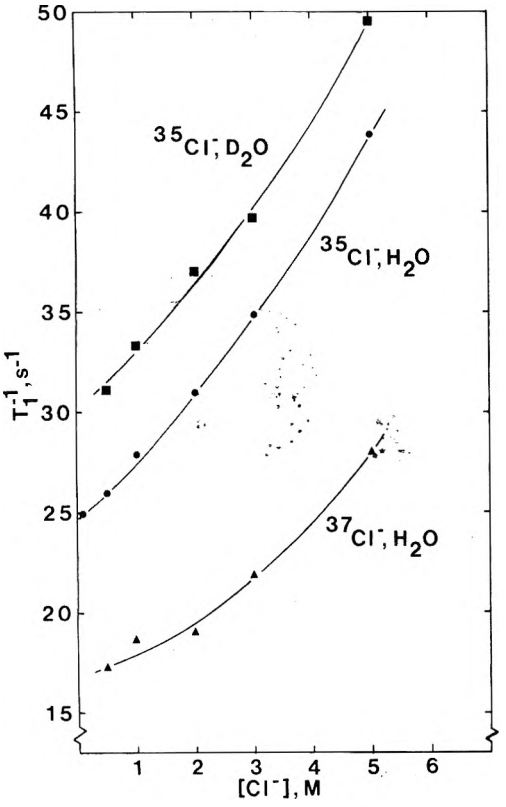

Figure 1. The Cl longitudinal relaxation rates (T_1^{-1}) for aqueous solutions of NaCl as a function of the NaCl concentration at a temperature of 301 K.

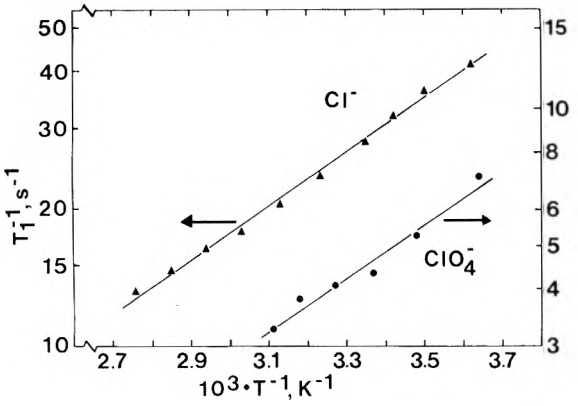

Figure 2. Temperature dependence of the ^{35}Cl longitudinal relaxation rate (T_1^{-1}) for 1.0 M NaCl (▲) and 1.2 M $NaClO_4$ (●) aqueous solutions. The right-hand scale pertains to $NaClO_4$ and the left-hand scale to NaCl. The solid lines represent results of the least-squares fits.

distance between the nucleus and a solvent dipole (taken as a point dipole) in the first solvation sheath. Reported Sternheimer factors for free Cl^- ions range from −49 to −83[16] so a detailed comparison with theory becomes difficult. Taking for aqueous solution τ_s to be 2.3×10^{-12} s and the other quantities as in Hertz's work,[11] we obtain $1/T_1$ to be in the range 27–79 s^{-1}. As noted previously by Hertz[11] the observed Cl^- quadrupole relaxation rate agrees well with the electrostatic theory.

Perchlorate Ion Relaxation

Cl relaxation data for the aqueous perchlorate ion are given in Figures 2 and 3. The ratio of the ^{35}Cl and ^{37}Cl relaxation rates is found to be 1.6 thus establishing the predominance of quadrupolar relaxation. Furthermore, the equality of T_1 and T_2 was verified for a number of aqueous alkali perchlorate solutions. The ratio of the relaxation rates of D_2O and H_2O solutions is found to be

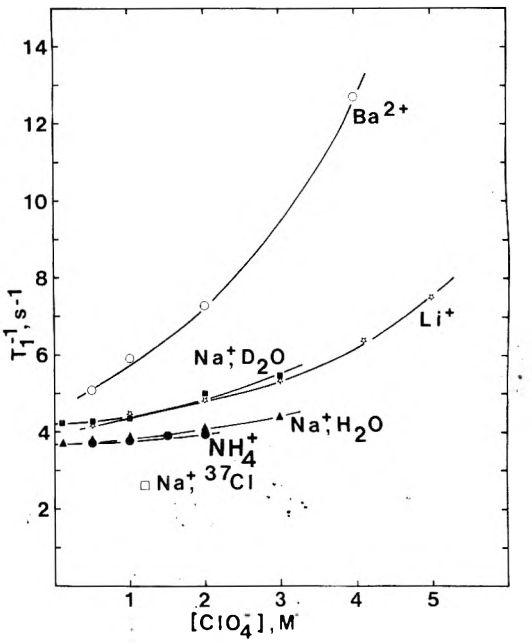

Figure 3. Variation of ^{35}Cl longitudinal relaxation rate (T_1^{-1}) of ClO_4^- with the perchlorate concentration for different cations: (○) $Ba(ClO_4)_2$, (☆) $LiClO_4$, (■) $NaClO_4$ in D_2O, (▲) $NaClO_4$ in H_2O, (●) NH_4ClO_4. □ gives the ^{37}Cl T_1^{-1} for 1.2 M $NaClO_4$ solution. The temperature was 301 K.

1.17 ± 0.08 for $NaClO_4$ in the concentration range 0–3 M and thus close to the isotope effect in water molecular motion and to the results for a number of monoatomic ions.[1] The relaxation rate can be seen to depend markedly on the cation (Figure 3). From the results for $NaClO_4$ solutions, where the concentration dependence of relaxation is weak, we obtain by extrapolation an infinite dilution relaxation rate of 3.6 s^{-1}. The variable temperature results give an Arrhenius activation energy of 11.3 kJ/mol for a 1.2 M $NaClO_4$ solution. In view of the weak concentration dependence of relaxation this corresponds probably to a good approximation to the energy of activation of the solvent-dependent relaxation.

The theoretical treatment of the Cl relaxation of ClO_4^- is more difficult than that of Cl^-; in addition to the time-dependent field gradients created by solvent dipoles and ionic charges one must also consider the possibility of field gradients arising from distortions from tetrahedral symmetry of the ClO_4^- ion. Such distortions which may arise from interactions with other ions and solvent molecules can potentially create very large electric field gradients which, through fluctuations in magnitude and/or orientation, produce relaxation. A further difficulty in attempting to account for the ClO_4^- relaxation lies in the problem of estimating the Sternheimer antishielding effects; this is further considered below.

By applying Hertz's electrostatic theory[10,11] in a straightforward way we obtain, for the limiting relaxation rate at infinite dilution in water, a value $1/T_1 = 0.00296(1 + \gamma_\infty)^2$ s^{-1} if r_0 is taken to be 4.25 Å and the correlation time to be that of pure water. As also other relaxation mechanisms (e.g., distortion effects) may be anticipated a rough upper limit estimate of the Sternheimer antishielding factor is given in this way, i.e., $|1 + \gamma_\infty| \lesssim 35$. If the water correlation time in the first hydration sphere of the perchlorate ion is taken to be 10^{-12} s[17] we deduce $|1 + \gamma_\infty| \lesssim 56$.

Relaxation in Other Tetrahedrally Symmetrical Ions

It is revealing to compare relaxation data for the per-

chlorate ion with data for other tetrahedrally symmetrical ions. In the chemically related periodate ion, IO_4^-, the transverse relaxation rate at low concentrations in water is found to be ca. 5×10^3 s^{-1} (unpublished continuous-wave studies by Gustavsson; see ref 1). On the basis of Hertz's electrostatic theory (eq 1) we estimate with $r_0 = 4.59$ Å and τ_c as for pure water the limiting relaxation rate $0.0489(1 + \gamma_\infty)^2$ s^{-1} which suggests $|1 + \gamma_\infty|$ has an upper limit of ca. 320. With $\tau_c = 10^{-12}$ s we obtain $|1 + \gamma_\infty| \lesssim 505$.

For the ammonium ion we obtain on the basis of the results of Kintzinger and Lehn[18] $|1 + \gamma_\infty| \lesssim 20$ using eq 1. This value is considerably larger than the value obtained by Baily and Story.[19] For ^{14}N relaxation of the $(CH_3)_4N^+$ ion we deduce analogously, from the results of ref 18, $|1 + \gamma_\infty| \lesssim 29$.

As a comparison of these deduced values with theoretically estimated Sternheimer factors may give an insight into the origin of the field gradients causing relaxation, a brief description of the theory of Sternheimer antishielding of polyatomic molecules and ions is appropriate.

Sternheimer Shielding in Tetrahedral and Octahedral Systems

At the center of systems with cubic symmetry the electrical field gradients are zero. If an electric perturbation is applied to such a system, field gradients at the center are created both directly and indirectly through polarization of the electrons and the positions of the nuclei. The electronic effect is called Sternheimer antishielding. In atomic systems, the Sternheimer antishielding is determined by a single parameter; in tetrahedral or octahedral systems, however, the field gradient at the center induced by an external field gradient is orientation dependent. Group theoretical arguments show that two parameters determine the Sternheimer shielding.

Tetrahedral systems lack inversion symmetry. This has the consequence that an external electric field can induce a field gradient to first order. This introduces additional complications in the interpretation of quadrupole relaxation data of for example the ClO_4^- ion. In this case the effective Sternheimer shielding factor will increase linearly with the distance to the external perturbation since the electric field decays slower with distance than the electric field gradient.

It is difficult to estimate the magnitude of the Sternheimer shielding in molecular systems. With one exception, calculations of γ_∞ have only been performed for atomic systems, and it is, for example, difficult to assess which of the systems Cl^{7+} or Cl^- is the most relevant for the description of the Sternheimer shielding in ClO_4^-. In a recent MO ab initio calculation[20] the Sternheimer shielding effects in NH_4^+ have been determined. In this study it was, for example, found that the induced field gradient at the nitrogen in the presence of a charge q at distance R on a z axis bisecting a HNH angle is

$$V_{zz} = 10.0R^{-3}q$$
$$V_{xx} = (4.0R^{-2} - 5.0R^{-3})q$$
$$V_{yy} = (-4.0R^{-2} - 5.0R^{-3})q$$

where all the quantities are in atomic units. The external field gradient is $V_{zz}^e = 2R^{-3}q$. At $R = 5.5$ (2.88 Å) the V_{yy} component is the largest one and the effective Sternheimer shielding factor $(1 + \gamma_\infty)_{eff} = -13$. This is in reasonable agreement with the value ±20 estimated from the observed relaxation rate. Assuming that the antishielding effects are similar in $(CH_3)_4N^+$ and NH_4^+ an R value of 8.0 au (4.2 Å) gives $(1 + \gamma_\infty)_{eff} = -18$. The ratios between the experimental and theoretical values of $(1 + \gamma_\infty)$ are thus the same for NH_4^+ and $(CH_3)_4N^+$. These considerations show that it is possible to rationalize the ^{14}N relaxation in ammonium ions using the electrostatic model, but distortion effects can of course not be excluded. Baily and Story[19] estimated $(1 + \gamma_\infty) = 5$ for the NH_4^+ ion by a comparison with experiments on a corresponding Rb^+ salt. In this study the field effect on NH_4^+ was neglected and this is probably not justified.

Conclusions

Studies of quadrupole effects of central nuclei in octahedral or tetrahedral ions are finding increasing applications in investigations of ion–ion and ion–solvent interactions in simple electrolyte solutions,[1,3-6] ion binding phenomena in amphiphilic systems such as model membrane systems,[21-24] and properties of functional binding sites in biological macromolecules such as proteins.[1,2] The present findings are of considerable significance as regards the interpretation of data in such systems. Thus it has been directly demonstrated for the aqueous NH_4^+ ion that Sternheimer antishielding effects in combination with the electrostatic model of quadrupole relaxation[10,11] predict a ^{14}N relaxation rate in good agreement with experimental findings. It is consequently not necessary to introduce distortion effects to explain the results. This finding is probably also important as regards the interpretation of relaxation data for other symmetrical ions but here no good estimates can presently be made. Clearly, our findings also indicate that ion quadrupole splittings in liquid crystals interpreted in terms of distortion effects may also be strongly influenced by Sternheimer antishielding effects.

The present treatment has dealt with the relaxation rate due to ion–solvent interactions. A detailed account of the ion–ion contributions to Cl relaxation in the ClO_4^- ion will be given at a later date.

Acknowledgment. Grants from the "T. H. Nordström testamentsfond" and from the Swedish Natural Sciences Research Council are gratefully acknowledged. We are indebted to Tom Bull for generous advice on relaxation experiments. Dennis Burton is gratefully thanked for linguistic criticism.

References and Notes

(1) B. Lindman and S. Forsén, "Chlorine, Bromine and Iodine NMR. Physico-Chemical and Biological Applications", Vol. 12 of "NMR, Basic Principles and Progress", P. Diehl, E. Fluck, and R. Kosfeld, Ed., Springer-Verlag, Heidelberg, 1976.
(2) P. Reimarsson, T. E. Bull, and B. Lindman, *FEBS Lett.*, **59**, 158 (1975).
(3) Y. M. Cahen, P. R. Handy, E. T. Roach, and A. I. Popov, *J. Phys. Chem.*, **79**, 80 (1975).
(4) H. A. Berman and T. R. Stengle, *J. Phys. Chem.*, **79**, 1001 (1975).
(5) K. L. Craighead and R. G. Bryant, *Mol. Phys.*, **29**, 1781 (1975).
(6) K. L. Craighead, P. Jones, and R. G. Bryant, *J. Phys. Chem.*, **79**, 1868 (1975).
(7) T. E. Bull, J. Andrasko, E. Chiancone, and S. Forsén, *J. Mol. Biol.*, **73**, 251 (1973).
(8) T. E. Bull, B. Lindman, R. Einarsson, and M. Zeppezauer, *Biochim. Biophys. Acta*, **377**, 1 (1975).
(9) T. E. Bull, B. Lindman, and P. Reimarsson, *Arch. Biochem. Biophys.*, **176**, 389 (1976).
(10) H. G. Hertz, *Z. Elektrochem.*, **65**, 20 (1961).
(11) H. G. Hertz, *Ber. Bunsenges. Phys. Chem.*, **77**, 531 (1973).
(12) H. G. Hertz, *Ber. Bunsenges. Phys. Chem.*, **77**, 688 (1973).
(13) H. G. Hertz, M. Holz, R. Klute, G. Stalidis, and H. Versmold, *Ber. Bunsenges. Phys. Chem.*, **78**, 24 (1974).
(14) H. G. Hertz, M. Holz, G. Keller, H. Versmold, and C. Yoon, *Ber. Bunsenges. Phys. Chem.*, **78**, 493 (1974).
(15) L. Endom, H. G. Hertz, B. Thül, and M. D. Zeidler, *Ber. Bunsenges. Phys. Chem.*, **71**, 1008 (1967).
(16) K. D. Sen and P. T. Narasimhan, *Adv. Nucl. Quadrupole Reson.*, **1**, 277 (1974).
(17) H. G. Hertz, *Water, Compr. Treat.*, **3**, 301 (1973).
(18) J.-P. Kintzinger and J. M. Lehn, *Helv. Chim. Acta*, **58**, 905 (1975).

(19) W. C. Baily and H. S. Story, *J. Chem. Phys.*, **60**, 1952 (1974).
(20) S. Engström, H. Wennerström, B. Jönsson, and G. Karlström, to be submitted for publication.
(21) H. Gustavsson, G. Lindblom, B. Lindman, N.-O. Persson, and H. Wennerström in "Liquid Crystals and Ordered Fluids", Vol. 2, J. F. Johnson and R. S. Porter, Ed., Plenum Press, New York, N.Y., 1974, p 161.
(22) N. O. Persson and B. Lindman, *Mol. Cryst. Liquid Cryst.*, in press.
(23) D. Bailey, A. D. Buckingham, F. Fujiwara, and L. W. Reeves, *J. Magn. Reson.*, **18**, 344 (1975).
(24) F. Fujiwara, L. W. Reeves, and A. S. Tracey, *J. Am. Chem. Soc.*, **96**, 5250 (1974).

Two Improved Methods for the Determination of Association Constants and Thermodynamic Parameters. The Interaction of Adenosine 5′-Monophosphate and Tryptophan

D. L. De Fontaine,† D. K. Ross, and B. Ternai*

La Trobe University, School of Physical Science, Bundoora, Victoria 3083, Australia *(Received November 8, 1976)*

A refinement of the Scatchard method for the determination of association constants in 1:1 complexes is presented which is not restricted by assumptions on the relative concentrations of the components. A temperature variation method is developed which is shown to yield accurate values of the association constant and thermodynamic parameters from one set of measurements using a smaller sample than is required by other methods.

For a 1:1 complex formed by two species A and B we have the equation

$$A + B \rightleftharpoons AB$$

and, in the equilibrium situation, we can define the association constant (K) which represents the proportion of complex formed. Thus

$$K = [AB]_e/[A]_e[B]_e \qquad (1)$$

where $[X]_e$ is the concentration of compound X at equilibrium. Now, let A_i and B_i be the initial concentration of A and B, respectively, and let p denote the fraction of A which is complexed. Then $A_i - pA_i$ is uncomplexed and eq 1 can be written in the form

$$K = \frac{pA_i}{(A_i - pA_i)(B_i - pA_i)} = \frac{p}{(1-p)(B_i - pA_i)} \qquad (2)$$

where B has an equal or larger concentration than A.

Now the fraction of A_i which is complexed at equilibrium can be identified with the ratio δ_i/δ_c where δ_i is the difference between a measured parameter such as a NMR chemical shift or an extinction coefficient of the completely uncomplexed A and the partially complexed A. Here δ_c is the difference between the values of the parameters in the completely complexed and the completely free A. The former value cannot be measured directly but is usually obtained by a graphical method.

Thus, we write

$$p = \delta_i/\delta_c \qquad (3)$$

Scatchard has reported[1] a method for calculating the association constant when the initial concentration of one species is very much in excess of the other. Therefore, if $B_i \gg A_i$, then (2) and (3) can be combined to give

$$\delta_i = \frac{K\delta_c B_i}{1 + KB_i}\left[1 - \frac{KA_i}{1 + KB_i} + \text{other terms in } A_i/B_i\right]$$

leading to Person's absorption isotherm[2]

$$\delta_i = \frac{K\delta_c B_i}{1 + KB_i}$$

A slight rearrangement of this equation leads to

$$\delta_i/B_i = K(\delta_c - \delta_i)$$

which is known as the Scatchard equation. K could be obtained from the slope and hence δ_c from the intercept of a straight line fit of the experimental data (δ_i/B_i vs. δ_i).

Prior to Scatchard's treatment, values of K and δ_c were usually found by using the reciprocal form proposed by Benesi and Hildebrand[3]

$$\frac{1}{\delta_i} = \left(\frac{1}{K\delta_c}\right)\frac{1}{B_i} + \frac{1}{\delta_c}$$

and fitting a straight line to the experimental data (δ_i,B_i) and so obtaining ($1/K\delta_c$) which is the slope and $1/\delta_c$ which is the intercept.

In an alternative procedure, Scott[4] plotted a straight line through the data given by (B_i/δ_i,B_i) in which case the slope is ($1/\delta_c$) and the intercept is ($1/K\delta_c$). Thus his equation is

$$\frac{B_i}{\delta_i} = \frac{B_i}{\delta_c} + \frac{1}{K\delta_c}$$

These two methods are clearly mathematically equivalent, and both depend upon the initial condition $B_i \gg A_i$.

Deranleau[5] points out that the Scatchard equation is the best method of the three for two reasons: (1) it is the only plot in which the errors are not open ended, and there is a constant error function between $S = 0.2$ and $S = 0.75$ where S is the saturation factor or the fraction of the total curve followed; and (2) it is the only method where the experimenter is not free to choose the scale for the plot, and it is obvious at a glance what portion of the complete curve has been covered (Figure 1).

Results and Discussion

Since the advent of computer technology, it has become possible to refine the methods of Scatchard, Benesi–

† Present address: Faculty of Medicine, Riyadh University, Riyadh, Saudi Arabia.

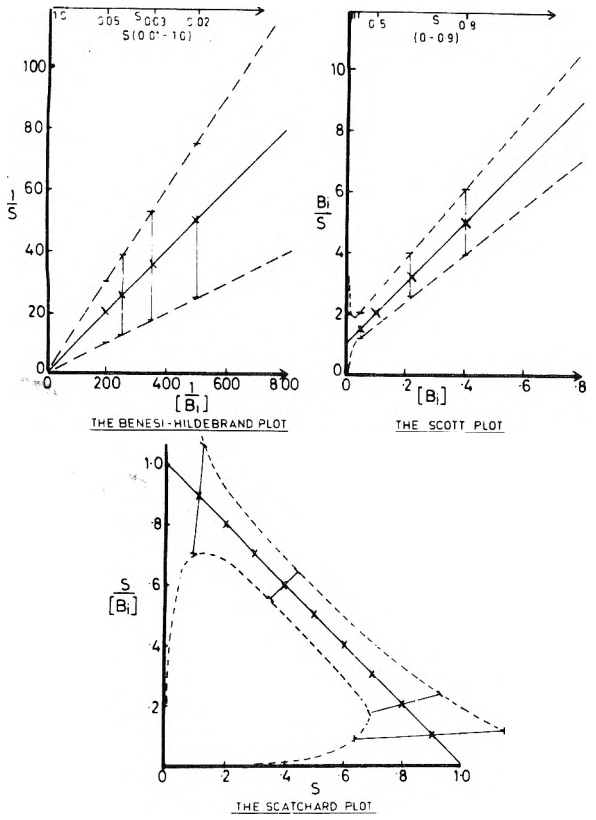

Figure 1. A comparison of the Scatchard, Benesi–Hildebrand, and Scott data treatments taken from ref 5.

Hildebrand, and Scott which are based on the fitting of straight lines to experimental data. The requirement that $B_i \gg A_i$ can be dropped and the full association equation (eq 2) can be used. Some non-linear least-squares methods in the determination of association constants have been mentioned in the literature.[6]

On combining eq 2 and 3, it can be shown that

$$\delta_i = (\delta_c/2A_i)[A_i + B_i + (1/K) - \{[A_i + B_i + (1/K)]^2 - 4A_iB_i\}^{1/2}] \quad (4)$$

where the negative root is appropriate because $\delta_i/\delta_c < 1$. At this stage it is convenient to write

$$l_i = A_i + B_i + (1/K) - \{[A_i + B_i + (1/K)]^2 - 4A_iB_i\}^{1/2} \quad (5)$$

The object of the exercise is to determine the constants K and δ_c for which the above eq 4 "best" fits the experimental data. The convention is adopted here that the "best" fit is the least-squares fit and this is defined so that

$$E = \sum_{i=1}^{n} [\delta_i - \delta_c l_i/2A_i]^2$$

is a minimum and where the summation is taken over all the experimental points. Thus, both $\partial E/\partial \delta_c$ and $\partial E/\partial K$ should vanish. The first of these leads to the condition

$$\delta_c \Sigma l_i^2/4A_i^2 = \Sigma \delta_i l_i/2A_i \quad (6)$$

and the second to the condition

$$\delta_c \Sigma \frac{l_i^2}{2A_i\{A_i + B_i + (1/K) - l_i\}} = \Sigma \frac{\delta_i l_i}{A_i + B_i + (1/K) - l_i} \quad (7)$$

Hence, on eliminating δ_c, a transcendental equation for K is obtained. The value of K can be calculated by using a numerical technique[7] which is a combination of the method of "false position" and the method of "trisection". A printout of the program is available from the authors.

It should be recalled that these equations all apply only if 1:1 complexes are formed. To test this it has been common practice to first obtain a Job plot[8,9] unless there is reason to assume a 1:1 complex initially. The relative concentrations of A and B are varied uniformly from 100% A through to 100% B, and one particular resonance is followed. For a 1:1 interaction, the Job plot has a maximum at 0.5 when $[A]\delta_i$ is plotted against mole fraction.

The greatest source of error when using concentration dependence to calculate K must lie in the preparation of samples, simply because each point on the concentration shift curve represents a different sample. If greater accuracy is required, the number of points must be increased and hence if expensive or inaccessible materials are to be used this requirement may (a) preclude the repetition of the experiment and/or (b) necessitate the use of dilute samples.

A Variable Temperature Method. In an attempt to overcome these difficulties, a different method to obtain the association constant was sought. As part of an extended NMR investigation, the interaction of A and B where at least one component contained an aromatic moiety, i.e., hydrophobic bonding, or π–π interactions were present, was of interest to us. Laszlo and Williams[10] reported an instance in which the association constant, K, was calculated by following the change in chemical shift as a function of temperature. Others[11-14] have also followed similar variable temperature procedures to determine K and thermodynamic parameters. The concept, at first glance, appears simple: protons within the complex which are located above the aromatic portion of an adjacent molecule experience an upfield shift in the NMR spectrum compared with the situation in the absence of the interaction. As the temperature is lowered, there is an increase in the chemical shift difference between the uncomplexed and partially complexed situations. This is consistent with the fact that at lower temperatures, molecular mobility, on the average, is less, and hence there is a greater degree of association present. As low solute concentrations are used, the solution viscosity can be ascribed entirely to the solvent, which in the present situation is water. Although the viscosity of water changes from approximately 9 mP at 20° to approximately 3.4 mP[15] at 80°, this change is not significant when using the temperature variation method, as the chemical shift due to complex formation at each temperature is determined from two solutions (one containing A and B and the other only one of these) of virtually the same viscosity. Therefore, raising the temperature can be thought of as the converse of adding an excess of one component (as is done with the concentration dependence method).

Laszlo and Williams[10] considered solvent–solute interactions. Here, eq 2 is applicable, where δ_t is substituted for δ_i, and as the concentration of A and in particular B are maintained constant, these symbols are not subscripted.

Thus, in the variable temperature method, eq 2 is the governing equation, as it is for the concentration method, but with the difference that now $p = \delta_t/\delta_c$. Here δ_t represents the difference in chemical shift of a particular resonance (or another suitable parameter, e.g., UV absorbance, etc.) in A at a given temperature when in the presence of B (i.e., δ_{A+B}) and in the absence of B (i.e., δ_A), i.e., $\delta_t = \delta_{A+B} - \delta_A$.

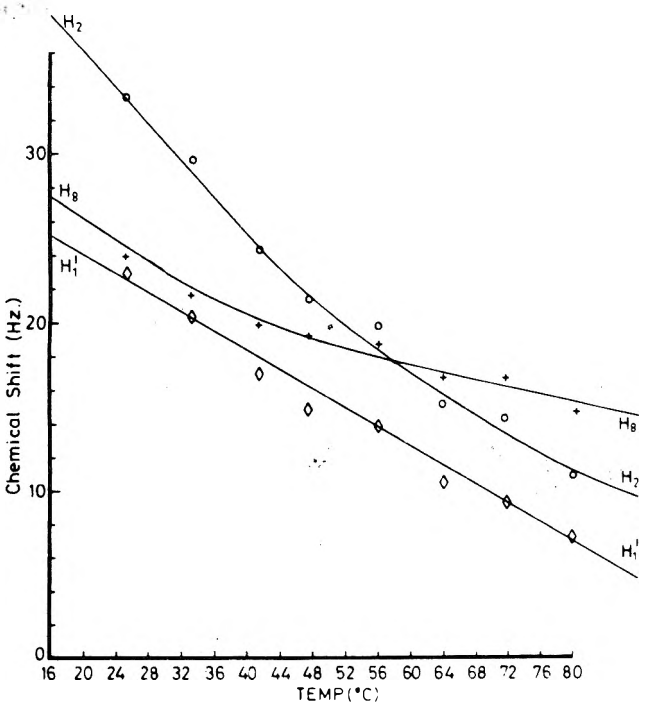

Figure 2. The variable temperature plot of the differences in chemical shifts of a mixture of AMP and tryptophan methyl ester HCl, compared with AMP only. 0.01 M AMP and 0.25 M tryptophan at pH 7 were used.

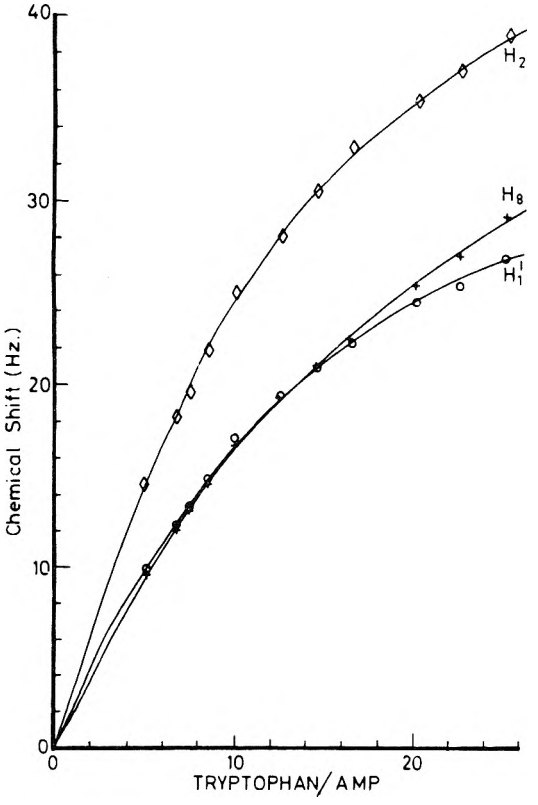

Figure 3. The concentration dependence of the chemical shifts of the AMP base protons from the interaction of AMP and tryptophan methyl ester HCl at 21 °C, pH 7. 0.01 M AMP was used.

A suitable example which may be considered here is the interaction of tryptophan and adenosine 5′-monophosphate (AMP); this and similar interactions have been studied by Hélène and Dimicoli[16,17] and others,[18-20] and hence the complex formation between these solutes is fairly well understood.

The ^{1}H resonances of AMP, i.e., H-8, H-2, and H′$_1$ anomeric, were followed principally because these resonances (cf. tryptophan) were sharp, well separated, and the protons were, fortunately, well distributed around the heterocyclic rings.

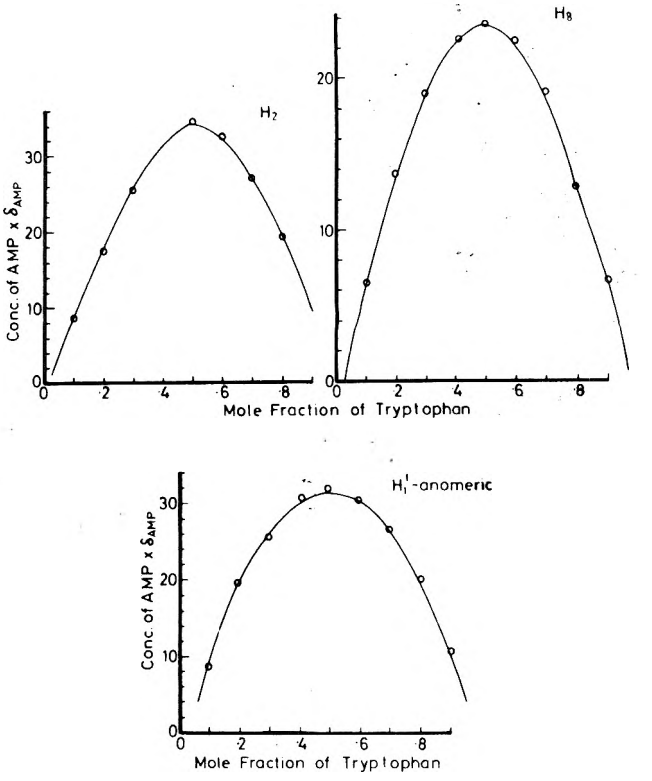

Figure 4. The Job plot for the interaction of AMP and tryptophan at 21 °C, pH 7.

TABLE I: A Comparison of the Association Constants (M^{-1}, 21 °C) as Determined by Concentration and Temperature Variation Methods for the AMP-Tryptophan Interaction

	Position		
Method	H-2	H-8	H$_1$′ (anomeric)
Concentration	6.36	4.07	5.96
Temperature	1.15	2.45	1.13

The δ_t vs. T (the chemical shift difference between the complexed and free forms of AMP vs. temperature for the AMP–tryptophan interaction) plots are shown in Figure 2.

The δ_i vs. ratio of tryptophan/AMP plots (concentration method) are shown in Figure 3.

As the previously mentioned equations for calculating the association constant only apply to 1:1 complexes, it is necessary to check the molecularity of the association. Therefore, a Job plot at 21 °C was obtained (Figure 4). As the curves were symmetrical about the concentration ratio of 0.5, the association was considered to be 1:1. Foster[21] suggested that the Job plot was not always capable of distinguishing between interactions of different stoichiometry but Hélène and Dimicoli[22] used the Job method to show that in acidic media, due to the changes borne by the solutes, the interaction between tryptophan and adenosine (compared with tryptophan and cytidine) contained some 2:1 as well as 1:1 complexes.

It can be seen that the concentration-shift curves have an asymptote to a δ_c, but it is not clear from the temperature curves what temperature should be considered to give the correct δ_c. The technique Laszlo and Williams used to solve this problem was to extrapolate their δ_t vs.

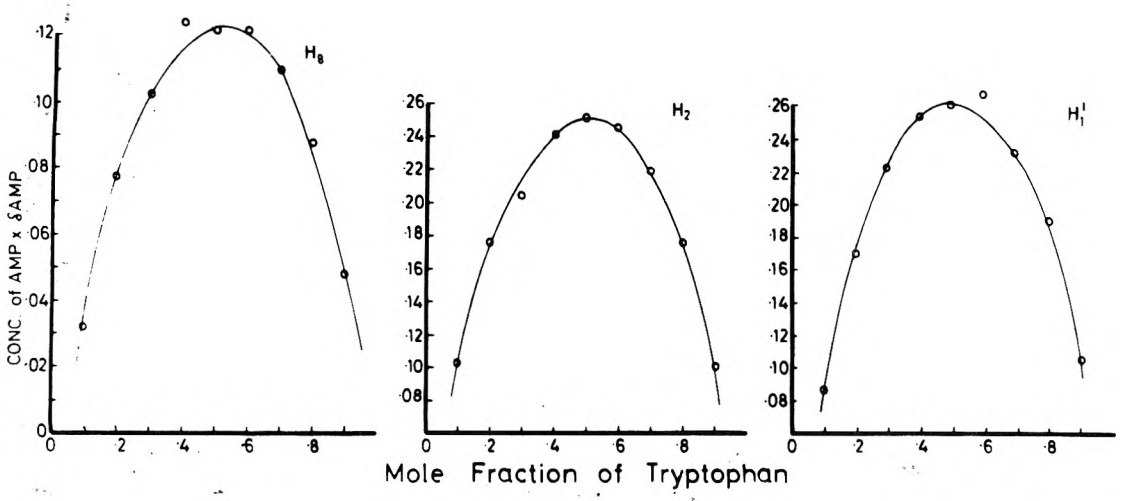

Figure 5. The Job plot for the interaction of AMP and tryptophan at 11 °C, pH 7.

TABLE II: The Chemical Shift Changes (Hz) which Would Occur in the Fully Bound Complexes (Concentration Compared with Temperature Methods) for the AMP-Tryptophan Interaction

	Position		
Method	H-2	H-8	H_1' (anomeric)
Concentration	64.5	57.8	45.7
Temperature	152.5	89.0	107.2

T curves back to 0 K, assume that the shift so obtained was in fact that of the fully associated complex, and to calculate K from this value. If their treatment is followed, the K values shown in Table I are obtained. It is also of interest to note the corresponding δ_c's, i.e., the shifts in the fully bound complexes (Table II).

It is clear that the association constant as determined from the temperature variation method is significantly smaller than that from the concentration method, and conversely, that the extrapolated δ_c shifts from the temperature method are much larger than those from the concentration method. The magnitude of K depends on δ_i (or δ_t) and δ_c. As $\delta_{21°C}$ (temperature method) is actually one point on the concentration curve, and these agree, therefore the point of disagreement between the two methods is most likely to be δ_c (temperature). In case the molecularity of the association should change with temperature, a Job plot at 11 °C was also obtained (Figure 5).

Once again the maxima are at concentration ratio 0.5, indicating a 1:1 association.

In addition, a check on the pH as a function of temperature was made, and it was found that the variation in pH was within the accuracy specifications of the pH meter. Hence, undue errors in the chemical shifts as a result of pH changes should not be present.

If the extrapolation back to 0 K is considered, the presence of a very slight curvature in the chemical shift–temperature plot within the observed relatively narrow temperature range, as compared with a straight line variation, could lead to a very large error in the estimation of δ_c (Figure 6). Thus, as the extrapolation back to 0 K appears to overestimate δ_c, this step should not be used in the calculation of K. Hence, there is a very real problem in calculating the correct value of δ_c.

Abraham[11] did not explicitly calculate the association constant, but eliminated K from a series of equations, and simultaneously matched the chemical shift–temperature data with the three parameters, δ_c, ΔH, and ΔS. Procedures such as these, where a number of parameters are

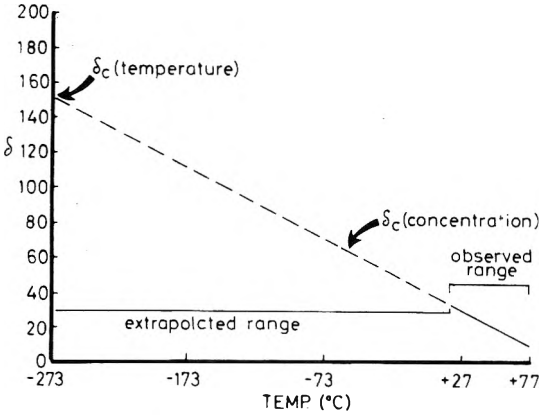

Figure 6. The chemical shift–temperature plot for H-2 in the AMP–tryptophan interaction, showing the relation between the observed range and that when an extrapolation to 0 K is carried out.

simultaneously solved, are prone to significant error. A more common procedure whenever temperature has been used in the context of association constants in the literature[23-25-27] has been to perform a series of concentration dependence experiments at different temperatures, and hence calculate K at these temperatures. From this, ΔH (the enthalpy of the interaction) and ΔS (the entropy of interaction) can be obtained.

The relationships between the various thermodynamic parameters are[28]

$$\Delta G = -RT \ln K \tag{8}$$

and

$$\Delta G = \Delta H - T\Delta S \tag{9}$$

Thus

$$\ln K = \frac{\Delta S}{R} - \frac{\Delta H}{RT}$$

where ΔG is the free energy of interaction, and R is the gas constant. Therefore, for a constant value of ΔS, plots of ln K vs. T^{-1} (van't Hoff plot) should be approximately linear, with a slope of $-\Delta H/R$. (The plot will be linear provided ΔH is independent of temperature.)

In order to ascertain the effect of δ_c on the linearity of the ln K vs. T^{-1} plot, and using the temperature-shift data of H-2 from the AMP–tryptophan interaction, the cor-

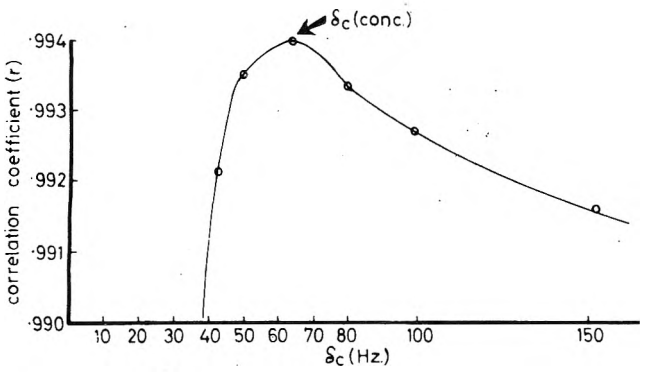

Figure 7. The δ_c vs. correlation coefficient curve for H-2 of the AMP–tryptophan interaction, showing a maximum at approximately 65 Hz.

relation coefficient (r) for eight cases were calculated with the following results:

(1) δ_c = 35.0 Hz, r = 0.9585

(2) δ_c = 40.0 Hz, r = 0.9875

(3) δ_c = 50.0 Hz, r = 0.9935

(4) δ_c = 64.5 Hz, r = 0.9940

(5) δ_c = 80.0 Hz, r = 0.9934

(6) δ_c = 100.0 Hz, r = 0.9927

(7) δ_c = 152.5 Hz, r = 0.9916

(8) δ_c = 1600.0 Hz, r = 0.9911

Cases 4 and 7 represent the δ_c values as determined by concentration and temperature dependence (0 K extrapolation), respectively.

A plot of δ_c vs. r forms a curve of the type shown in Figure 7, and it appears that the value of δ_c at which maximum correlation between ln K and T^{-1} is achieved is $\delta_c \sim 65$ Hz.

The relationship between δ_c and r suggests that a possible method to calculate δ_c from variable temperature

TABLE III: The Calculated δ_c and Association Constants (21 °C) for the AMP–Tryptophan Interaction, as Derived from the Variable Temperature Method (Using the Linearization of the van't Hoff Plot)

	Position		
	H-2	H-8	H_1' anomeric
δ_c, Hz	57.9	54.2	41.5
K, M^{-1}	6.60	3.17	5.60

data would be to assume an initial value for δ_c, and obtain the correlation coefficient for the relationship ln K vs. T^{-1}. Then, the value of δ_c could be varied until the maximum value of the correlation coefficient is found. To ascertain if this procedure does yield a unique value for δ_c, a detailed computer listing of the δ_c vs. r values in the region of r (maximum) was generated and plotted (Figure 8) for a number of cases.

It is obvious that there is, usually, noise about the maximum point (because increments in r are very small compared with increments in δ_c) and, in addition, that in the region r_{max} ±2 Hz the curve can be approximated by a parabola.

In general it was found that parabolic curve fitting resulted in a shift in δ_c of not more than 0.5 Hz from the value obtained without it.

The δ_c and association constant values for the three base positions in AMP in the AMP–tryptophan interaction as determined by the linearization of the van't Hoff plot are listed in Table III, and Figure 9 shows the plot of ln K vs. T^{-1} for AMP + tryptophan (H-2 resonance).

Varying δ_c to improve the linearity of ln K vs. T^{-1} is in effect the same as optimizing the value of ΔH which satisfies the data, and comparisons of Tables I, II, and III indicate that this is indeed a valid method for the determination of K.

Prior to this method of δ_c (temperature) determination, the K values were far too low and δ_c values too large when compared with the corresponding values obtained by the concentration method. While it is not necessary that the δ_c (temperature) values should agree with δ_c (concentration)

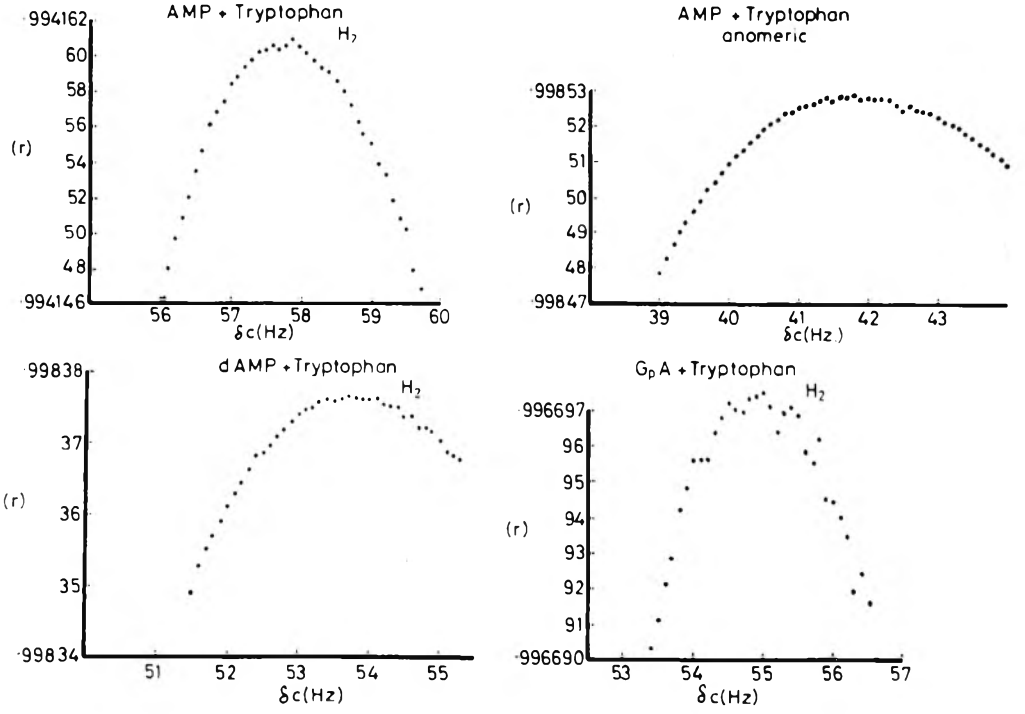

Figure 8. Correlation coefficient (r) vs. δ_c (from temperature data) for a number of amino acid–nucleotide combinations.

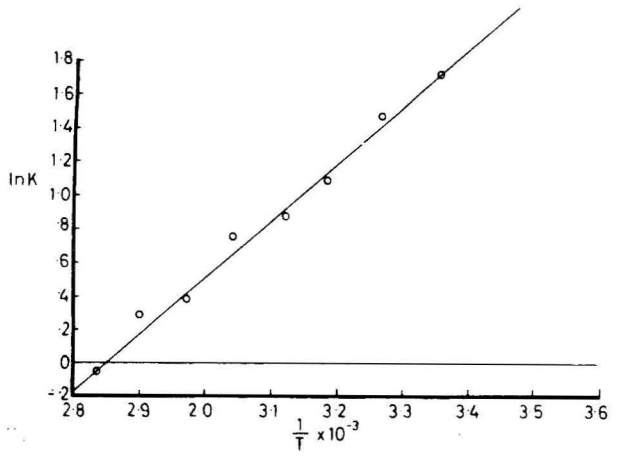

Figure 9. The van't Hoff plot for the H-2 resonance of the AMP–tryptophan interaction.

TABLE IV: A Comparison of the Thermodynamic Parameters for the Interaction between AMP and Tryptophan at 25 °C as Determined by Morita[a] and from the Present Work

		$-\Delta G$, kcal/mol	$-\Delta H$, kcal/mol	$-\Delta S$, cal/mol deg
(a) Morita[a]		1.28	6.8	18.5
(b) Present work	H-2	1.02	6.7	19.0
	H_1'	0.96	6.7	19.3
	H-8	0.70	2.6	6.6

[a] Reference 18.

exactly as, after all, the physical processes involved are different, the agreement should be better than that obtained when extrapolation to 0 K is used, if K values are to agree at all. Considering the H-2 resonance in AMP, the K value (concentration) is 6.36 M^{-1}, compared with 6.60 M^{-1} via linearization of the van't Hoff plot and 1.15 M^{-1} via extrapolation to 0 K.

Figure 10 shows the correlation of K as determined by concentration variation compared with the two methods of temperature variation (linearization of ln K vs. T^{-1} and extrapolation to 0 K) for a number of different amino acid–nucleotide combinations. It is clear that the agreement between the association constant as determined by (a) concentration variation and (b) that determined by optimization of ln K vs. T^{-1} is much better than between (a) and (c) when the chemical shift is extrapolated to 0 K to give δ_c by temperature variation.

Morita[18] used UV spectroscopy to determine the association constant, and hence ΔG, for AMP + tryptophan. In addition, ΔH and ΔS were determined from the traditional van't Hoff plot. For comparison purposes, Table IV lists the values of ΔG, ΔH, and ΔS at 25 °C for the interaction (a) as determined by Morita, and (b) as determined by us.

The values of ΔH and ΔS for H-2 and H_1' are in surprisingly good agreement with Morita's work. The correlation coefficient for the van't Hoff plot for H-8 is significantly poorer than for H-2 or H_1' (0.988 compared with 0.998) and this may explain the lack of agreement between ΔH and ΔS for H-8 and the other positions within AMP. The association constant at 25 °C as calculated by Morita is 8.67 M^{-1}, and from the present work (H-2) is 5.62 M^{-1}. Morita used UV spectroscopy and, with that technique, the association constant and thermodynamic parameters are determined for the molecule as a whole. This is compared with the NMR method, where these values are determined for different positions within the molecule.

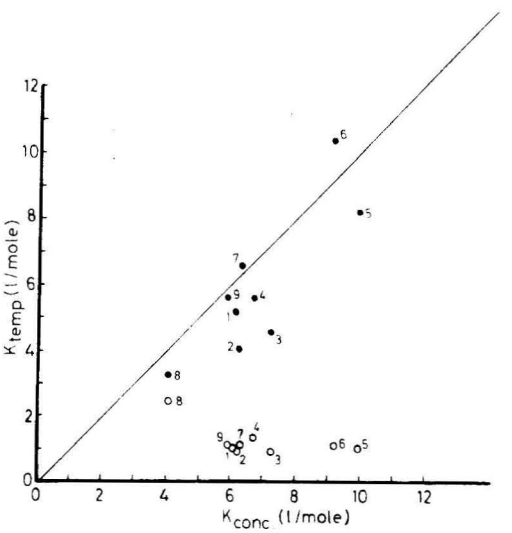

Figure 10. The correlation of K determined by concentration variation compared with the two methods of temperature variation for a number of tryptophan–amino acid interactions: (●) represents the linearization of the van't Hoff equation; (○) represents the extrapolation to 0 K, and the straight line indicates the position of exact correlation between association constants determined by concentration compared with temperature methods. The number refers to the following sites in tryptophan–amino acid interactions: GpA (1) A-8 (2) A-2 (3) A-anomeric, dAMP (4) A-8 (5) A-2 (6) A-anomeric; AMP (7) A-2 (8) A-8 (9) A-anomeric.

As the values of ΔH and ΔS (H-2 and H_1') from the two techniques agree so well (compared with the association constants or ΔG), this might indicate that ΔH and ΔS as determined via NMR may be applicable to the interaction as a whole, as compared with K values which refer to particular positions within the molecule.

Therefore, depending on the information required, it is possible to determine the association constant with equal validity by varying the concentration or the temperature and, in general, if ΔH (and ΔS, ΔG) is required, the determination of K by the variable temperature method would require less expenditure of effort and, from the point of view of sample preparation, would possibly involve less error. A computer program is available from the authors upon request.

Experimental Section

All chemical shift work was performed on a JEOL PFT-100 NMR spectrometer with D_2O solvent supplying the deuterium lock. A Metrohm precision compensator E388 was used to measure the pH. Adenosine 5′-monophosphate sodium salt and L-tryptophan methyl ester HCl were obtained from Sigma Chemical Co. Both were of high purity and used without further purification. Deuterium oxide (99.75%) was obtained from the Australian Atomic Energy Commission, and solutions were adjusted to pH 7 with citric acid–phosphate buffer.

The association constant determinations (concentration variation) were carried out at the NMR probe temperature (21 °C) and the temperature was controlled by the built-in variable temperature accessory, and calibrated with standard samples. It is estimated that the stated temperatures are accurate to ±1 °C.

AMP (2 mg/0.5 mL) was used in both the concentration and temperature variation methods. When determining the association constant by the concentration method, the ratio of tryptophan/AMP was varied (the concentration of AMP was constant), and the chemical shift of the AMP resonances were noted. Acetonitrile was used as an internal reference (δ = 2.02).

A 1:1 sample of AMP:tryptophan gave chemical shifts which were considered too small to be used accurately, i.e., the proportion of complexed AMP/tryptophan was relatively small. Therefore, for variable temperature work, samples were prepared in which the ratio of AMP:tryptophan was 1:25.

References and Notes

(1) G. Scatchard, *Ann. N.Y. Acad. Sci.*, **51**, 660 (1949).
(2) W. B. Person, *J. Am. Chem. Soc.*, **87**, 167 (1965).
(3) H. A. Benesi and J. H. Hildebrand, *J. Am. Chem. Soc.*, **71**, 2703 (1949).
(4) R. L. Scott, *Recl. Trav. Chim. Pays-Bas.*, **75**, 787 (1956).
(5) D. A. Deranleau, *J. Am. Chem. Soc.*, **91**, 4044 (1969).
(6) J. A. Ibers, D. V. Stynes, H. C. Stynes, and B. R. James, *J. Am. Chem. Soc.*, **96**, 1358 (1974).
(7) F. S. Aston, "Numerical Methods That Work", Harper and Row, New York, N.Y., 1970.
(8) P. Job, *Compt. Rend.*, **180**, 928 (1925).
(9) R. Sahai, G. L. Loper, S. H. Lin, and H. Eyring, *Proc. Natl. Acad. Sci. U.S.A.*, **71**, 1499 (1974).
(10) P. Laszlo and D. H. Williams, *J. Am. Chem. Soc.*, **88**, 2799 (1966).
(11) R. J. Abraham, *Mol. Phys.*, **4**, 369 (1961).
(12) J. V. Hatton and W. G. Schneider, *Can. J. Chem.*, **40**, 1285 (1962).
(13) J. N. Murrell and V. M. S. Gill, *Trans. Faraday Soc.*, **61**, 402 (1965).
(14) S. Wold, *Acta Chem. Scand.*, **25**, 336 (1971).
(15) E. W. Washburn, Ed., "International Critical Tables of Numerical Data, Physics, Chemistry, and Technology", Vol. V, McGraw-Hill, New York, N.Y., 1929, p 10.
(16) J. L. Dimicoli and C. Hélène, *Biochimie*, **53**, 331 (1971).
(17) C. Hélène, T. Montenay-Garestier, and J. L. Dimicoli, *Biochim. Biophys. Acta*, **254**, 349 (1971).
(18) F. Morita, *Biochim. Biophys. Acta*, **343**, 674 (1974).
(19) K. G. Wagner and R. Lawaczeck, *J. Magn. Reson.*, **8**, 164 (1972).
(20) M. Guéron, C. Chanchaty, and T. D. Son, *Ann. N.Y. Acad. Sci.*, **222**, 307 (1973).
(21) R. Foster, Ed., "Molecular Complexes", Vol. II, Elek. Science, London, 1974.
(22) J. L. Dimicoli and C. Hélène, *J. Am. Chem. Soc.*, **95**, 1036 (1973).
(23) I. D. Kuntz, Jr., and M. D. Johnson, Jr., *J. Am. Chem. Soc.*, **89**, 6008 (1967).
(24) D. R. Eaton, *Can. J. Chem.*, **47**, 2645 (1969).
(25) V. Balevichius and L. Kimtys, *Org. Magn. Reson.*, **8**, 180 (1976).
(26) H. L. Liao and D. E. Martire, *J. Am. Chem. Soc.*, **96**, 2058 (1974).
(27) J. B. Homer and M. C. Cooke, *J. Chem. Soc. A*, 2862 (1969).
(28) F. C. Andrews, "Thermodynamics: Principles and Applications", Wiley-Interscience, New York, N.Y., 1971, p 225.

Emission Spectra of CH_3O, C_2H_5O, and i-C_3H_7O Radicals

Keiji Ohbayashi, Hajime Akimoto,[1] and Ikuzo Tanaka*

Department of Chemistry, Tokyo Institute of Technology, Ohokayama, Meguro-ku, Tokyo, 152, Japan

(Received March 19, 1976; Revised Manuscript Received February 7, 1977)

Emission spectra of CH_3O, C_2H_5O, i-C_3H_7O, and NO are obtained in the photolysis of corresponding alkyl nitrites by iodine, mercury, xenon, and krypton lamps. The excitation thresholds to produce RO fluorescence are also determined as 6.02 eV (CH_3O), 5.90 eV (C_2H_5O), and 5.82 eV (i-C_3H_7O). The (0, 0) band of the electronic transition of CH_3O between the ground state and the first excited state is estimated to lie near 305 nm. The ratios of electronic quenching rates to fluorescence rates of RO with 13 foreign gases are determined and from the self-quenching rates the fluorescence lifetimes are estimated as follows: ~3 μs (CH_3O), ~1 μs (C_2H_5O), and ~0.3 μs (i-C_3H_7O).

Introduction

Alkoxyl radicals are supposed to be important intermediates in the combustion and hydrocarbon oxidation processes.[2] However, the spectroscopic information has been scarcely obtained thus far even for the prototype alkoxyl radical, CH_3O.

The near ultraviolet photolysis ($300 < \lambda < 400$ nm) of alkyl nitrites in the gas phase has been considered to produce alkoxyl radicals in the major primary process[3]

$$RONO + h\nu \rightarrow RO + NO \quad (1)$$

However, although first ascribed to CH_3O,[4] the transient species whose absorption spectrum was observed in the flash photolysis of methyl nitrite was later reassigned to HNO which would be formed in the secondary process.[5] Thus the absorption spectra of CH_3O and higher homologues have not been found.

Emission spectra were first observed by Style and Ward[6] in the photolysis of CH_3ONO and C_2H_5ONO using a hydrogen continuum lamp. The species giving the emission bands in the near-ultraviolet to visible region were proposed to be CH_3O and C_2H_5O, respectively.

In order to establish the fluorescence of alkoxyl radicals, the emission spectra in the photolysis of CH_3ONO, C_2H_5ONO, i-C_3H_7ONO, and t-C_4H_9ONO using iodine (206.2, 187.6 nm), mercury (184.9 nm), xenon (147.0, 129.5 nm), and krypton (123.6, 116.5 nm) lamps as well as a deuterium continuum lamp were investigated. Photolysis by the iodine or the mercury lamp gave the emission spectra between 290 and 450, 330 and 500, and 360 and 520 nm for CH_3ONO, C_2H_5ONO and i-C_3H_7ONO, respectively.

From the threshold energies of the exciting photons required to give the emissions, the emitters are most likely the first electronically excited states of CH_3O, C_2H_5O, and i-C_3H_7O, respectively. No emission was observed when t-C_4H_9ONO was photolyzed by the iodine or the mercury lamp. When these nitrites were photolyzed by the xenon or the krypton resonance lamp, β and γ bands of NO were observed but no emission of alkoxyl radicals was observed. The ratios of electronic quenching to fluorescence rates for the excited CH_3O, C_2H_5O, and i-C_3H_7O radicals by 13 foreign gases were obtained.

Experimental Section

Methyl, ethyl, and isopropyl nitrites were prepared by the dropwise addition of 50% H_2SO_4 to saturated solutions of $NaNO_2$ in methanol, ethanol, and 2-propanol, respectively. They were purified by gas chromatography (column, dimethylsulfolane), degassed, and stored in darkened traps at −80 °C. Commercially available *tert*-butyl nitrite (Tokyo Kasei Co.) and ethyl nitrate (Tokyo Kasei Co.)

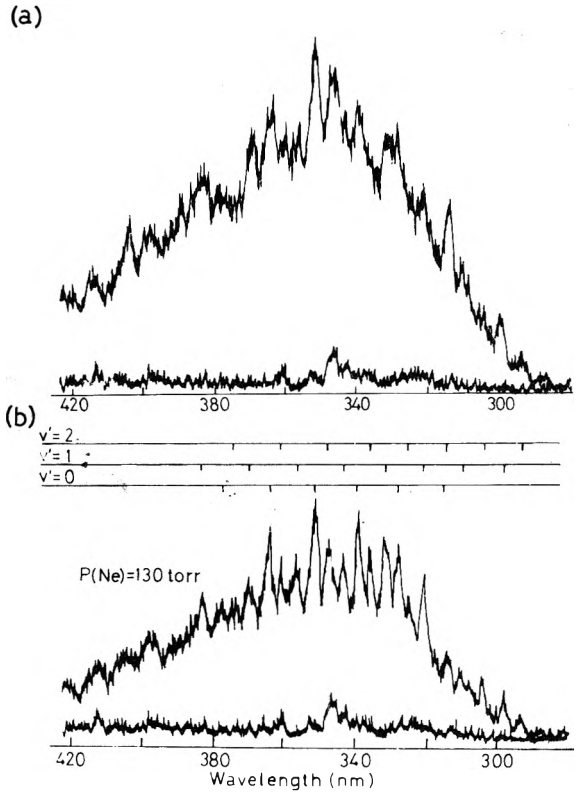

Figure 1. Emission spectra obtained in the photolysis of (a) 0.5 Torr of CH_3ONO and (b) 0.5 Torr of CH_3ONO + 130 Torr of Ne using an iodine lamp. Background at the bottom. Spectral slit width was 1.0 nm.

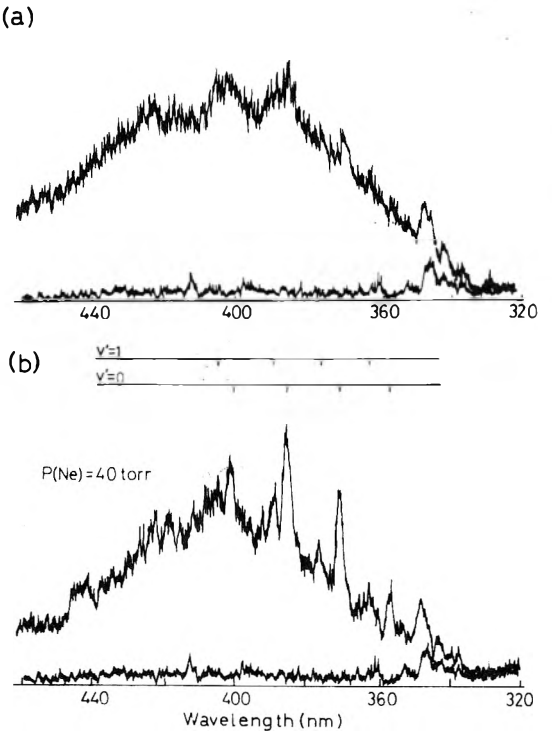

Figure 2. Emission spectra obtained in the photolysis of (a) 0.5 Torr of C_2H_5ONO and (b) 0.5 Torr of C_2H_5ONO + 40 Torr of Ne using an iodine lamp. Background at the bottom. Spectral slit width was 1.0 nm.

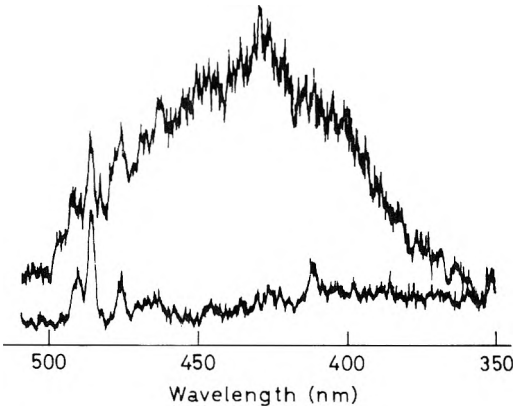

Figure 3. Emission spectrum obtained in the photolysis of 0.5 Torr of i-C_3H_7ONO using an iodine lamp. Spectral slit width was 1.5 nm. Any noticeable change in the spectrum was not observed when inert gas was added.

were also purified and stored by the same method as above. Dimethoxylmethane, $(CH_3O)_2CH_2$, (Tokyo Kasei Co.) was used without further purifications except degassing. Quenching gases (Takachiho Co.) were used without further purifications. The photolysis cell was made of pyrex and had one LiF window on the side of incident light and one quartz window at a right angle to it for the detection of emitted light. On the opposite sides of both these windows were two light traps. Iodine, mercury, xenon, and krypton lamps were operated with a 2450-MHz microwave generator. An iodine lamp was used with cooling of the side arm to -10 ± 1 °C in order to diminish emission lines from iodine molecules. The fluorescence spectrum was taken by means of a Nikon monochromator (Model P-250, f = 4.5) with a 1200 grooves/mm grating and Hamamatsu T.V. R-585S photomultiplier (spectral sensitivity, 160–650 nm). The output was fed to a pulse amplifier and recorded on a strip chart recorder after analogue integration.

In the experiments determining the threshold energies required to give the emissions and the electronic quenching rates, the excitation source was replaced by a deuterium lamp coupled with a Nikon P-250 monochromator and the fluorescence intensity was monitored through a glass filter. In measuring the quenching rates, the excitation wavelength was set at 199 ± 1 nm where interference by the fluorescence of small amounts of NO formed in the photolysis was found to be minimum.

Results

Emission Spectrum. Figures 1a, 2a, and 3 show the emission spectra (spectral slit width, 1.0, 1.0, and 1.5 nm, respectively) obtained in the photolysis of CH_3ONO, C_2H_5ONO, and i-C_3H_7ONO, respectively, using the iodine lamp. The emitters are most likely electronically excited CH_3O, C_2H_5O, and i-C_3H_7O, respectively, as will be discussed later. The emission intensity was found to be maximum at a pressure of about 0.5 Torr of nitrite. No correction was made for the spectral sensitivity of the detection system. When these nitrites were excited by the mercury lamp, the same spectra as in Figures 1a and 2a were obtained although the much intense scattered lines from the lamp obscured the details of the spectra. Photolysis of $(CH_3O)_2CH_2$ by the krypton lamp and $C_2H_5ONO_2$ by the xenon lamp gave same spectra as in Figures 1a and 2a, respectively. However these emission spectra were much weaker than those obtained in the photolysis of alkyl nitrites. Photolysis of t-C_4H_9ONO by either the iodine or the mercury lamp gave no emission.

As shown in the figures, the emission spectrum of CH_3O starts at about 290 nm and extends over 450 nm with a maximum at about 350 nm. Similarly the spectrum of C_2H_5O starts at about 330 nm and extends over 500 nm with a broad maximum at about 400 nm. With a spectral resolution of 1.0 nm, both spectra show diffuse banded

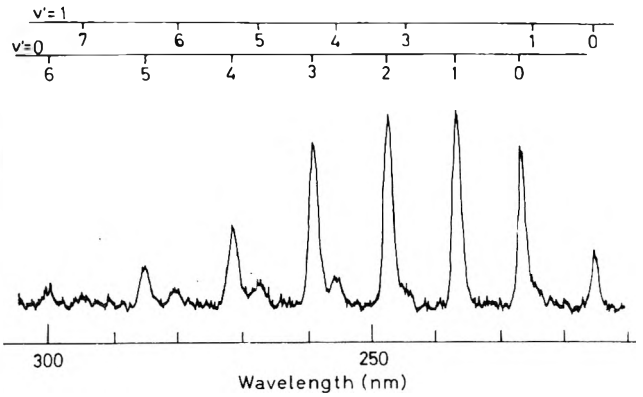

Figure 4. Emission spectrum of γ bands of NO in the region 210–300 nm obtained in the photolysis of 0.5 Torr of C_2H_5ONO at 147.0-nm irradiation. Spectral slit width was 0.9 nm.

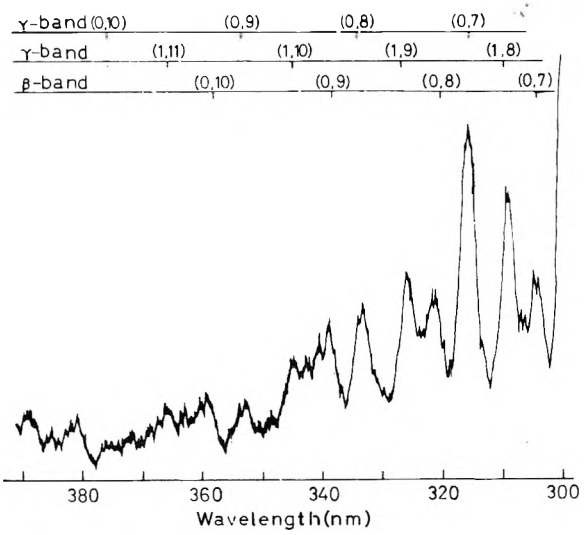

Figure 5. Emission spectrum of β and γ bands of NO in the region 300–400 nm obtained under the same experimental conditions as in Figure 4.

structures. When Ne, Ar, or N_2, which was found to be an inefficient electronic quencher, was added to the nitrites, several bands in the spectrum became sharper and better resolved. Figures 1b and 2b show the emission spectra obtained when CH_3ONO with 130 Torr of Ne and C_2H_5ONO with 40 Torr of Ne were photolyzed by the iodine lamp, respectively. The spectral slit width was the same as in Figure 1a or 2a. The emission spectrum of i-C_3H_7O is red-shifted compared with C_2H_5O and almost structureless even when inert gas was added.

In order to measure the threshold wavelengths required to give the emission spectra, the fluorescence intensity was monitored by scanning the incident light through a monochromator with a spectral resolution of 1.0 nm. These were determined to be at 206 ± 1 nm for CH_3ONO, 210 ± 1 nm for C_2H_5ONO, and 213 ± 1 nm for i-C_3H_7ONO.

Photolysis of CH_3ONO, C_2H_5ONO, i-C_3H_7ONO, and t-C_4H_9ONO by using either the xenon or the krypton resonance lamp all gave β and γ bands of NO, but no emission spectrum of alkoxyl radicals was observed. Figures 4 and 5 show the emission spectra of NO in the regions of 210–300 and 300–400 nm, respectively, in the photolysis of C_2H_5ONO using a xenon resonance lamp. The γ bands consist of $v' = 0$ and 1 progressions and β bands consist of $v' = 0$ progression as shown in Figures 4 and 5. The appearance of γ bands are much the same for other nitrites and also in the photolysis by the krypton resonance line. The emission intensity of NO was found

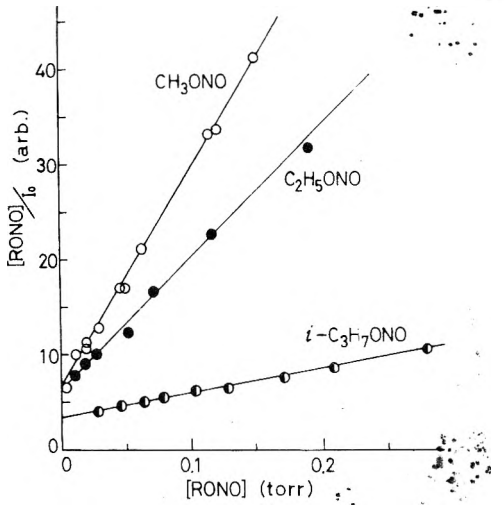

Figure 6. Stern–Volmer plots corresponding to eq 8 for methyl, ethyl, and isopropyl nitrites. The ratios of slope to intercept give 36 $Torr^{-1}$ (CH_3ONO), 20 $Torr^{-1}$ (C_2H_5ONO), and 6.5 $Torr^{-1}$ (i-C_3H_7ONO).

to be maximum at a pressure of about 0.5 Torr. The apparent intensity ratios of β to γ bands decrease for CH_3ONO, C_2H_5ONO, and t-C_4H_9ONO, in that order.

Electronic Quenching. When methyl, ethyl, and isopropyl nitrites are photolyzed with irradiation at 199 ± 1.0 nm, electronically excited CH_3O^*, $C_2H_5O^*$, and i-$C_3H_7O^*$ radicals are formed, respectively.

$$RONO + h\nu \rightarrow RO^* + NO \quad \phi \qquad (1')$$

The deactivation processes of these excited alkoxyl radicals are supposed as follows:

$$RO^* \rightarrow RO + h\nu' \qquad k_r \qquad (4)$$

$$RO^* \rightarrow RO \qquad k_{nr} \qquad (5)$$

$$RO^* + RONO \rightarrow \text{quenching and/or reaction} \qquad k_{sq} \qquad (6)$$

and, when the foreign gas is added, the following process should be included:

$$RO^* + M \rightarrow \text{quenching and/or reaction} \qquad k_q \qquad (7)$$

It should be noted that reactions 6 and 7 involve both overall physical and chemical quenching processes.

Steady-state analysis leads the following relations when M is absent or present:

$$\alpha\frac{[RONO]}{I_0} = k_{sq}[RONO] + k_{nr} + k_r \qquad (8)$$

$$I_0/I = 1 + \frac{k_q}{k_{sq}[RONO] + k_{nr} + k_r}[M] \qquad (9)$$

where I and I_0 indicate the fluorescence intensities with and without M, respectively, and α is a constant independent of [RONO].

The plots based on eq 8 are shown in Figure 6. The ratios of slope to intercept give 36 $Torr^{-1}$ (CH_3ONO), 20 $Torr^{-1}$ (C_2H_5ONO), and 6.5 $Torr^{-1}$ (i-C_3H_7ONO). Then from the value of $k_{sq}/(k_{nr} + k_r)$ and the slope of the plots for eq 9, the values of $k_q/(k_{nr} + k_r)$ are obtained for various quenchers. In Table I the values of $k_q/(k_{nr} + k_r)$ and $k_{sq}/(k_{nr} + k_r)$ are given. Relative quenching cross sections normalized to that for CO, $\sigma(M)/\sigma(CO)$, are also given in Table I.

Discussion

Emission Spectrum. The wavelengths of some of the vibrational bands in the emission spectrum shown in

TABLE I: Quenching Rates of CH_3O^*, $C_2H_5O^*$, and i-$C_3H_7O^*$

Collision partner	CH_3O^* $k_q/(k_{nr}+k_r)$, cm³ molecule⁻¹	CH_3O^* $\sigma(M)/\sigma(CO)$	$C_2H_5O^*$ $k_q/(k_{nr}+k_r)$, cm³ molecule⁻¹	$C_2H_5O^*$ $\sigma(M)/\sigma(CO)$	i-$C_3H_7O^*$ $k_q/(k_{nr}+k_r)$, cm³ molecule⁻¹	i-$C_3H_7O^*$ $\sigma(M)/\sigma(CO)$
CO	3.2×10^{-16}	1.0	1.3×10^{-16}	1.0	3.3×10^{-17}	1.0
Ne	$<3 \times 10^{-18}$	<0.01				
Ar	$<3 \times 10^{-18}$	<0.01				
Kr	2.8×10^{-17}	0.11	6×10^{-18}	0.06	$<1.5 \times 10^{-18}$	<0.06
Xe	3.4×10^{-16}	1.4	1.4×10^{-16}	1.5	3.7×10^{-17}	1.6
CO_2	1.8×10^{-16}	0.65	6.1×10^{-17}	0.51	1.6×10^{-17}	0.53
O_2	1.0×10^{-16}	0.33	3.0×10^{-17}	0.23	8.5×10^{-18}	0.26
N_2	5×10^{-18}	0.01	$<1 \times 10^{-16}$	<0.01		
H_2	2.3×10^{-16}	0.25	7.6×10^{-17}	0.19	1.6×10^{-17}	0.15
CH_4	3.6×10^{-16}	0.97	1.3×10^{-16}	0.79	3.0×10^{-17}	0.71
C_2H_6	6.4×10^{-16}	2.0	2.7×10^{-16}	2.1	6.7×10^{-17}	2.1
C_3H_8	1.1×10^{-15}	3.7	3.6×10^{-16}	3.1	1.0×10^{-16}	3.6
C_4H_{10}	9.1×10^{-16}	2.9	3.3×10^{-16}	2.5	6.8×10^{-17}	2.0
CH_3ONO	1.1×10^{-15}	4.0				
C_2H_5ONO			6.2×10^{-16}	5.7		
i-C_3H_7ONO					2.0×10^{-16}	8.1

TABLE II: Wavenumbers of CH_3O Emission Bands in cm^{-1} (nm)

v''	$v'=0$			$v'=1$			$v'=2$	
0	[32 800	(305)	800][a]	33 600	(298)	500	34 100	(293)
	1 100			1 300			1 200	
1	[31 700	(315)	600][a]	32 300	(310)	600	32 900	(304)
	1 100			1 000			1 100	
2	30 600	(327)	700	31 300	(320)	500	31 800	(314)
	1 100			1 100			1 000	
3	29 500	(339)	700	30 200	(331)	600	30 800	(325)
	1 000			1 000			900	
4	28 500	(351)	700	29 200	(343)	700	29 900	(335)
	1 000			1 100			1 100	
5	27 500	(364)	600	28 100	(356)	700	28 800	(347)
	1 000			1 000			1 000	
6	26 500	(377)	600	27 100	(365)	700	27 800	(360)
				1 000			1 000	
7				26 100	(383)	600	26 700	(374)

[a] These values are estimated from vibrational frequencies.

Figure 1 agree well with those observed in the early work of Style and Ward, and the emitting species is the CH_3O radical. The fact that the same spectrum was obtained when dimethoxylmethane was photolyzed by a krypton resonance lamp supports the above assignment.

The vibrational structure was better resolved upon the addition of 130 Torr of Ne and some of the bands were found to be enhanced as can be seen in Figure 1b. This effect would be due to the vibrational and rotational relaxations by collisions in the electronic excited state of CH_3O. The relatively enhanced bands at 364, 351, 339, and 327 nm would most likely be assigned to the $v' = 0$ progression. It would then be easy to assign other bands to $v' = 1$ and 2 progressions. Results are given in Table II. The bands at 304 and 293 nm were assigned to the members of the $v' = 2$ progression rather than that of the $v' = 0$ progression taking the expected Franck–Condon factors into consideration. Although the v'' numbering could not be determined unambiguously, the energetic limitation, $E_0(CH_3O) \leq 4.21 \pm 0.05$ eV ($\geq 295 \pm 3$ nm), as will be derived below, leaves the only limited choice of the v'' numbering, where $E_0(CH_3O)$ is the energy of the (0, 0) fluorescence band of CH_3O. If the band at 293 nm is assigned to (2, 0) band, the (0, 0) band should lie at 305 ± 1 nm from the vibrational spacing obtained in Table I. Alternatively if the band at 293 nm is assigned to the (2, 1) band, the (0, 0) band should be at 294 ± 1 nm. Although the latter assignment barely satisfies the above energetic requirements, the former assignments would be much more probable, since the above energy limit was based on the assumption that the fragments have no excess internal or kinetic energies at the threshold. Slight excitation in any of the internal or external mode lowers the $E_0(CH_3O)$ value and the (0, 0) band at 294 ± 1 nm would then be energetically impossible. Thus the (0, 0) band of the CH_3O fluorescence can be determined at 305 ± 1 nm or 4.07 ± 0.02 eV.

Table II shows that the vibrational frequencies are 1000–1100 cm^{-1} in the lower state and 500–700 cm^{-1} in the upper state. Recent ab initio calculation of $CH_3O(X^2E)$ and $CH_3O^*(A^2A_1)$[7] showed that the length of CH_3–O bond increases from 1.44 Å in the ground state to 1.65 Å in the excited state. The difference of geometry between the ground state and the excited state is consistent with the difference of the above vibrational frequencies. Although the calculated excitation energy of 3.59 eV (346 nm) is somehow smaller than our experimental value of 4.07 ± 0.02 eV (305 ± 1 nm), the emission bands in Figure 1 are most likely assigned to the $A^2A_1 \rightarrow X^2E$ transition of CH_3O.

The spectrum in Figure 2a obtained in the photolysis of C_2H_5ONO by the iodine lamp is more diffuse than that of CH_3O and the vibrational structures can hardly be resolved. However the spectrum in Figure 2b obtained after the addition of 40 Torr of Ne has much clearer vibrational structure. Several bands which are enhanced in Figure 2b would belong to the $v' = 0$ progression. The other progression observed in Figure 2b would then cor-

TABLE III: Wavenumbers of C_2H_5O Emission Bands in cm^{-1} (nm)

v''	v' = 0			v' = 1		
v'' + 0	28 200	(355)				
	1 100					
1	27 100	(369)	600	27 700	(361)	
	1 100			1 000		
2	26 000	(384)	700	26 700	(375)	
	900			1 100		
3	25 100	(399)	500	25 600	(390)	
				800		
4				24 800	(404)	

respond to that from the $v' = 1$ level. The assignment of these vibrational bands are given in Table III, although the v'' numbering could not be determined. The vibrational spacings are 1000–1100 cm^{-1} in the lower state and 500–700 cm^{-1} in the excited state. The similarity of these vibrational frequencies to those of CH_3O strongly suggests that the emitting species in Figure 2 is the C_2H_5O radical, and the above vibrational spacings would correspond to the C_2H_5–O stretching mode. The fact that the same spectrum was obtained in the photolysis of $C_2H_5ONO_2$ by the xenon lamp further supports this assignment.

The emission spectrum observed in the photolysis of isopropyl nitrite by the iodine lamp was much more diffuse than that of C_2H_5O. This spectrum is further red-shifted than that of C_2H_5O and the emitter would be the i-C_3H_7O radical.

The photodissociative excitation process

$$RONO + h\nu \rightarrow RO^* + NO$$

is assumed to be responsible for the emission spectrum of RO* observed in this study. Then the energy of (0, 0) band of RO fluorescence, $E_0(RO^*)$, may be calculated as

$$E_0(RO^*) \leqslant E_0(h\nu_0) - D^0(RO\text{-}NO) \qquad (10)$$

by assuming that either the internal or external mode of the fragments is not excited at the excitation threshold, where $E_0(h\nu_0)$ is the threshold energy of incident light to give the fluorescence of RO. The values of $D^0(RO\text{–}NO)$ have recently been determined[8] to be 1.81, 1.84, and 1.80 ± 0.04 eV for methyl, ethyl, and isopropyl nitrite, respectively. For these nitrites, the values of $E_0(h\nu_0)$ have been determined in this study to be 6.02, 5.90, and 5.82 ± 0.03 eV, respectively. Then the upper limits of $E_0(RO^*)$ can be calculated as 4.21, 4.06, and 4.02 ± 0.05 eV or 295, 305, and 308 ± 3 nm for methoxyl, ethoxyl, and isopropoxyl radicals, respectively. In consideration of this energy limitation and the vibrational analysis of the CH_3O fluorescence, the value of $E_0(CH_3O^*)$ was determined to be 4.07 ± 0.02 eV or 305 ± 1 nm.

Electronic Quenching. The values of the relative quenching cross section of CH_3O^*, $C_2H_5O^*$, and i-$C_3H_7O^*$ for each collision partner show the same trends. They are relatively large for parent molecules, hydrocarbons, Xe, CO, and decrease for CO_2, O_2, H_2 in that order. The electronic quenching cross sections for Ne, Ar, and N_2 are very small and these molecules seem to contribute to vibrational and rotational relaxations in the electronically excited state as seen in Figures 1 and 2.

It should be noted that the values of $k_q/(k_{nr} + k_r)$ for the same quenchers and of $k_{sq}/(k_{nr} + k_r)$ for the parent molecules decrease from CH_3O^* to i-$C_3H_7O^*$. This trend may be due to the fact that the value of $k_{nr} + k_r$ increases from CH_3O^* to i-$C_3H_7O^*$, i.e., the fluorescence lifetime of larger RO* radical is shorter than that of smaller one. If

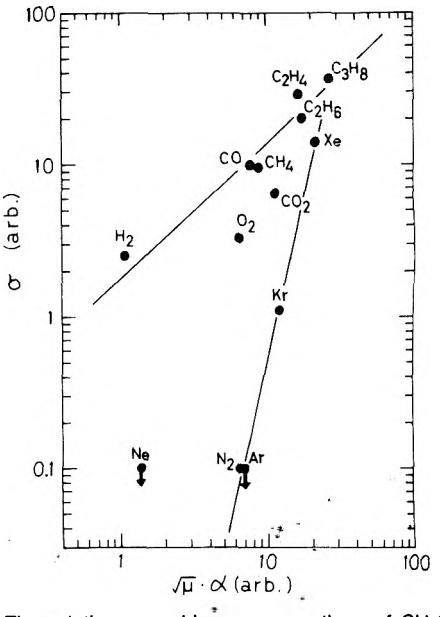

Figure 7. The relative quenching cross sections of CH_3O^* vs. the parameter of Rossler[10] for 13 molecules.

the electronic quenching of RO* occurs at the rate of every collision with the parent molecule, the maximum rate constant of $k_{nr} + k_r$ or the minimum fluorescence lifetime $\tau_f = (k_{nr} + k_r)^{-1}$ may be calculated. The minimum values of τ_f thus estimated are 3, 1, and 0.3 μs for CH_3O^*, $C_2H_5O^*$, and i-$C_3H_7^*$, respectively. These values are of the same order of magnitude as the fluorescence lifetime of OH radical in the $A^2\Sigma^+$ state, which is about 1 μs.[9]

Concerning electronic quenching, three models[10-12] have been proposed to date. All models were based on only physical quenching processes. In an early model[10] the quenching cross section was correlated briefly to the dipole polarizability and the reduced mass. In two other models,[11,12] collision-induced radiationless transitions were assumed to be caused by the mixing of the initial and final states of the system, which is due to a long-range dispersion force. However, application of these models to the electronic quenching of RO* gave unsatisfactory results. For example, the plots of σ vs. $\mu^{1/2}\alpha$ for CH_3O^* based on an early model[10] are shown in Figure 7. As seen in the figure, quenching cross sections with 13 gases are classified in two groups, viz., rare gases and N_2, and other eight molecules. This result would suggest that CH_3O^* is quenched by chemical reactions as well as by physical processes for eight molecules.

References and Notes

(1) Present address: The National Institute for Environmental Studies, P.O. Yatabe, Ibaraki 300-21, Japan.
(2) (a) P. H. Leighton, "Photochemistry of Air Pollution", Academic Press, New York, N.Y., 1961; (b) K. L. Demerjian, J. A. Kerr, and J. G. Calvert, *Adv. Environ. Sci. Technol.*, **4**, 1 (1974).
(3) (a) G. R. McMillan, J. Kumari, and D. L. Snyder, "Chemical Reactions in Urban Atmospheres", American Elsevier, New York, N.Y., 1971, p 35; (b) H. A. Wiebe and J. Heicklen, *J. Am. Chem. Soc.*, **95**, 1 (1973); (c) H. A. Wiebe, A. Villa, T. M. Heilman, and J. Heicklen, *ibid.*, **95**, 7 (1973).
(4) W. D. McGrath and J. J. McGarvey, *Nature (London)*, **201**, 991 (1964).
(5) (a) A. B. Callear and P. M. Wood, *Trans. Faraday Soc.*, **67**, 3399 (1971); (b) J. F. Ogilvie, *Nature (London)*, **208**, 1315 (1965).
(6) D. W. G. Style and J. C. Ward, *Trans. Faraday Soc.*, **49**, 999 (1953).
(7) D. R. Yarkony, H. F. Schaefer, III, and S. Rotherberg, *J. Am. Chem. Soc.*, **96**, 656 (1974).
(8) L. Batt, K. Christie, R. T. Milne, and A. J. Summers, *Int. J. Chem. Kinet.*, **6**, 877 (1974).
(9) K. H. Becker and D. Haaks, *Z. Naturforsch. A*, **28**, 249 (1973).
(10) F. Rössler, *Z. Phys.*, **96**, 251 (1935).
(11) J. E. Selwyn and J. I. Steinfeld, *Chem. Phys. Lett.*, **4**, 217 (1969).
(12) C. A. Thayer and J. T. Yardley, *J. Chem. Phys.*, **57**, 3992 (1972).

Pulse Radiolysis of the Cyanate Anion in Aqueous Solution

J. G. Leopold and M. Faraggi*

Atomic Energy Commission, Nuclear Research Centre-Negev, P.O.B. 9001, Beer Sheva, Israel *(Received August 5, 1976)*

The reaction of OH radicals with NCO^- (X^-) has been investigated by the pusle radiolysis technique. Irradiation of cyanate anion solutes produced a transient species absorbing at λ_{max} 330 nm (ϵ 1000 M^{-1} cm^{-1}). The spectrum has been assigned to a complex form of the cyanate radical which arises from a reaction of OH with the solute. The second-order rate constant was established via competition with alcohols and was found to be $OH + NCO^- (H^+) \rightarrow HNCOOH$ (1), $k = 5.9 \pm 0.7 \times 10^7$ M^{-1} s^{-1}. The $HNCO_2^-$ radical (XOH^-) complexes with a solute anion according to $HNCO_2H + NCO^- \leftrightarrows (NCO)_2^- + H_2O$ (5), $K = 100 \pm 20$ M^{-1} with $k_5 = 4.5 \times 10^6$ M^{-1} s^{-1} and $k_{-5} = 4.4 \times 10^4$ s^{-1}. The decay of $(NCO)_2^-$ is of second order and depends on solute concentration. A radical–radical recombination set of reactions is proposed.

Introduction

Pulse radiolysis and flash photolysis oxidation of halides and some pseudohalides (X^-) produce transients absorbing in the 330–500-nm region. The mechanism of the oxidation reaction has been interpreted by the production of the corresponding radical anion (X_2^-).

The simple mechanism adopted assumed the formation of the radical (X) by an electron transfer reaction from the halide anion.[1-5] In pulse radiolysis, OH radicals are generated and the electron transfer reaction is

$$X^- + OH \rightarrow X + OH^- \quad (1)$$

Similarly, in flash photochemistry of some halide and pseudohalide anions an appropriate photon will cause the emission of an electron from an excited state:

$$X^- \xrightarrow{h\nu} X^{-*} \rightarrow X + e_{aq}^- \quad (1a)$$

These reactions, producing by different pathways the same transient, are followed by the reaction:

$$X + X^- \leftrightarrows X_2^- \quad (2)$$

forming the radical anion (X_2^-).

Matheson et al.[6] studied the reaction of Br^- with OH radicals and suggested replacing reaction 1 by the sequence of reactions:

$$X^- + OH \leftrightarrows XOH^- \quad (3)$$

$$XOH^- \leftrightarrows X + OH^- \quad (4)$$

Recently, Zehavi and Rabani[7,8] and Behar, Bevan, and Scholes,[9,10] studying the oxidation of Br^- and NCS^-, concluded that the formation of the radical ion could be a result of an additional reaction:

$$XOH^- + X^- \leftrightarrows X_2^- + OH^- \quad (5)$$

Thus, the mechanism of X_2^- formation could be described by reactions 2–5. Very recently Behar and Fessenden[14] studied the cyanate system by the radiolysis–ESR method and came to the conclusion that the transient is a proton containing radical ($HNCO_2^-$ or HNCOOH) produced via reaction 3.

The absorbing transient species was suggested to be X_2^-; however, it should be mentioned that other intermediates (XOH^-) could absorb in the same wavelength region.[10,13]

In view of the above knowledge on the oxidation of halide and pseudohalide anions, we investigated the cyanate system (NCO^-) by pulse radiolysis. Unfortunately, due to the chemical properties of this anion, alkaline solutions (pH >9) could not be studied.

Experimental Section

The pulse radiolysis apparatus, the experimental methods involved, and the analysis of the results have been described elsewhere.[15] Electron pulses of 0.2–1.0 μs (OH radical concentration from 1.4 to 9.4 $\times 10^{-6}$ M) were used. Dosimetry was carried out using N_2O saturated 10^{-2} M $Fe(CN)_6^{4-}$ solutions assuming $G(Fe(CN)_6^{3-}) = 6.1$.[16] For calculation of the extinction coefficient of the transients, $G(OH) = 2.7$ for argon saturated solutions and $G(OH) = 5.6$ for N_2O saturated solutions were assumed over all the concentration ranges used.[4]

The rate constants measured from the oscilloscope traces are defined as $k_{obsd} = 1/[X^-]\, d \ln (D_{max} - D_t)/dt$. It is the observed second-order rate constant of formation when direct measurements of the absorbing species were investigated (D_{max} is the maximum optical density of the transient absorbing species; D_t is the measured optical density at time t).

Potassium cyanate (KNCO, Fluka purum) was recrystallized at least three times from a water–methanol mixture.[17] The purity of this compound was checked spectroscopically (λ_{max} 195 nm; ϵ_{max} 1.1 $\times 10^3$ M^{-1} cm^{-1}). All other materials were of analytical grade.

Solutions were made up in triply distilled water deaerated by ultrapure gases (i.e., argon or N_2O).

Dilute analytical grade acid ($HClO_4$) or base (NaOH) was added to adjust the pH. Usually neutral solutions (pH 5.0 ± 0.4) were studied.

Results and Discussion

When fast electrons are absorbed in water the effect may be described by the overall reaction

$$H_2O \rightsquigarrow e_{aq}^-, H, OH, H_2, H_2O_2, H_3O^+ \quad (6)$$

and the ensuing chemistry occurring in aqueous solutions can be accounted for in terms of these initial entities; the yields of the products G (G = number of species per 100 eV) were as follows: $G_{e_{aq}^-} = 2.7$, $G_H = 0.55$, $G_{OH} = 2.7$, $G_{H_2} = 0.45$, $G_{H_2O_2} = 0.7$.

When N_2O saturated NCO^- neutral solutions are irradiated by a single pulse, a transient species is formed with an absorption maximum at 330 nm (Figure 1). When oxygenated solutions were used, the absorption at 330 nm was exactly one half of that observed in the N_2O saturated solutions. Addition of alcohols suppressed the absorption at 330 nm.

* Present address: Chemistry Department, Ohio State University, Columbus, Ohio 43210.

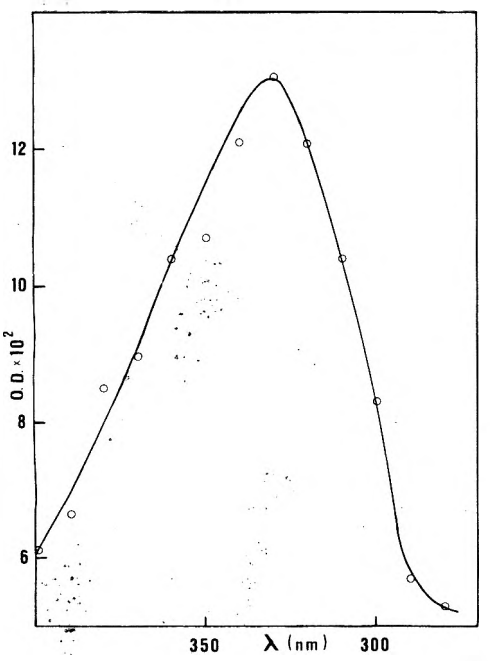

Figure 1. Absorption spectrum of transient obtained from the reaction of OH radicals with NCO^-. N_2O saturated solution of $[NCO^-] = 10^{-1}$ M, $[OH] = 9.7 \times 10^{-6}$ M at pH 5.0 ± 0.2.

These results seem to indicate that OH radicals formed during the radiolysis of water react with NCO^- to produce the transient absorbing species.

In N_2O saturated solutions where all e_{aq}^- are converted to OH

$$N_2O + e_{aq}^- \rightarrow N_2 + OH + OH^- \quad (7)$$

thus $G(OH) = G_{e_{aq}^-} + G_{OH} = 2G_{OH}$ in oxygen saturated solution

$$e_{aq}^- + O_2 \rightarrow O_2^- \quad (8)$$

and $G(OH) = G_{OH}$ in alcohol solutions, suppression of the transient is due to

$$RCH_2OH + OH \rightarrow RCHOH + H_2O \quad (9)$$

The reaction between NCO^- and OH could be the electron transfer–addition reactions similar to those observed in other halide and pseudohalide systems or, even though unlikely on thermodynamic grounds, an oxygen abstraction reaction resulting in the production of H_2O_2, followed by

$$NCO^- + OH \rightarrow CN^- + HO_2 \quad (10)$$

$$HO_2 + HO_2 \rightarrow H_2O_2 + O_2 \quad (11)$$

or

$$NCO^- + OH + H^+ \rightarrow CN + H_2O_2 \quad (12)$$

This last possibility was nevertheless investigated. As expected no increase in $G_{H_2O_2}$ (0.75) was found (both in γ and pulse radiolysis). This eliminated the possibility of an abstraction reaction.

The formation rate constant of the transient and its absorbance was found to depend on the cyanate concentration (Figure 2). Since this rate constant was found to be equal to $5.9 \pm 0.7 \times 10^7$ M^{-1} s^{-1} (vide infra), it is readily shown that for the concentration range used ($8 \times 10^{-2} \geq [NCO^-] \geq 5 \times 10^3$ M and $9.7 \times 10^{-6} \geq [OH] \geq 2.9 \times 10^{-6}$M) the interference of the OH recombination reaction

$$OH + OH \rightarrow H_2O_2 \quad (k_{13} = 1 \times 10^{10}\ M^{-1}\ s^{-1})^{17} \quad (13)$$

is negligible.

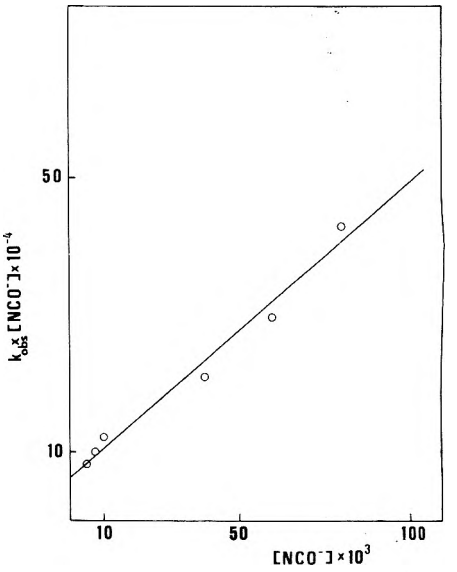

Figure 2. The variation of the pseudo-first-order formation rate constant ($k_{obsd}[NCO^-]$) with NCO^- concentration at pH 5.1 ± 0.2. Each rate constant in the curve is a mean value calculated from values obtained at various doses (OH radical concentration of 2.9, 3.9, 5.7, 8.5, and 9.7×10^{-6} M). The deviation in these rate constant was ±10% or better.

At lower concentrations of NCO^- the recombination reaction should be taken into account.

The possibility of the formation of the NCO radical from the $HNCO_2^-$ radical ion (the OH adduct intermediate, reaction 3) or its protonated form HNCOOH, which differs from an activated complex by its lifetime and its ability to react with solutes, was investigated by the alcohol competition method as suggested by Zehavi and Rabani.[7,8] They showed that if XOH^- is an intermediate reacting with X^- to form X_2^- via reaction 5, and equilibrium 2 is shifted to the X_2^- side, the competition with alcohol on the OH radicals will effect the X_2^- concentration as follows

$$\frac{D^0_{max}}{D_{max}} = 1 + \frac{k_9}{k_3}\frac{[RCH_2OH]}{[X^-]}\left(1 + \frac{k_{-3}}{k_4 + k_5[X^-]}\right) \quad (I)$$

where D^0_{max} and D_{max} are the absorption of X_2^- in the absence of alcohol and in the presence of alcohol RCH_2OH, respectively. From eq I it seems that D^0_{max}/D_{max} is a function of the relative concentration of alcohol to X^- and of the absolute concentration of X^-. The results of the alcohol competition reaction are shown in Figure 3. Regardless of the alcohol used (methanol ($k_9 = 8.6 \times 10^8$ M^{-1} s^{-1}), 2-methyl-2-propanol ($k_9 = 5.2 \times 10^8$ M^{-1} s^{-1})[18]) the absolute concentration of X^- had no effect on the optical density ratio.

From Figure 3 the rate constant of the reaction between OH radicals and cyanate was evaluated to be $5.9 \pm 0.7 \times 10^7$ M^{-1} s^{-1}. These results seem to indicate that only one transient is formed during the oxidation reaction of the cyanate anion. In view of Behar and Fessenden[14] finding that the transient is a proton containing radical ($HNCOO^-$ or HNCOOH) the reaction proposed is

$$NCO^- + OH \rightarrow HNCOO^- \overset{H^+}{\rightleftharpoons} HNCOOH \quad (3)$$

However the fact that the experimentally observed second rate constant of reaction 3 k_{obsd} decreases with the cyanate concentration (Table I) has to be explained. Baxendale et al.[4] developed a solution for the halide system where the oxidation reaction is followed by an equilibrium reaction of the solute with the formed solute radical i.e.

$$HNCOO^- + NCO^- \rightleftarrows (NCO)_2^- + OH^- \quad (5)$$

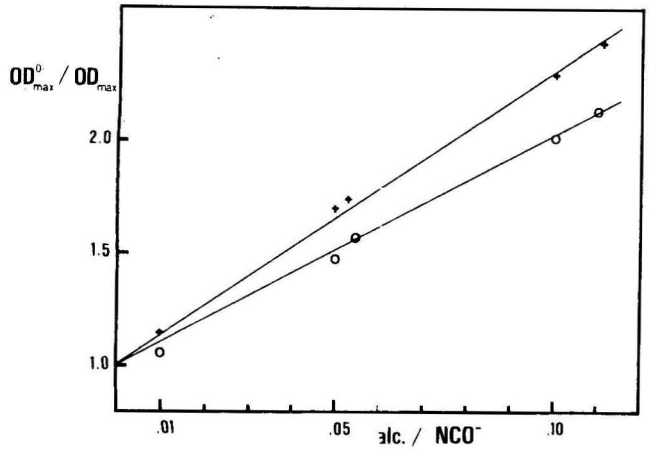

Figure 3. Competition for the OH radical by NCO^- and alcohols plotted according to eq I. The upper and lower lines are for methanol and 2-methyl-2-propanol, respectively. Each point in the graphs is a mean of several determinations at different NCO^- concentrations at a constant ratio of [alcohol]/[NCO^-]. N_2O saturated solutions of 10^{-3} M ≤ [NCO^-] ≤ 10^{-1} M. [alcohol] = 0 to 10^{-2} M and [OH] = 9.7×10^{-6} M at pH 5.0 ± 0.4.

or

$$HNCOOH + NCO^- \rightleftharpoons (NCO)_2^- + H_2O \qquad (5')$$

$$([X_2^-]_\infty - [X_2^-]_t)/[X_2^-]_0 = \{k_5'[(k_5' + k_{-5}') \exp(-k_3't) - k_3' \exp(-(k_5' + k_{-5}')t)]\}/[(k_5' + k_{-5}')(k_5' + k_{-5}' - k_3')] \qquad (II)$$

where $k_5' = k_5[X^-]$, $k_3' = k_3[X^-]$, $[X_2^-]_\infty$ and $[X_2^-]$ are the concentration of $(NCO)_2^-$ at infinity (i.e., the concentration attained at equilibrium) and time t correspondingly; $[X_2^-]_0$ is the concentration of $(NCO)_2^-$ which could be obtained if all the OH present yielded $(NCO)_2^-$. This equation holds on the condition when the initial concentration of OH radicals produced by the electron pulse is small compared to the NCO^- concentration, i.e., the kinetics of $(NCO)_2^-$ formation reactions will be first order.

If $k_5[NCO^-] + k_{-5}' > k_3[NCO^-]$, the rate of the overall reaction will be determined by $k_3[NCO^-]$, and k_{obsd} will not be a function of NCO^- concentration. However, if $k_3[NCO^-] > k_5[NCO^-] + k_{-5}'$, then the rate at high concentration of NCO^- will be determined by $k_5[NCO^-] + k_{-5}'$. Under these conditions the above equation will be

$$([(NCO)_2^-]_\infty - [(NCO)_2^-]_t)/[(NCO)_2^-]_0 = [k_5[NCO^-] \exp(-(k_5[NCO^-] + k_{-5}')t)]/(k_5[NCO^-] + k_{-5}') \qquad (III)$$

or

$$\ln \frac{\Delta(OD)}{(OD)_0} = \ln \frac{k_5[NCO^-]}{k_5[NCO^-] + k_{-5}'} - (k_5[NCO^-] + k_{-5}')t \qquad (IV)$$

Plotting log Δ(OD) vs. the time will give $k_5[NCO^-] + k_{-5}'$ as the slope of the linear curve. This slope is in fact the observed slope determined experimentally from the oscilloscope traces.

$$k_{obsd}[NCO^-] = k_5[NCO^-] + k_{-5}' = d(\ln D_{max} - D_t)/dt \qquad (V)$$

Figure 2 shows the curve obtained for $k_{obsd}[NCO^-]$ as function of [NCO^-]. This line gives $k_5 = 4.5 \times 10^6$ M^{-1} s^{-1}, $k_{-5}' = 4.4 \times 10^4$ s^{-1}, and $k_5 = k_5/k_{-5}' = 100$ M^{-1}. Hence the rate constant measure at low concentration of NCO^- (<1 × 10^{-3}), where $k_2[NCO^-] \simeq k_5[NCO^-] + k_{-5}'$ should represent the value of a mixed rate constant. This is the reason why its value is lower than that observed in the competition reaction. It was impossible to follow the rate at lower concentrations of NCO^- (<1 × 10^{-4} M), where $k_3[NCO^-] < k_5[NCO^-] + k_{-5}'$ and thus determine k_3 directly, because of very low absorbance changes.

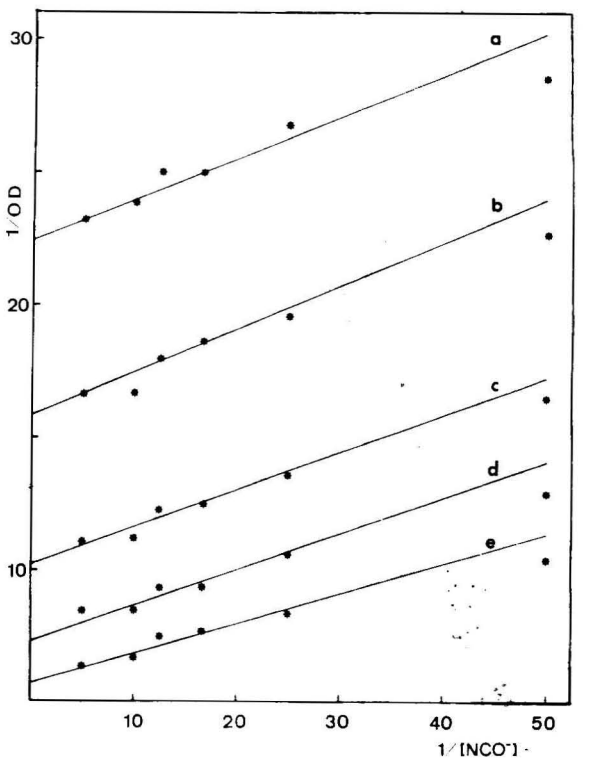

Figure 4. Effect of concentration of NCO^- on the absorption of the transient (λ 330 mm) at various doses (the OH radical concentration was as follows: (a) 2.9 × 10^{-6}; (b) 3.9 × 10^{-6}; (c) 5.7 × 10^{-6}; (d) 8.5 × 10^{-6}; (e) 9.7 × 10^{-6}M) at pH 5.1 ± 0.2.

The pseudo-first-order value of k_{-5}' suggests that the protonated HNCOOH species is formed and that reaction 3 is followed by reaction 5′ rather than reaction 5. In fact, reaction 5 cannot account for a rate constant of 4.4×10^4 s^{-1} even if we assume that k_{-5} is 10^{10} M^{-1} s^{-1} (diffusion controlled). At the pH studied the OH^- concentration is of the order of 10^{-9} M; this will give a pseudo-first-order rate constant for k_{-5}' of the order of 10 s^{-1}.

An alternative reaction from the disappearance of the HNCOOH radical (reaction 5) is

$$HNCOOH + NCO^- \rightleftarrows HOOCNH\text{-}NCO^- \qquad (5'')$$

which predicts that the radical and the radical ions formed during the reaction of OH radicals with CNO^- are protonated (HNCOOH and $HNCOO^-$ and $HOOCNH\text{–}NCO^-$ respectively). Assuming that only the two radical ions exist in our solutions seems more compatible with Behar and Fessenden results.[14] However, at the concentration range used in this study (5×10^{-3} to 8×10^{-2} M) and that of Behar and Fessenden[14] (10^{-2} M) and an equilibrium constant of 100 M^{-1} for either reaction 5′ or 5″ still leaves a nonnegligible concentration of radicals in the form of HNCOOH. (At 10^{-2} M NCO^- the concentrations of HNCOOH and $HOOCNH\text{–}NCO^-$ are equal.)

The equilibrium constant of reaction 5 could be determined from the equation

$$\frac{(OD)_0}{OD} = 1 + \frac{1}{K_5[NCO^-]} \qquad (VI)$$

where $(OD)_0$ is the optical density in a solution containing only $(NCO)_2^-$ (high concentration of NCO^-). Plots of this

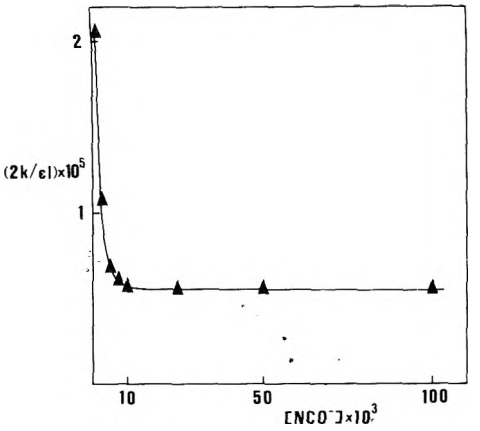

Figure 5. Dependence of the decay rate constant on the concentration of NCO^-: [OH] = 9.7×10^{-6} M, pH 5.1 ± 0.2.

equation are shown in Figure 4 for different doses. The value obtained for k_5 is 120 ± 20 M^{-1}. Extrapolated values of $(OD)_0$ also allow determination of the absorption coefficient of $(NCO)_2^-$ (1000 ± 100 M^{-1} cm^{-1}). This determination assumed that in the range of concentration of NCO^- studied the yield of the OH radical (G(OH)) was constant.

The decay of the transient was studied in the concentration range 10^{-3} to 10^{-1} M of NCO^- and at 2.9 to 5.7 × 10^{-6} M of OH radicals. The decay rate was found to vary with the dose of NCO^- concentration. In all experiments the decay plot was clearly second order. Assuming the following reaction scheme:

$$(NCO)_2^- + (NCO)_2^- \rightarrow P_1 \quad (14)$$

$$(NCO)_2^- + HNCOOH \rightarrow P_2 \quad (15)$$

$$HNCOOH + HNCOOH \rightarrow P_3 \quad (16)$$

the rate of the $(NCO)_2^-$ decay is

$$-d[(NCO)_2^-]/dt = (2\{k_{14} + k_{15}/(K_5[NCO^-]) + k_{16}/(K_5^2[NCO^-]^2)\}[(NCO)_2^-]^2)/(1 + 1/(K_5[NCO^-])) \quad (VII)$$

Hence for a given NCO^- concentration

$$-d[(NCO)_2^-]/dt = k_d[(NCO)_2^-]^2$$

where k_d is the observed decay rate given by

$$k_d = [2\{k_{14} + k_{15}/(K_5[NCO^-]) + k_{16}/(K_5^2[NCO^-]^2)\}]/[1 + 1/(K_5[NCO^-])] \quad (VIII)$$

For each concentration of NCO^- and dose the second-order decay rate was calculated. The rate is expressed by a $2k/el$ value which is the slope of the 1/OD vs. time line.[19] The second-order decay rate dependence on NCO^- concentration is shown in Figure 5.

Conclusion

This study shows that when OH radical reacts with NCO^- it forms a radical suggested to be an adduct radical. Following this reaction the adduct radical enters into a radical–solute equilibrium. The adduct radical and the radical–solute species absorb at 330 nm and decay via a second-order reaction mechanism.

Acknowledgment. The authors thank Mrs. A. Saraf for her technical help and Mr. Y. Ogdan for the maintenance of the Lineac system.

References and Notes

(1) L. I. Grossweinger and M. S. Matheson, *J. Phys. Chem.*, **61**, 1089 (1957).
(2) L. M. Dorfman, I. A. Taub, and R. E. Buhler, *J. Chem. Phys.*, **36**, 3051 (1962).
(3) G. E. Adams, J. W. Boag, and B. D. Michael, *Proc. Chem. Soc.*, 114 (1964).
(4) J. H. Baxendale, P. L. T. Bevan, and D. H. Stot, *Trans. Faraday Soc.*, **64**, 2389 (1968).
(5) Y. Tendler and M. Faraggi, *J. Chem. Phys.*, **58**, 848 (1973).
(6) M. S. Matheson, W. A. Mulac, J. L. Weeks, and T. Rabani, *J. Phys. Chem.*, **70**, 2092 (1966).
(7) D. Zehavi and J. Rabani, *J. Phys. Chem.*, **75**, 1738 (1971).
(8) D. Zehavi and J. Rabani, *J. Phys. Chem.*, **76**, 312 (1972).
(9) D. Behar, P. L. T. Bevan, and G. Scholes, *Chem. Commun.*, **22**, 1486 (1971).
(10) D. Behar, P. L. T. Bevan, and G. Scholes, *J. Phys. Chem.*, **76**, 1537 (1972).
(11) M. Schoneshofer and A. Henglein, *Ber. Bunsenges. Phys. Chem.*, **73**, 289 (1969).
(12) M. Schoneshofer, *Int. J. Radiat. Phys. Chem.*, **1**, 505 (1969).
(13) M. Schoneshofer and A. Henglein, *Ber. Bunsenges. Phys. Chem.*, **74**, 303 (1970).
(14) D. Behar and W. Fessenden, *J. Phys. Chem.*, **76**, 1074 (1974).
(15) M. Faraggi and Y. Tendler, *J. Chem. Phys.*, **56**, 3287 (1972).
(16) D. Zehavi, Ph.D. Thesis, The Hebrew University, Jerusalem, Israel, 1972.
(17) J. Leopold, D. Shapira, and A. Treinin, *J. Phys. Chem.*, **74**, 4585 (1970).
(18) L. M. Dorfman and G. E. Adams, *Natl. Stand. Ref. Data Ser., Natl. Bur. Stand.*, **No. 46** (1973).
(19) M. S. Matheson and L. M. Dorfman, "Pulse Radiolysis", The M.I.T. Press, Cambridge, Mass., 1969, p 53.

COMMUNICATIONS TO THE EDITOR

Alternative to Tunneling in Proton-Transfer Reactions Exhibiting High Isotope Effects

Publication costs assisted by Department of Chemistry, Tel-Aviv University

Sir: High kinetic isotope effects in proton transfer reactions have been reported by Lewis[1,2] and Caldin[3,4] and summarized by Bell.[5] The conclusions reached after a careful and extensive study by Caldin[4] along with discussion of this and other work by workers in the field of proton transfer[6] focused on proton tunneling as the explanation for the results.

All but one of the cases in which a high isotope effect is found involve a nitroalkane derivative as the proton donor, and hindered bases in medium or low polarity solvents. Another aspect of the behavior of nitroalkanes in proton transfer reactions is that anomalous Bronsted coefficients (α) (>1, <0) are found. Bordwell[7,8] introduced another intermediate, a pyramidal (i.e., nonplanar) nitroalkane anion, to account for such behavior (eq 1).

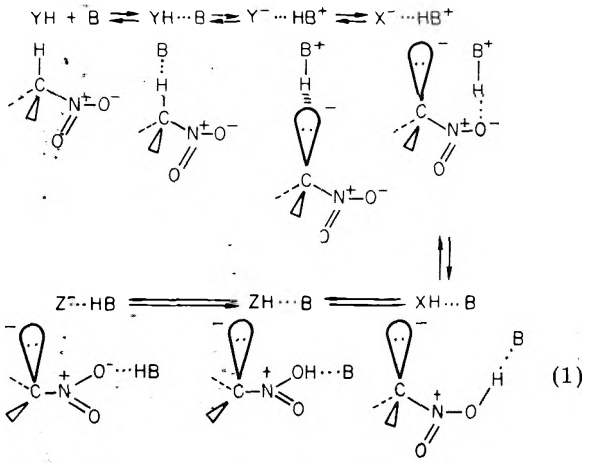

(1)

The purpose of this note is to point out that there may be another pair of intermediates along the reaction pathway. These intermediates, the isomeric nitronic acids, can easily explain the high kinetic isotope effects (see below) and are equivalent to Bordwell's intermediate insofar as the Bronsted α is concerned. The mechanism of formation of the nitronic acid involves internal return within an ion pair, a pathway discovered by Young, Winstein, and Goering for α,α-dimethylallyl chloride.[9] The pathway is outlined in eq 1.

Different responses to substitution for the nitroalkanes and the related "*aci*-nitro compounds" (i.e., the nitronic acids) have been pointed out by Ingold[10] using the data of Turnbull and Maron.[11] An isomeric protonated form is also possible for a nitrile (the one non-nitroalkane on Bell's list), as indicated by the work of Kosower and Dodiuk, who actually reported substantial isotope effects for processes involving such protonated species.[12] (eq 2).

$$RRCHCN \rightleftarrows RRC^{-}\text{-}C{\equiv}N \rightleftarrows RRC{=}C{=}NH \qquad (2)$$

An explicit expression for the rate constant may be based on the minimal eq 3 as shown in eq 4. The first

$$YH\cdots B \underset{k_{-YH}}{\overset{k_{YH}}{\rightleftharpoons}} Y^{-}\cdots HB^{+} \underset{k_{-Y^-}}{\overset{k_{Y^-}}{\rightleftharpoons}} ZH\cdots B \xrightarrow{k_{ZH}} Z^{-}\cdots HB^{+} \qquad (3)$$

$$k = \frac{k_{ZH}}{k_{ZH}+k_{-Y^-}}\cdot\frac{k_{Y^-}}{k_{Y^-}+k_{-YH}}k_{YH} = A_{ZH}B_{Y^-}k_{YH} \qquad (4)$$

factor, A_{ZH}, can be estimated from the dissociation constants ($pK_a \sim 4.0$) for nitronic acids.[10] We can safely assume that the rate constant for the combination of nitronate ion and proton (or protonated solvent) is close to diffusion controlled, and unlikely to be very different for the corresponding reaction with the deuteron. On the other hand, the equilibrium constants for deuterated acids are lower than those for protonated acids in which the proton is attached to oxygen. Bell[13] cites values of 2.5–4.5, and the value for K_W^H/K_W^D for H_2O and D_2O is 7.47. Thus the rate constant for the reaction of water with the nitronic acids must be about 10^5 dm^3 mol^{-1} s^{-1}. It is difficult to make accurate estimates of this rate constant for the nonpolar solvents utilized in the studies which revealed abnormal isotope effects, but the constant would no doubt be lower than that in water. We may conclude that the dissociation of nitronic acids to nitronate ions has a rate constant comparable to that of the overall process as cited by Caldin[4] (10^3–10^4 dm^3 mol^{-1} s^{-1} in nonpolar solvents). Since an isotope effect may be expected for this step, the isotope effect on the overall process can be as much as the product of the two isotope effects, i.e., 15–45. The factor A_{ZH} should be 10^3 or less. The factor B_{Y^-} is probably about 0.5. We have not tried to analyze these processes in detail (experiment would be much more useful in this connection).

Our discussion does not preclude some contribution from proton tunneling to anomalous isotope effects, but does suggest that further consideration be given to the identification of the elementary steps involved in the removal of a proton from nitroalkanes and related compounds.

Acknowledgment. Helpful correspondence with Professors F. G. Bordwell and E. F. Caldin is appreciated.

References and Notes

(1) E. S. Lewis and L. Funderburk, *J. Am. Chem. Soc.*, **86**, 2531 (1964); **89**, 2322 (1967).
(2) E. S. Lewis and J. K. Robinson, *J. Am. Chem. Soc.*, **90**, 4337 (1968).
(3) E. F. Caldin and S. Mateo, *J. Chem. Soc., Faraday Trans. 1*, **71**, 1876 (1975); **72**, 112 (1976).
(4) E. F. Caldin and C. J. Wilson, *Discuss. Faraday Soc.*, **No. 10**, 121 (1975).
(5) R. P. Bell, *Chem. Soc. Rev.*, **3**, 513 (1974).
(6) R. P. Bell and others, *Discuss. Faraday Soc.*, **No. 10** (1975).
(7) F. G. Bordwell and W. J. Boyle, *J. Am. Chem. Soc.*, **97**, 3447 (1975).
(8) F. G. Bordwell, *Discuss. Faraday Soc.*, **No. 10**, 100 (1975).
(9) W. G. Young, S. Winstein, and H. L. Goering, *J. Am. Chem. Soc.*, **73**, 1958 (1951).
(10) C. K. Ingold, "Structure and Mechanism in Organic Chemistry", 1st ed, Cornell University Press, Ithaca, N.Y., 1953, pp 560–561.

(11) D. Turnbull and S. H. Maron, *J. Am. Chem. Soc.*, **65**, 212 (1943).
(12) E. M. Kosower and H. Dodiuk, *J. Am. Chem. Soc.*, **98**, 924 (1976).
(13) R. P. Bell, "The Proton in Chemistry", 2nd ed, Chapman and Hall, London, 1973, pp 233–234.

Department of Chemistry **Edward M. Kosower**
Tel-Aviv University
Ramat Aviv, Tel Aviv, Israel and
Department of Chemistry
State University of New York
Stony Brook, New York 11794

Received October 18, 1976

Oriented Adsorption of HD on ZnO and Catalytic Addition of HD to Butadiene on It

Sir: Kokes, Dent, Chang, and Dixon[1] found a remarkable orientation in the adsorption of the HD molecule on ZnO; the orientation in

I

prevails at room temperature but in

II

at the lower temperatures. In the previous paper,[2] it was found that the reaction of butadiene with HD on a MoS_2 catalyst brings about an oriented addition giving 1.5 times more 1-butene-3-d_1 than 1-butene-4-d_1. This oriented addition of the HD molecule was well explained by the isotope effect for half-hydrogenated intermediates formation. It should be quite interesting whether such prominent orientation in the HD adsorption on ZnO, being dependent on adsorption temperature, will reflect on the orientation of the HD addition reaction.

The reaction of butadiene with HD and/or with an equilibrated mixture of H_2, HD, and D_2 was performed on ZnO catalyst (Kadox-25 from New Jersey Zinc Co.) at the two temperatures: room temperature and −40 °C. The catalyst was evacuated at 450 °C for about 4 h and cooled in vacuo immediately before the experiments. The results are summarized in Table I. The hydrogen molecular identity is highly maintained in the addition reaction as has been reported by several investigators. The apparent isotope effect for the reaction with H_2 and D_2 was undoubtedly very small, however, the addition of HD molecule represents a remarkable orientation giving 75% 1-butene-3-d_1 and 25% 1-butene-4-d_1 at room temperature. The most surprising result is that the orientation of the HD addition to butadiene is not influenced by reaction temperatures, although the adsorption of HD on ZnO prefers configuration I at room temperature by 75% and configuration II at −40 °C by 75–80%.[1]

One unsettled problem in the hydrogenation of unsaturated hydrocarbons on ZnO catalyst is the addition process of the hydrogen to the double bond of hydrocarbons. So far two mechanisms have been proposed: (1) H_2 is dissociatively adsorbed on ZnO and followed by an addition reaction, and (2) H_2 reacts directly with the double bond adsorbed on ZnO, where no dissociation of hydrogen is required. The former mechanism was proposed by Kokes and co-workers,[1,4] and they concluded that only reversible adsorption of hydrogen named *type 1 adsorption* would participate in the hydrogenation reaction. The type 1 adsorption saturates at pressures higher than about 30–40 Torr at room temperature, whereas the kinetics in hydrogen pressures are half-order for the hydrogenation of ethylene and first-order for the hydrogenation of butadiene in wider range of hydrogen pressure. Such a discrepancy has been pointed out by adsorption measurements of hydrogen during the hydrogenation of ethylene[6] and of butadiene,[3] that is, that the adsorption of hydrogen may be a type 1 adsorption during the hydrogenation reactions, does not correlate with the reaction rates. Tamaru and co-workers[3] proposed a second mechanism, direct attack of the hydrogen molecule on the double bond adsorbed on ZnO to account for the discrepancy between kinetics and adsorption of hydrogen and for the maintenance of hydrogen molecular identity in the hydrogenated product. The direct addition of the hydrogen molecule to the double bond, however, might not be feasible in accordance with the orbital symmetry rule.[5]

The results obtained in this paper, the temperature independent remarkable orientation in the HD addition with little isotope effect for H_2 and D_2 addition, may rule out the direct addition of the hydrogen molecule, and oblige us to rectify the stepwise addition infered by Kokes et al. In conformity with rather facile σ–π interconversion during the isomerization of 1-butene on ZnO,[3,7] the isoelectronic intermediates for 1-butene formation and *cis*-2-butene formation from the hydrogenation of butadiene should be quite interesting The reaction of butadiene with D_2 and ZnO gives 1-butene-d_2 in more than 90% yield accompanying several percent of *cis*-2-butene-d_2. The NMR spectrum of the *cis*-2-butene-d_2 formed as a minor product showed that the intensity ratio of methyl hydrogens to olefinic hydrogens was 2.04, which indicated the strict 1,4 addition of a deuterium molecule to butadiene forming *cis*-2-butene. These findings clearly indicate that the 1,2 addition giving 1-butene and the 1,4 addition giving 2-butene take place independently on the ZnO catalyst via different intermediates.

In conformity with the kinetic facility of HD adsorption on ZnO to take the orientation of configuration II, independent 1,2 and 1,4 addition of hydrogen to butadiene may be described as shown in Scheme I. Recently, Hattori et al.[8] found 1,4 addition of hydrogen to butadiene on a MgO catalyst evacuated at temperatures as high as 1100 °C. The active sites for *cis*-2-butene formation on ZnO may have similar characteristics as that on MgO, on which a π-allyl anion intermediate formation is prominent. In

TABLE I: Hydrogenation of Butadiene on ZnO

Run	Temp, °C	Conv, %	Hydrogen used			Products: 1-Butene			cis-2-Butene[a]			Hydrogen		
			H_2	HD	D_2	d_0	d_1	d_2	d_0	d_1	d_2	H_2	HD	D_2
101	RT	5.7	25.0	52.3	22.7	23.2	55.4[b]	21.4	30.8	50.6	18.5	24.7	51.7	23.6
102	RT	13.0	1.7	97.4	0.9	6.6	91.0[c]	2.3	13.1	83.3	3.6	4.2	92.9	2.9
112	−40	5.6	1.7	97.7	0.6	3.5	95.4[d]	1.0				2.1	97.1	0.8

[a] The amount of *cis*-2-butene in the products was 10% in run 101 and 9.1% in run 102. [b] 72.8% 1-butene-3-d_1, 27.2% 1-butene-4-d_1. [c] 75.4% 1-butene-3-d_1, 24.6% 1-butene-4-d_1. [d] 75.2% 1-butene-3-d_1, 24.8% 1-butene-4-d_1.

Scheme I

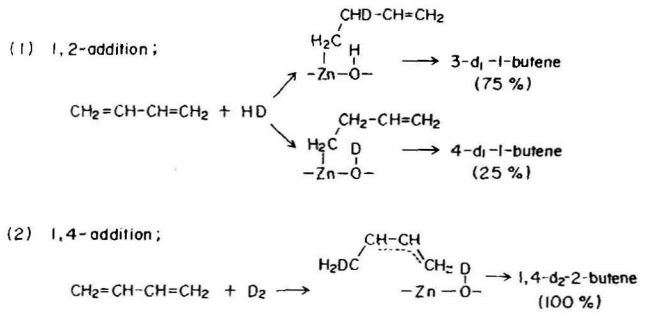

the 1,2 addition in Scheme I, the orientation forming 1-butene-3-d_1 might be kinetically facile as has been observed on ZnO adsorption. The apparent small isotope effect for H_2 and D_2 addition reaction may be attributable to lack of orientation of H_2 and D_2 molecules and to the compensation between the bonds forming and breaking at the transition state. If this is the mechanism, the pressure dependence will be first order in hydrogen pressure, and hydrogen molecular identity will be maintained.

References and Notes

(1) R. J. Kokes, A. L. Dent, C. C. Chang, and L. T. Dixon, *J. Am. Chem. Soc.*, **94**, 4429 (1972).
(2) T. Okuhara and K. Tanaka, *J. Chem. Soc., Chem. Commun.*, 199 (1976); T. Okuhara, T. Kondo, and K. Tanaka, *Chem. Lett.*, 717 (1976).
(3) S. Naito, Y. Sakurai, H. Shimizu, T. Ohishi, and K. Tamaru, *Bull. Chem. Soc. Jpn.*, **43**, 2274 (1970); *Trans. Faraday Soc.*, **67**, 1529 (1971).
(4) A. L. Dent and R. J. Kokes, *J. Phys. Chem.*, **73**, 3772 (1969); **74**, 3653 (1970).
(5) R. G. Pearson, *J. Am. Chem. Soc.*, **94**, 8287 (1972).
(6) K. Tanaka and G. Blyholder, *J. Phys. Chem.*, **76**, 1394 (1972).
(7) C. C. Chang, W. C. Conner, and R. J. Kokes, *J. Phys. Chem.*, **77**, 1957 (1973).
(8) H. Hattori, Y. Tanaka, and K. Tanabe, *J. Am. Chem. Soc.*, **98**, 4652 (1976).
(9) Sagami Chemical Research Center, Nishi-Ohnuma, Kanagawa, Japan.

Research Institute for Catalysis **Toshio Okuhara**
Hokkaido University **Toshihiko Kondo**[9]
Sapporo, Japan **Ken-ichi Tanaka***

Received November 15, 1976

On the Temperature Dependence of Multiple Charge-Transfer Bands in $\pi-\pi$ Electron Donor–Acceptor Complexes

Publication costs assisted by the National Research Council of Canada

Sir: The double charge-transfer (CT) absorption bands observed for complexes of tetracyanoethylene (TCNE) with substituted benzenes have been attributed to transitions from the highest and second highest occupied donor levels to the lowest empty acceptor level of TCNE[1-6] as was proposed originally by Orgel,[7] but have also been attributed to rotational isomers.[8] Resonance Raman excitation profiles of charge-transfer transitions of TCNE complexes recently obtained in this laboratory indicated that the two charge-transfer bands involve different excited electronic states and thus different complex geometries.[9] The present study was undertaken to obtain more direct evidence of the existence or not of distinct complex isomers associated with the double transitions. On the basis of the results obtained from a study of the temperature dependence of the relative intensities of the two bands for various TCNE complexes we conclude that two most stable

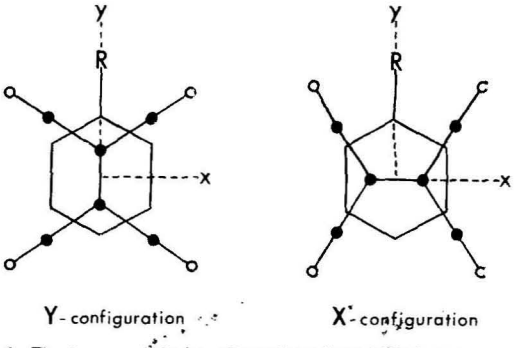

Figure 1. The two predicted configurations for a TCNE–monosubstituted benzene complex.

isomeric structures exist for each appropriate complex corresponding to maximum overlap for the highest and second highest donor orbital, respectively, with the same (lowest empty) acceptor orbital (Figure 1). This result has particular significance in determining the relative contributions for the various interactions involved in donor–acceptor complexation. Theoretical calculations by Lippert, Hanna, and Trotter[8] on the *p*-xylene–TCNE complex have predicted two stable rotational isomers corresponding to the X and Y configurations in Figure 1. These calculations, done for the complex in the gas phase, predict that the exchange repulsion interaction (contributing a 4 kcal mol^{-1} barrier between preferred conformations) is of primary importance in determining complex geometry. In contrast, CNDO/2 calculations have predicted only a single preferred conformation for the *p*-xylene–TCNE complex with the X and Y configurations corresponding to energy maxima.[10] The concept of multiple configurations has been used by Holder and Thompson[11] to rationalize the CT band intensities of increasingly sterically hindered alkylbenzenes with TCNE. They concluded that substitution of bulkier groups favored the X configuration of TCNE in the complex.

The EDA complexes were studied in inert polymer films of poly(methyl methacrylate) which allowed us to determine the temperature dependence of the CT bands over a wide range, 4–300 K. The data and results are summarized in Table I and Figure 2. For each complex, except *p*-xylene–TCNE, the ratio of the absorbance of the high-energy band maximum to the low-energy band maximum, A_X/A_Y, is reduced at the lower temperature. For benzene substitution by electron-donating groups, theory predicts the low-energy band to arise from the Y configuration and the high-energy band from the X configuration of the complex.[4] Thus, the Y configuration is energetically preferred for all the complexes investigated except *p*-xylene–TCNE for which the X configuration is preferred.

The relative populations, N_X/N_Y, of complex in two configurations with an energy difference, ΔE, can be expressed by the Boltzmann factor

$$N_X/N_Y = \exp(-\Delta E/RT)$$

Assuming Beer's law to hold, the optical absorbance, A, of a particular conformation is proportional to the number of complex molecules in that configuration and to its extinction coefficient, ϵ. Hence, the relation between the ratio of absorbances for two conformations and the temperature would be

$$\ln A_X/A_Y = \ln \epsilon_X/\epsilon_Y - \Delta E/RT$$

If the absorbance is measured at the maxima of two resolved bands, then to a good approximation the ratio,

TABLE I: Absorbance Ratios and Configurational Energy Differences for Complexes of TCNE in Poly(methyl methacrylate)[a]

Donor	High-energy band $\bar{\nu}_{max}$, $cm^{-1} \times 10^3$	Low-energy band $\bar{\nu}_{max}$, $cm^{-1} \times 10^3$	A_X/A_Y[b] (296 K)	A_X/A_Y[b] (77 K)	ΔE, kcal/mol ($E_X - E_Y$)
Anisole	26.7	20.5	0.92	0.82	0.13 ± 0.03
Thioanisole	*27.1*	*18.4*	*0.41*	*0.28*	*0.52 ± 0.07*
o-Dimethoxybenzene	24.1	17.6	0.62	0.52	
p-Dimethoxybenzene	27.0	16.1	0.68	0.57	0.18 ± 0.03
1,2,4-Trimethoxybenzene	23.5	14.7	0.47	0.34	0.47 ± 0.07
p-Xylene	25.6	21.6	1.08	1.17	−0.13 ± 0.03

[a] Bands resolved with a Dupont 310 curve resolver; approximate concentrations 0.5 M, 1:1 donor to acceptor. [b] Approximate error ±2.5%.

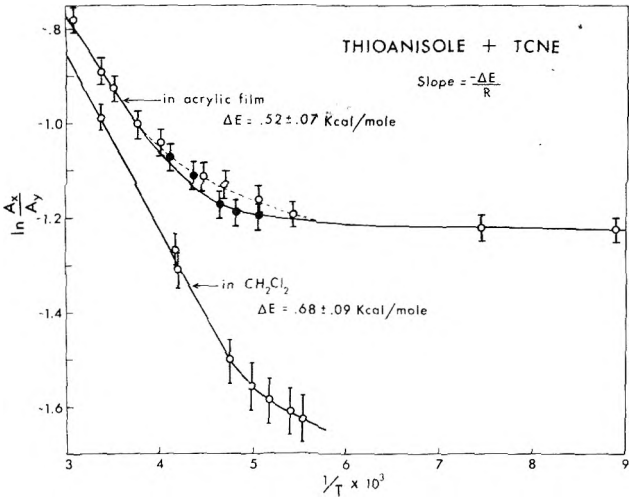

Figure 2. Temperature dependence of the absorbance ratio A_X/A_Y for thioanisole–TCNE in acrylic film and CH_2Cl_2: open circles (O), decreasing temperature; filled circles (●), increasing temperature.

ϵ_X/ϵ_Y, is independent of temperature. Thus, a plot of ln A_X/A_Y vs. $1/T$ should be linear with a slope of $-\Delta E/R$ and an intercept at ln ϵ_X/ϵ_Y.

Results for the thioanisole–TCNE complex are representative of those obtained for the various complexes studied. Figure 2 shows plots of ln A_X/A_Y vs. $1/T$ for thioanisole–TCNE in acrylic film and in dichloromethane. In the high temperature region the plot for the complex in acrylic film has a linear slope with a leveling off of the ratio A_X/A_Y as the temperature is reduced. We attribute this leveling off of the plot to a "freezing in" of conformations when the energy barrier between conformations becomes high relative to kT thus inhibiting attainment of thermodynamic equilibrium. This is supported by the fact that the ratios determined by consecutive lowering of the temperature differed from those found when the temperature was again raised: a hysteresis effect is observed (Figure 2). The other complexes in Table I show a temperature dependence similar to that of thioanisole–TCNE. Complexes of TCNE with anisole and *p*-dimethoxybenzene in acrylic were examined to 4 K with no noticeable change in the absorbance ratios below 77 K.

From the initial slopes of the plots in Figure 2, we have determined the difference in energy between the X and Y configurations to be 0.52 ± 0.07 kcal mol^{-1} for thioanisole–TCNE in acrylic film and 0.68 ± 0.09 kcal mol^{-1} in dichloromethane. The values obtained for the energy difference, ΔE, for other complexes in acrylic film are presented in Table I. A comparison of the values obtained for ΔE shows that with increasing electron-donating power of the substituent groups the Y configuration is increasingly favored. The behavior of the *p*-xylene–TCNE complex is not surprising since methyl substitution perturbs the π-electron distribution of the benzene ring but weakly (ionization potential of benzene 9.245 eV, of toluene 8.82 eV).

In Figure 2, the plots of ln A_X/A_Y vs. $1/T$ for both acrylic film and dichloromethane solution have an intercept at ~0 indicating that the ratio for the extinction coefficients is ~1. This ratio approximates that for the transition overlap integrals which are related to the charge-transfer contribution to the stabilization of each conformation. This indicates that CT stabilization is approximately equal in both complex conformations and that other factors, such as for instance, steric factors and exchange repulsion interactions, may be determining which is the preferred complex geometry. Preliminary studies suggest a ratio of ~1 for the extinction coefficients to be a general trend for complexes of TCNE with substituted benzenes which have double CT bands. Thus, the relative intensities of the two bands can provide a measure for the relative stabilities of the two possible isomers.

Acknowledgment. The research reported here was supported by grants from the National Research Council of Canada to E. M. Voigt and K. E. Rieckhoff.

References and Notes

(1) E. M. Voigt, *J. Am. Chem. Soc.*, **86**, 3611 (1964).
(2) E. M. Voigt and C. Reid, *J. Am. Chem. Soc.*, **86**, 3930 (1964).
(3) A. Zweig, *J. Phys. Chem.*, **67**, 506 (1963).
(4) A. Zweig, *Tetrahedron Lett.*, 89 (1964).
(5) G. G. Aloisi, S. Santini, and S. Sorriso, *J. Chem. Soc., Faraday Trans. 1*, **70**, 1908 (1974).
(6) H. Sakurai and M. Kira, *J. Am. Chem. Soc.*, **97**, 4879 (1975).
(7) L. E. Orgel, *J. Chem. Phys.*, **23**, 1352 (1955).
(8) J. L. Lippert, M. W. Hanna, and P. J. Trotter, *J. Am. Chem. Soc.*, **91**, 4035 (1969).
(9) K. H. Michaelian, K. E. Rieckhoff, and E. M. Voigt, *Proc. Natl. Acad. Sci. U.S.A.*, **72**, 4196 (1975).
(10) W. C. Herndon and J. Feuer, *J. Am. Chem. Soc.*, **90**, 5914 (1968).
(11) D. D. Holder and C. C. Thompson, *J. Chem. Soc., Chem. Commun.*, 277 (1972).

Departments of Chemistry and Physics
Simon Fraser University
Burnaby, British Columbia,
Canada V5A 1S6

Michael J. Mobley
Klaus E. Rieckhoff
Eva-Maria Voigt*

Received December 14, 1976

Journal of Chemical and Engineering Data

APRIL 1977, Vol. 22, No. 2

TABLE OF CONTENTS

NEW COMPOUND SECTION

There is no supplementary material for this issue.

* In papers with more than one author, the asterisk indicates the name of the author to whom inquiries about the paper should be addressed.

BETTER BET ON THE RABBIT

In the fable, the tortoise wins.
Of course, everybody knows it didn't really happen that way.
That's why they call it a fable.
No two ways about it. . .
THE RACE IS TO THE SWIFT.

To keep current on developments in the fast-moving discipline of physical chemistry, you need a journal that publishes up-to-date articles, communications, and symposia. Biweekly—now *that's* up to date. And you'll get biweekly information in. . .

THE JOURNAL OF PHYSICAL CHEMISTRY.

Swift is fine, but it's not nearly enough for an authoritative publication of ACS. You'll find more than 20 papers in every issue, covering spectroscopy, thermodynamics, reaction kinetics, and other areas of experimental and theoretical physical chemistry.

Would you like to be a little bit ahead of the rest of your field—the people who *don't* use the Journal? Then, just . . . *Complete, clip, and mail the coupon below.* Now?

- **new concepts**
- **new techniques**
- **new interpretations**
  . . . plus reports on classical areas

The editors of the Journal of Physical Chemistry strive to select material that is useful in the classical areas of chemistry as well as in modern structural quantum mechanical areas. Start your subscription now. We'll do the rest.

Another service of ACS

The Journal of Physical Chemistry
American Chemical Society **1977**
1155 Sixteenth Street, N.W.
Washington, D.C. 20036

Yes, I would like to receive the JOURNAL OF PHYSICAL CHEMISTRY at the one-year rate checked below:

	U.S.	Foreign and Canada	Latin America
ACS Member *	☐ $24.00	☐ $ 34.00	☐ $ 33.00
Nonmember	☐ $96.00	☐ $106.00	☐ $105.00

Bill me ☐ Bill company ☐ Payment enclosed ☐

Air freight rates are available on request.

Name _____

Street _____ Home ☐ Business ☐

City _____ State _____ Zip _____

Journal subscriptions start in January '77.
Allow 60 days for your first copy to be mailed.
* NOTE: Subscriptions at ACS member rates are for personal use only.

MAN and MOLECULES

A Sound Bank of Science from the American Chemical Society

MAN and MOLECULES Cassettes:

An easy way to keep up with what's happening in science

Outstanding scientists are interviewed in language that everyone can understand. Each cassette has two 15-minute programs.

	ACS Members	Nonmembers
Single Cassette	**$5.95**	**$6.95**
Any Eight Cassettes	**$4.95**/cassette	**$5.95**/cassette
Any 20 or more cassettes to one address		**$4.00**/cassette

10% discount if payment accompanies order

NAME

ADDRESS

CITY STATE ZIP

select your choices and mail to

Dept. M&M
American Chemical Society
1155 16th St., N.W.
Washington, D.C. 20036

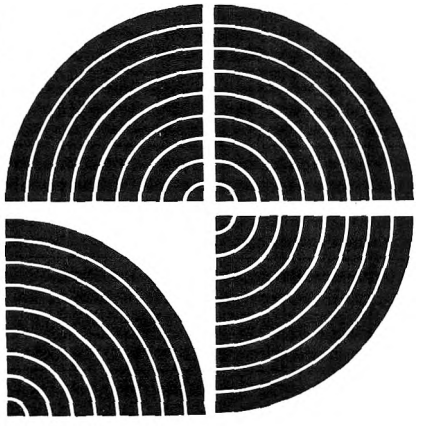

SCIENCE AND SOCIETY

- ☐ **World Energy** Dr. G. T. Seaborg
  The Recycle Society Dr. G. T. Seaborg
- ☐ **Science and the Future** Dr. L. Pauling
  Society and the Future Dr. L. Pauling
- ☐ **Consumer Science** Dr. C. Snyder
  Think Metric J. Odom
- ☐ **Science at Home** Dr. F. Long
  Science in the Developing World Dr. F. Long
- ☐ **Probing Creation** Dr. M. A. Coler
  Community Needs in Research Dr. H. G. Stever

CANCER

- ☐ **Toward a Cancer Vaccine** Dr. R. Hunter
  Cancer and the Cell Membrane Dr. R. Barnett
- ☐ **Cancer and Immunotherapy** Dr. A. Barker
  Chemicals Combating Cancer Dr. D. Grassetti
- ☐ **Improving Cancer Drugs** Dr. P. Shein
  Plants Against Cancer Dr. S. M. Kupchan
- ☐ **Cancer and Chemicals Part I** Dr. C. Heidelberger
  Cancer and Chemicals Part II Dr. C. Heidelberger
- ☐ **Screening for Cancer Agents** Dr. B. Ames
  Chemicals in the Environment Dr. S. Epstein

SCIENCE & SPACE

- ☐ **Discovery of Element 106** Drs. G. T. Seaborg, A. Ghiorso
  Superheavy Elements Dr. E. Anders
- ☐ **How Time Has Changed** Sir G. Porter
  Analyzing with Light Dr. R. Nathan
- ☐ **Fighting the Nation's Fires** Dr. J. Lyons
  Tomorrow's Polymers Dr. R. Deanin
- ☐ **Preserving the Past** Dr. S. Lewin
  The Attraction of Magnets D. Kelland
- ☐ **The Earliest Days** Dr. S. Fox
  Mapping Molecular Fossils Dr. M. Rossman
- ☐ **Optical Communications** J. Cook, B. DeLoach, D. Pearson
  Tomorrow's Transportation F. Kovac
- ☐ **How Smells Shape Up** Dr. J. Amoore
  The Language of Odors Dr. S. Freeman
- ☐ **Neutron Activation and History** Dr. E. Sayre
  Neutron Activation and Hair Dr. A. Gordus, Mrs. J. Gordus

THE NATURAL WORLD

- ☐ **Sun and Climate** Dr. S. Schneider
  Particles and Climate L. Thompson
- ☐ **Foods for the Future** Dr. R. Wiley
  Unconventional Protein Dr. J. Litchfield
- ☐ **Single Cell Agriculture** Dr. I. Zelitch
  The Need for Nitrogen Dr. R. Hardy
- ☐ **Cultures and Climate** Dr. R. Stuckenrath
  The Dating Game in Archeology Dr. F. Rainey
- ☐ **Jojoba Power** Dr. M. Harris
  Nature's Light: Bioluminescence Dr. M. Cormier
- ☐ **Davy Jones' Treasure** Dr. S. Gerard
  The Future of Minerals Dr. V. McKelvey
- ☐ **Water: A Mystery** Dr. W. Drost-Hansen
  The Secrets of Salmon Dr. A. Hasler
- ☐ **Earthquakes: Progress in Prediction** Dr. C. Scholz
  The Seas in Motion Dr. W. Broecher
- ☐ **The Future of Wood I** Dr. H. Tarkow, W. Youngquist
  The Future of Wood II Dr. H. Tarkow, W. Youngquist
- ☐ **History from the Ocean Floor** Dr. J. Heirtzler
  Underwater Communications Dr. J. Atema
- ☐ **How Green the Revolution?** L. Brown
  Hope for the Hungry Dr. D. Oswalt

HEALTH AND MEDICINE

- ☐ **Cataract: The Clouded Eye** Dr. A. Spector
  Nuclear Medicine Dr. W. Wolf
- ☐ **Emphysema Update** Dr. A. Janoff
  Heart and Kidney Help Drs. H. Grotta, D. Fink
- ☐ **Building Better Bones** Dr. L. Hench
  The Sickled Cell Dr. R. Jackson
- ☐ **Nutrition and the Brain** Dr. J. Fernstrom
  Chemical Look at Mental Illness Dr. S. Kety
- ☐ **Menacing Molds** Essay Report
  The Aflatoxin Problem Essay Report
- ☐ **Frogs and Medicine** Dr. J. Daly
  Sickle Cell Progress Dr. W. Brown
- ☐ **Diabetes and the Forgotten Hormone** Dr. H. Tager
  Diabetes: A Progress Report Dr. D. Steiner
- ☐ **The Brain's Own Morphine** Dr. S. Snyder
  Narcotics and the Brain Dr. A. Goldstein
- ☐ **Fighting the Flu** Dr. E. Kilbourne
  Interferon: From Colds to Cancer Dr. S. Baron
- ☐ **Fighting Fat** Dr. J. J. Marshall
  Fiber: Forgotten Nutrient Dr. J. Scala
- ☐ **Dental Vaccines** Dr. W. Bowen
  Tackling Tooth Decay Dr. J. Cassel
- ☐ **New Look at Stroke** Dr. R. Wurtman
  New Key to Heart Disease Dr. A. Gotto
- ☐ **Marijuana and Medicine** Dr. L. Harris
  Artificial Blood Dr. L. Clark
- ☐ **Remodeling the Body** Dr. S. Carr
  Copying Coral for Bones Dr. D. Roy
- ☐ **Herbal Medicine in China** Dr. S. M. Kupchan
  Natural Food Toxicants Dr. J. M. Coon
- ☐ **The Phosphate Problem** Dr. H. DeLuca
  Vitamin D: An Update Dr. H. DeLuca
- ☐ **Nuclear Medicine I** Dr. H. Wagner
  Nuclear Medicine II Dr. H. Wagner
- ☐ **The American Diet: A Critique** Dr. A. E. Schaefer
  Unintended Food Additives Dr. H. Kraybill
- ☐ **Aging: Dissonant Harmony** Dr. D. Harman
  The Molecules of Memory Dr. L. Iverson
- ☐ **Early Hope for the Male Pill** Dr. R. Whistler
  Birth Control: Problem and Prospects Dr. C. Djerassi
- ☐ **Aspirin vs. Prostaglandins** Dr. J. Vane
  The Drug Interaction Problem Dr. D. Hussar
- ☐ **Enzyme Replacement Therapy** Dr. R. Brady
  Prenatal Disease Diagnosis Dr. M. L. Moss
- ☐ **Monitoring High Risk Pregnancies** Drs. G. Stiles, J. Hobbins
  Safety for Premature Infants Dr. J. Morrison
- ☐ **Help for the Critically Ill** Dr. J. Moylan
  A Tilt at Genetic Ills Dr. V. Aposhian

ENERGY

- ☐ **Saving Energy at Home** R. Carlsmith
  Energy and Environmental Thrift Dr. S. Berry
- ☐ **Solar Cells** D. Carmichael
  Solar Homes for the Future Researchers from University of Delaware, Institute of Energy Conversion
- ☐ **Fusion: An Update** Dr. R. Parker
  Geothermal: Fire in the Earth P. Witherspoon
- ☐ **Energy and the Coastal Zone** B. Manowitz
  Energy and the Environment Dr. S. Manahan
- ☐ **Green Thumb Energy** Dr. D. Klass
  Tapping the Oceans Dr. O. Roels
- ☐ **Energy and Industry** A. Waterland
  Energy on the Shelf Dr. F. Kalhammer
- ☐ **Methane from Coal Beds** Dr. R. Stefanko
  Coal's New Face Dr. B. Lee